Adriana Morales Marín

PhD Thesis
February, 2022

eman ta zabal zazu
Universidad del País Vasco
Euskal Herriko Unibertsitatea

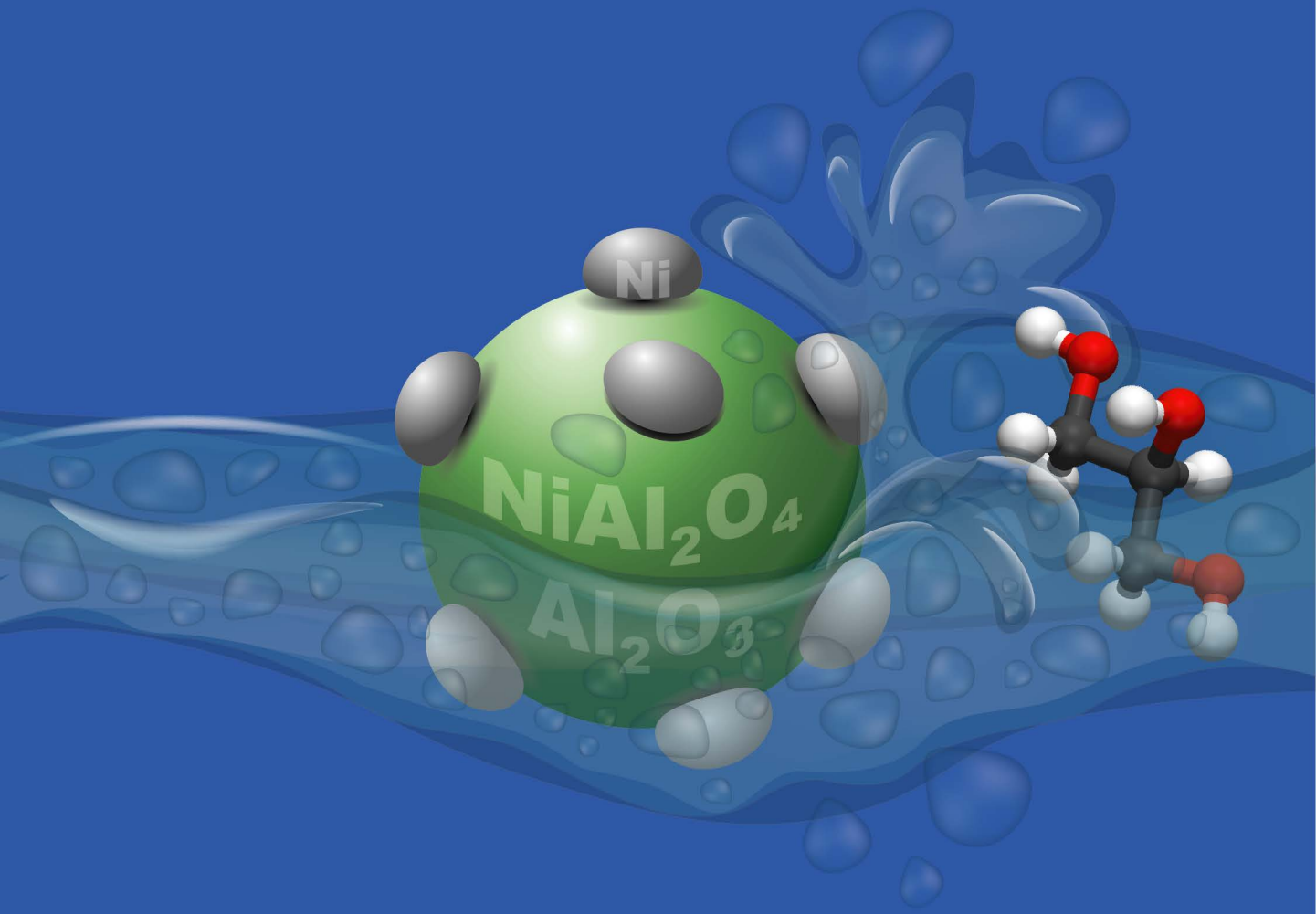

Ni-based catalysts derived from nickel aluminate spinel for hydrogen production by Aqueous-Phase Reforming of glycerol

Universidad del País Vasco
Euskal Herriko Unibertsitatea

DEPARTAMENTO DE INGENIERÍA QUÍMICA
INGENIARITZA KIMIKOA SAILA

Ni-based catalysts derived from nickel aluminate spinel for hydrogen production by Aqueous-Phase Reforming of glycerol

Adriana Morales Marín

Leioa, febrero de 2022

Index

INDEX OF CONTENTS

1. BACKGROUND AND OBJECTIVES 3

1.1 HYDROGEN AS RENEWABLE ENERGY CARRIER 5

1.1.1 Economic actors of the H_2 transition 6

1.1.2 Hydrogen storage 8

1.1.3 Hydrogen to electricity: fuel cells 9

1.1.4 Hydrogen production methods 10

1.2 AQUEOUS-PHASE REFORMING (APR) 15

1.2.1 Bioglycerol valorisation 17

1.2.2 Reactions and thermodynamics of APR 19

1.3 CATALYSTS FOR GLYCEROL APR 23

1.3.1 Noble metal-based catalysts 28

1.3.2 Transition metal-based catalysts 28

1.3.3 Spinel-type catalytic precursor 30

1.3.4 Promoters 32

1.4 OBJECTIVES AND SCOPE 33

2. MATERIALS, METHODS AND CALCULATIONS 39

2.1 MATERIALS 39

2.2 CHARACTERIZATION OF CATALYSTS 39

2.2.1 Catalysts chemical composition and leached metal analysis 41

2.2.2 Textural properties 42

2.2.3 Structural Analysis (XRD and Electronic Microscopy) 44

2.2.4 Solid state spectroscopic analysis (UV-vis-DRS, FTIR and ^{27}Al NMR) 50

2.2.5 Reducibility analysis of samples (H_2-TPR) 53

2.2.6 Surface properties 54

2.3 CATALYTIC TESTS 61

2.3.1 Reaction system 61

2.3.2 APR products analysis 65

2.3.3 Reaction procedures and calculations 68

2.3.4 WGS and CO hydrogenation reactions 71

2.3.5 Mass transfer limitations 72

2.4 DESIGN OF EXPERIMENTS FOR THE OPTIMIZATION OF APR OPERATION CONDITIONS 74

3. CATALYST SCREENING AND INITIAL OPTIMIZATION OF OPERATION VARIABLES 79

3.1 VIABILITY OF Ni-BASED CATALYSTS FOR GLYCEROL APR 79

3.1.1 Synthesis of the Ni-based catalysts 80

3.1.2 Catalysts screening for the glycerol APR 81

3.1.3 Physicochemical characteristics of bulk and supported Ni-based catalysts 84

3.2 OPTIMIZATION OF THE OPERATION VARIABLES 92

3.2.1 Glycerol conversion (X_{Gly}) 93

3.2.2 Conversion to gas (X_{Gas}) 96

3.2.3 Hydrogen yield (YH_2) 98

3.2.4 Selectivity to hydrogen (SH_2) 101

3.3 GENERAL OVERVIEW AND CONCLUSIONS 104

4. NICKEL ALUMINATE SPINEL AS CATALYST PRECURSOR EFFECT OF THE REDUCTION TEMPERATURE 109

4.1 TEXTURAL PROPERTIES 110

4.2 REDUCIBILITY AND PHASE IDENTIFICATION 112

4.3 CRYSTALLINE PHASES AND MORPHOLOGY 117

4.4 SPECIATION ANALYSIS BY FTIR AND UV-vis-NIR DRS 123

4.5 ^{27}Al MAS NMR 126

4.6 SURFACE ACID-BASE CHARACTERISTICS 128

4.7 GENERAL OVERVIEW AND CONCLUSIONS 131

5. EFFECT OF THE REDUCTION TEMPERATURE OF $NiAl_2O_4$ PRECURSOR ON THE GLYCEROL APR PERFORMANCE 135

5.1 GAS PRODUCTS FROM GLYCEROL APR 137

5.2 LIQUID PRODUCTS FROM GLYCEROL APR 142

5.3 REACTION NETWORK 143

5.4 EFFECT OF THE COUPLED TEMPERATURE AND PRESSURE 147

5.4.1 Effect on the gas products distribution 151

5.4.2 Effect on the liquid products distribution 152

5.4.3 Activation energy for glycerol APR....154
5.5 CATALYSTS STABILITY STUDY....156
5.6 CHARACTERIZATION OF USED CATALYSTS....161
5.6.1 Leaching of metals....161
5.6.2 Phase transitions and crystallinity....166
5.6.3 Reducibility and speciation....168
5.6.4 Carbonaceous deposits....171
5.7 GENERAL OVERVIEW AND CONCLUSIONS....171

6. Mg AND Ce PROMOTERS FOR $NiAl_2O_4$ PRECURSOR TO IMPROVE THE APR PERFORMANCE....175
6.1 SYNTHESIS OF MODIFIED CATALYSTS....175
6.2 Mg-MODIFIED NiAl SPINEL....177
6.2.1 Characterization of Mg modified samples....177
6.2.2 Glycerol APR with Mg modified catalysts....190
6.3 Ce-MODIFIED NiAl SPINEL....194
6.3.1 Characterization of Ce-modified solids....194
6.3.2 Glycerol APR with Ce-modified catalysts....206
6.4 CHARACTERIZATION OF USED Mg- AND Ce-MODIFIED CATALYSTS....210
6.4.1 Leaching of metals....210
6.4.2 Textural properties....211
6.4.3 Phase transition and crystallinity....213
6.4.4 Reducibility and speciation....216
6.5 COMPARATIVE ANALYSIS OF Mg AND Ce MODIFIERS FOR NiAl....221
6.5.1 Nickel dispersion and size distribution....222
6.5.2 CO hydrogenation and Water-Gas Shift activity....224
6.5.3 General Discussion....225
6.6 GENERAL OVERVIEW AND CONCLUSIONS....227

7. NANOCASTING SYNTHESIS FOR THE STRUCTURAL OPTIMIZATION OF $NiAl_2O_4$....231
7.1 NANOCASTING SYNTHESIS....231
7.1.1 Hydrothermal synthesis of SBA-15....231
7.1.2 Loading of metals over SBA-15....233

7.1.3 Template removal 233
7.2 CHARACTERIZATION OF NANOCASTED SOLIDS 234
7.2.1 Chemical composition 234
7.2.2 Textural properties 235
7.2.3 Phases and morphology 238
7.2.4 Dispersion and morphology by TEM 243
7.2.5 Reducibility and speciation 246
7.2.6 Surface acid-base properties 250
7.3 GLYCEROL APR WITH NiAl/SBA-15 AND NANOCASTED CATALYSTS 252
7.3.1 Catalytic performance 252
7.3.2 Comparison of NiAl-NCN and NiAl catalysts performance over a range of X_{Gly} 257
7.4 CHARACTERIZATION OF THE USED NiAl/SBA-15 AND NANOCASTED CATALYSTS 260
7.4.1 Leaching of metals 261
7.4.2 Textural properties 261
7.4.3 Phase transition and crystallinity 263
7.4.4 Reducibility and nickel speciation 265
7.5 GENERAL OVERVIEW AND CONCLUSIONS 268

8. SUMMARY AND CONCLUSIONS 273
8.1 SUMMARY 273
8.2 MAIN CONCLUSIONS 275
8.3 FUTURE WORKS 277
9. NOMENCLATURE 281
10. REFERENCES 291
APPENDICESS A3
A. COMPLETE 2^k FACTORIAL DESIGN: 2^k+2, k= 3 (T, P, W/F_0) A3
A.1. Analysis of variance and probability test A7
A.2. Single replicate 2^k factorial design and centre point replicates A8
A.3. Modelling fitting and response surface methodology A9
B. MASS TRANSFER LIMITATION B1
C. DERIVED CONTRIBUTIONS C1

Chapter 1

Introduction

The research into new sources of energy holds the key to preventing the worst effects of climate change, since the energy sector is the major source of global GHG emissions. This chapter introduces the current state of the hydrogen economy including information regarding the economical actors of the transition and progress in hydrogen usage as an energy carrier. Focusing on hydrogen production methods, the advantages of processes involving renewable sources over production from fossil fuels are addressed. An interesting alternative to contribute to possible synergies between the biodiesel industry and hydrogen renewable energies is the Aqueous-Phase Reforming process for production of H_2-rich streams, with low-CO content. Although expensive, noble metal based catalysts present high activity and selectivity. The Ni-based spinel catalytic precursors could be a more economical alternative, with promising catalytic behaviour.

1. BACKGROUND AND OBJECTIVES

The uncertain character of the global reliance on fossil fuels and its important contribution to greenhouse gas (GHG) emissions have challenged the scientific and energy sectors to address climate change mitigation and adaptation while ensuring the growth of energy demand [1]. In this context, scientists from over 150 countries launched a climate emergency warning in 2020 [2], just when our ability to understand, prevent, and manage global emergencies is now greater than ever before, due to the lessons that have been learned from the COVID-19 crisis [3].

Global warming has been historically cyclic, but it has recently accelerated, as a consequence of the economic and population growth, leading to widespread negative impact on human and natural systems. Figure 1.1 documents a comprehensive set of changes the climate system has undergone, which has been compiled by the *Intergovernmental Panel on Climate Change* (*IPCC*) in the 2021 report [4].

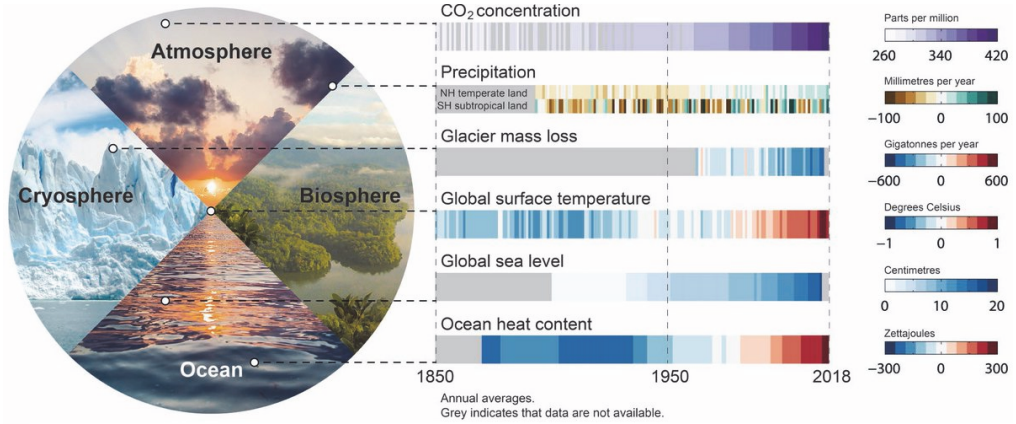

Figure 1.1. Climate system changes. Stripes refer to annual mean values with colors indicating their value [4].

The changes recently observed in the atmosphere, biosphere, cryosphere, and oceans, taking 1850-1900 as a starting point to beyond the yearly and even decadal variability, evidence the climate emergency. In the most recent decade (2011-2020), the global mean surface temperature has increased to 1.09 ºC (0.95-1.20 ºC). The Earth's oceans have warmed by 10^{24} joule between 1971 and 2018, and in response, the global mean sea level had risen by 0.20 meters by 2018. Snow cover decrease and the shrinking

of glaciers has led to the lowest total glacier mass. The annual land area mean precipitation in the Northern Hemisphere temperate regions has increased, while the sub-tropical dry regions have experienced a decrease [4]. In addition, severe wildfires and the resulting deforestation have also increased [5].

According to the *IPCC*, the substantial increase in anthropogenic GHG emissions (52 $GtCO_2$-eq/yr) has boosted global warming in recent years [6]. Anthropogenic GHG emissions include carbon dioxide (CO_2), methane (CH_4), nitrous oxide (N_2O) and fluorinated gases. GHG absorb the radiated heat from Earth towards space and emit radiant energy in the infrared range producing the so-called greenhouse effect. The key main events in the timeline of global warming are industrialization, electric energy use, the discovery of the internal combustion engine and motorcar development. In 2018, the main global GHG emissions came from economic sectors such as electricity generation (44%), transportation (23%), transport (14%) agriculture (12%) and industry (5.9%) [7].

Despite signing climate action commitments at the *United Nations Framework Convention on Climate Change* (*UNFCCC*) in 1992, the overall picture is still troubling, since CO_2 emissions from energy (e.g. electricity and transport) and industry have increased by 60%. Besides, by only reducing CO_2 emissions global warming is not being halted, since the CO_2 that already exists in the atmosphere will remain for hundreds of years and cuts to other GHG could reduce global warming faster. Therefore, the *National Determined Contributions* (*NDCs*) that have been stated by the parties belonging to the *UNFCCC* in the *COP 26* (Glasgow, November 2021), must be clear in three policy areas: (i) the scope of emissions reductions; (ii) their adequacy and fairness; and (iii) concrete steps towards achieving the net-zero emission goal by mid-century. Without this, the goal of limiting global warming to between 1.5-2 ºC of the *Paris Climate Agreement* signed in 2015 will not be achieved, leading to disastrous consequences [8]. It is worth mentioning that *NDCs* are at the heart of the Paris Agreement, and their accomplishment is very important for the achievement of these long-term goals.

In addition to GHG and other pollutant mitigation, the energy sector has to face several challenges regarding the growth in energy demand and its coupling with demographical as well as economic drivers, such as the phasing out of traditional forms

of energy use [1]. In this line, the future transformation of the energy sector could connect climate change mitigation and adaptation challenges, with social development and equity, as *The United Nations* submitted in the 2030 Agenda for Sustainable Development [9]. The *Sustainable Development Goal* (*SDG)* number 7 covers three interlinked areas commonly referred to as "sustainable energy": energy access, renewable energy and energy efficiency. This goal has strong positive interactions with other *SDGs*, including on climate action (*SDG 13*), no poverty (*SDG 1*), zero hunger (*SDG 2*), and good health and well-being (*SDG 3*) [10, 11].

It is widely known that the energy sector is the major source (around three-quarters) of global GHG emissions. This sector holds the key to preventing the worst effects of climate change, perhaps the greatest challenge that humankind has faced, therefore research into new sources of energy has become a necessity. The *International Energy Agency* (*IEA)*, in the analysis of *Net Zero Emissions (NZE*), indicates that most of the reductions in CO_2 emissions through to 2030 will come from technologies already on the market today. Nonetheless, by 2050, almost half of the reductions will come from technologies that are currently at the demonstration or prototype phase, suggesting that major innovation efforts must take place this decade, in order to bring these new technologies to the markets in time [12].

The biorefinery (production of biofuels and chemical products from renewable raw materials) is one of the pillars for the implementation of the bioeconomy, which is a key factor towards achieving sustainable development. The work resulting in this thesis is driven to contribute to possible synergies between biofuels and hydrogen renewable energies, by producing H_2-rich streams from an oxygenated co-product (bioglycerol) from biodiesel production.

1.1 HYDROGEN AS RENEWABLE ENERGY CARRIER

Hydrogen has attracted growing interest as an enabler for a multisectoral transition towards sustainable energy production to meet the bulk of the energy needs of society. In fact, the *IEA* reports that this is a time of unprecedented momentum for hydrogen technologies [13]. In the fast-emerging so-called hydrogen economy, the current dependence on fossil fuels will be substituted by sustainable hydrogen in electricity generation, in the transport sector and in hard-to-abate sectors of the economy such as

heavy industry. The *International Renewable Energy Agency* (*IRENA*) states that hydrogen can replace hydrocarbons in transport, e.g. heavy road transport, rail, aviation, and shipping, which can be a competitive feedstock in the chemical, iron, steel, as well as cement industries [14]. H_2 is a carbon-free fuel, its usage as a fuel depletes GHG emissions since it is a clean-combustion molecule. Notably, given the best scenario, hydrogen could meet up to 24% of the world's energy needs by 2050 [15].

Among other applications, hydrogen can be employed as a storage compound in hydrogen-based systems, not only as power-to-power but also as power-to-fuel and power-to-gas. H_2 is not an energy source but rather an energy carrier, as it allows translocation and storage of energy that can be used at a distance in time or space from the primary production site. The main advantage of H_2 is its permanent energy availability as an energy vector, which allows intermittent and variable renewable energy to continue to be used instead of being curtailed, at times when supply surpasses demand [13]. In other words, integration of H_2 technologies solves the seasonal and daily variations in the availability of some renewable energies (solar and wind energy) making them more efficient [16]. The main advantage of hydrogen over other energy carriers is related to its energy content, having approximately three times more energy per unit mass than most liquid hydrocarbons [17].

Hydrogen is the most abundant element in the universe, although gaseous H_2 is scarce on Earth. In nature, hydrogen is found combined with other elements, like oxygen (water), carbon (hydrocarbons or coal) or with both oxygen and carbon (biomass) [17]. Chemical and/or electrolytic processes are needed to obtain pure H_2 from those compounds, meaning that energy is needed to generate H_2, which then could be used as a fuel for end-use conversion processes, e.g. using fuel cells to produce power and heat. One interesting characteristic of this is the possibility of delocalized production, which could contribute to the energetic independence of diverse regions.

1.1.1 Economic actors of the H_2 transition

Nowadays hydrogen is mainly used as a chemical reagent for fuel upgrading, metallurgical processes and ammonia production, and to a lesser extent, as an energy vector in power and transport sectors. However, H_2 can be employed for other purposes in order to decarbonise the world economy, as depicted in Figure 1.2.

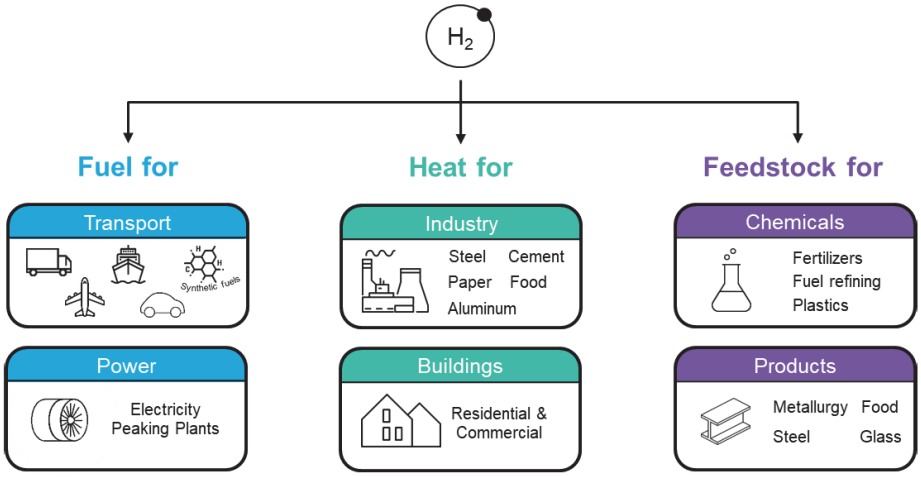

Figure 1.2. Hydrogen uses towards the decarbonization of the economy [15].

In power-to-gas applications, hydrogen can be produced from electric power. Thus, as collected sustainable energy H_2 enhances flexibility and grid integration. A volumetric level of around 15%–20% blended H_2 could be the allowable proportion when being injected into the gas grid to address the embrittlement problem [18].

Hydrogen can also be used to satisfy energy storage needs. In fact, its storage capacity can reach up to MWh, even TWh, owing to its high energy density, while batteries tend to be used in kWh to MWh applications. Moreover, hydrogen storage duration is more efficient than that of batteries; up to weeks or months more, compared to the hourly or weekly storage capacity of batteries [18]. Therefore H_2 storage comprises a wider range of applications. On the one hand, in the short-term range aiming to lower the cost of electricity, by allowing control in the system frequency. On the other hand, in large periods for meet seasonal fluctuations.

Regarding the recent uses of hydrogen in transport, fuel cell vehicles, H_2-fuelled electric powertrains and fuel cell ships have been found, and are gaining commercial interest. To reduce the capacity needs of grid infrastructure for vehicle charging, on-board H_2 applications could help while compensating range limitations of battery-powered vehicles [18]. Although, H_2 can be employed as a fuel for internal combustion engines, hydrogen-only engine applications are still facing challenges regarding efficiency, durability, and low storage capability. Nonetheless, dual hydrogen-fossil fuel engines, which offer better results, have to be taken into

consideration, since they can increase combustion stability and thermal efficiency while reducing the CO and unburned hydrocarbons emissions [19].

In this line, several economic sectors are promoting the hydrogen transition. This interest is not only motivated by the possibility of decarbonisation with the direct use of hydrogen as an energy vector and feedstock, but also by the current energy system transition that drives great pivot opportunities for economical actors related to the oil and gas sector. This includes manufacturers of motor vehicles, chemicals, equipment (electronic and electrical), electricity and gas companies, companies active in transport and storage (including ports), as well as companies engaged in professional, scientific, and technical activities. Particularly, strong supporters are natural gas companies of all scales, large manufacturers of chemicals, transportation and motor vehicle manufacturers (e.g., Toyota and Hyundai), medium-sized enterprises active in professional, scientific, and technical activities, as well as machinery and electronic or electrical equipment manufacturers. [16].

1.1.2 Hydrogen storage

To reach more mature installation technologies and economies of scale of the hydrogen systems, different efforts have been carried out to develop strategies ranging from supply chain to system structure. While the major focus is the hydrogen generating technologies, H_2 transportation and storage should not be neglected, as those represent two big challenges within the hydrogen economy.

Petrol and diesel contain 12 $kWh \cdot kg^{-1}$ of energy while hydrogen has 33 kWh, although storing the same amount of hydrogen requires a larger volume [18]. The most common way of storing large volumes is compressing the H_2 into steel gas cylinders under 700 bar, but the heat transfer and weight of the cylinders still need to be addressed further. Hydrogen underground storage such as depleted deposits of natural gas and oil, and other natural deposits (aquifers, salt caverns, etc.) are the principal solutions for mid and long-term storage. Solid storage technologies are of great interest, but still not commercially viable. Solid storage combines hydrogen with solid materials through adsorption, providing one of the safest modes of H_2 storage, e.g., metal hydrides, metal-organic frameworks, and carbon materials. Liquid hydrogen is another

way to store small volumes of hydrogen, but liquefaction is a time and energy consuming process [18].

Potential hydrogen transport and delivery methods are compressed gas pipelines, cryogenic liquid trucks, and compressed tube trailers [19]. Delivery distance is important in the selection of the hydrogen transport system. For long distances, specific pipelines that fulfil the requirements for hydrogen transportation need to be built, e.g., high-purity stainless steel piping. Other solutions are the decentralized methods of production, which could reduce the cost of hydrogen delivery from the production factories to the refuelling stations.

1.1.3 Hydrogen to electricity: fuel cells

Hydrogen, together with fuel cells (FCs), have a promising role in the global energy market since it is possible to transform the chemical energy contained in the H-H bond into electrical energy with an efficiency of 60- 80% [18], water being the only by product. Although FCs have lower efficiency compared to batteries, the volumetric energy density of a hydrogen FC is much higher than the equivalent electrical capacity of a battery [19].

Different FCs are nowadays used in a variety of stationery and transportation applications, e.g., combined heat and power systems, mobile power systems, portable computers and military communications equipment [20]. Despite the available range of different types of FCs, such as Proton Exchange Membrane (PEMFC), Solid Oxide (SOFC), Alkaline (AFC), Molten carbonate (MCFC) and Phosphoric Acid (PAFC), their working principle is similar, and the general electrochemical reaction is as shown in the following equation.

$$2H_2(g)+O_2(g) \rightarrow 2H_2O+\text{energy} \quad (1.1)$$

Oxygen (or air) and hydrogen are charged at the cathode and the anode respectively. The ionization of H_2 into protons and electrons occurs in the anode, this process is optimized by a catalyst. Generated electrons travel through the external circuit and provide electric power, whereas the oxygen is reduced into oxide species and reacts to form water. Different charge transfer depends on the fuel cell type, thus differing in

their directions and charge carriers in the electrolyte so that the water may be produced on both sides [18].

Generally, FCs are connected in parallel (stack) to increase the output current so as to reach multi-MW scales [18]. It should be mentioned that PEMFCs are widely used in transport and stationary applications. Those operate at low (80-100 ºC) or high (200 ºC) temperatures, presenting a stack voltage efficiency of around 50-60% [18]. PEMFCs present the advantage of fast start-up and disadvantages such as the usage of expensive catalysts that can be easily poisoned by carbon monoxide (CO), limiting the CO content in the H_2 stream feed. In this line, life span of fuel cells shortens by pulse demands and impurities in the gas stream feed.

1.1.4 Hydrogen production methods

An important aspect of the fossil-to-renewable transition is the H_2 production method and feedstocks. Hydrogen is a carbon-free fuel, but its lifecycle carbon emission is determined by both, the primary energy source and the carbon source used for its production [13]. On the one hand, hydrogen produced by diverse energy-demanding thermochemical, electrochemical, and biological technologies, can be classified as a function of CO_2 emissions in *grey, blue, yellow and green*. The H_2 produced by coal-gasification or steam reforming of natural gas is labelled *grey hydrogen*, as considerable amounts of CO_2 are emitted during its production by energy-intensive thermal processes.

Nevertheless, so called *blue, yellow* and *green hydrogen*, are presented as alternatives to improve hydrogen decarbonisation potential. When strategies of CO_2 capture and storage (CCS) are employed during natural gas reforming or coal-gasification, the hydrogen obtained is called *blue hydrogen*. Instead, *yellow hydrogen* refers to that produced electrolytically from nuclear energy, without CO_2 emission. Finally, *green hydrogen* is produced from renewable energy sources, which leads to higher CO_2 emissions reduction. This process has great potential in the long-term, due to cost reduction by massive production and associated technologies development. *Grey hydrogen* is by far the most produced in the industry due to it being the cheapest to produce (1.5 to 2.5 USD·kg^{-1}). In comparison, *green hydrogen* from wind and solar energies, currently costs between 2.5 and 7 USD·kg^{-1}, but recent economical

predictions indicate that the cost of *green hydrogen* will reach around 2 USD·kg^{-1} by 2030 and 1 USD·kg^{-1} by 2050 [11].

On the other hand, H_2 can be produced from an extensive range of substances, such as water, oil, gas, biomass, biofuels, and sewage sludge. As previously mentioned, hydrogen is mainly produced by methods that employ conventional (non-renewable) fossil fuels as feedstock, such as hydrocarbons pyrolysis, coal gasification and natural gas steam reforming. However, a cleaner way of producing H_2 is from renewable resources, such as water and biomass. This route includes H_2 production processes such as water splitting by (photo)electrolysis, biomass (photo)fermentation, pyrolysis or gasification and reforming of oxygenated compounds or sugars. Nonetheless, those production methods are still in the development stage [21]. Hereunder, the main industrially deployed H_2 production methods are divided according to their feedstock: non-renewable or renewable.

1.1.4.1 *Hydrogen production from non-renewable feedstocks*

Nowadays, the hydrogen used in the industry is mainly produced from fossil fuels. In fact, it accounts for approximately 96% of the hydrogen generated worldwide. The main H_2 production processes from fossil fuels are summarized in Table 1.1.

Table 1.1. Processes for H_2 production from fossil fuels.

Process	Description
Gasification Feedstock: coal, pet. coke and oil shale.	• Energy-intensive thermal process (T= 850-1700 °C). • Employs oxygen deficient atmosphere (with or without H_2O). • Further purification is required to remove SO_x of syngas. • Takes place in moving or fluidized bed reactors to favour G-S reaction.

Table 1.1. Processes for H_2 production from fossil fuels. (cont.).

Process	Description
Steam Reforming Feedstock: natural gas, and other methane-containing gases, incl. various mixtures of light HC as ethane, propane, butane, pentane, as well as light and heavy naphtha.	• Endothermic catalytic reaction between hydrocarbons (HC) and steam into H_2 and CO_x (T= 700-800 ºC). • Specifically, Methane Steam Reforming (MSR) accounts for 85% of H_2 produced globally [17]. • Requires purification of H_2 streams by two-step WGS and further methanation reactions to meet CO concentration threshold for ammonia synthesis or PEMFCs apps. • CCS processes to reduce CO_2 emissions [21], e.g., solution with ammine scrubbing or adsorption in zeolite materials through the PSA technique.
Partial Oxidation Feedstock: heavy oil residues and coal.	• Exothermic process (T= 700-900 ºC). • Requires the same purification processes as the SR. • Most appropriate technology for H_2 production from heavy HC feedstock. • POX plants are capital intensive due to the cost of oxygen plant and the desulphurization steps [21].
Autothermal reforming Feedstock: natural gas, heavy oil residues and coal.	• The high exothermicity of POX process provides the energy required for the endothermic SR reactions [17]. • Reforming and oxidation reactions occur at the same time (feeding steam and oxygen). • ATR investment costs are about 15% and 50% lower than SR and coal gasification, respectively. • Advanced large-scale ATR plants enable the lowest hydrogen production cost: 1.48 $\$\cdot kg^{-1}$ [21].

1.1.4.2 *Hydrogen production from renewable feedstocks*

- Electrolysis of water

The production of hydrogen by electrolysis of water is gaining a relevant place to obtain high-quality hydrogen (~100% pure hydrogen). Life cycle assessment (LCA) points out that electrolysis using renewable energy showed the best results among different hydrogen production methods [22]. In fact, the abundance of water on earth assures the production of hydrogen in a rather sustainable way, offering promising opportunities for synergy with renewable energy [18]. The electrochemical obtention of hydrogen is carried out in an electrolysis cell, which is composed of two electrodes (anode and cathode), separated by the electrolyte solution. The electrodes are connected to the power supply and high voltage is applied between them, converting water into hydrogen on the cathode and oxygen on the anode. Current water electrolyser technologies are the Alkaline Electrolyser (AEL), Solid Oxide Electrolyser (SOEL) and Proton Exchange Membrane Electrolyser (PEMEL) [18].

General disadvantages of the electrolytic production of hydrogen is that it requires large amounts of water and electricity and the use of rare earth metals as catalysts. Nevertheless, electrolysers enable the production of clean hydrogen from low-carbon electricity by integrating them with solar and wind power, which is critical for hydrogen to contribute to clean energy transition [23].

- H_2 production from biomass

Biomass that stems from plants is organic matter, in which the energy of sunlight is stored in chemical bonds via photosynthesis. Employment of biomass and derived compounds as feedstock leads to a carbon-neutral cycle, since the amount of CO_2 emission is equal to the amount absorbed by organisms' growth [21]. In this sense, biohydrogen production could meet the desired criteria for a decarbonized economy. The main methods for hydrogen production from biomass are summarised in Table 1.2.

Table 1.2. Processes for H_2 production from biomass.

Process	Description
Biological conversion Feedstock: biohythane (10% hydrogen, 30% methane), lignocellulosic biomass and organic rich waste streams [24].	• Bio-photolysis: water is converted into hydrogen by some bacteria or algae directly through their hydrogenase or nitrogenase enzyme system. • Dark fermentation: the carbohydrate contained in the biomass is converted to organic acids, and then to H_2 [21].
Bio Gasification Feedstock: corn stover, willow, poplar and wood logging residue, corn stover and biogas [20].	• Incomplete combustion of biomass-derived feed into syngas employing steam, air, or oxygen as gasifiers. • High temperatures (between 500- 1400 ºC). • Disadvantages: production of a great quantity of tar and energy-intensive requirement. • Real application: *BioSOFC* plant, biomass gasifier and reformer integrated in a SOFC system to efficiently produce H_2.
Steam Reforming Feedstock: alcohols ($C_nH_{2n+2}O$), bio-oils (e.g,. acid acetic) and sugar alcohols (e.g., xylitol, sorbitol, and glucose)	• Less endothermic reactions compared to hydrocarbons reforming. • The best alternative to gasification and pyrolysis of biomass for H_2 production. • Employs by-products (oxygenates) of biodiesel industry improving its economy. • Generation of large amounts of CO, requiring further purification steps to fuel PEMFCs [17, 22]
Supercritical Water Reforming Feedstock: oxygenated compounds	• Employed for the synthesis of green biobased chemicals and H_2 production. • Main products: acrolein and acetaldehyde as liquid compounds, and a gaseous mixture containing mainly H_2, CO_2 and CO [25]. • Advantages: H_2 yield is favoured by dilute feedstocks. • Challenges: formation of large amounts of carbon. Plugging issues in the reactor. Catalyst deactivation.

Table 1.2. Processes for H_2 production from biomass (cont.).

Process	Description
Aqueous-Phase Reforming Feedstock: C2+ oxygenates, such as glucose, glycerol, and ethylene glycol.	• Reforming of oxygenates (e.g., glycerol) in liquid water into H_2 as well as light alkanes. • Feedstocks: by-products from biomass conversion processes that are partially or totally soluble in water. • Takes place at low operating temperature (T= 150-270 ºC) • Process conditions favour WGS reaction, yielding less CO.

1.2 AQUEOUS-PHASE REFORMING (APR)

One of the most promising methods to produce hydrogen is to use oxygenated biomass products (e.g. alcohols, ketones, polyols and sugars) [26]. This H_2 production route allows valorisation of biorefinery waste streams and does not employ fossil sources. Although biomass thermochemical processing requires high-temperature treatments, much lower temperature regimes are used for biomass-derived oxygenated compounds processing. Figure 1.3 shows a qualitative diagram of the temperature and pressure conditions at which petroleum and carbohydrate feedstock are commonly processed [27]. It is noticeable that petroleum processes are usually conducted at higher temperatures and in the vapour phase, while some biomass-derived carbohydrate processes are carried out in the liquid phase. The latter is the case of the APR, which involves low temperature reforming at moderate pressure to ensure the liquid phase of the reagents.

The APR is one-step processing for obtaining hydrogen where the energy-intensive process of steam generation is avoided, which translates into noteworthy energy costs savings and prevents the decomposition of the oxygenated feedstock. The APR operating at low temperature enhances the Water-Gas Shift (WGS) reaction for the obtention of fuel cell-grade H_2 with very low CO contents. These streams can be directly fed to the fuel cell to produce power, heat or gas fuel [28]. At the same time, the high pressure employed makes the produced gaseous stream more suitable for in-situ purification and sequestration of CO_2.

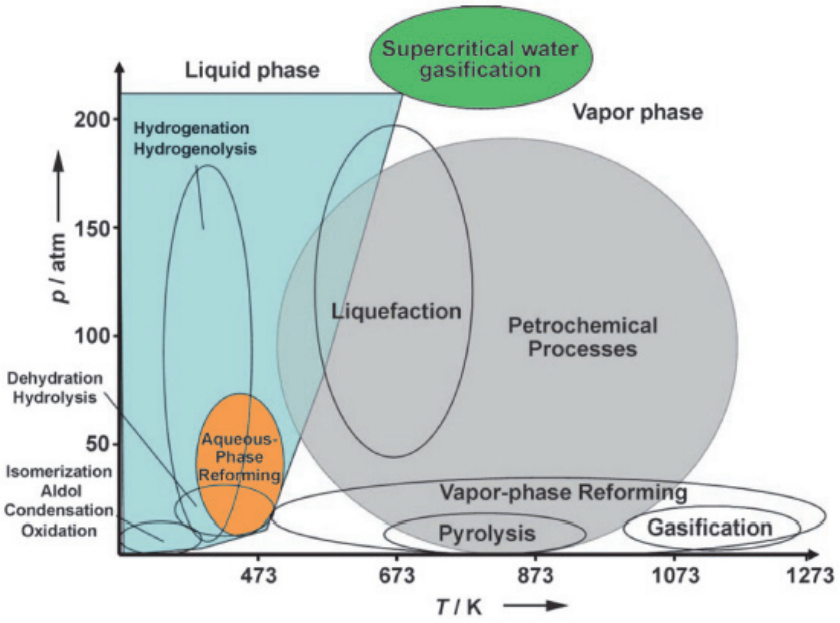

Figure 1.3. Diagram of approximate reaction conditions for the catalytic processing of petroleum versus biomass-derived carbohydrates [27].

APR was first reported in 2002 by the group of Dumesic et al., who studied hydrogen production by low-temperature reforming. They employed Pt-based catalysts for the APR of oxygenated hydrocarbons derived from biomass [29]. High H_2 yields were obtained by using sorbitol, glycerol, and ethylene glycol as feed model compounds, and proposed its application on integrated electric generation. Additionally, they suggested the use of FC/liquid-phase reformer systems, in which some FCs might not require extensive purification of the reformer gas effluent, owing to its very low CO content (< 300 ppm) and other main components in the gas (CO_2 and CH_4) acting only as diluents [29].

Although various biomass-derived substrates can be used for hydrogen production by APR, including glucose [30], ethanol [31], methanol [32], ethylene glycol [33], glycerol [34-36], xylitol [37] and sorbitol [38], the present thesis work addresses the hydrogen obtention by APR of bioglycerol, which is a co-product in the industrial production of biofuels.

As previously mentioned, development in advanced biofuels production is urgent, aimed only at the usage of non-food raw materials, as well as APR integration to biorefineries that improve the economic cost of biofuels [12]. For that purpose, the challenge to develop an efficient catalysed reaction system for the production of gas streams with high H_2 concentration by APR must be addressed, regarding less expensive and active catalysts, optimal operation conditions, and higher selectivities, which is the main objective of this doctoral thesis.

1.2.1 Bioglycerol valorisation

Many liquid hydrocarbon production processes generate organic aqueous-phase streams mainly composed of oxygenated compounds (including glycerol), which are co-products that require treatment before disposal. Among these processes are biomass gasification followed by Fisher-Tropsch (FT) synthesis; pyrolysis of biomass and subsequent pyrolysis-liquid refining; the FT synthesis of reverse WGS effluents, and especially, the biodiesel and bioethanol production from transesterification and fermentation processes [39], are the most relevant. Commercialization of these biorefinery processes involves high investment and production costs, which can be optimised through APR of the side streams (water fractions) for the production of hydrogen and other added-value products [39]. As a proof of this concept, Shell Company started a pilot unit with the same technology, using bio-H_2 obtained from APR of biomass feedstock (sugar, non-food cellulosic derived biomass, etc.) for producing gasoline, diesel and jet fuels [28].

The industrial intensification in biodiesel production and related bioglycerol cogeneration is depicted in Figure 1.4. The boom experienced in the bioglycerol production in the last 20 years is attributable to a rising trend in biofuel production activities, especially that of biodiesel, which accounts for 64% [40]. As glycerol is the major by-product (10% w/w) of the biodiesel production process, a considerable surplus of bioglycerol has been generated causing a fall in its market. Note that this fall is also related with pollution, storage, treatment, and disposal problems caused by glycerol overproduction [41]. Consequently, the need for valorisation strategies to transform the crude glycerol into higher value-added products has driven several efforts to expand the usage of glycerol beyond traditional uses, in order to maintain its commodity chemical

status [28, 40, 41]. Note that glycerol can serve as a substrate in the production of various higher value-added products. In fact, it has been included as one of the 12 platform molecules for biorefineries by the Department of Energy of the United States [42].

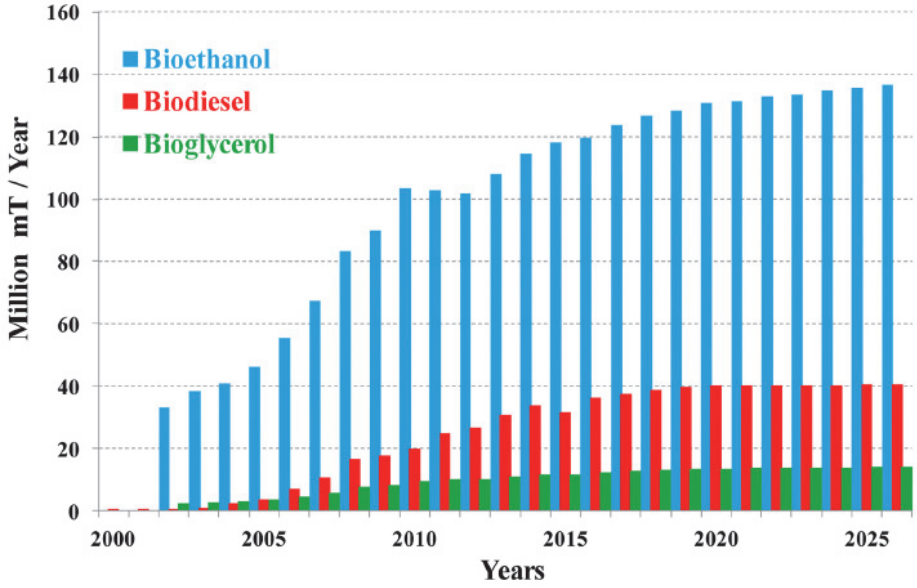

Figure 1.4. Evolution of biofuels production and bioglycerol co-generation [28].

Glycerol (propane-1,2,3-triol) is a colourless, odourless, viscous liquid and non-toxic multi-functional organic compound, with amphiphilic properties owing to its stable chemical structure provided with three hydroxyl groups. It is also thermally stable, i.e., high energetic availability is required for bond breaking and the formation of other compounds [43]. Glycerol co-produced in biodiesel production is called crude glycerol or bioglycerol, which normally contains several impurities leftover from the transesterification reaction. Those impurities vary depending on the biodiesel production process and affect the physical, chemical, and biological properties of the glycerol. Among others, typical impurities are water, free fatty acids (FFA), methanol, fatty methyl esters (FAMES), soaps, salts and/or vegetable colours. Although the price of bioglycerol is low, its applications are limited by its degree of purity. Refining it is an expensive process consisting of neutralization to remove the soaps and salts, vacuum evaporation to eliminate methanol and water, and further refining to improve glycerol purity [43].

Unrefined bioglycerol has low demand in traditional industries, even though it can be a low-cost feedstock with several practical applications in the renewable energy sector. Integration of bioglycerol into renewable energy production processes not only benefits those processes but also helps to reduce the cost of biodiesel production [41]. Hence, glycerol has been projected as a potential biomass-derived feedstock for the production of hydrogen and other value-added chemicals [44]. It has been proved that crude glycerol, derived from biodiesel production, produces hydrogen through APR [45]. In fact, Seretis & Tsiakaras [45] studied the effect of some impurities on the APR process, using a commercial SiO_2-Al_2O_3-supported nickel catalysts and they found that the selectivity of the gaseous and liquid products are not strongly affected by the addition of a low concentration of impurities. In this context, the production of H_2 from bioglycerol is presented as an interesting low–carbon solution. However, until now, solutions of glycerol without impurities have been the preferred feedstock in APR studies since it allows a better understanding of the APR reaction pathways and the catalytic performance [39].

Regarding the forecast of biorefineries production, there may be a smoothing out on the growing slope of bioglycerol generation, due to a stabilization or even a decline in biodiesel production during the next decade. In any case, several factors influence the future of biodiesel production, such as the availability of raw material, internal policies, markets, etc., in some cases leading to a local production rise against the international trend, becoming a stable crude glycerol source [46]. It is noteworthy that the oncoming second and third-generation biofuels production involves advanced bioenergy feedstock (non-food), including waste streams from other processes, short-rotation wood crops and feedstock that does not require the use of arable land [12], as well as novel production technologies such as the hydrotreatment of vegetable oil [47]. Note that the latter promises to occupy 11% of the forecast global biodiesel production in 2022 [48].

1.2.2 Reactions and thermodynamics of APR

APR of oxygenated compounds with carbon to oxygen ratio of 1:1 is a one-step catalytic process, which operates in the liquid phase at low temperature (150-270 ºC) and pressure high enough to keep the reactants in the liquid phase (usually 15-60 bar)

[27]. The glycerol reforming follows the overall reaction shown in equation 1.2, to ideally yield 7 mol of H_2 and 3 mol of CO_2 per mol of glycerol reacted.

$$C_3H_8O_3(l) + 3H_2O(l) \rightarrow 3CO_2 + 7H_2 \qquad \Delta H^0_{25°C} = 215\ kJ/mol \qquad (1.2)$$

The overall reforming reaction (equation (1.2) consists of many reactions, but it can be described as the sum of two consecutive steps corresponding to the decomposition of glycerol (DG) by C- C cleavage and subsequent WGS reactions, (equations 1.3 and 1.4, respectively).

$$C_3H_8O_3(l) \rightarrow 3CO + 4H_2 \qquad \Delta H^0_{25°C} = 338\ kJ/mol \qquad (1.3)$$

$$CO + H_2O \rightleftarrows CO_2 + H_2 \qquad \Delta H^0_{25°C} = -41\ kJ/mol \qquad (1.4)$$

However, the reaction products of APR are broader than only CO_2 and H_2 due to the occurrence of side reactions. One of the most undesired reactions is the hydrogenation of CO (equation 1.5) and CO_2 (equation 1.6), which affects the hydrogen yield and selectivity.

$$CO + 3H_2 \rightleftarrows CH_4 + H_2O \qquad \Delta H^0_{25°C} = -206\ kJ/mol \qquad (1.5)$$

$$CO_2 + 4H_2 \rightleftarrows CH_4 + 2H_2O \qquad \Delta H^0_{25°C} = -165\ kJ/mol \qquad (1.6)$$

Fisher-Tropsch [44, 49], dehydration and subsequent hydrogenation [50], as well as decarbonylation along with hydrogenolysis reactions [45] are also unwanted reactions, since they consume H_2 in detriment of the H_2 selectivity. In this line, the effect of the catalysts in the selectivity plays a major role in the resulting product distribution.

In the APR of glycerol, a series of liquid intermediates are obtained, including 1,2-propanediol, ethylene glycol and lactic acid. It is worth mentioning that these compounds can be employed as useful chemicals after proper separation strategies, e.g., 1,2-propanediol, which is produced by selective hydrogenation of propylene oxide [28], is used as a commodity chemical in the pharmaceutical industry, in customer care products and/or as antifreeze. On the other hand, efficient separation of the compounds in the gaseous effluent of the APR is also a keystone for the practical use of APR. For

example, proper separation of hydrogen or methane for energy generation is necessary downstream the APR reactor [29]. Fortunately, this high pressure operation favours an easy CO_2 capture and separation by Pressure Swing Adsorption (PSA) or membrane technologies [49].

In APR, glycerol is catalytically converted to products in both phases, liquid and gaseous. The reforming is a three-phase reaction between the reagents in the aqueous-phase, the solid catalyst and products in the gas phase. In the WGS, water has to come in contact with both the solid catalyst and the gaseous CO and the reaction takes place at the gas-liquid-solid interface [51]. The gaseous product stream contains H_2 and CO_2, as well as CO and light alkanes, while the liquid product is usually composed of oxygenated hydrocarbons. The formation of these products involves several reactions over a catalyst, as suggested by Dumesic et al. [29]. Accordingly, the reactant undergoes dehydrogenation, followed by the cleavage of C–C bonds, which leads to the formation of CO and H_2. Then CO reacts with water to form CO_2 and H_2 by the WGS reaction. The further reaction of CO and/or CO_2 with H_2 leads to alkanes and water by methanation and Fischer–Tropsch reactions. Alkanes can be formed on the catalyst surface by cleavage of C–O bonds, followed by hydrogenation of the resulting adsorbed species. Furthermore, dehydration reaction of glycerol (C-O bond cleavage) could be catalysed by acidic sites from the catalyst support, or catalysed by protons in the aqueous solution, which is followed by hydrogenation reactions on the catalyst [29].

Reaction conditions (temperature and pressure) for producing hydrogen from glycerol are dictated by thermodynamics [49]. However, the range of possible APR operating conditions (T/P) is determined by vapour-liquid equilibrium (VLE) to prevent the evaporation of reactants. Qualitatively, Figure 1.5 shows the changes in the standard Gibbs free energy (ΔG) associated with the main reactions involved in the glycerol APR. The glycerol reforming (GR) at vapour-phase reported shows decreasing negative values for ΔG with temperature, indicating that GR is spontaneous at the APR temperature (170 ºC-270 ºC) [28]. Methanation reaction also presents a negative ΔG under the same conditions, but increases with temperature. Noteworthy, the ΔG of WGS reaction does not vary considerably within the temperature range.

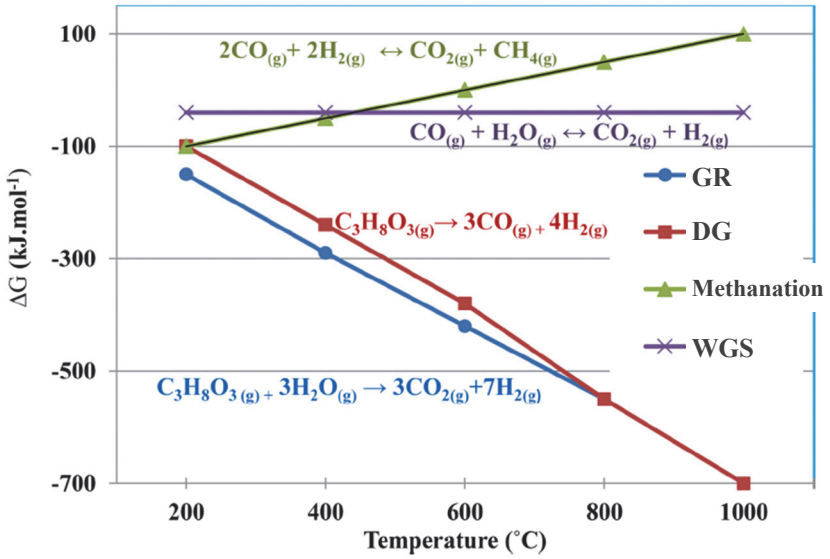

Figure 1.5. Evolution of Gibbs free energy (ΔG) as a function of the temperature for the main reactions involved in the SR of glycerol [28].

Recent thermodynamic estimation at aqueous-phase conditions (37 ºC and 1 atm) determined that the enthalpy of the WGS reaction becomes positive (endothermic reaction), whereas at atmospheric pressure and temperatures above the boiling point of water, the WGS is exothermic [51]. In the same line, it was found that the ΔG is positive for GR at atmospheric aqueous-phase conditions. Nonetheless, the reaction is exergonic (ΔG< 0) above 37 ºC, for the glycerol APR and for the WGS. Therefore, a higher temperature not only will favour spontaneity but will also lead to increased reaction rate. Observe that applying a higher pressure might be beneficial for kinetic reasons, even though it is not required from a thermodynamic point of view [51].

Seretis and Tsiakaras [52] performed a thermodynamic study for the APR of glycerol for hydrogen production, employing the Gibbs free energy minimization method. The findings were that higher glycerol conversions are achieved at higher temperatures, which involves an increase in pressure to ensure VLE, but at expense of hydrogen selectivity decrease. Besides, the methanation reaction can be reduced at high temperatures and low pressures but not eliminated, indicating that methanation is thermodynamically favoured over H_2 production. On the contrary, the chemical equilibrium of the WGS reaction (equation 1.4) is favoured by low temperatures,

converting CO into CO_2 and additional H_2. That study also showed that carbon formation can be removed when the ratio of total pressure to the saturated vapour pressure is less than 1.4 and the temperature greater than 127 ºC.

APR is also influenced by water, which can alter the thermodynamics of catalytic surface species that participate in APR reactions system. By the development of microkinetic models, some roles of H_2O on the catalytic mechanism of glycerol APR have been identified, including the supplying of OH^-/H^+ groups in the surface needed to oxidize surface CO via WGS; the promoting of C–H and O–H bond cleavages; and the thermodynamic inhibition of C3 species decarbonylation [36]. The undesirable product formation, under APR operating conditions, should be addressed to improve the catalytic process, through the optimization of the reaction conditions and the design of an active, selective and stable catalyst.

With regards to the thermodynamic implications for the optimization of the glycerol APR for H_2 production, this doctoral thesis includes a study of the optimal T/P operating conditions carried out by means of a statistical design of experiments.

1.3 CATALYSTS FOR GLYCEROL APR

The efficiency of the glycerol APR to produce H_2 depends on the proper formulation of the catalyst, which should ideally provide high selectivity to H_2, resistance against deactivation, and high reaction rates under optimal operating conditions. Taking into account the reactions described in the previous section, catalytic materials must be effective in breaking the C-C, O-H, and C-H bonds. In addition, the catalyst should promote the WGS reaction of adsorbed CO, since it prevents catalysts poisoning as well as avoiding hydrogenation reactions of CO and/or CO_2 to form alkanes via methanation and FT reactions. Note that these undesired side reactions lead to the consumption of H_2, comprising a selectivity challenge [29, 49]. Regarding the surface properties of the support, basic nature improves the activity and selectivity to H_2, while acid supports promote the formation of alkanes and induce the deposition of carbonaceous material [53]. Other requirements for the catalyst are related to a high specific surface area, smaller crystals (high dispersion), and hydrothermal and chemical stability.

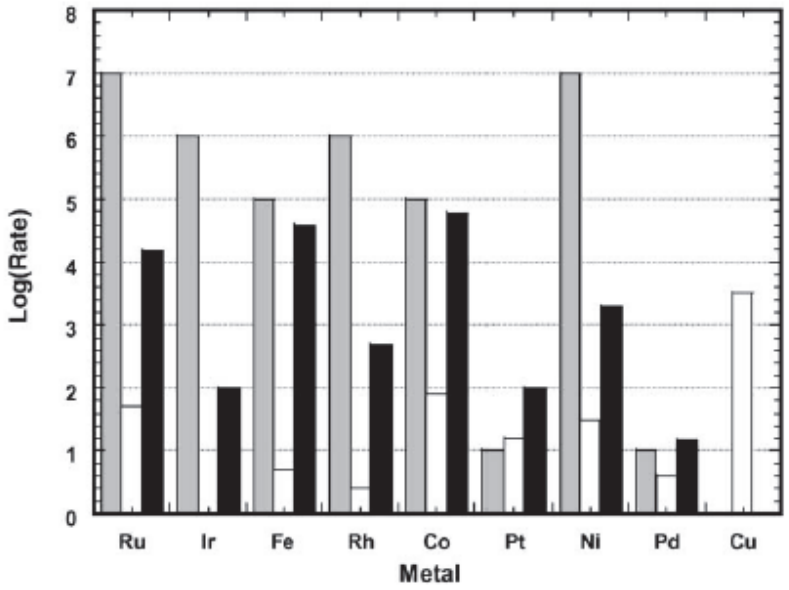

Figure 1.6. Relative rates of C-C cleavage (grey), Water-Gas Shift reaction (white) and methanation reaction (black) [49].

For the purpose of comparison, the catalytic activity of different metals for C-C bond cleavage during hydrogenolysis of ethane (model reforming reaction), as well as their activity in WGS reaction (supported on alumina), and relative rates of methanation (supported on alumina) are depicted in Figure 1.6. Both, noble and transition metals are included in this comparison. Activity rates of the noble metals indicate that Ru present the highest rate for C-C bond cleavage, although relevant activity for undesired methanation reactions. Nonetheless, Pt and Pd have presented equilibrated characteristics such as moderate activity for C-C bond cleavage as well as higher H_2 selectivity owing to their WGS activity and low methanation rates. Studies of the activity of Pt and Pd catalysts have proved those advantages in the APR [54-56]. Nonetheless, Pd catalysts presented severe deactivation issues [57].

Table 1.3 summarizes relevant research works on hydrogen production by APR process of oxygenated compounds using various types of catalysts.

Table 1.3. Catalysts studied for hydrogen production by APR.

Metal	Loading (wt%)	Support	Promotor	Synthesis*	Calcination	Reduction	Substrate**	Ref.
Pt	3%	γ-Al_2O_3	n/a	IWI	260 ºC	260 ºC	G, S, Gly, EG and MeOH	[29]
Pt	0.5- 3.4%	γ-Al_2O_3	n/a	IWI	100 ºC, 12h	250 ºC, 2 h	MeOH and EG	[54]
Pt	1.5- 10%	γ-Al_2O_3 and mixture of γ-, δ- and θ-phases	n/a	IWI	260– 600 ºC, 2 h	250 ºC, 2 h	Gly and crude Gly	[55]
Pt	0.3- 1.2%	γ-Al_2O_3	n/a	WI	260 ºC, 2 h	260 ºC, 2 h	Gly	[35]
Pt	0.7%	MgO, γ-Al_2O_3, CeO_2, TiO_2 and SiO_2	n/a	Pt CD + RD or WI	n.d.	n.d.	Gly	[58]
Pt	0.25- 0.5%	NaY	n/a	IE	260 ºC, 2 h	260 ºC, 2 h	MeOH and EtOH	[59]
Pt	0.6%	γ-Al_2O_3	n/a	WI	260 ºC, 2 h	260 ºC, 2 h	Gly	[60]
Ni	10%	γ-Al_2O_3	n/a	WI	500 ºC, 10 min	843 ºC, 2 h	Gly	[60]

*IWI: Incipient Wetness Impregnation; WI: Wet Impregnation; CD: Colloidal Dispersion; RD: Reflux Deposition; IE: Ion Exchange; DP: Deposition-Precipitation; CP: Co-Precipitation;

**G: Glucose; S: Sorbitol; Gly: Glycerol; EG: Ethylene Glycol; MeOH: Methanol; EtOH: Ethanol

Table 1.3. Catalysts studied for hydrogen production by APR (cont.).

Metal	Loading (wt%)	Support	Promotor	Synthesis*	Calcination	Reduction	Substrate**	Ref.
Pt, Ni, Rh, Ru and Pd	4%	SiO_2	n/a	IWI	260 ºC, 3 h	450 ºC, 2 h	EG	[56]
Pt or Pd (bimetallic)	3%	γ-Al_2O_3	Ni, Co and Fe	IWI	260 ºC, 3 h	450 ºC, 2 h	EG	[56]
Pt	5%	Carbon nano-fibers	n/a	IWI	300 ºC, reductive atmosphere	n/a	EG	[61]
Co, Ni and Co	15%	Carbon nano-fibers	n/a	IWI	400 ºC, reductive atmosphere	n/a	EG	[61]
Pt	4.3-9.8%	SAPO-11, active carbon, HUSY, SiO_2, MgO, γ-Al_2O_3	n/a	IWI	450 ºC, 3 h	450 ºC	Gly	[62]
Ni, Co, Cu	17%Ni, 15%Co and 6%Cu	γ-Al_2O_3	n/a	IWI	450 ºC, 3 h	550 ºC, 2 h	Gly	[62]
Pd	5%	Fe_3O_4	n/a	CP	300 ºC, 3 h	200 ºC, 3 h	EG	[57]

*IWI: Incipient Wetness Impregnation; WI: Wet Impregnation; CD: Colloidal Dispersion; RD: Reflux Deposition; IE: Ion Exchange; DP: Deposition-Precipitation; CP: Co-Precipitation;

**G: Glucose; S: Sorbitol; Gly: Glycerol; EG: Ethylene Glycol; MeOH: Methanol; EtOH: Ethanol

Table 1.3. Catalysts studied for hydrogen production by APR (cont.).

Metal	Loading (wt%)	Support	Promotor	Synthesis*	Calcination	Reduction	Substrate**	Ref.
Pt-Ni bimetallic	1%Pt-6%Ni	CeO_2-γ-Al_2O_3	n/a	WI	600 ºC, 6 h	800 ºC, 1 h	Gly	[63]
Ni	15%	$LaAlO_3$, CeO_2, MgAl	n/a	DP	400 ºC, 5 h	n.d.	Gly	[64]
Raney-Ni	Sn/Ni atomic ratio= 0.075	n/a	Sn	Reduction, Sn addition, heating (inert atmosphere).	n/a	260 ºC, 2 h	Gly	[65]
Ni	16-17%	MxOy-γ-Al_2O_3	M=Zr, Ce, La or Mg	WI	500 ºC, 4 h	700 ºC, 2 h	Gly	[34]
Ni-Co bimetallic	3.3-16.7%Ni/ 16.7- 3.3%Co	γ-Al_2O_3	CeO_2	Combustion (Urea)	500 ºC, 10 min	483 ºC, 2 h	Gly	[66]
Ni-Cu hydrotalcite precursors	20% NiO/ 0-10% CuO	n/a	n/a	CP	800 ºC, 3 h	950 ºC, 1 h	Gly	[67]

*IWI: Incipient Wetness Impregnation; WI: Wet Impregnation; CD: Colloidal Dispersion; RD: Reflux Deposition; IE: Ion Exchange; DP: Deposition-Precipitation; CP: Co-Precipitation;

**G: Glucose; S: Sorbitol; Gly: Glycerol; EG: Ethylene Glycol; MeOH: Methanol; EtOH: Ethanol

Generally, the catalytic studies for hydrogen production by APR have focused on noble metal catalysts. Nonetheless, the search for an alternative active metal, which costs less and is more readily available, has driven the development of catalytic formulations based on transition metals due to their potential for breaking the C-C bond [68], as can be observed in Figure 1.6. In fact, Ni and Co have been tested in the APR reaction showing favourable results, though they still have more limited hydrogen yield due to their increased activity in methanation reaction (Figure 1.6) [57, 66, 69].

1.3.1 Noble metal-based catalysts

Among APR active catalysts, Pt-based ones have been extensively studied for APR. Pt/γ-Al_2O_3 was the earliest catalyst investigated for APR [29] and hence more in-deep studies regarding APR thermodynamics [60], kinetics [70] and operational conditions effect [35] have been carried out using supported Pt catalysts since then [49, 71]. Furthermore, Pt has shown good stability properties, such as difficulty to be oxidized, related leaching inhibition [61], and presenting minimal carbon deposition [54]. Nonetheless, problems related to the support hydroxylation, which lead to leading to blocking of the Pt active sites have also been reported [55]. In this line, support properties have been investigated, and it has been found that the acidity of the catalysts containing Pt is specifically related to the support and decrease in the following order: γ-Al_2O_3> MgO> SiO_2> activated carbon. In general, Pt supported on basic support gave high hydrogen molar concentration as well as increased hydrogen formation rate due to the alkali enhancement of APR reactions by remarkable absorption of CO_2 on the support [62].

1.3.2 Transition metal-based catalysts

Less costly catalysts based on transition metals are being studied, using novel synthesis techniques that could lead to similar characteristics to those of noble metals [64]. Ni-based catalysts proved good catalytic activity in APR, especially Ni/Al_2O_3, despite its poor H_2 selectivity [72]. After Pt, Ni is considered the most active transition metal for C-C and C-H cleavage as well as WGS promotion [28]. In fact, bimetallic supported Pt-Ni catalysts have shown great glycerol conversion, H_2 yield and stability under the hydrothermal conditions of the APR [56, 73]. However, this solution is still limited regarding the objective of cost optimization and so, efforts towards designing much

cheaper Ni-based catalysts are being driven. Nickel is a metal with high potential in the aqueous-phase reforming due to its low price, reporting a cost of $ 16.393/T in the London Metal Exchange at the beginning of 2021 [74]. Nickel has attracted considerable attention due to its good intrinsic activity in C-C scission (Figure 1.6), which is especially elevated on small particles [34, 67, 75]. Another non-precious metal with comparable performance to that of Pt-base catalysts, in H_2 production by APR, is Raney-Ni. Huber et al. [65] reported that Raney-Ni-Sn catalysts proves to decrease the methanation while maintaining high rates of C-C bond cleavage. The addition of Sn to nickel decreases the rate of methane formation from C-O bond cleavage while maintaining the high rates of C-C bond cleavage required for hydrogen formation.

Observable drawbacks of the transition metal-base catalysts to be taken into consideration are the incomplete conversion of carbon atoms, leading to the generation of coke and side products, as well as lixiviation problems, e.g. Co [76].

With regards to the support, it has been demonstrated that alumina-supported catalysts provide higher ability of WGS and better APR activity. For instance, Guo et al. [58] found that conversion of C to gas on typical alumina oxides supports was high enough, observing an extremely low amount of CO at reactor exit. Besides, γ-Al_2O_3 is relatively inert against non-desirable C-O scission, owing to its mild Brønsted acidity [28]. Nonetheless, stability is compromised by the presence of water. Ni catalysts supported on alumina normally provide mechanical resistance and chemical stability, but under the hydrothermal conditions of the APR, they could suffer a severe deactivation [77]. This hydrothermal effect provokes γ- Al_2O_3 phase transition to boehmite [36], thus disrupting the chemical stability of Ni.

In order to inhibit the aforementioned drawbacks, in this thesis work, the catalysts design strategy is addressed by nickel aluminate spinel catalytic formulations, as the catalytic precursor. Upon reduction, nickel can be highly dispersed on the surface if it is previously incorporated into the spinel structure of alumina to form nickel aluminate ($NiAl_2O_4$) [78]. $NiAl_2O_4$ is obtained by synthesis techniques such as simultaneous nickel and alumina precipitation (co-precipitation) and nanocasting. Additionally, this work proposes an approach to surface modification, which contributes to the selectivity challenge by means of promoters impregnation. This work also studied the viability of

nickel-loaded NaY catalyst for APR, obtained by ion-exchange synthesis. Tang et al. [59] reported high activity of zeolite-based catalysts in APR, with the advantage of reduced use of precious metals, and low cost of zeolite materials, which deserve further investigation. Zeolites are well known as excellent supports and promoters of metal catalysts in hydrocarbon reforming [59].

1.3.3 Spinel-type catalytic precursor

The oxide spinels are a group of compounds with the general formula AB_2O_4, where usually A is a divalent cation and B trivalent. Nickel aluminate is a typical example of this spinel formula ($NiAl_2O_4$). As depicted in Figure 1.7, spinels crystallized in the cubic Fd-3m space group, with oxide anions closed-packed in a face-centred cubic (fcc) arrangement. The cations occupy two distinct kinds of crystallographic sites, one of them is tetrahedrally (Td) coordinated by the anions and the other octahedrally (Oh). There are one tetrahedral and two octahedral sites per formula unit of 4 anions [79]. In many cases, the single A cation in the formula unit occupies the tetrahedral site, while the two B cations occupy the two octahedral sites. Such an arrangement is known as the "normal" cation distribution, denoted $(A)[B_2]O_4$. The opposite extreme is the "inverse" arrangement, $(B)[AB]O_4$, which occurs almost as frequently.

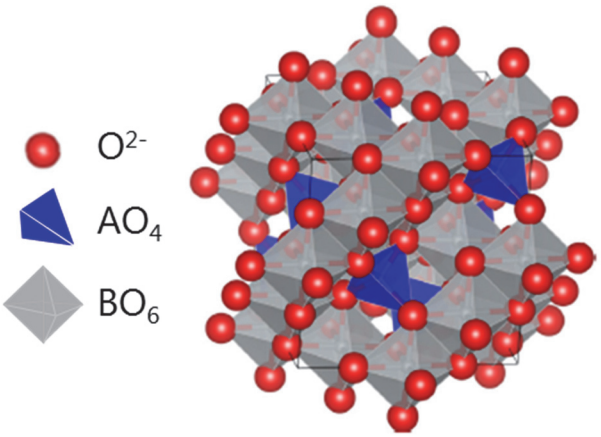

Figure 1.7. Cubic crystal structure of AB_2O_4 spinel-type oxides [80].

Spinel-type structures can show variable degrees of disorder of the A and B cations over tetrahedral (Td) and octahedral (Oh) sites. The inversion parameter (i_s) is used to describe this disorder and is defined as the fraction of the B cations at the Td sites; i_s can

vary from 0, in the completely normal spinel ($^{Td}(A)^{Oh}(B_2)O_4$) to 1, in the completely inverse spinel ($^{Td}(B)^{Oh}(AB)O_4$). A totally disordered configuration is obtained for i= 0.67 [81]. The synthesis method influences the spinel inversion degree, especially the calcination temperature [79].

Nickel aluminate spinels tend to present a large inversion, since the octahedral site preference energy of Ni^{2+} is large and positive (37.6 $kJ \cdot g^{-1}$), and much higher than that of Al^{3+}(−10.5 $kJ \cdot g^{-1}$) [80]. Furthermore, nickel aluminate spinel presents a cation distribution which depends on temperature, tending to random arrangements with increasing temperature [79]. Note that the inversion degree influences the nature of the surfaces and their catalytic properties [82].

In some catalytic applications, $NiAl_2O_4$ plays the role of catalytic precursor, meaning that once it is reduced a Ni/Al_2O_3 catalyst is obtained, by exudation of metallic nickel from spinel structure and forming metallic nickel nanoparticles over alumina. The reduction step, indeed, can alter the structural properties. It has been reported that reduction at high temperatures promotes the rearrangement of nickel in the aluminate matrix, and relatively small metallic Ni crystallites with good textural stability can be obtained. Furthermore, if metal-support interactions are improved, a better catalytic behaviour could be obtained [83], which would imply a significant advantage for APR applications. $NiAl_2O_4$ has been used as a catalytic precursor in applications other than APR, such as, cracking [84] and reforming [83, 85, 86]. Furthermore, dehydrogenation activity of $NiAl_2O_4$, after reduction above 450 ºC has been reported by Murthy et al. [87]. Specifically, in the TQSA research group, the nickel aluminate has been successfully applied in the gas-phase reforming of methane [88, 89] and isooctane [90].

Diverse methods have been addressed for the spinel synthesis. Nickel/aluminium co-precipitation [91, 92]; sol-gel, which employs the dissolution of cation precursors in a citric acid aqueous solution [93]; combustion with urea or glycine that reaches temperatures above 1000 ºC, thus requiring proper heat dissipation to avoid metal sintering [94]; and nanocasting for the obtention of mesoporous spinels with large surface-to-volume ratios and uniform pore diameters [95, 96]. In this thesis work, the selected synthesis methods for the spinel-type catalytic precursors are the basic

co-precipitation of nickel and aluminium precursors and nanocasting technologies employing a siliceous mesoporous template.

The co-precipitation method is commonly used since it is a simple and scalable synthesis method. Co-precipitation is convenient to synthesise a highly active Ni catalyst because of its good chemical homogeneity, phase purity and morphology [97]. Therein, co-precipitation leads to a well-defined and crystalline precursor compound with a mixed cationic lattice that contains all metal species of the final catalyst. The anions are thermally decomposed to give the mixed oxides and the active component, in this current case nickel, finally segregates on a nanometric level to yield supported and uniform metal nanoparticles [92]. Upon reduction with hydrogen, it is expected that the active nickel sites are present in a monodisperse fixed form on special sites provided by the nickel aluminate structure [91].

Nanocasting is a synthesis where nanoscale templates are used to prepare mesoporous solids replicating those templates. This technique allows the synthesis of materials within a controlled structure and highly interconnected pores with high surface areas [98]. This could lead to a nanostructured nickel aluminate with improved accessibility and stability properties [96], which are particularly desirable for processes taking place at the phase boundary between solid particles and a liquid phase [95]. The usage of mesoporous silica materials as templates, such as SBA-15, have drawn much attention owing to their uniform structure, large surface areas and large pore volumes, which make them perfect candidates to serve as hard templates for nanocasting synthesis [99].

1.3.4 Promoters

While support acidity is counterproductive for the H_2 selectivity and stability of the catalysts, an interesting alternative to diminish the support acidity effect is the usage of bimetallic catalysts. High WGS activity makes Cu a potential candidate, since bimetallic alloys (e.g. Pt-Cu, Ni-Cu) have reported high hydrogen selectivity, though low reforming activities [100, 101]. Sn-modified Ni catalysts have also shown high selectivity for the production of H_2 and great stability when Raney-Ni is used to form resilient Ni_3Sn alloys surrounding a Ni core in the catalysts [102]. Co is expected to improve H_2 selectivity. However, Co is vulnerable to oxidation and subsequent leaching by acids formed in the

aqueous solution, which leads to rapid deactivation [100]. For example, Luo et al. reported good activity for glycerol APR of a bimetallic Ni-Co catalyst and a beneficial synergic effect between the metals for hydrogen selectivity. Nonetheless, the addition of cerium was required to decline methane selectivity and suppress the sintering phenomenon during the reaction [66].

Ceria (CeO_2) and magnesium oxide (MgO) have been commonly employed as support modifiers for APR catalysts, but not as surface promotors. On the one hand, ceria has reported good activity for WGS reaction. Rahman et al. [63] obtained high H_2 yield with Pt/NiCeAl catalysts, as well as Iriondo et al. [34] who found close surface interaction between Ce ions and NiO phases, leading to improved initial glycerol conversion in APR with Ni/Ce-Al_2O_3. On the other hand, the ability of MgO as structural promoter, to both inhibit carbon deposition and increase the stability of the Ni/Al_2O_3 catalysts, has also been reported [103]. Hydrotalcite-derived Mg-Al oxides have presented high surface area, basic surface properties and structural stability, and has been used in alcohol dehydrogenation reactions [104]. Nonetheless, the activity and selectivity of the catalyst in ethanol conversion reaction were highly dependent on the Mg/Al ratio. Based on the above considerations, within this thesis work, the strategy of impregnation of Ce or Mg over the nickel aluminate is addressed for the modification of surface properties.

1.4 OBJECTIVES AND SCOPE

The recent fast-paced evolution of various hydrogen technologies regarding production, storage and transportation, and energy and heat production are required for the accelerated implementation of the hydrogen economy seen nowadays. All this effort to transition to decarbonised energies and fuels aims to significantly contribute to the world challenges regarding sustainability. Consequently, advanced biofuels are another player in the sustainability challenge as effective low-emission fuels.

This thesis work aims to contribute to hydrogen production technologies, while also contributing to biorefinery profitability, by means of studying hydrogen production from glycerol by Aqueous-Phase Reforming (APR). The APR is optimal for processing derived-biofuels side streams in a single step, with low energy requirements and, under favourable reaction conditions, for the production of hydrogen streams with low CO

content. Nonetheless, APR faces important efficiency challenges. The viability of this technology is conditioned to the development of active catalysts, selective to the formation of reforming products (H_2, CO and CO_2), stable for long periods of operation and economically viable.

This doctoral thesis proposes the use of spinel-type catalytic precursors with $NiAl_2O_4$ formulation, the performance of which can be comparable to that of noble metal catalysts. The formulation of these new catalytic materials aims to obtain higher intrinsic activity of metal crystallites. Regarding the catalysts design, optimization efforts are performed by novel nanocasting synthesis and surface modifications, as well as concerning the APR process by evaluating operation conditions.

Based on these considerations, the main objective of this thesis is the production of low-CO hydrogen streams from glycerol by APR on novel nickel-based catalysts with improved performance, using nickel aluminate as the catalytic precursor. To accomplish this goal, the following specific objectives have been proposed:

- Definition of the most suitable formulation of Ni catalytic precursor for the synthesis of active, selective, and stable APR catalysts.
- Determination of the optimal activation conditions for nickel aluminate spinel precursor to be used in the APR reaction.
- Comprehensive physicochemical characterisation of synthesised catalysts.
- Evaluation of catalytic performance in the aqueous-phase reforming of glycerol and determination of the key catalytic properties.
- Optimization of the APR operative conditions and protocols, in a continuous reaction system.
- Optimization of the catalyst formulation by using either nanocasting synthesis method to obtain mesostructured catalysts or by using surface promoters (Ce and Mg).

The following chapters of this thesis are arranged as follows:

Chapter 1 presents the actual environmental situation and the input of renewable energies in the zero-emissions challenges and sustainability objectives. Thus, it describes the current state of the hydrogen economy, regarding economical actors of the transition and progress in hydrogen use as an energy carrier, production, storage, transportation, and fuel cells. This chapter also includes the evolution of biorefinery, the current general scene and the low carbon fuel expectations, as well as the possibilities for economical improvements. Finally, the bases for the APR process are described, accompanied by an overview of the catalysts involved and the consequent proposal to develop this thesis work.

Chapter 2 describes the materials and analytical techniques employed in the synthesis and characterization of catalysts, as well as the followed protocols. In addition, the employed reaction setup for the catalytic test is described, along with the employed corresponding protocols, methods for product analysis and calculations.

Chapter 3 consists of two parts. The first part addressing an evaluation of various Ni-based catalysts in glycerol APR. A sort of supported and bulk nickel-based precursors were synthesized, and their basic physicochemical properties characterized. Based on the catalytic screening, the best catalyst formulation has been chosen. A revealing comparison is included, between the activity and physicochemical characteristics of the nickel aluminate bulk catalytic vs. nickel supported on alumina precursors. The second part comprises the development of a factorial design of experiments and the response surface methodology in the optimization of H_2 production by glycerol APR using bulk nickel aluminate precursor.

Chapter 4 includes a comprehensive characterization of bulk nickel aluminate spinels and the effect of the reduction temperature in their physicochemical characteristics. The results of several characterization techniques regarding textural, structural, morphological and surface properties are examined.

Chapter 5 presents the catalytic performance of the nickel aluminate materials, introducing plausible reaction pathways, based on the activity results obtained with $NiAl_2O_4$ precursor reduced at different temperatures. The catalytic results are discussed based on the physicochemical characteristics studied in Chapter 4. Besides, the results at three different operative conditions (temperature/pressure), applied in the APR

reactions: 235 ºC/35 bar, 250 ºC/45 bar, 260 ºC/52 bar, are included. The results of stability for 50 h TOS test for the two best catalysts, as well as the modifications suffered by the used catalysts, are also included.

Chapter 6 deals with the optimization of catalyst derived from nickel aluminate spinel precursor by incorporating basic promoters. The effect of modification of NiAl catalyst by impregnating Ce and Mg, at three loadings, is studied. The differences in their catalytic behaviour with respect to the non-doped nickel aluminate are described. Characterization of the used catalysts is also discussed.

Chapter 7 addresses the catalysts optimization by the nanocasting synthesis. The structural and morphological characteristics of the synthesized siliceous template SBA-15 are shown. Besides, this chapter describes the synthesis of the three nanocasted catalysts studied: one keeping the SBA-15 as support and the other two, with different SBA-15 template removal. The characterization results and catalytic performance in the glycerol APR of the synthesised catalysts are evaluated. Also dealt with is a comparative study of performance, over a range of glycerol conversions, between best-nanocasted catalysts and nickel aluminate synthesised by coprecipitation. Characterization of the used catalysts is also discussed.

Chapter 2

Materials, Methods and Calculations

This chapter includes overall information regarding materials, methods, equipment, and protocols employed for the characterization of catalysts developed within this doctoral thesis work. In addition, a description of the catalytic performance evaluation setup for the Aqueous-Phase Reforming is provided. Firstly, the materials employed for the synthesis and characterization analysis of catalysts, are detailed. It is followed by the description of the characterization techniques and protocols, including ICP, N_2 physisorption, TGA-MS, XRD, Electronic Microscopy, UV-vis-DRS, FTIR, NMR, H_2-TPR, CO_2-TPD, NH_3 chemisorption, IR-Pyridine, H_2 chemisorption, and quantification of carbonaceous deposits. Finally, the reaction system, experimental setup, and the statistical analysis for operative optimization are described.

2. MATERIALS, METHODS AND CALCULATIONS

In this chapter, materials, equipment, methods, and protocols used during the development of this thesis work are described. First, the reagents employed for the synthesis of catalysts are summarised. Following, the techniques of characterization of the catalysts are addressed. Finally, a detailed description of the reaction system, operation conditions used and the definitions of equations of the calculated reaction parameters are included. Additionally, the fundamentals of the statistical study carried out for the experimental setup are also included.

2.1 MATERIALS

The catalysts studied in this doctoral thesis were synthesized in the laboratories of the Chemical Technologies for the Environmental Sustainability Group (TQSA) in the UPV/EHU, except the zeolite-supported one, which was synthesized in the laboratories of the Technische Chemie II research group at the Technical University of Munich (TUM), Germany. Different synthesis methods were performed, such as co-precipitation, wetness impregnation and nanocasting. The precursors, reagents and other chemicals employed are summarized in Table 2.1.

In addition, different gases were employed during the characterization of the catalysts, sample conditioning treatments and in the experimental reaction unit, including Ar, He, N_2 and H_2, all with 99.999% purity. Mixtures employed were: 5% H_2/Ar, 5% O_2/He 10% NH_3/He, 5% CO_2/He. The gas cylinders were provided by Air Liquid and Praxair suppliers. For reaction, analytical grade glycerol and water (MilliQ quality) were used.

2.2 CHARACTERIZATION OF CATALYSTS

The analysis techniques employed for the characterization of the catalysts are addressed in this section. Brief technique descriptions and corresponding experimental protocols are described for the analysis of the chemical composition, textural and structural properties, active phase dispersion and particle size, composition and speciation, reducibility, surface properties, and C-content quantification.

Table 2.1. Characteristics of synthesis precursors, reagents and other chemicals.

	Name	Lineal Formula	Supplier	Assay	Function
SYNTHESIS PRECURSORS	Nickel(II) acetate tetrahydrate	$Ni(OCOCH_3)_2{\cdot}4H_2O$	Sigma-Aldrich	99.998%*	Catalytic precursor
	Nickel(II) nitrate hexahydrate	$Ni(NO_3)_2{\cdot}6H_2O$	Sigma-Aldrich	99.999%*	Catalytic precursor
	Aluminium nitrate nonahydrate	$Al(NO_3)_3{\cdot}9H_2O$	Fluka	≥98%	Catalytic precursor
	Cobalt(II) nitrate hexahydrate	$Co(NO_3)_2{\cdot}6H_2O$	Sigma-Aldrich	≥98%	Catalytic precursor
	Magnesium nitrate hexahydrate	$Mg(NO_3)_2{\cdot}6H_2O$	Sigma-Aldrich	99%	Catalytic precursor
	Cerium(III) nitrate hexahydrate	$Ce(NO_3)_3{\cdot}6H_2O$	Sigma-Aldrich	99.998%*	Catalytic precursor
	Tetraethyl orthosilicate (TEOS)	$Si(OC_2H_5)_4$	Sigma-Aldrich	98%	SBA-15 precursor
SYNTHESIS REAGENTS	Pluronic P-123	$EO_{20}PO_{70}EO_{20}$**	Sigma-Aldrich	n/a	SBA-15 precursor
	Sodium hydroxide	NaOH	PanReac	>98	SBA-15 remover
	Ammonium hydroxide solution	NH_4OH	Sigma-Aldrich	~25% NH_3	Precipitating agent
	Ethanol	H_3CCH_2OH	VWR Chemicals	100%	Impregnation solvent
OTHER CHEMICALS	Glycerol	$C_3H_8O_3$	PanReac	>99.5%	APR reagent
	Zeolite NaY Powder (CBV 100)	---	Zeolyst Inter.	n/a	Support
	Sodium carbonate	Na_2CO_3	Riedel-de Haën	≥99.8	C-quantification standard
	Poly(tetrafluoroethylene) (PTFE)	$(CF_2CF_2)_n$	Sigma-Aldrich	n/a	SBA-15 remover
	Potassium bromide	BrK	Sigma-Aldrich	≥99%*	IR pelletizer

*trace metals basis **EO: poly(ethylene oxide), PO: poly(propyleneoxide)

2.2.1 Catalysts chemical composition and leached metal analysis

Inductively Coupled Plasma (ICP) analysis is capable of quantifying the concentration of several elements in a single sample, with very low detection limits (in the ppb region) and the advantage of low sample consumption [105]. In the ICP spectrometry, plasma is generated by electrically heating an inert, monoatomic gas (e.g. argon) to a high-temperature plasma (4000- 6000 ºC) by induction with an electromagnetic coil. The ionization is initiated by a spark from a tesla coil to generate an electron that initiates the chain reaction towards the plasma stabilization [106]. Two ICP analyses were done in this work: (i) ICP-Mass Spectrometry (ICP-MS) for determining the chemical composition of the catalysts, and (ii) ICP-Atomic Emission Spectrometry (ICP-AES) to detect the number of leached metals in the overall liquid product collected after each reaction.

In the ICP analysis, the analyte atomization and excitation convert the sample into gas phase atoms and ions, providing sufficient energy to promote the valence electrons of the atoms from their ground state to an excited state.

In ICP-MS, the ions generated by ICP are separated and quantified by the mass spectrometer, according to their mass/charge (m/z) ratio. The ICP-MS is highly precise and sensitive.

In ICP-AES, the wavelength of the photons emission released when the atoms relax from the reached excited state back to the ground state is measured. This wavelength is characteristic of each element (e.g. 393 nm for Ni) and its intensity is related to the concentration of the element [106].

Experimental protocol

The catalysts' chemical composition was determined by ICP-MS in an Inductively Coupled Plasma Quadrupole Mass Spectrometer (Q-ICP-MS) *XSeries 2*, branded *Thermo Fisher Scientific,* with Peltier cooled impact bead spray chamber together with concentric glass PFA micro nebulizer, screened torch and equipped with a *Cetac ASX-510* autosampler. The Q-ICP-MS was coupled to an *Xt* interface for high total dissolved solids.

The dispersion of the samples (30 mg) was done in three steps. First, with *aqua regia* for 24 h at 90 ºC. $HClO_4$ was added during evaporation (second step) to prevent the formation of insoluble fluorides. Then, the residue was treated with HCl and heated overnight, dried, and finally acidified with HNO_3 (third step).

ICP-MS analysis was performed by the Isotopic Geochronology and Geochemistry Analysis Service of the Advanced Research Facilities (SGIker) from the University of the Basque Country (UPV/EHU).

ICP-AES was carried out in *Agilent 5100* equipment to quantify leached metals in the liquid product, without any conditioning step. The percentage of metal (M) leached was calculated as follows (equation 2.1):

$$\text{Leached M}(\%) = \frac{t \times F_{feed} \times M_{liq}}{M_{cat}^{0}} \times 100 \qquad (2.1)$$

being t the time of reaction (min); F_{feed} the feed liquid flow ($mL \cdot min^{-1}$); M_{liq} the concentration of the metal in the liquid effluent at the end of the reaction ($mg \cdot mL^{-1}$); and M_{cat}^{0} metal loading in the fresh catalyst (mg).

ICP-AES analysis were performed by the Central Analysis Service Unit of Bizkaia (SCAB) from SGIker.

2.2.2 Textural properties

N_2 physisorption analysis has been carried out to obtain the textural properties of the solids. The specific surface area (S_{BET}) and pore size distribution were calculated.

Adsorption is defined as the enrichment of molecules, atoms, or ions in the vicinity of an interface. Physisorption occurs whenever an adsorbable gas (the adsorptive) is brought into contact with the surface of a solid (the adsorbent). The material in the adsorbed state is called the adsorbate. The intermolecular forces involved are those related to van der Walls and the condensation of vapours [107].

Physisorption in mesopores (2- 50 nm) takes place in different stages. In monolayer adsorption, the adsorbed molecules are in direct contact with the surface of the adsorbent. In multilayer adsorption, more than one layer of molecules are

accommodated in the adsorption space, so that not all the adsorbed molecules are in contact with the surface layer of the adsorbent. The isotherm curve describes the adsorption phenomena of a gas on a solid surface, whereby the amount of gas adsorbed on the solid is represented with respect to the pressure at a given temperature. The absorption isotherms are obtained by the manometric method usually employing N_2 at cryogenic temperature (–196 ºC). The shape of the isotherm is dependent on the solid porosity and the differences of interaction energies between adsorptive and adsorbent.

The surface area of a solid is commonly calculated from its adsorption isotherm, using the Brunauer-Emmett-Teller (BET) method:

$$\frac{P}{V_a(P_0-P)}=\frac{1}{V_mC}+\frac{C-1}{V_mC}\times\frac{P}{P_0} \qquad (2.2)$$

where V_a is the volume of adsorptive ($cm^3 \cdot g^{-1}$) at the relative pressure (P/P_0); V_m is the specific monolayer capacity ($cm^3 \cdot g^{-1}$); and C is a constant factor exponentially related to the energy of monolayer adsorption. V_m and C can be obtained by plotting the first term of equation 2.2 vs. P/P_0. This representation is limited to the P/P_0 values corresponding to the monolayer, often within P/P_0= 0.05 0.35 range, for type ll and lV isotherms, where a lineal range is obtained. Then, the slope and the intercept from this linearization are used to estimate V_m and C [106].

Once V_m and C are known, the surface area of the adsorbent is assessed as the area effectively occupied by the adsorbed molecules in the monolayer:

$$S_{BET}(m^2 \cdot g^{-1})=\frac{V_m \cdot \sigma_m \cdot N}{W \cdot V_{mol}}\times 10^{-18} \qquad (2.3)$$

where σ_m is the molecular cross-sectional area (nm^2); N is the Avogadro´s number ($6.022 \cdot 10^{23}$ at.$\cdot mol^{-1}$); W is the mass used in the experiment (adsorbent) (g); and V_{mol} is the molar volume of an ideal gas at normal conditions ($cm^3 \cdot mol^{-1}$).

At P/P_0= 0.99 the total gas volume that the sample adsorbs on its pores, which is used for the estimation of the total pore volume is calculated. The pore size distribution is also assessed by the Barrett, Joyner and Halenda method (BJH) [108]. The BJH method is applied to the desorption isotherm, and it is based on the Kelvin equation, which

describes capillary condensation in cylindrical pores and allows the quantification of the pore radius (r_P) for different values of P/P_0, as shown in equation 2.4:

$$r_P(nm) = \frac{2 \cdot \sigma \cdot V_l \cdot \cos\upsilon}{RT \times \ln(P/P_0)} x10^3 + t_l \quad (2.4)$$

being σ the surface tension of liquid N_2 ($N \cdot m^{-1}$); V_l the liquid molar volume of N_2 ($L \cdot mol^{-1}$); υ the contact angle between the condensed phase and the adsorbent surface (rad); R the ideal gas constant ($atm \cdot L \cdot mol^{-1} \cdot K^{-1}$); T the absolute temperature of the analysis (K); and t_l the thickness of the adsorbed layer (nm). Depending on P/P_0, the t_l parameter can be estimated from different correlations, such as the Halsey correlation presented in equation 2.5 that gives satisfactory results for mesoporous materials:

$$t_l(nm) = 3.54 \left[\frac{-5}{\ln(P/P_0)} \right]^{\frac{1}{3}} \quad (2.5)$$

Experimental protocol

The specific surface area (S_{BET}) together with pore volume (V_P) of the mesoporous solids were calculated from N_2 adsorption-desorption isotherms measured at 77 K in *Micromeritics TRISTAR II 3020* equipment. Before the adsorption, catalysts were degassed with N_2 at 300 ºC for 10 h, using a *Micromeritics SmartPrep* portable degasser, to completely clean and dry the surface. All textural properties were determined by BET and BJH methods.

The isotherms were automatically obtained by the equipment, consisting of the successive addition of a known volume of N_2 to the adsorption system and further recording of equilibrium pressures from the lowest value to almost saturation pressure (~1–101 kPa). The hysteresis loop was recorded similarly but by registering the equilibrium pressure after removing a certain volume of N_2.

2.2.3 Structural Analysis (XRD and Electronic Microscopy)

Structural analysis of catalysts was done by means of XRD and Electronic Microscopy. The crystalline phase analysis was carried out to obtain information in the

samples about the repetitive distribution of the atoms in the space, as well as to quantify crystallite sizes. Instead, electronic microscopy was used to analyse the shape and size distribution of the particles.

2.2.3.1 *X-Ray Diffraction (XRD)*

X-ray spectroscopy is based on the measurement of the emission, adsorption, dispersion, fluorescence, and diffraction of the electromagnetic radiation, giving highly useful information related to composition and structure. X-ray diffraction (XRD) is a technique capable of determining the crystalline structure and distinguishing allotropic or isomorphic forms.

X-ray is electromagnetic radiation of a short wavelength (0.01-10 nm). In a diffractometer, X-rays are generated in a cathode ray tube by heating a filament to produce electrons, which are accelerated by applying a voltage and then bombarded onto the target material. When electrons have sufficient energy to dislodge the inner shell electrons of the target material, characteristic X-ray spectra are produced. These spectra consist of several components, the most common being K_α and K_β. K_α consists, in part, of $K_{\alpha1}$ and $K_{\alpha2}$. To filter radiation by foils or crystal monochromators is required to produce monochromatic X-rays employed in XRD method. $K_{\alpha1}$ and $K_{\alpha2}$ are sufficiently close in wavelength so that a weighted average of the two is used [109].

The XRD technique is based on optical phenomena (diffraction) produced when monochromatic X-ray radiation interacts with a crystallite, producing a diffracted X-ray and constructive interference only when Bragg's Law (equation 2.6) is satisfied,

$$n \cdot \lambda = 2d_{hkl} \cdot \sin\theta \tag{2.6}$$

where λ is the wavelength of the X-ray radiation (Å); θ is the diffraction angle (rad); and d_{hkl} is the lattice spacing in a crystalline sample (Å).

Crystallites have a regular distribution of atoms in the space, being the distance between those of the same magnitude (d_{hkl}). Thus, crystallites can diffract the X-ray, behaving as a three-dimensional diffraction grating, where the light is passing through the *d-spacing* and produce diffraction [106]. The diffracted X-rays are then detected. By scanning the sample through a range of 2θ angles, all possible diffraction directions of

the lattice should be attained due to the random orientation of the powdered material. By the conversion of the diffraction peaks to *d*-spacing, the crystallites are identified based on standard reference patterns registered in databases, such as the *International Center for Diffraction Data* (ICDD-PDF), due to each mineral having a unique set of *d*-spacing [109].

In addition, from the broadening in the diffraction patterns, the average crystallite size can be calculated using Scherrer equation:

$$d_{crystal} = \frac{K \cdot \lambda}{\beta \cdot \cos\theta} \tag{2.7}$$

$$\beta^2 = \beta_{obs}{}^2 + \beta_{ins}{}^2 \tag{2.8}$$

where K is a shape factor (K= 0.89, for sphere-like particles); β (in rad) is the peak broadening from the full width at half maximum (FWHM), which is corrected by adding the instrumental broadening (β_{ins}= 0.09º 2θ) to the experimental broadening (β_{obs}). FWHM values are obtained by processing the maxima diffraction peaks in the WinPLOTR software.

A crystallite pattern is defined to be periodic in three linearly independent directions, which defines the crystallite symmetry or unit cell. For cubic crystals the lattice parameter (a, in nm) is calculated by equation 2.9, using the relationship derived from the inter-planar distance in a cubic structure and applying Bragg's equation together with Miller indices (h k l), which indicate the plane orientation.

$$a = \frac{\lambda}{2\sin\theta}\sqrt{h^2 + k^2 + l^2} \tag{2.9}$$

The mesoporous template SBA-15 synthetized in this work was also analysed by XRD to determine the pore size and wall thickness. The distance between the centres of adjacent pores (a_0) was determined from the (1 0 0) interplanar spacing (d_{100}):

$$a_0 = \frac{2 \times d_{100}}{\sqrt{3}} \tag{2.10}$$

Accordingly, the pore wall thickness (W_t, in nm) was given by equation 2.11, wherefrom d_p (pore diameter) was calculated by N_2-physisorption:

$$W_t(nm)=a_0-d_p \quad (2.11)$$

Experimental protocol

The polycrystalline sample diffractometer used was a *PANalytical Xpert PRO* diffractometer with Bragg-Brentano geometry, equipped with a copper tube with $\lambda Cu_{K\alpha}$= 1.5418 Å ($\lambda Cu_{K\alpha1}$= 1.54060 Å and $\lambda Cu_{K\alpha2}$=1.54439 Å) and secondary graphite monochromator adjusted to copper radiation. It is an automated system with a programmable divergent slit, with a *PixCel* solid-state fast detector set to an active length of 2θ of 3.347º.

The analysis method employed was that of randomly oriented powder. Each sample was scanned from 10º-80º 2θ, with a step size of 0.026º and a counting size of 2 s, and the *PANalytical X´pert HighScore* software was used for treatment and identification of the diffractograms. Besides, the diffractograms of the mesoporous template SBA-15 were recorded in the 2θ range of 0.8º-5º with a 2θ step size of 0.01º and a step time of 10 s using the same apparatus. The XRD analysis was performed by the Rock and Minerals Analysis Unit from SGIker.

Additionally, reductive thermodifractometric studies were carried out in a PANalytical XPert PRO diffractometer equipped with ultrafast detector, X-Ray tube anode of Cu (λ= 1.5406 Å) and an Anton Paar XRK900 reaction chamber. Diffraction profiles were recorded at dynamic conditions, operating at 45 kV and 40 mA, in 2θ steps of 0.04º in the 4º ≤ 2θ ≤ 90º range, counting for 20 s per step. Data sets were recorded from 26 ºC to 800 ºC every 100 ºC with 5 ºC·min^{-1} heating rate. The analysis was performed by the Institute of Catalysts and Petrochemistry (CSIC) in Madrid.

2.2.3.2 *Electronic Microscopy*

For the visualization of the metal particles in heterogeneous catalysts, Transmission Electron Microscopy (TEM) represents a well-established method. If particles of metals are supported on an amorphous oxide material, they can be recognized by TEM, and further information about the shape of the particles can be gained [110]. In function of

physical processes of interaction between a high energy electron beam (20-1500 kV) and the sample direct information of the sample can be obtained. With modern TEM microscopies, it is possible to obtain area information and chemical composition coupling with X-ray Energy Dispersive Spectroscopy (EDX).

In this doctoral thesis work TEM was used to estimate the particle size distribution and exposed metallic surface area. Although TEM presents drawbacks related to sample size and uniformity, electron beam interactions and possible magnifications, modern TEM microscopies achieve an ultimate resolution of around 0.5 nm that allows accurately determining particle size and morphology. Besides, applying counting statistics (>240 particles) and comparison with XRD results, the obtained particle size analysis is reliable.

In the TEM technique, an electron beam is generated and accelerated by an electron gun, travelling down through the column, and reaching the condenser lens(es) (electromagnetic lens) and the condenser pinhole (aperture). Then, those steer the electron beam toward a thin sample, which is able to pass through some sample areas. This interaction with the sample leads to elastic processes, in which the directly transmitted or forward scattered electrons are refocused by the objective lens and the objective pinhole to form an image. Regions that appear darker are the thicker ones, due to a higher atomic number or higher mass density.

In Electron Microscopy, the micrographs can be taken in bright or dark field imaging modes. The bright field images are obtained from the electrons that are transmitted, while for the obtention of dark field (DF) images, only diffracted beams are used. The strong interaction occurring between the diffracted beams with the sample in the obtention of DF images, leads to highly useful information. In this thesis work it is used to visualize the metal distribution within mixed oxides.

On the other hand, STEM coupled with high-angle annular dark field (HAADF) allows the identification of metal particles and the determination of their distribution. The HAADF detector is a large disk with a hole, capable of detecting electrons that are scattered to higher angles [111]. By the HAADF-STEM method, heavy atoms in the catalysts can be imaged in a matrix of light atoms since the contrast is approximately

proportional to Z^2 (Z: atomic number). The metal particles, which have high Z compared to the matrix, are imaged as bright dots [110].

Experimental protocol

TEM analysis was done on a *TECNAI G2 20 TWIN* microscope operated at 200 kV and equipped with LaB6 filament. STEM micrographs along with elemental EDX-maps were obtained by an *FEI Titan Cubed G2 60-300* microscope with very high resolution. This microscope is composed of a high-brightness X-FEG Schottky field emission electron gun, monochromator, CEOS Gmbh spherical aberration corrector and Super-X EDX system with HAADF detector for Z contrast imaging in STEM configuration.

The samples were prepared by dispersion into ethanol solvent and keeping the suspension in an ultrasonic bath for 15 min. Then, a drop of the suspension was spread onto a copper grid (300 mesh) covered by a holey carbon film and was then dried under a vacuum.

Samples were reduced before the microscopic analysis, at the same conditions used in the catalytic experiments. The particle size distribution was determined by measuring the diameter (d, in nm) of at least 240 particles. After that, the mean Ni^0 dispersion (D_{Ni^o}) was estimated applying d-FE model proposed by Borodziński et al. [112], as follows:

$$D_{Ni^o}=(\%)=100\times\frac{5.01d_{at}\sum_j n_j d_j^{\,2}+2.64d_{at}^{\,0.81}\sum_k n_k d_k^{\,2.19}}{\sum_i n_i d_i^{\,3}} \qquad (2.12)$$

where d_i, d_j and d_k are the particles of "i", "j" and "k" diameter; n_i is the number of particles with diameter d_i; n_j is the number of particles with diameter d_j ($d_j > 24d_{at}$); n_k is the number of particles with diameter d_k ($d_k \leq 24d_{at}$); and d_{at} is the atomic diameter of Ni^0.

The volume-to-surface mean diameter of the nickel particle ($d_{Ni^o(TEM)}$) was estimated as follows:

$$d_{Ni^0\,(TEM)}(nm)=\frac{\sum_i n_i d_i^{\,3}}{\sum_i n_i d_i^{\,2}} \qquad (2.13)$$

The metallic nickel surface area ($A_{S\text{-}Ni^o(TEM)}$, in $m^2 \cdot g^{-1}$) was calculated from the dispersion ($D_{Ni^o(TEM)}$) and metallic Ni content in the samples (C_{Ni^o}), as shown in equation 2.14. Note that, C_{Ni^o} depends on the fraction of nickel reduced in the sample ($C_{Ni^o} = M_{Ni} \times f_{red}$), where f_{red} is the fraction of Ni reduced at corresponding reduction temperature:

$$A_{S\text{-}Ni^o(TEM)}(m^2/g) = \frac{A_{at\text{-}Ni} \times C_{Ni^o} \times D_{Ni^o} \times N}{MW_{Ni}} \quad (2.14)$$

where, $A_{at\text{-}Ni}$ is the atomic area of Ni ($m^2 \cdot at.^{-1}$); N is the Avogadro´s number; and MW_{Ni} is the molecular weight of Ni ($g \cdot mol^{-1}$).

The analysis were performed by the Polymer Characterization Service and the Electron Microscopy and Material Microanalysis Service (SGIker).

2.2.4 Solid state spectroscopic analysis (UV-vis-DRS, FTIR and ^{27}Al NMR)

The speciation analysis integrates the study of the molecular structure and the valence, which is normally conditioned by the surroundings of the atoms. Diffuse reflectance analysis was performed for the determination of the structural species and the coordination state. Infrared spectroscopy allowed the identification of the chemical species, and NMR was done to analyse the interactions between the nucleus of the aluminium with the surroundings.

2.2.4.1 *Diffuse Reflectance of Ultraviolet–Visible-Near Infra-Red (UV-vis-NIR DRS)*

The effect of the different types of radiation over a sample is explained as a function of the energy of its photons ($E = h \cdot c/\lambda$). The UV-VIS radiation induces electronic transitions regarding its high energies (1- 25 eV) [106]. Diffuse Reflectance Spectroscopy (DRS) is a valuable technique in the analysis of solids, in which the sample is irradiated with a monochromatic light that is diffusely reflected. This happens when the irradiated light is adsorbed and then scattered in many directions, being the particles the source of reflection. A photosensitive cell is used to detect the reflected radiation, which will transform radiation energy into an electric signal readily used for information processing.

The Kubelka–Munk function is applied to provide the equivalent absorption spectrum from the diffuse reflectance spectrum (equation 2.15) to overcome the induced spectral distortions by variations of the effective wavelength step in rough materials analysis. The DRS intensity is independent of the wavelength of the incident light and only depends on the absorption and scattering coefficients of the sample, as follows [106]:

$$F(R_\infty) = \frac{(1-R_\infty)^2}{2R_\infty} \quad (2.15)$$

being R_∞ the diffuse reflectance of a layer of infinite thickness.

The electronic absorption spectra are obtained in the region of 200- 2500 nm. Moreover, the near-infrared part of the spectrum provides information about the narrow IR overtone and combination bands originating from the metal ligands or the support, which may effectively complement mid-range IR spectra [113].

Experimental protocol

DRS analysis was carried in an Agilent Cary 5000 UV-Vis-NIR spectrophotometer coupled to Diffuse Reflectance Internal 2500. Obtained spectra are smoothed to a 1:25 scale. The number and position of absorption bands in those spectra are interpreted to define the electronic configuration of the element, as well as the nature of its chemical environment. The DRS analysis was performed by the SCAB from SGIker.

2.2.4.2 *Fourier Transform Infra-Red Spectroscopy (FTIR)*

Incident IR radiation produce changes in the vibrational state of a molecule, due to the adsorption of photons with energy related to the IR region. When IR radiation interacts with a sample, some of the radiation is absorbed by the sample and some passes through (is transmitted). The FTIR spectroscopy uses a Michelson's interferometer that splits the radiation beam in two, employing a *beam splitter*. The separated beams are directed to a fixed and a moving mirror, thus travelling paths of different lengths. Next, the beam is recombined to create interference, which is directed to the sample material and finally to the detector. Owing to the interference phenomena, the beam

intensity that is read by the detector changes in the function of differences in the travelled paths, leading to the interferogram that contains the spectral information.

Experimental protocol

FTIR transmittance spectra were recorded in the 400- 4000 cm^{-1} range, in *a Cary 600 Series* FTIR apparatus, with *Resolutions Pro* software for data manipulation. The spectra acquisition resolution was 4 cm^{-1} with an average of 50 scans. The samples were pelletized with KBr for the measurements.

2.2.4.3 *Nuclear Magnetic Resonance (^{27}Al NMR)*

The NMR is a technique for local analysis, which allows determining coordination of the atoms, tetrahedral polymerization grade, or other parameters such as the thermic or chemical alteration of materials. The NMR phenomena is based on the interactions of the magnetic momentum of a nucleus (μ_n) with an applied magnetic field (B_0), being the nucleus spin usually aligned with B_o. Then, the irradiation of the sample with a radio-frequency (RF) field (B_1), produces a resonance, which is related to the transition between consecutive energy levels and modifications in the orientation of the nuclei magnetic field, with respect to B_0. The frequency of RF radiation that is absorbed induces resonance, which causes a peak to appear in the spectrum at that specific frequency.

The chemical shift and the quadrupolar interactions lead to an understanding of the coordination and the distortions in the polyhedron of atoms coordination. An increase in the coordination number produces a shift to lower values in the NMR. The resonance study of ^{27}Al (Spin= 3/2) allows the study of aluminium coordination.

Experimental protocol

^{27}Al NMR measurements were performed on a *9.4 T Bruker AVANCE III 400* spectrometer operating at resonance frequencies of 104.26 MHz for ^{27}Al. Chemical shifts were referenced externally to the $AlCl_3$ aqueous solution at 0 ppm. The spectra were acquired at a spinning frequency of 60 kHz employing a *PH MASDVT400W BL* 1.3mm ultrafast probe head. A single pulse of 0.3 microseconds duration was applied and a recycle delay of 0.2 s and 36000 scans were used. This analysis was performed by the SCAB of SGIker in UPV/EHU.

2.2.5 Reducibility analysis of samples (H_2-TPR)

Through the reduction analysis of a catalytic sample valuable information is obtained, such as finding the most efficient reduction conditions for a catalytic precursor. It also helps to identify the supported precursor phases and their interactions with the support, as well as to characterize complex systems, such as bimetallic catalysts, allowing to determine the role of the second component and promotion effects [114]. The reducibility of the prepared samples was studied by Temperature-Programmed Reduction with hydrogen diluted in argon (H_2-TPR).

When an oxidized sample is heated under programmed temperature ramp in a stream of hydrogen-containing inert gas, it will react with hydrogen as a function of the temperature/reactivity relationship of the oxide species [115]. The decrease in H_2 concentration in the effluent gas, in comparison to the initial percentage, monitors the reduction reaction progress [114]. The H_2 consumption rate was monitored in a previously calibrated Thermal Conductivity Detector (TCD), which is capable of detecting differences in the concentration of gases flowing into and out of the sample reactor.

Experimental protocol

In the full reduction experiments (TPR_{950}), 50 mL·min^{-1} stream of 5% H_2/Ar was constantly made to flow through a U-shaped quartz reactor containing a fixed bed of approximately 70 mg of sample. The reactor is placed in a furnace with a programmable temperature controller, where the temperature was programmed to increase constantly at a rate of 10 ºC·min^{-1} up to 950 ºC and hold for 1 h. Before the gas reached the TCD, it went through a cold trap for retention of the generated water during the reduction reaction, which could interfere with the TCD measurements. The H_2 uptake in this experiment was H_2-TPR_{950}.

In addition, H_2-TPR was carried out for the partially reduced samples in order to study the catalysts under the same conditions they are at the beginning of the APR reaction. In this line, the fraction of metals being reduced (f_{red}) was estimated, being T_{red} the used temperature of reduction prior to the reaction. The sequence of reducibility analysis is shown in Figure 2.1. First, each sample was reduced following the same protocol as for TPR_{950} described above, heating up to the corresponding T_{red}. The

amount of H_2 consumed in this stage was defined as H_2-TPR_{Tred}. Then, it was cooled down to room temperature in He flow. Subsequently, a full TPR run is carried raising the temperature to 950 ºC. The amount of H_2 consumed in this stage was defined as H_2-$TPR_{Tred-950}$.

The f_{red} value for each sample was defined as the fraction of the amount of H_2 consumed during its reduction at temperature T_{red} (TPR_{Tred}) with respect to the total amount of H_2 consumed during the full reduction (TPR_{950}). The TPR profiles were subjected to Gaussian deconvolution to estimate the content of the different nickel species as well.

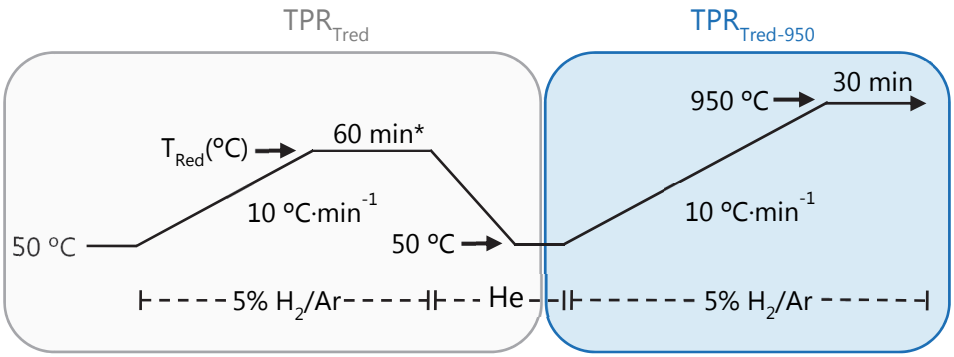

Figure 2.1. The sequence of the reducibility analysis for the partially reduced catalysts. *Isotherm time varies in experiments of Chapter 4 (30 min).

H_2-TPR analysis was performed in a *Micromeritics AutoChem 2920* instrument with a TCD detector. Before the analysis, samples were flushed with 50 mL·min^{-1} of He stream at 550 ºC for 1 h (heated at 10 ºC·min^{-1}) to remove humidity and possible adsorbed compounds.

2.2.6 Surface properties

Surfaces of metal oxides entail coordinatively unsaturated cations (M^{n+}) and oxide (O^{2-}) ions, and finally OH^- groups. The OH^- groups are formed as a result of dissociative adsorption of H_2O molecules, which occurs to reduce the coordinative unsaturation. OH^- groups are normally removed when the metal oxide is treated at an elevated temperature. Surfaces of dispersed oxide materials are highly irregular and defective,

and their properties may be dominated by some particularly energetic and reactive minority defect sites [116].

In chemisorption, the intermolecular forces involved lead to the formation of chemical bonds. The experimental approach of using adsorbed surface probe molecules for surface characterization is highly informative. In this thesis work, those experiments were used to characterize the metallic surface area, surface acid-base properties and to study the possible formation of carbonaceous and/or organic deposits (in the spent samples). The probe molecule interacts with the sample producing gas-solid interactions of different bounding energies. This leads to different species of adsorbed gases: strongly and weakly chemisorbed. While the gas that is strongly bonded to the surface can be removed only by increasing the temperature and applying vacuum or a flow of inert gas (thermal desorption), the gas molecules weakly bound can be removed at the same analytical temperature by only applying vacuum or inert flow [114].

It is worth mentioning that in surface characterization of catalytic samples, it is very important to perform each test under analytical conditions as close as possible to the operative conditions of the catalytic reaction. Thus, characterization of previously reduced samples at the corresponding temperature T_{red} was performed. When the in-situ reduction was not possible, the reduction was carried out ex-situ in a quartz reactor under 20% H_2/He flow of 50 mL·min^{-1} at T_{red} temperature for 1 h (heating at 5 ºC·min^{-1}). Finally, the sample was cooled down to room temperature in He flow and passivated under 1% O_2/He at 4 ºC for 15 min.

2.2.6.1 *Surface basicity (CO_2-TPD)*

Generally, a base site can react with an acid molecule. In a solid sample, the base sites density and strength can be obtained by Temperature-Programmed Desorption (TPD), after the chemisorption of an acid probe molecule (typically CO_2).

The TPD has been used most commonly to study the binding of adsorbates to catalytic surfaces. In this technique, as temperature linearly increases, the desorbed molecules are diluted into a flow of carrier gas and reach the detector, where their concentration is recorded as a function of the temperature. The temperature of the desorption peak (maximum) is indicative of the strength with which the adsorbate is

bound to the surface. The more strongly the adsorbate is bound to the surface, the higher the temperature of the desorption peak is [115].

Experimental protocol

The CO_2-TPD analysis was carried out in a *Micromeritics AutoChem 2920* instrument coupled to Mass Spectroscopy branded *MKS, Cirrus 3000*. About 70 mg of the calcined precursor was initially pre-treated in He stream at 550 ºC for 1 h (heating rate of 10 ºC·min^{-1}) and cooled to room temperature. After the cleaning treatment, the sample was reduced to the corresponding temperature in 5% H_2/ Ar flow (heating rate 10 ºC·min^{-1}), held for 1 h and cooled down in He flow to 40 ºC. Then, 5% CO_2/ He flow was passed through the sample until it was saturated (1 h). Subsequently, the sample was exposed to He flow for 1 h to remove reversibly and physically bound CO_2. Finally, the desorption was performed by raising the temperature to 900 ºC (heating rate 10 ºC·min^{-1}) and the resultant signal was followed by MS.

2.2.6.2 *Surface acidity analysis by NH_3 chemisorption*

Generally, an acid site is defined as a site that can react with a basic molecule. Thus, the characterization of the surface acid sites is performed by chemisorption measurement using a basic gas, which is adsorbed by an acid site and transformed into its conjugated acid form [114].

The evaluation of surface properties by NH_3 chemisorption was carried out by constantly flowing a carrier gas (He) through the sample, in which a pulse of diluted reactive gas (10% NH_3, 95% He) is periodically injected. Several pulses are injected into the system until the sample saturates. Between the pulses, pure He gas stream flows through the sample to remove possible physisorbed NH_3 and to guarantee that the measurements are related only to the monolayer adsorption.

Using a TCD detector, the amount of NH_3 adsorbed is calculated by integrating the peaks generated by the detector signal as a function of time. This analysis required a calibration where the generated peak area by the pulse of known volume is determined. The volume of NH_3 chemisorbed (V_{NH3}, cm^3·g^{-1}) was determined as follows:

$$V_{NH_3} = V_{NH_3,pulse}\left(n_p - \sum_{i=1}^{n}\frac{A_i}{A_0}\right) \quad (2.16)$$

where n_p is the number of pulses; $V_{NH3,pulse}$ is the NH_3 volume in a pulse ($cm^3 \cdot g^{-1}$); A_i (V·min) is the peak area of each pulse; and A_0 (V·min) is the peak area of the non-chemisorbed peak.

Note that the strength of adsorption of the acid sites could not be determined due to phenomena such as spill over and decomposition of NH_3 catalysed by the solid at the high temperatures at which the TPD analysis is carried out [114].

Experimental protocol

NH_3 pulse chemisorption was carried out in a *Micromeritics AutoChem 2920* instrument with a TCD detector. About 70 mg of the calcined precursor was initially pre-treated in He stream at 550 ºC for 1 h (heating rate of 10 ºC·min^{-1}) and cooled to room temperature. Then, it was reduced at T_{red} in 5%H_2/ Ar flow (heating rate 10 ºC·min^{-1}), held for 1 h and cooled down in He flow to 90 ºC, which was the temperature of the acidity measurements. A series of 10% NH_3/He pulses (0.5080 mL) were introduced until constant peak area was achieved (saturation reached).

2.2.6.3 *Infrared spectroscopy of pyridine adsorption (IR-Pyr)*

In catalyst characterisation, it is very useful to define the nature of the acid sites (Lewis or Brønsted). The spectroscopy analysis of sorbed surface probe molecules is a very informative experimental approach towards surface characterization [116]. Pyridine probe molecule forms pyridinium ions (1544 cm^{-1}) on Brønsted acid sites and, additionally, it is coordinatively adsorbed on Lewis acid sites. Coordinatively adsorbed pyridine molecules can be further differentiated into pyridine adsorbed on strong (1455 cm^{-1}) and weak Lewis acid sites (1448- 1442 cm^{-1}) [116].

Experimental protocol

The sample, previously reduced in an external oven at the corresponding temperature and pressed into a waffle, was pre-treated in vacuum at 300 ºC for 1 h and then reduced using 99% H_2 flow at 230 ºC for 1 h, to clean the surface and remove the

passivation layer of the pre-reduced samples. Subsequently, the sample was cooled down in N_2 flow to 150 ºC and after reaching vacuum pressure (10^{-5} mbar), the first spectrum was recorded (blank, s_1). Then, pyridine gas was added stepwise until equilibrated pressure was obtained, and a second spectrum was recorded (saturation, s_2). Finally, the sample was evacuated under vacuum for 30 min and the third spectra was recorded, which corresponds to the strongly sorbed molecules (acidity, s_3). The s_3 spectra were used for assessing the pyridine absorbance by deconvolution of the corresponding bands.

The determination of acid site concentration from the absorbance measured on the wafer is based on the Emeis formula as well as integrated molar extinction coefficients of the respective bands of adsorption [117] as presented in equation 2.17 and 2.18, for the concentration of Lewis (LAS) and Brønsted (BAS) acid sites, respectively:

$$LAS\left(\frac{mmol}{g}\right) = \frac{1.42 \cdot IA_{1450cm^{-1}} \cdot r^2}{W} \tag{2.17}$$

$$BAS\left(\frac{mmol}{g}\right) = \frac{1.88 \cdot IA_{1545cm^{-1}} \cdot r^2}{W} \tag{2.18}$$

where IA is the integrated absorbance of Lewis or Brønsted band (cm^{-1}); r is the radius of the wafer (cm); and W is the weight of the sample (wafer) (mg).

An FTIR spectrometer branded *Nicolet 5700* connected to a vacuum system with a gas dosing facility was used for spectra recording with a resolution of 4 cm^{-1}. The IR-Pyr analysis was carried in the laboratories of the *Technische Chemie II* research group at *TUM* in Germany.

2.2.6.4 *Metallic surface area and metal dispersion (H_2 chemisorption)*

H_2 chemisorption is commonly used to define the surface area of the free active sites in a catalyst ($A_{S\text{-}Ni^o}$) and exposed metallic Ni atoms. Due to the formation of metal aggregates, only a small part of the active phase is physically free to react with the measuring gas [114]. The chemisorption techniques evaluate the free metal surface by titrating the number of surface metal atoms available on the metal aggregates. The volume of hydrogen adsorbed was estimated by equation 2.16. The exposed metal

atoms were calculated assuming H : Ni stoichiometry of 1 : 1 [118], and consequently, the exposed metal surface, considering spherical Ni^0 particles, with a cross-sectional area of 0.065 nm^2 [119].

The H_2 chemisorption is carried out by constantly flowing a carrier gas, and periodically injecting pulses of reactive gas (5% H_2/Ar) through the sample, by a loop injection system until the sample is saturated. The experiment is carried out at constant temperature, using a TCD detector for measurements of the amount of adsorbed gas. The injected pulses are calibrated associating the peak area with the known loop volume (reference peak).

Experimental protocol

The H_2 chemisorption was carried out with Micromeritics AutoChem 2920 equipment. Before analysis, the sample was heated in a He stream at 550 ºC to obtain a clean surface. Then, it was reduced under 5% H_2/Ar flow for 1 h at the corresponding reduction temperature (T_{red}) and later cooled down to 40 ºC under Ar flow. Subsequently, the H_2 pulses (loop volume of 0.5312 mL) were injected to saturation point. In between pulses, pure Ar stream flowed through the sample to remove physiosorbed reactive gas.

2.2.6.5 *Carbonaceous deposits quantification (TPO-TG and TPH-TPR-MS)*

Thermal analysis was performed to quantify the carbon deposits on the surface of the catalysts during the APR reaction [114] by either Temperature-Programmed Oxidation followed by Thermal Gravimetry (TPO-TG-MS) and simultaneous Temperature-Programmed Hydrogenation and Reduction (TPH-TPR-MS).

Carbon deposits on spent catalysts were evaluated by Temperature-Programmed Oxidation (TPO) followed by thermogravimetry (TG) and Mass Spectrometry (MS). In the TPO, the sample is submitted to a programmed temperature increase, as an oxidative mixture of gas flows through the sample. The oxidation rates of carbon deposits are continuously measured by monitoring the m/z signals 44 (CO_2) and 18 (H_2O) by MS, as well as the evolution of the sample weight.

Experimental protocol

The TPO-TG-MS experiments were carried in a *Setaram Setsys evolution* thermobalance with cylindrical graphite furnace and PID integrated temperature control. The thermobalance was coupled to a mass spectrometer branded *Pfeifer OmniStar* to monitor the gas effluent. Approximately 5 mg of calcium carbonate (used as reference) was added to about 25 mg of sample. The mixture was pre-treated under He, at 150 ºC for 1 h and then heated up to 1000 ºC at a heating rate of 5 ºC·min^{-1}. A mixture of 5% O_2/He was used as oxidizer.

TPH-TPR-MS analysis was carried out for the spent catalysts aiming to estimate the amount of carbonaceous material deposited over the surface of the spent catalyst. The hydrogenation of C- containing material leads to CH_4 formation.

Simultaneously to the hydrogenation, reduction reactions may take place, especially when the catalyst suffers from oxidation of its metallic particles. The TPH-TPR-MS makes it possible to obtain an accurate estimation of oxidation. First, the H_2 uptake for CH_4 formation ($Meth_{H2}$, assuming 2 mol H_2/ mol CH_4) is subtracted from the total H_2 uptake. Thus, the remaining H_2 uptake can be ascribed to the oxidation of nickel species ($TPR_{used\text{-}NiO}$) reduction. The percentage of oxidized Ni is calculated as follows:

$$\text{Ni oxidized}(\%) = \frac{TPR_{used\text{-}NiO} - Meth_{H2}}{TPR_{700}} \times 100 \qquad (2.19)$$

Experimental protocol

The TPH-TPR-MS analysis was conducted on a *Micromeritics AutoChem 2920* instrument with TCD detector coupled to Mass Spectrometer (Hiden Analytical). Before the analysis, samples were flushed with 50 mL·min^{-1} of He stream at 220 ºC for 1 h (heated at 10 ºC·min^{-1}) to remove humidity and possible adsorbed atmospheric compounds. Then, the TPH-TPR-MS were performed following the aforementioned protocol for TPR_{950} but removing the cold trap in this case. Note that the evolved gas was analysed by TCD coupled with a mass spectrometer, following the evolution of m/z signals 18 (H_2O), 16 (CH_4) and 2 (H_2).

2.3 CATALYTIC TESTS

In this section, the reaction system and protocols used in the evaluation of the catalyst performance are addressed. Details of the reaction and analysis system are described in sections 2.3.1 and 2.3.2. The protocol of reaction employed for the different activity evaluation experiments are detailed in section 2.3.3, as well as the reaction data estimations.

2.3.1 Reaction system

The catalysts performance in the Aqueous-Phase Reforming of glycerol were carried out in an automated *Microactivity Effi, PID Eng&Tech* (*Ma-Effi*) unit, which has been acquired and set up in the development of this doctoral thesis. The *Ma-Effi* unit flow diagram is shown in Figure 2.2.

The pipes (1/16''), valves and other connections have low dead volume. This computer-controlled laboratory scale reactor allows the study of the catalytic performance under different reaction conditions by *Process@* software, which includes distributed control for data monitoring and acquisition as well as remote control via Ethernet. There is also a touch screen to operate the system manually if desired. Moreover, the *Ma-Effi* unit includes a safety system integrated to an external alarm system and proportional integral derivative (PID) controllers to regulate the process variables. This system is composed of three zones.

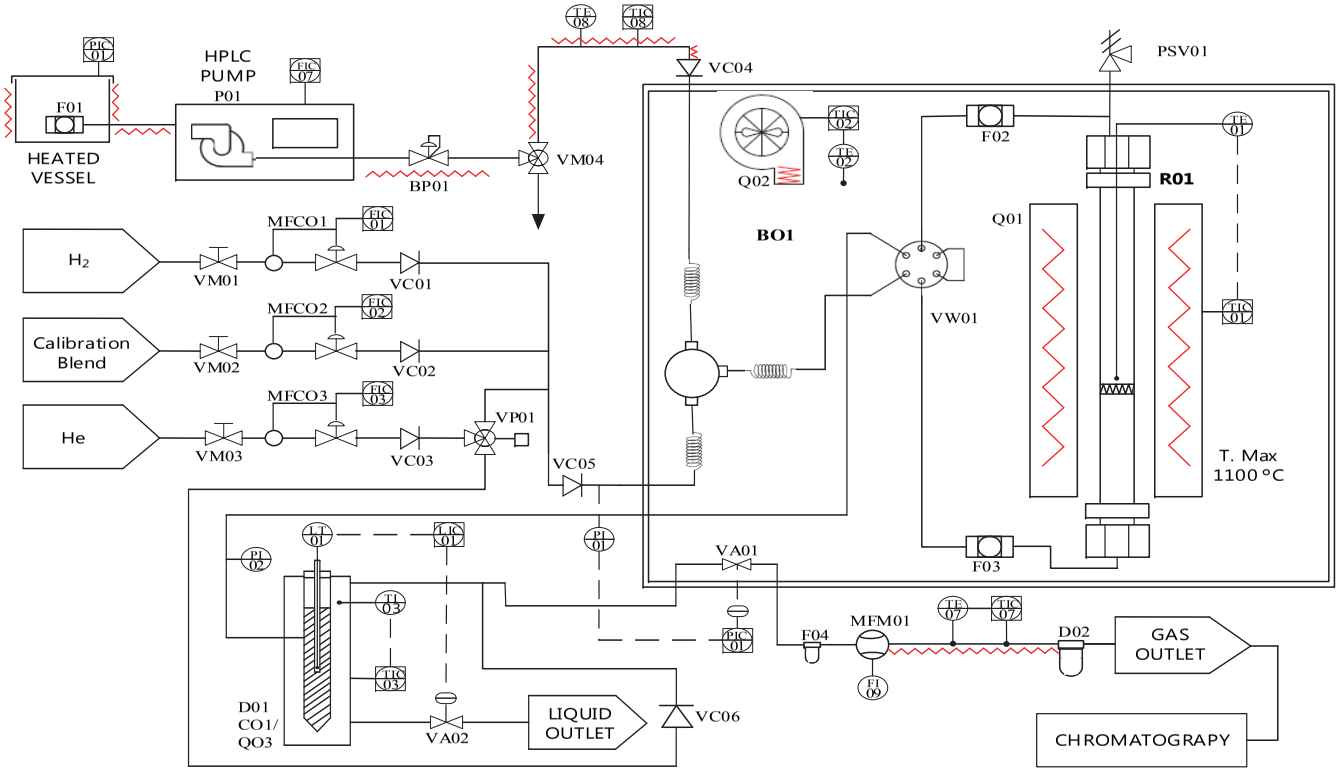

FIC and FI	Flow control and indicator	**BP**	Back-pressure valve	**PSV**	Safety relief valve	**D**	Vessel
TIC and TI	Temperature control and indicator	**VM**	Manual operated valve	**MFC**	Mass flow controller	**P**	Pump
PIC and PI	Pressure control and indicator	**VC**	Check Valve	**MFM**	Mass flow meter	**B**	Blower
LIC and LT	Level control and sensor	**VAP**	Actuated plug valve	**F**	Inlet Filter	**R**	Reactor
VA	Servocontrolled needle valve	**VW**	6-way/2-position valve	**Q**	Heat exchanger	**C**	Peltier cell

Figure 2.2. Flow diagram of the APR reaction system.

2.3.1.1 *Feed zone*

Gases are fed by three *EL-Flow* thermal mass flow controllers, branded *Bronkhorst High-Tech,* with an individual PID control loop. H_2, He and calibration gas mixtures are commonly fed in diverse experiments. Each gas line has a manually operated valve and a turbulent flow mixer. In the APR reaction, the liquid reagent is fed with each of the two HPLC pumps, *GILSON 307* and *Eldex 5985 optos 1LMP*, operative for different flow scales ranging from 0.02 to 5 $mL \cdot min^{-1}$ and from 0.002 to 2.5 $mL \cdot min^{-1}$, respectively. The head, reservoir and lines of the liquid pumps are equipped with a heating system for viscous fluids (maximum temperature= 90 ºC). The *Ma-Effi* unit has *Vici Valco* automatic 6-way valve to select the direction of flow in the reactor, it is a pneumatic valve controlled by an electro valve.

2.3.1.2 *Reaction zone*

The reactor used is a bench-scale fixed-bed up-flow tubular reactor integrated into a hot box. It is made of Hastelloy X and presents an internal diameter and height of 5.1 mm and 300 mm, respectively. There is a porous plate inside the reactor designed to ensure that the catalyst bed remains in the same position and inside the furnace's isothermal temperature zone. A thermocouple (type K) is housed inside the reactor of a single reading point directly into the catalyst bed.

The reactor is placed into a radiant furnace with a PID temperature control loop. The design of the furnace distributes heat along the entire length, creating an isothermal zone of about 5 cm, inside which the catalyst bed and the thermocouple are located. The desired temperature is entered through *Process@* and the order is sent to the programmable logic controller (PLC) that communicates with the furnace PID. The PLC also receives the signal measured by the thermocouple and the alarm system and executes the necessary actions.

The *Ma-Effi* unit can operate with atmospheric pressure of up to 100 bar. The pressure control consists of a high-speed precision servo-controlled needle valve, which allows extremely sensitive flow regulation and a rapid response for control. Pressure readings are taken at the equipment's gas inlet and the control valve is located after the

liquid/gas separator. The aim of this is to ensure that all points in the system have the same pressure and release pressure before sending the sample to the analysis system.

2.3.1.3 *Separation zone*

The liquid/gas separator is placed at the reactor outlet, allowing continuous collection of condensed products for later analysis. Due to the high pressure of operation, the liquid/gas separator has a PID control loop which, based on a measurement of the level of liquid, operates the control valve to maintain a constant level of liquid.

The liquid/gas separator is connected to a Peltier cell operating at 4 ºC, avoiding the condensed phase being carried by the gas phase. The liquid/gas separator features a capacitive level sensor. In this system, the condensed liquid product presented between the isolated probe and the housing of a metal reservoir acts as a dielectric, changing the electrical capacity of the condenser system. An oscillating resistor-capacitor circuit will then supply a frequency signal proportional to the system's capacitance or capacity, which is therefore proportional to the amount of liquid in the reservoir. Finally, the PID level control loop moves the micrometre regulating valve, similar to the one described for pressure control, after reading the level inside the reservoir, allowing to automatically remove and collect liquids in real-time without affecting the pressure system.

2.3.1.4 *Analysis zone*

After separation of the reaction products, they are analysed. On the one hand, the gas flow is measured by a flow meter (EL-Flow, Bronkhorst) and analysed on-line by gas chromatography with TCD (GC-TCD). On the other hand, liquid product samples are taken every 15 min in vials, sealed and later analysed by either gas-phase chromatography with FID (GC-FID), liquid-phase chromatography (HPLC-IR) and Total Organic Carbon (TOC) measurements. Further, the total liquid product is weighed and subjected to elementary composition analysis to determine the degree of leaching. The procedure of each of the analyses is described below.

2.3.2 APR products analysis

2.3.2.1 *Gas products analysis*

The gas-phase analysis was carried out in an *Agilent 490 Micro GC* working with *Agilent OpenLAB CDS*, which supports instrument control and digital data acquisition. The Micro GC features a Micro-Gasifier, which ensures controlled evaporation of residual condensate in the gas line before the sample is introduced into the GC injector. It presents a quad-channel configuration (4 channels) with electronic gas control. In each independent channel, the sample being analysed is injected and travels through a narrow-bore column, which is located inside a temperature-controlled oven. A Thermal Conductivity Detector (TCD) is placed at the end of the column to identify components as they arrive with different retention times and to further measure the concentration of each compound. Note that channels 1 to 3 are also equipped with traditional back flush configuration.

Channels 1 and 2 consist of 10 m CP-Molsieve 5 Å columns for permanent gas analysis (i.e., H_2, O_2, N_2, CH_4 and CO) except for carbon dioxide (CO_2). The difference between them is the carrier gas (Ar in Channel 1 and He in Channel 2). Channel 3 is a 10 m CP-PoraPLOT U column for CO_2 and C2 (Ethane) detection using He as carrier gas. Channel 4 has a 10 m CP-Al_2O_3/KCl column for C3+ compounds analysis using He as carrier. A typical chromatogram obtained during the APR reaction is shown in Figure 2.3.

2.3.2.2 *Liquid products analysis*

- FID-Chromatography (GC-FID)

The composition of the liquid was analysed by GC-FID (*Agilent 6890N*). Its operation is similar to that of GC except that it employs a Flame Ionization Detector (FID) rather than TCD. This detector is based on the detection of ions formed during combustion of compounds in a hydrogen flame, the amount of which is proportional to the concentration of compounds in the sample. The employed GC-FID is equipped with capillary column of a 25 m *HP-Wax,* bonded with polyethylene glycol. For the analysis, 3 µm of liquid sample is injected (Split 20:1) and evaporated. The carrier gas employed is H_2 at 1 mL·min^{-1} flow rate. The FID detector operates at 250 °C with N_2 as makeup gas. The flame is fed with H_2 and combined air flow of 17 mL·min^{-1}.

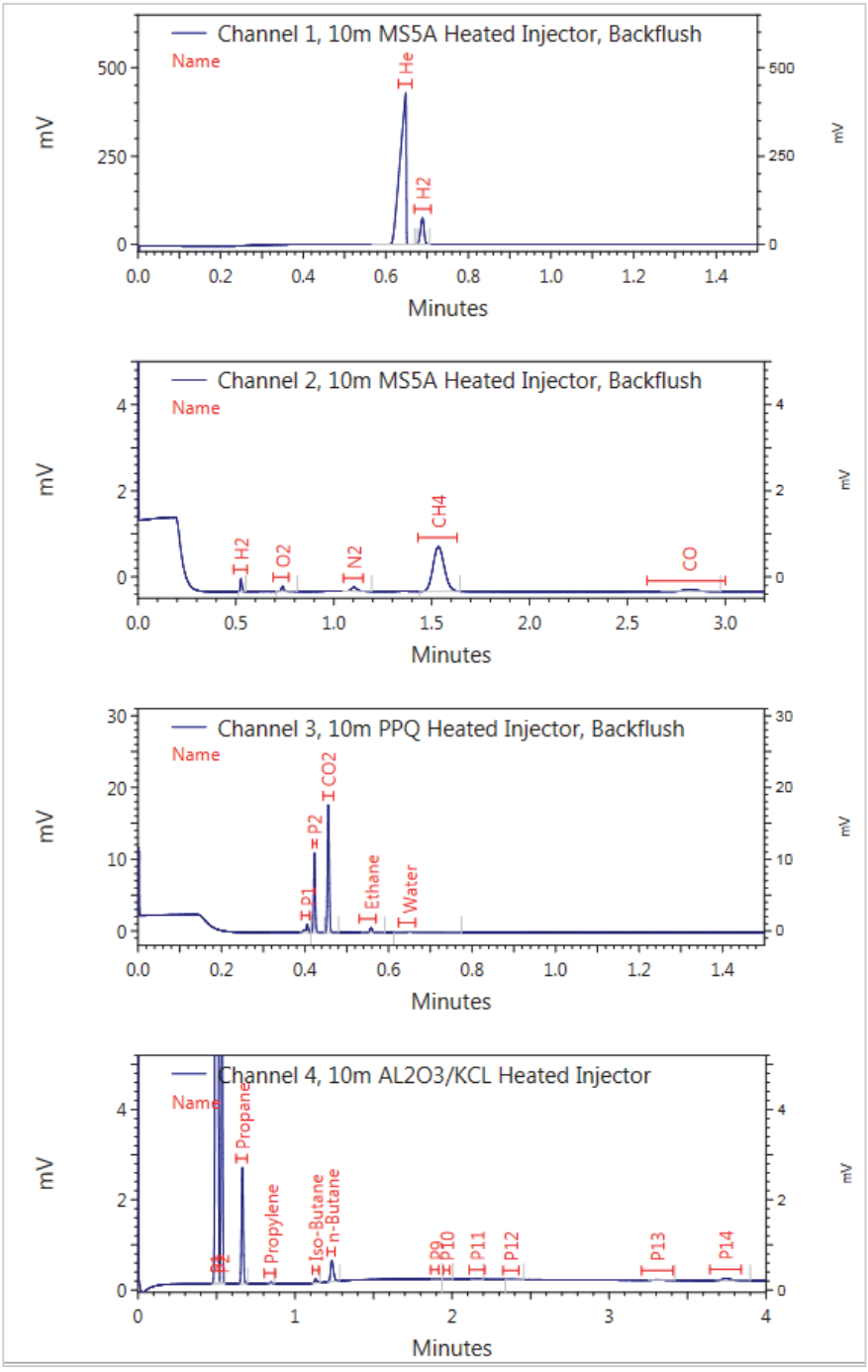

Figure 2.3. Typical chromatograms of gas products of glycerol APR in the μGC.

The oven heating protocol consists of first rising temperature to 60 ºC for 6 min, then to 160 ºC for 3 min and finally to 250 ºC for 10 min at 30 ºC·min^{-1} in all cases. This analysis allowed the quantification of the liquid products.

- Liquid-phase chromatography (HPLC-RI)

Due to the lack of linearity of glycerol in GC-FID, its analysis was carried out by high-performance liquid chromatography (HPLC). In HPLC, a high-pressure pump moves the mobile phase (a solvent) through the system at a specified flow rate and an injector periodically introduces the sample into the continuously flowing mobile-phase stream, which travels through the HPLC column. The column contains the chromatographic packing material needed for the effective separation of products (stationary phase). The separated compounds are then identified by a Refractive Index (RI) detector, which detects all substances that have a significantly different refractive index from that of the mobile phase [120].

The analysis protocol for the quantification of the glycerol concentration in the liquid samples was carried in a *Waters* unit with *Empower Pro v.2*. control system. The unit features a *Waters 515* HPLC pump and *Waters 717* injector. The column employed was a *Hi-plex H*, a strong cation-exchange resin consisting of sulfonated crosslinked styrene-divinylbenzene copolymer in the hydrogen form. The RI detector was a *Water 2414* operating at 50 ºC. 10 µl of the liquid sample were injected and carried in water (mobile phase) at a flow of 0.2 mL·min^{-1} into the column, operating at 30 ºC. The total analysis time was 120 min.

- Total Organic Carbon (TOC)

The carbon content in the liquid product is also included in the reaction monitoring. It is measured by Total Organic Carbon (TOC) analysis of the liquid samples, which allows us to determine the reagent conversion into gas-phase products. The TOC analyser oxidizes the carbon in a small aliquot of the sample to CO_2 using the high-temperature catalytic oxidation employing a platinum-based catalyst. The CO_2 formed is measured in a non-dispersive infrared cell (NDIR) by integration of the peak area. As the IR light passes through the sample, the CO_2 gas molecules absorb the specific band of IR light while letting other wavelengths of light pass through.

The amount of infrared absorbed is proportional to the density of the gas, according to the Lamberts-Beer law. Finally, the IR detector reads the remaining IR light and measures it based on the difference with respect to the IR radiated.

The TOC measurement is carried out first by measuring the total carbon (TC) and then the inorganic carbon (IC) by acidification and sparging process. The IC could contain the CO_2 possibly dissolved in the liquid phase. Subtraction of IC from TC provides the TOC concentration.

A Shimadzu TOC-L instrument was used for TOC analysis, with an autosampler and remote computer control (TOC-control L). The sample, after acidification and bubbling, is injected into a vertical furnace using a glass syringe. The combustion tube, made of quartz, is filled with a catalyst and its temperature is fixed at 680 ºC. The volume injected was 350 µL, of the previous diluted sample. Each value was determined from a minimum of three injections.

2.3.3 Reaction procedures and calculations

The performance of catalysts in the glycerol APR is tested, using a mixture of synthetic glycerol (Table 2.1) and distilled water (10 wt.% glycerol). The reaction conditions of temperature and pressure (T/P) for the different catalytic tests carried out, are depicted in Table 2.2.

In a typical reaction test, a corresponding mass of pelletized catalyst (0.04-0.16 mm) was first loaded to the reactor, ensuring that the bed was in the isothermal zone of the reactor. Then, quartz wool and a SS tube of a small diameter were placed to fix the bed, the lock nut as well as the sealing ring were placed, and the reactor was locked.

After leak detection probe and prior to the reaction, a mixture of H_2 diluted in He was fed to the conditioning of samples (reduction with 20% H_2/ He flow at the corresponding temperature (T_{red}) and atmospheric pressure for 1 h). Once the reactor was pressurised with 40 mL·min^{-1} of He flow up to the pressure of operation (Table 2.2), the He flow was switched to bypass using the six-way valve towards the liquid/gas separator and then to the gas outlet. Thereafter, the glycerol solution was pumped into the reactor while the temperature was progressively raised at 5 ºC·min^{-1} to the set point.

Table 2.2. Catalytic tests and conditions.

Test	T/P	WHSV/ Space time
Catalysts screening	235ºC/ 35 bar	24.5 h^{-1} / 2250 g_{cat}·min·mol_{Gly}^{-1}
Factorial design 2k+c	210ºC - 240ºC 35 bar – 50 bar	123- 26.4 h^{-1}/ 450-2100 g_{cat}·min·mol_{Gly}^{-1}
Activity of NiAl-T catalysts	245 ºC/ 45 bar	24.5 h^{-1}
Effect of T/P on NiAl-T catalysts	235ºC/ 35 bar; 240 ºC/ 45 bar; 250 ºC/ 50 bar	24.5 h^{-1}
Stability of NiAl-T catalysts	235ºC/ 35 bar	24.5 h^{-1}
Effect of Ce and Mg promoters	235ºC/ 35 bar	24.5 h^{-1}
Nanocasted assays activity	235ºC/ 35 bar	24.5 h^{-1}
Effect of the space velocity (Nanocasted catalyst)	235ºC/ 35 bar	74-6 h^{-1} / 600-9500 g_{cat}·min·mol_{Gly}^{-1}

Downstream of the separator, gas products were swept with 40 mL·min^{-1} of He and introduced immediately after the backpressure regulator to GC. The liquid product was collected every 15 min in 2 mL glass vials and off-line analysed using the techniques described above. Note that zero time was considered when reactants attained the catalyst bed and the reaction temperature and steady state were reached.

Analysis of the catalytic performance

The performance of the catalysts is evaluated in terms of glycerol conversion, conversion to gas, as well as hydrogen yield and selectivity, among other parameters.

The glycerol conversion (X_{Gly}) was obtained by HPLC chromatographic analysis of liquid samples. Part of the total converted glycerol is transformed into a gas product, while the other to a liquid product. X_{Gly} is calculated by equation 2.20, as the molar ratio of glycerol reacted to the glycerol fed (F_{Gly}^0). Note that X_{Gly} is a reference value for further estimation of the hydrogen yield (YH_2) and selectivity.

$$X_{Gly}(\%) = 100 \times \frac{F_{Gly}^{\ 0} - F_{Gly}}{F_{Gly}^{\ 0}} \qquad (2.20)$$

where F_{Gly} the molar flow at the reactor outlet ($mmol_{Gly} \cdot min^{-1}$).

The conversion of C-atoms from glycerol reagent into gas-phase products (X_{Gas}) was determined by the TOC analysis, in terms of C-atoms converted. The X_{Gas} was calculated as a rate of total organic carbon concentration in the liquid sample at reactor outlet (TOC) to that in the feed solution (TOC^0):

$$X_{Gas}(\%) = 100 \times \frac{TOC^0 - TOC}{TOC^0} \tag{2.21}$$

The yield of H_2 (YH_2) was defined as the moles of hydrogen produced, with respect to the moles of hydrogen that are ideally produced if the glycerol is completely reformed (7 mol H_2/ mol $C_3H_8O_3$):

$$YH_2(\%) = 100 \times \frac{F_{H_2}}{F_{Gly}^{\ 0}} \times \frac{1}{7} \tag{2.22}$$

where F_{H2} are the molar flow of H_2 produced.

The selectivity to gas (S_{Gas}) is calculated by the sum of atomic carbon gas flows for each compound (*n*) divided by the glycerol converted. As the production of the atomic carbon gas flow cannot be higher than 3, this stoichiometric factor of glycerol reforming was used:

$$S_{Gas}(\%) = 100 \times \frac{\sum_n F_{Gas\text{-}n} \times C_{at,n}}{F_{Gly}^{\ 0} - F_{Gly}} \times \frac{1}{3} \tag{2.23}$$

where $F_{Gas\text{-}n}$ is the molar flow of the *n* compound ($mmol_C \cdot min^{-1}$); and $C_{at,n}$ are the number of carbons in the *n* compound.

Selectivity to hydrogen (SH_2) was defined as the ratio between the moles of H_2 obtained and moles of glycerol reacted, multiplied by 3/7 (the inverse of the stoichiometric reforming ratio):

$$SH_2(\%) = 100 \times \frac{F_{H_2}}{F_{Gly}^{\ 0} - F_{Gly}} \times \frac{3}{7} \tag{2.24}$$

Selectivity to hydrogen in the gas phase ($S_{H2\text{-}gas}$) was defined as the ratio between the moles of H_2 obtained and H moles released in gas-phase products:

$$S_{H_2\text{-}gas}(\%) = 100 \times \frac{F_{H_2}}{F_{H_2} + \sum (n+1) \cdot F_{C_nH_{2n+2}}} \quad (2.25)$$

The selectivity to CH_4 (SCH_4) was calculated as the ratio of moles of CH_4 produced (F_{CH4}) to the moles of glycerol reacted.

$$SCH_4(\%) = 100 \times \frac{F_{CH_4}}{F_{Gly}^{\ 0} - F_{Gly}} \quad (2.26)$$

The selectivity of the C-containing products is calculated from atomic carbon gas flows ($F_n x C_{at,n}$). Thus, S_{Alkane} was calculated for C1 (methane), C2 (ethane), C3 (propane) and C4+ (butane plus others not identified).

$$S_{Alkane}(\%) = 100 \times \frac{F_n}{F_{Gly}^{\ 0} - F_{Gly}} \times \frac{C_{at,n}}{3} \quad (2.27)$$

The total carbon flow of liquid products $F_{C\text{-}Liq}$ ($mmol_C \cdot min^{-1}$) was estimated based on the molar flow of each liquid compound *n*, multiplied by the number of carbons in the *n* molecule.

$$F_{C\text{-}Liq} = \sum F_{Liq,n} \times C_{at,n} \quad (2.28)$$

The yield of the liquid compound ($Y_{Liq\text{-}n}$) was calculated as the carbon molar flow of a given liquid compound ($F_{Liq\text{-}n} x C_{at,n}$) divided by $F_{C\text{-}Liq}$:

$$Y_{Liq\text{-}n}(\%) = 100 \times \frac{F_{C\text{-}Liq,n}}{F_{C\text{-}Liq}} \quad (2.29)$$

2.3.4 WGS and CO hydrogenation reactions

Additional experiments were conducted in the gas phase, consisting of CO hydrogenation and WGS reactions. Both reactions were performed isothermally at 350 ºC and atmospheric pressure, operating at GHSV 12,000 h^{-1}, in a fixed bed reactor

(P&ID EngTech). The feedstream composition was (in vol.%): $CO/H_2/He$: 7.5/10/82.5 for CO hydrogenation; and $CO/H_2O/H_2/He$: 7.5/25/10/57.5 for WGS reaction.

CO conversion (X_{CO}) and selectivity to CO_2 (S_{CO2}) in CO hydrogenation and WGS experiments were calculated as follows:

$$X_{CO}(\%) = 100 \times \frac{F_{CO}^{\ 0} - F_{CO}}{F_{CO}^{\ 0}} \tag{2.30}$$

$$S_{CO_2}(\%) = 100 \times \frac{F_{CO_2}}{F_{CO}^{\ 0} - F_{CO}} \tag{2.31}$$

where F_{CO}^{0} and F_{CO} are the molar flow of CO at the reactor inlet and outlet, respectively, and F_{CO2} is the molar flow of CO_2 at the reactor outlet.

2.3.5 Mass transfer limitations

In order to ensure that experiments were performed in a kinetic regime, i.e., in the absence of mass transfer limitations, the Weisz-Prater and Mears criteria were applied for the internal and external mass transfer limitations, respectively. The fastest reaction rate and the larger catalyst particle size were taken as the most critical condition [121].

- Weisz-Prater criterion (Φ_{WP})

The Weisz-Prater criterion Φ_{WP} analyses the absence of internal mass transfer limitations, as significant pore diffusion limitation, for values of $\Phi_{WP} < 6$ for a zero-order reaction, $\Phi_{WP} < 0.6$ for a first-order reaction and $\Phi_{WP} < 0.3$ for a second-order reaction [121]. The Φ_{WP} is calculated as follows:

$$\Phi_{WP} = \frac{r_{obs} \cdot \rho_{cat} \cdot r_d^{\ 2}}{D_{Gly\text{-}W,eff} \cdot C_{Gly,S}} \tag{2.32}$$

where r_{obs} is the observed reaction rate ($mol \cdot kg^{-1} \cdot s^{-1}$); ρ_{cat} is the catalyst density ($kg \cdot m^{-3}$); r_d is the catalyst particle radius (m); $D_{Gly\text{-}W,\ eff}$ is the effective diffusion coefficient of glycerol in water ($m^2 \cdot s^{-1}$); and $C_{Gly,S}$ is the glycerol concentration at the catalyst surface ($mol \cdot m^{-3}$).

The largest catalysts particle size is $1.6 \cdot 10^{-4}$ m (160 μm). $C_{Gly,S}$ is assumed equal to that of the feed solution concentration (10 wt.% glycerol/water). Catalysts studied in this work are spinel-based with similar density (ρ_{cat}), varying within a range from 2280 to 3530 $kg \cdot m^{-3}$, depending on the composition of the catalyst.

The effective diffusion coefficient is calculated by means of the ratio between porosity (ξ) and tortuosity (χ), which is taken 0.1 [121].

$$D_{Gly\text{-}W,eff} = D_{Gly\text{-}W} \frac{\xi}{\chi} \tag{2.33}$$

The diffusion coefficient of glycerol in water ($D_{Gly\text{-}W}$) is calculated according to Siddiqi-Lucas correlation, suitable for diluted mixtures:

$$D_{Gly\text{-}W} = 2.98 \times 10^{-7} \cdot V_{Gly}^{-0.5473} \cdot \mu_w^{-1.026} \cdot T \tag{2.34}$$

where T is the reaction temperature (K), μ_w is the water viscosity at the reaction conditions (cP), and V_{Gly} is the glycerol molar volume at boiling point (91 $cm^3 \cdot mol^{-1}$), calculated by Le Bass additive method [121].

- Mears criterion (MR)

The resistance to mass transfer outside the catalyst particle is estimated by the Mears criterion MR. The absence of external mass transfer is confirmed when the MR criterion meets:

$$\frac{MR}{n} = \frac{r_{obs} \cdot \rho_{bed} \cdot r_P}{k_c \cdot C_{Gly,S}} < 0.15 \tag{2.35}$$

where n is the reaction order; and ρ_{bed} is the packed bed density ($kg \cdot m^{-3}$); reaction order (n) was assumed to be first order in glycerol; k_c is the mass transfer coefficient ($m \cdot s^{-1}$). k_c has been estimated according to Chilton-Colburn analogy [122], as follows:

$$k_c = \frac{Sh \cdot D_{Gly\text{-}W}}{d_p} \tag{2.36}$$

d_p being the catalyst particle diameter (m). The Sherwood number is calculated by Wilson-Geankoplis correlation (equation 2.37), for liquid mass transfer at very low Re numbers (0.0015< Re <55) [122]:

$$Sh = \frac{1.09}{\varepsilon_e} \cdot Re^{1/3} \cdot Sc^{1/3} \quad (2.37)$$

being ε_e the external porosity equal to 0.32, calculated by the apparent density equation.

The Reynolds dimensionless number is defined as follows:

$$Re = \frac{d_p \cdot \nu_S \cdot \rho}{\mu_w} \quad (2.38)$$

where ν_S and ρ and μ_w are the liquid velocity ($m \cdot s^{-1}$), density ($kg \cdot m^{-3}$) and viscosity ($kg \cdot m^{-1} \cdot s^{-1}$), respectively.

In addition, the Schmidt number (S_c) is calculated as shown in equation 2.39:

$$Sc = \frac{\mu_W}{\rho \cdot D_{Gly\text{-}W}} \quad (2.39)$$

Estimations of Φ_{WP} and MR have been done for all catalysts, at comparative values of reaction conditions, i.e., employing a feedstock concentration of 10 wt.% glycerol/water. Results are reported in Appendix B.

2.4 DESIGN OF EXPERIMENTS FOR THE OPTIMIZATION OF APR OPERATION CONDITIONS

The design of experiments (DOE), the theoretical fundamentals of which are addressed in Appendix A, comprises the starting point to set up the APR reaction system, as well to obtain the optimal performance for the catalytic evaluation in this doctoral thesis. The employed complete factorial design with single replicate method, its analysis of variance and modelling basis, are briefly described below.

Complete $2^k + n_c$ factorial design, with k= 3 and n_c= 2 was employed. The influence of the factors k temperature (T), pressure (P) and space time (W/F_0), on the catalyst

performance in glycerol APR was evaluated. Two replicates at the centre point n_c were included. The selected response variables were glycerol conversion, conversion to gas, hydrogen yield and hydrogen selectivity. The employed method allowed detecting interaction effects between the factors.

In order to fix the variations of the factors between 1 and -1, each factor was normalised as follows:

$$k^* = \frac{k - k_c}{\Delta k} \tag{2.40}$$

where k* is the normalized factor; k_c is the value of the factor in the central point; and Δk is the maximum variation of the factor.

The analysis of variance (ANOVA) was used to identify the influence of the factor in the response variables. In addition, F-distribution was used to calculate the confidence intervals. The experimental results were given as empirical models by multiple linear regression to facilitate understanding and predictions. This statistical analysis was done by using Statistica 10 software.

Chapter 3

Catalyst screening and initial optimization of operation variables

In the first part of this chapter a screening with two families of Ni-based catalysts, bulk and supported, were performed for the glycerol APR. The catalysts were synthesized by impregnation, ion exchange and co-precipitation methods, from which the coprecipitated bulk samples show good performance in the APR, specifically $NiAl_2O_4$, which after reduction, achieves 67% of glycerol conversion and 24% conversion to gas. After characterization of the samples through N_2 physisorption, ICP, XRD, H_2-TPR, H_2-chemisorption and NH_3-chemisorption, it was found that the joint effect of properties such as Ni content, reducibility, and accessible metallic surface play an important role in the activity of the catalysts, while the acidity in the hydrogen yield plays the key role. Following, in the second part of the chapter, a factorial design of experiments (2^k+n_c) was carried out to evaluate the performance of the APR reactor system, and to identify the optimal ranges of the operation variables for glycerol APR reactions using $NiAl_2O_4$ as catalytic precursor. It was found that high ranges of values of temperature and space time enhance the glycerol conversion and hydrogen production, while pressure has little effect.

3. CATALYST SCREENING AND INITIAL OPTIMIZATION OF OPERATION VARIABLES

This chapter aims to establish the potential of the Ni-based catalysts for the glycerol APR, as well as the selection of a suitable catalyst, based on the enforcement of the activity, selectivity and stability in the H_2 production. The physicochemical properties of catalysts are an outcome of the synthesis method and the several variables involved. The approach of this chapter is to study each step (synthesis, properties, and APR performance) to base the catalyst selection on an integrative analysis of those parameters. Therefore, the catalytic APR test of two families of catalysts is included: (i) bulk catalysts synthesized by co-precipitation method; and (ii) supported catalysts, obtained by wet impregnation and ion exchange synthesis. Then, basic characterization of the synthesized solids is done focusing on the physicochemical properties analysis, and its relation to the catalytic performance is stablished.

Once the most suitable catalyst for the H_2 production by glycerol APR is identified, a second screening is carried out, this time regarding the APR operation variables. A statistical approach was pertinent since the design of experiments of this work was the starting point of the Aqueous-Phase Reforming in the *TQSA* research group, involving the new *Ma- Effi* reaction unit. Therefore, the second part of this chapter addresses the study of the effect of the main operation variables (temperature, pressure, and space time) over the conversion of glycerol, conversion to gas, hydrogen yield, and selectivity, using a factorial design 2^k+n_c, to efficiently get the desired performance of the APR system out. Besides, the operation range of the variables will be optimized.

3.1 VIABILITY OF Ni-BASED CATALYSTS FOR GLYCEROL APR

The catalyst outcome must be determined by its ability to present good catalytic behavior in the glycerol APR, presenting high H_2 selectivity by promotion of the C-C and C-H bond cleavage and a good activity for WGS reaction, as afore explained in Chapter 1. In addition, the catalysts should minimize the C-O cleavage to be selective for H_2.

3.1.1 SYNTHESIS OF THE Ni-BASED CATALYSTS

Two families of nickel-based catalysts are studied in the glycerol APR: (i) bulk catalysts group, including nickel aluminate spinel, besides Mg and Co are also added as dopants; and (ii) supported catalyst group, comprising a sample of Ni supported over γ-Al_2O_3, besides a sample of Ni supported over Na-Y zeolite.

The bulk catalyst family is composed by stoichiometric nickel aluminate spinel ($NiAl_2O_4$), and Mg- and Co-doped nickel aluminate (MgNiAl and CoNiAl, respectively). $NiAl_2O_4$ catalysts was synthesized by co-precipitation from nickel(II) acetate tetrahydrate and aluminium nitrate nonahydrate precursors (Table 2.1), with nominal molar ratio Ni/Al= 0.5, by adding drop by drop a 0.6 M aqueous solution of NH_4OH, rising from pH 4 (initial pH) to pH 8. The as-obtained slurry was aged for 30 min, then separated by filtration and washed with hot distilled water to eliminate remnants of NH_4^+ ions. The obtained solids were dried overnight (110 ºC) and then calcined in a muffle at 850 ºC for 4 h. The high temperature was selected for the calcination step with the purpose of forming spinels.

For the MgNiAl and CoNiAl synthesis the co-precipitation was subjected to either Mg or Co addition, called hereafter as Md (doping metal), with nominal molar ratios of Mg/Ni= 1 and Co/Ni= 0.20 and fulfilling the ratio (Ni+Md)/Al= 0.5. As Md precursor, magnesium nitrate hexahydrate and cobalt (ll) nitrate hexahydrate were employed. The ageing was extended to 20 h for CoNiAl. After the respective ageing of each solid, filtration and drying at 110 ºC were carried out. Finally, the solids were calcined at 850 ºC for 4 h, using a heating rate of 10 ºC·min^{-1}.

The supported catalysts family comprises the Ni/Y zeolite catalysts and Ni over γ-Al_2O_3 (Ni/Al). Ni/Y was synthesised by the metal ion exchange of the sodium form of Na-Y zeolite (Si/Al= 5.1). The Na-Y zeolite was added to an aqueous solution of 0.06 M of nickel(II) nitrate hexahydrate, the suspension was kept for 16 h at 80 ºC while stirring. Then, the solid was separated from the residual solution by centrifugation and washed thrice with deionized water. After drying overnight at 110 ºC, it was calcined at 600 ºC for 6 h, heating at 10 ºC·min^{-1} rate.

Ni/Al with nominal loading of 18 wt.% was synthesized by wetness impregnation (WI) of an aqueous solution of nickel(II) acetate tetrahydrate precursor in a rotary evaporator. After impregnation, the solvent was evaporated at 40 ºC and 2 mbar for 5 h approximately. The obtained solid was dried overnight at 110 ºC. Then, calcined in a muffle at 850 ºC for 4 h, with a heating rate of 10 ºC·min^{-1}. All samples have been pelletized at 0.04-0.16 mm before the catalytic test.

3.1.2 Catalysts screening for the glycerol APR

The catalytic performance was evaluated in the APR of an aqueous solution of 10 wt.% glycerol. The reactions were carried in a fixed bed reactor operating at 24.5 h^{-1}. Catalysts were in situ reduced at 700 ºC for 1 h, heating at 5 ºC·min^{-1} rate, in 20%H_2/Ar flow. For the screening, the reaction was carried out at 235 ºC and 35 bar.

The obtained glycerol conversion (X_{Gly}) and conversion to gas (X_{Gas}) is depicted in Figure 3.1 (a). Clearly, bulk catalysts present much better performances than the supported ones. For instance, at 1 h TOS, CoNiAl and NiAl achieve 69% and 67% X_{Gly}, respectively, while MgNiAl achieves 22% X_{Gly}. The achieved X_{Gly} by supported catalysts is much lower, Ni/Al presents around 11% X_{Gly}, and Ni/Y 3% X_{Gly}. For Ni/Y, results are taken for WHSV= 6.1 h^{-1} (steady state reached after 3 h). Regarding catalysts stability, after 3 h TOS, X_{Gly} decreases 11% for CoNiAl catalyst, and only 6% for NiAl and MgNiAl catalysts. Among the bulk catalysts, NiAl achieves the highest X_{Gly} after 3 h (63%).

In line with X_{Gly}, X_{Gas} follows a similar trend, as can be observed in Figure 3.1 (b). NiAl shows the highest conversion of carbon to gas (27%), closely followed by CoNiAl (25%). The slightly lower X_{Gas} of CoNiAl can be related to the lower capacity of Co in the C-C bond breakage with respect to Ni [123]. Among the bulk catalysts, MgNiAl presents the lowest X_{Gas} (6%). Very low X_{Gas} values are achieved by both supported catalysts (3% and 1% by Ni/Al and Ni/Y, respectively), confirming their poor performance for the glycerol APR. After 3 h, X_{Gas} decreases by 18% for CoNiAl catalyst. This decay is lessened for NiAl, with 6% decay, which reaches the highest X_{Gas} among all catalysts (27%), as it does for X_{Gly}. Other authors also reported stability issues for Co-based catalysts in liquid-phase reactions [76, 124], which would explain the downward trend in APR activity of CoNiAl catalyst.

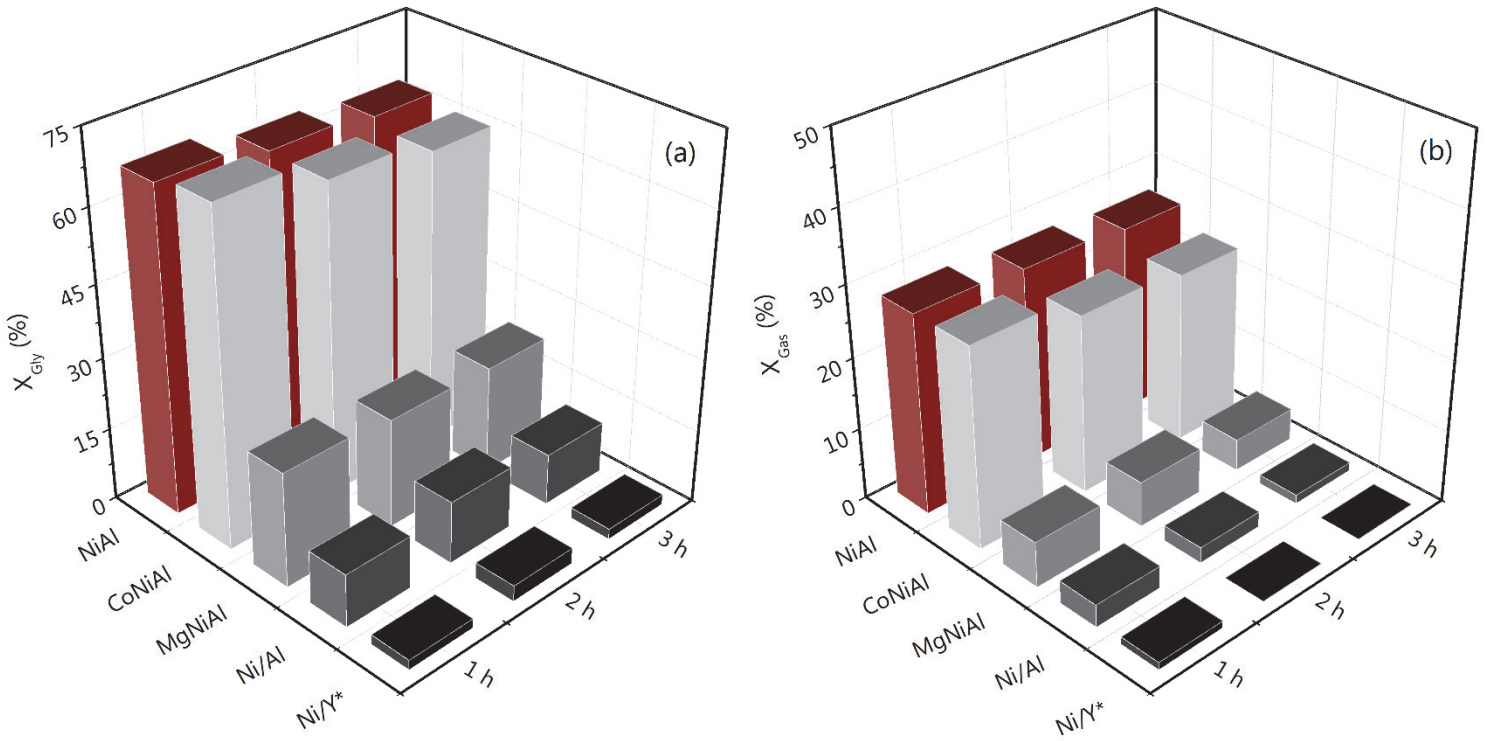

Figure 3.1. Catalysts screening for the glycerol APR. (a) glycerol conversion; (b) conversion to gas. Reaction conditions: 235 ºC/ 35 bar, WHSV= 24.5 h^{-1}. *Data at WHSV= 6.1 h^{-1}.

In addition to high X_{Gly} and X_{Gas}, an efficient catalyst for the glycerol APR to produce H_2 should reach high hydrogen selectivity (SH_2) and yield (YH_2), assuring that the consumption of the produced H_2 inside reactions, such as CH_4 (or higher alkanes) formation, is minimized. Hence, low selectivity to methane (SCH_4), the most probable alkane, is preferable. Figure 3.2 shows the hydrogen yield, and selectivities to hydrogen and to methane, which is the main alkane in the gas phase.

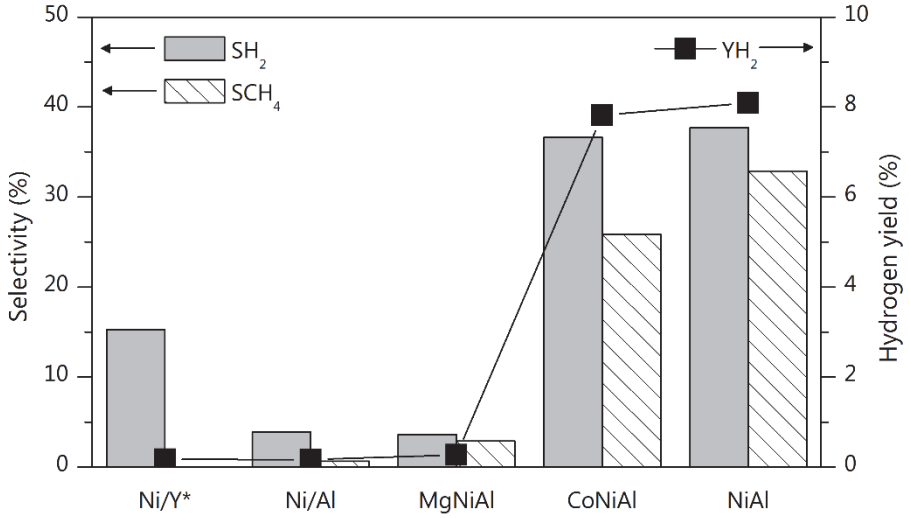

Figure 3.2. Selectivity to H_2 and CH_4, and H_2 yield. Reaction conditions: 235 ºC/35 bar, WHSV= 24.5 h^{-1}, 2 h steady state. * Data at WHSV= 6.1 h^{-1}.

Again, big difference between supported and bulk catalysts is appreciated. Supported Ni/Al catalyst shows limited SH_2 and very low YH_2, thus confirming the poor catalytic behaviour of Ni supported on γ-Al_2O_3. Ni/Y catalyst gives 15% SH_2, though accompanied by very low conversions.

Among bulk catalysts, NiAl and CoNiAl present similar SH_2 and YH_2, being slightly higher for NiAl. However, selectivity to methane was about 20% higher for NiAl than that for CoNiAl. Very poor YH_2 is achieved by MgNiAl catalyst, with SH_2 and SCH_4 around 5%.

NiAl catalyst presents a good catalytic performance in terms of conversion of glycerol and its respective conversion to gas. In the same line, hydrogen selectivity and yield of NiAl are the highest among the studied catalysts. Even though CoNiAl presents

interesting catalytic behaviour, especially due to the lowest selectivity to CH_4, it seems more likely to deactivate since its activity and H_2 yield decline rapidly with time.

Such a large difference in X_{Gly} and X_{Gas} had a remarkable effect on the H_2 yield, being below 0.3% for Ni/Al and around 8% for NiAl. These results indicated that spinel-derived nickel catalysts were much more efficient for H_2 production, by glycerol APR, than the catalyst obtained by impregnation onto γ-alumina or Na-Y zeolite.

Thus far, bulk catalysts represent the best option for the glycerol APR. Even though cobalt addition seems to improve the catalytic behaviour at the initial time, the improvement is not stable within the reaction time.

3.1.3 Physicochemical characteristics of bulk and supported Ni-based catalysts

The actual chemical composition of the bulk and supported solids is shown in Table 3.1. In addition, the leaching grade of the metals after 3 h of APR reaction are also presented.

Ni/Al catalyst has 19.4 wt.% of nickel content, which is close to the nominal value, while 7.7 wt.% of Ni loading is achieved by the ion exchange method for Ni/Y. Noticeably, Ni/Y has 3.2 wt.% of Na, indicating not complete exchange of sodium ions by nickel ions.

The coprecipitated NiAl solid has a Ni/Al molar ratio of 0.49, reasonably accurate to the nominal (Ni/Al= 0.5). In the same way, CoNiAl solid presents a (Ni+*Md*)/Al molar ratio of 0.59. Nonetheless, the Co/Ni molar ratio is higher than the nominal (0.32 vs 0.21). Much lower Mg content than the nominal (Mg/Ni: 0.014 vs 1.0) is found for MgNiAl (Table 3.1), which could be attributed to limitations of simultaneous co-precipitation using ammonia as a chelating agent. NH_4OH could re-dissolve nickel above pH 8 by forming a soluble ammonia nickel complex, while magnesium needs higher pH values than the ones used to precipitate ($K_{sp}= 1.8 \cdot 10^{-11}$) [125].

After 3 h of reaction, Ni leaching varies from 0.1% for Ni/Al to 1% for CoNiAl (Table 3.1). Leaching of Al is restrained, with a maximum of 0.07%. Concerning *Md* metal leching in MgNiAl and CoNiAl catalysts, 9.5% of Mg leached is found by only 1.0% of Co.

Table 3.1. Composition, grade of leaching, textural and chemical properties of the supported and bulk Ni-based catalysts.

Sample	Composition[a] (wt. %)			Leaching[a] (%)			Textural properties[b]			Reducibility[c]	Accesible metal[d]	Acid sites density[e]
	Ni	Al	*Md*	Ni	Al	*Md*	S_{BET} (m^2/g)	Vp (cm^3/g)	Dp (nm)	H_2 consumption (mmol H_2/g_{cat})	H_2 uptake (μmol H_2/g_{cat})	NH_3 uptake (μmol NH_3/m^2)
Ni/Al	19.4	44.0	n/a	0.1	0.03	n/a	69.7	0.1	43.1	3.0	1.1	1.89
Ni/Y	7.7	10.8	n/a	0.1	0.03	n/a	523.3	0.03	12.8	1.1	1.0	1.04
NiAl	32.0	29.6	n/a	0.7	0.05	n/a	98.0	0.3	8.3	5.6	19.5	1.66
CoNiAl	29.9	30.7	9.5	1.0	0.07	1.1	87.4	0.2	8.0	6.2	152.8	2.04
MgNiAl	21.5	38.9	0.3	0.3	0.01	9.5	89.5	0.4	12.8	3.5	21.4	1.92

[a] ICP; [b] N_2 physisorption; [c] H_2-TPR; [d] H_2-chemisorption; [e] NH_3 chemisorption.

3.1.3.1 *Textural properties of Ni-based catalysts*

The catalysts textural properties were analysed by N_2 physisorption. The obtained isotherms and pore size distributions are shown in Figure 3.3.

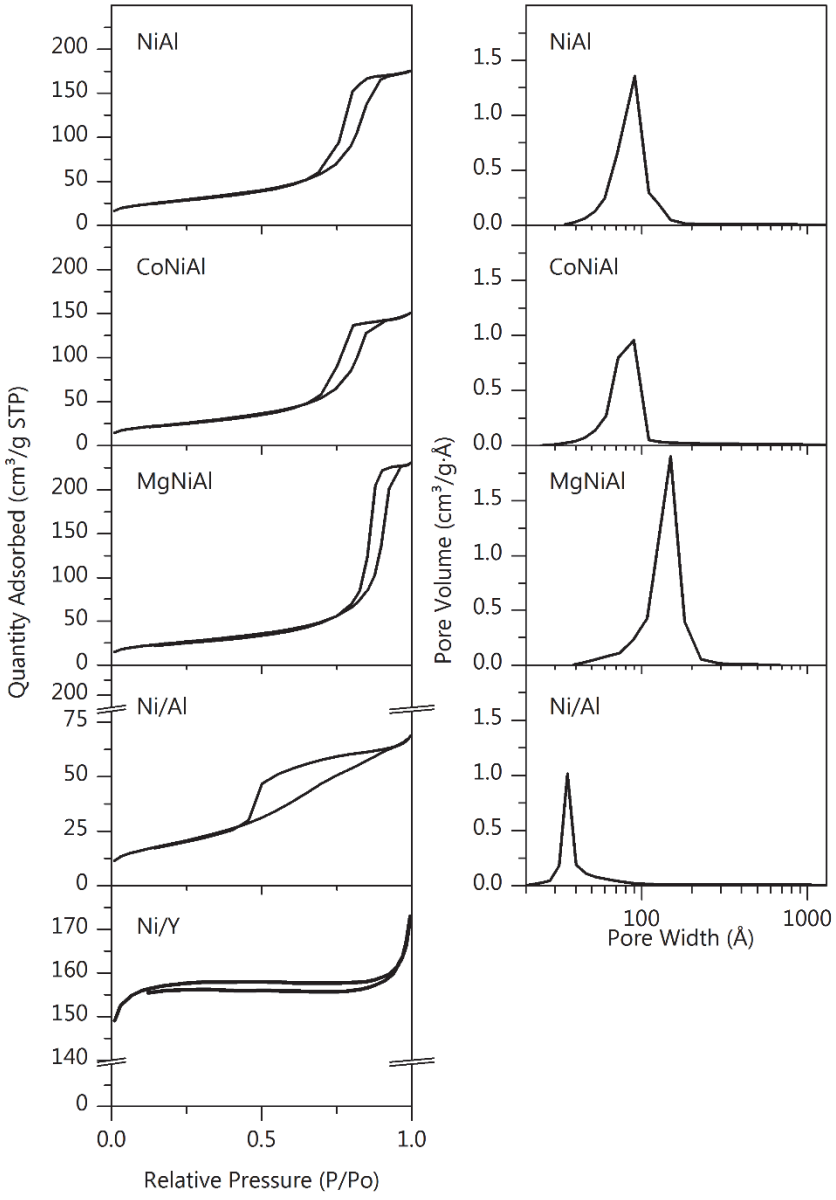

Figure 3.3. Isotherms and pore size distributions for supported and bulk Ni-based catalysts.

Ni/Al supported solid presents Type IV isotherms (according to IUPAC classification), corresponding to monolayer-multilayer N_2 adsorption followed by pore condensation in mesopores. The H2 type hysteresis loop is related to disordered porous materials of wider diameter than 4 nm [107]. Very different textural properties are found for Ni/Y, where the shape of the isotherms is related to a microporous structure (Type I) with a great amount of N_2 adsorbed at very low pressures (155 $cm^3 \cdot g^{-1}$) by microporous, with consequently low mesoporous adsorption, common textural characteristic of Y-zeolitic materials [126]. All bulk solids also present Type IV isotherms and the same type of hysteresis H2 (see Figure 3.3). Unimodal pore size distributions are observed for NiAl, MgNiAl and CoNiAl solids.

The textural properties of the supported and bulk Ni-based catalysts are given in Table 3.1. Among bulk samples, S_{BET} lowers in the following order: NiAl> MgNiAl> CoNiAl. The pore volume (Vp) and average pore size (Dp) are similar for NiAl and CoNiAl solids, while the magnesium-containing coprecipitated solid shows two-fold higher Vp and Dp values. S_{BET} of coprecipitated solids is higher than that of the impregnated Ni/Al. Ni/Y solid has the highest S_{BET} (>500 $m^2 \cdot g^{-1}$), in agreement with its zeolitic nature.

The 30% lower S_{BET} of Ni/Al solid, as compared to NiAl, could contribute to its very low APR activity. Note that slight differences in the textural properties of the bulk catalysts do not seem to influence their catalytic behaviour, thus the effect of the Ni content is higher than that of the S_{BET} of the materials. Similarly, the low Ni content of Ni/Y catalysts (7.7%) seems to influence in the negligible activity in the APR, despite having submitted high S_{BET}.

3.1.3.2 *Crystalline phases and morphology of Ni-based catalysts*

The morphological study and identification of crystalline phases of the supported and bulk Ni-based catalysts was carried out by XRD analysis. The diffractograms are presented in Figure 3.4. Ni/Al catalyst contains three cubic crystallographic phases, γ-Al_2O_3 (JCPDS 01-79-1558), NiO (JCPDS 01-78-0643) and $NiAl_2O_4$ spinel (JCPDS 00-010-0339). NiO diffraction peaks are narrow, indicative of the presence of large crystallites on the catalyst surface, as a consequence of the impregnation method used, which is known to favour the formation of large metal oxide clusters.

The XRD pattern of the zeolite Ni/Y matches that of the cubic faujasite structure ($Na_2Al_2Si_4O_{12}{\cdot}8H_2O$) according to JCPDS 00-039-1380. Unlike for catalyst Ni/Al, NiO phase is not detected for Ni/Y (Figure 3.4), which suggested that NiO concentration is low and that the high crystallinity of the zeolite could hide NiO diffraction signals.

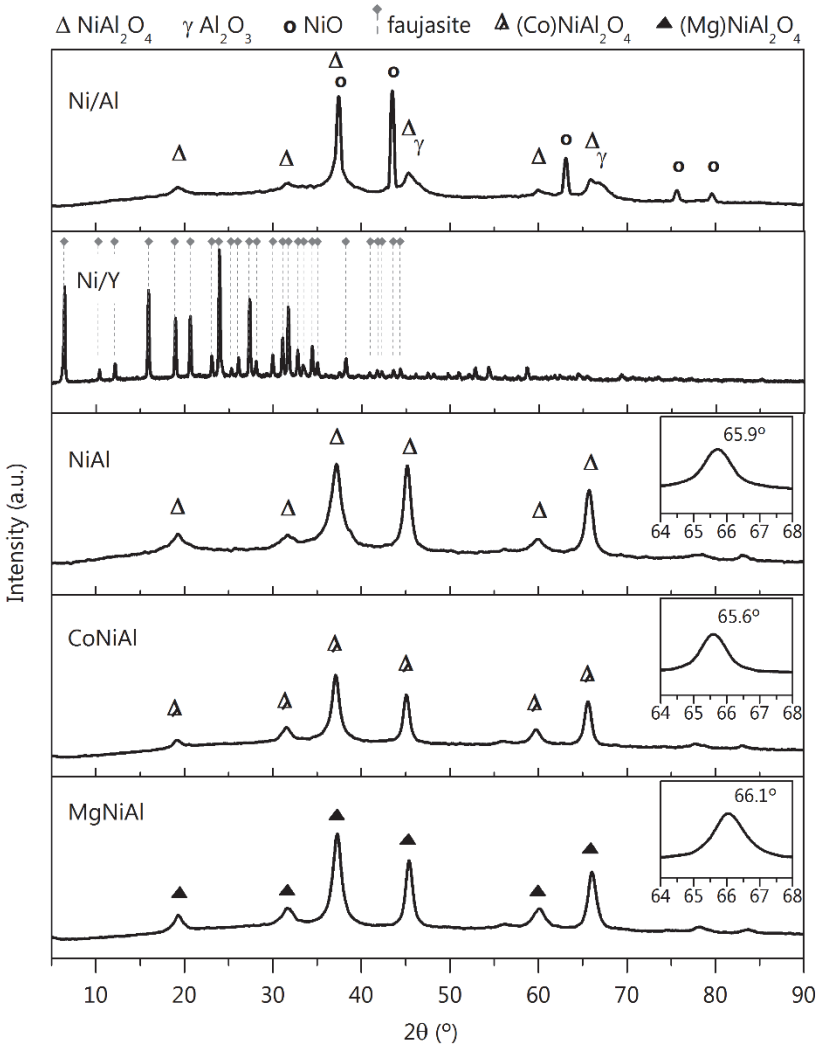

Figure 3.4. XRD patterns of the supported and bulk Ni-based catalysts. Inset includes detailed spectra at 65 ° peak.

NiAl bulk catalysts displays diffraction signals typical from cubic $NiAl_2O_4$ spinel, which suggested that Ni incorporation into spinel phase is favoured by the co-precipitation synthesis and further calcination at 850 °C. No separate peaks from

MgO or Co_3O_4 are observed in the XRD patterns of MgNiAl and CoNiAl solids. Instead, both bulk catalysts present diffraction signals from spinel phase. Nonetheless, it has to be considered that spinels can form solid solutions in which the ion 2+ could be placed not only by Ni^{2+}, but also by Mg^{2+}or Co^{2+}. Thus, the formation of spinel solid solutions like $NiAl_2O_4$-$MgAl_2O_4$ ((Mg)$NiAl_2O_4$, JCPDS 00-021-1152) and $NiAl_2O_4$-$CoAl_2O_4$ ((Co)$NiAl_2O_4$, JCPDS 00-044-0160) cannot be discarded, as the 2θ positions of the three spinels varied, as shown in insets of Figure 3.4.

3.1.3.3 *Reducibility of Ni-based catalysts*

The reducibility of the solids was studied by H_2-TPR and the obtained reduction profiles are shown in Figure 3.5. The H_2 consumption is summarised in Table 3.1.

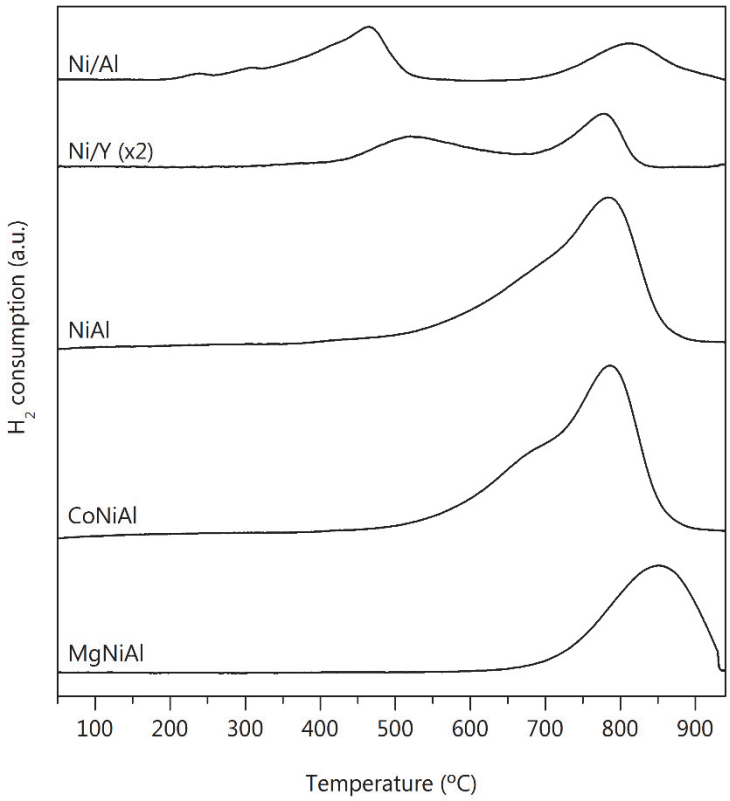

Figure 3.5. H_2-TPR profiles of supported and bulk Ni-based catalysts. Ni/Y: signal magnified by 2.

Ni/Al catalyst shows two reduction events indicating the presence of at least, two Ni^{2+} species. The low-temperature peak, with its maximum at around 460 ºC, is assigned to NiO particles weakly interacting with the alumina support. The peak asymmetry suggests the presence of NiO particles of different sizes and strength of interaction with the support [78]. The high temperature peak, centred at around 810 ºC, is ascribed to nickel in the spinel structure ($NiAl_2O_4$) [127]. The total H_2 uptake of Ni/Al indicates 100% of reduction degree of nickel species.

The H_2-TPR profile of Ni/Y presents three H_2 consumption maxima. The barely appreciable peak at 370 ºC is attributed to the reduction of surface NiO with low interaction with the zeolitic support, which is located externally. The peak at 520 ºC is associated with the reduction of Ni^{2+} species located on super cages and sodalite cages of the zeolite. Finally, the peak at the highest temperature (780 ºC) is related to the reduction of Ni^{2+} exchanged in hexagonal prisms, i.e. within the structure [126]. The total H_2 consumption of Ni/Y also evidences 100% of reduction degree of Ni species.

Catalyst NiAl showed a large and intense reduction event starting at 225 ºC. The left tail indicated again the existence of different nickel species. Deconvolution allowed differentiating three main peaks. First, a small reduction peak at a low temperature (around 460 ºC) ascribed to surface free NiO particles. Second, the medium temperature peak (around 680 ºC) associated with reduction of NiO interacting with the support (remaining phases) and sub-stoichiometric nickel spinel ($Ni_{1-X}Al_2O_{4-X}$) [85]. The third reduction peak with maxima at high temperature (around 790 ºC) is associated with $NiAl_2O_4$ spinel reduction. Complete reduction of Ni^{2+} species is accomplished for NiAl solid, as indicates the total H_2 uptake (Table 3.1).

The reduction profile of the bulk CoNiAl sample is very similar to that of the NiAl catalyst. Peaks related to Co_3O_4 reduction below 500 ºC are hardly identified. Slight differences are observed for CoNiAl of high intensities in peaks at 680 ºC and 790 ºC, associated to Co^{2+}. The H_2 consumption for CoNiAl was 15% lower than the theoretical for Ni^{2+} plus Co^{2+}(exclusive as Co_3O_4) reduction, with reduction stoichiometric ratios of H_2 : Ni and H_2 : Co of 1 : 1 and 4 : 3, respectively. Thus, for CoNiAl solid, the H_2 uptake of 6.15 mmol $H_2 \cdot g^{-1}$ points out the formation of aluminate species with lower reducibility

than Co_3O_4. Recall the reduction stoichiometry of 1 : 1 (H_2 : $CoAl_2O_4$). Similar findings have been reported by Choya et al. [128] in Co-Ni supported over γ-Al_2O_3 solids.

Reduction profile of MgNiAl solid is notably different than those for the other bulk catalysts. This case presents a notable upshift of the high temperature peak to 850 ºC. This behaviour could be ascribed to a lessening of reducibility of Ni^{2+} species in close proximity to MgO, due to the formation of $MgAl_2O_4$ [129]. It should be noted that the experimentally measured values of H_2 uptake for MgNiAl are close to the theoretical H_2 required for the complete reduction of Ni^{2+} species, considering the irreducibility of the MgO phase.

The high X_{Gly} and X_{Gas} obtained with NiAl and CoNiAl agree with their good reducibility, coupled with the high Ni content in those samples. MgNiAl presents high Ni content, though the lowest reduction degree negatively affects its activity in the glycerol APR.

3.1.3.4 *Surface properties of Ni-based catalysts*

The metal dispersion in the surface of the catalyst was calculated by means of H_2 chemisorption in the reduced samples (700 ºC) and results are given in Table 3.1. Bulk catalysts present significantly higher metal surfaces with respect to that of supported catalysts. The dispersion increases with the addition of a third metal, in the order CoNiAl> MgNiAl> NiAl, being CoNiAl about seven-fold greater than other bulk catalysts. Worth noting that the chemisorbed H_2 of MgNiAl and CoNiAl correspond to the bimetallic dispersion (Ni-*Md*), besides the H_2 : Co stoichiometry will be determined by the type of Co^{2+} species present in the reduced CoNiAl catalysts [128].

The improvement of the accessible metal surface by the co-precipitation synthesis is confirmed by these results. Besides, the metal dispersion could influence the catalytic behaviour in the glycerol APR, where bulk catalysts display much higher activity than that of supported catalysts (Table 3.1). Nonetheless, NiAl achieves the highest X_{Gly} and X_{Gas}, which can be explained as the joined effect between dispersion (accessible metal surface), nickel species reducibility and Ni content, rather than as an isolated dispersion effect. The active metallic phase in the APR reaction are mainly Ni^0, on which glycerol and water are adsorbed and proceeds the C-C cleavage and WGS reactions [130]

In addition to the presence of Ni^0 on the γ-Al_2O_3 surface, which as aforementioned, ensures the activation of the reagents, H_2 selectivity in the APR could be affected by the electron-accepting acid sites of support [131]. It may facilitate the transfer of hydrogen from metal particles and the consequent alkane (methane) formation. Also, the acidic support promotes glycerol dehydration. Therefore, the surface acidity of the catalysts was studied by NH_3-chemisorption, and the obtained results are shown in Table 3.1. As expected, Ni/Y presents the highest acidity (542.8 μmol $NH_3 \cdot g_{cat}^{-1}$), approximately three-fold greater than the acidity of the γ-Al_2O_3-containing solids, owing to the acidic nature of the Y-zeolitic support, which could contribute to the low activity of Ni/Y [62]. However, due to its high S_{BET}, the surface acid sites density of this solid (1.04 μmol $NH_3 \cdot m^{-2}$) is the lowest among all solids, regardless of the synthesis method employed, since little differences between Ni/Al and coprecipitated catalysts are found (Ni/Al: 1.89; bulk solids: 1.66-2.04, in μmol $NH_3 \cdot m^{-2}$). Nonetheless, it was noticed that among the bulk catalysts, NiAl has the lowest acid sites population (1.66 μmol $NH_3 \cdot m^{-2}$), which is reflected in its highest hydrogen yield (8%) achieved in the APR reaction.

3.2 OPTIMIZATION OF THE OPERATION VARIABLES

The optimization of the reaction conditions for the glycerol APR to produce hydrogen was done by statistical analysis, using a design of experiments (DOE) methodology for NiAl catalyst, which is the one that has shown the best outputs in the previous catalysts screening. The DOE allows obtaining the desired performance of the reaction system more efficiently than by using the common one-factor-at-a-time approach. In addition, it allows the study of the effect of the variable's interaction. The evaluation of the main response variables of the process: temperature, pressure and space time was included, and the obtained results are discussed in this section.

Table 3.2 shows the results of the single replicated factorial design of the glycerol APR using NiAl as catalyst, previously reduced at 700 ºC. The design of the experiments comprises eight runs, carried out in random order, besides two replicates at the centre point (0) that were included. The high-level values (1) are 240, 50 and 2100, and the low-level values (-1) are 210, 35 and 450 for T (ºC), P (bar) and W/F_0 ($g_{cat} \cdot min \cdot mol_{Gly}^{-1}$), respectively. The response variables are X_{Gly}, X_{Gas}, YH_2 and SH_2, and the data are reported at 2 h of APR reaction.

Table 3.2. Factorial designs 2^3+2 for the glycerol APR: levels, experiments sequence and response variables.

Run	T / T* (ºC)	P / P* (bar)	W/F_0 / W/F_0* (g_{cat}·min·mol_{Gly}^{-1})	X_{Gly} (%)	X_{Gas} (%)	YH_2 (%)	SH_2 (%)
8	240/1	50/1	2100/1	78.2	41.9	5.9	22.7
1	210/-1	35/-1	450/-1	12.6	1.7	0.01	0.2
4	210/-1	50/1	2100/1	33.7	11.6	0.05	0.4
6	240/1	35/-1	2100/1	75.1	35.2	10.3	41.1
9C	225/0	42.5/0	1275/0	42.0	14.3	0.6	3.9
2	210/-1	35/-1	2100/1	29.6	9.8	0.2	1.6
3	210/-1	50/1	450/-1	4.0	2.9	~0	0.02
10C	225/0	42.5/0	1275/0	37.0	12.1	0.4	3.5
5	240/1	35/-1	450/-1	27.7	11.8	2.8	29.8
7	240/1	50/1	450/-1	29.9	10.4	0.8	7.5

3.2.1 Glycerol conversion (X_{Gly})

The effect of the factors T, P and W/F_0 on the X_{Gly} was evaluated and the analysis of variance (ANOVA) is presented in displaying the sums of squares (SS), degrees of freedom (df), mean square (MS), F-statistic (F) and p-value (p) of each factor and the interaction between variables, as well as the curvature check (Curvatr.).

The ANOVA evidences that the W/F_0* has the highest effect in the variation of X_{Gly} (MS= 2532.94), followed by T* (MS= 2149.38), both marked in red in . Notice that W/F_0* mean square is much larger than the pure error mean square (12.65), evidencing the unlikeliness of obtaining equal X_{Gly} in experiments with different values of this operative variable. Consequently, from the $F_{1,1}$ distribution, p-values lower than α_s are found (p= 0.05 for 95% of confidence), for W/F_0* and T*, which means that those variables significantly affect the mean conversion of glycerol, contrary to the pressure variable. The effect of P* on X_{Gly} has turned out to be non-significant with MS= 0.08 and p-values much higher than α_s. Neither the joint two-factor interactions (see 1 by 2, 1 by 3 and 2 by 3 in), or the joint three-factor interactions (1*2*3), present significant effect on X_{Gly}, due to all of them presenting p-values <0.05 (α_s).

Table 3.3. Analysis of variance for X_{Gly}.

Factor	ANOVA; Var.:X_{Gly}; R^2=.9975; Adj:.97752 2**(3-0) design; MS Pure Error=12.65045 DV: X_{Gly}				
	SS	df	MS	F	p
Curvatr.	16.12	1	16.12	1.27	0.4616
(1)T* (°C)	2149.38	1	2149.38	169.91	0.0487
(2)P* (bar)	0.08	1	0.08	0.01	0.9489
(3)W/F_0^*	2532.94	1	2532.94	200.23	0.0449
1 by 2	12.03	1	12.03	0.95	0.5080
1 by 3	301.47	1	301.47	23.83	0.1286
2 by 3	22.95	1	22.95	1.81	0.4066
1*2*3	17.67	1	17.67	1.40	0.4470
Pure Error	12.65	1	12.65		
Total SS	5065.30	9			

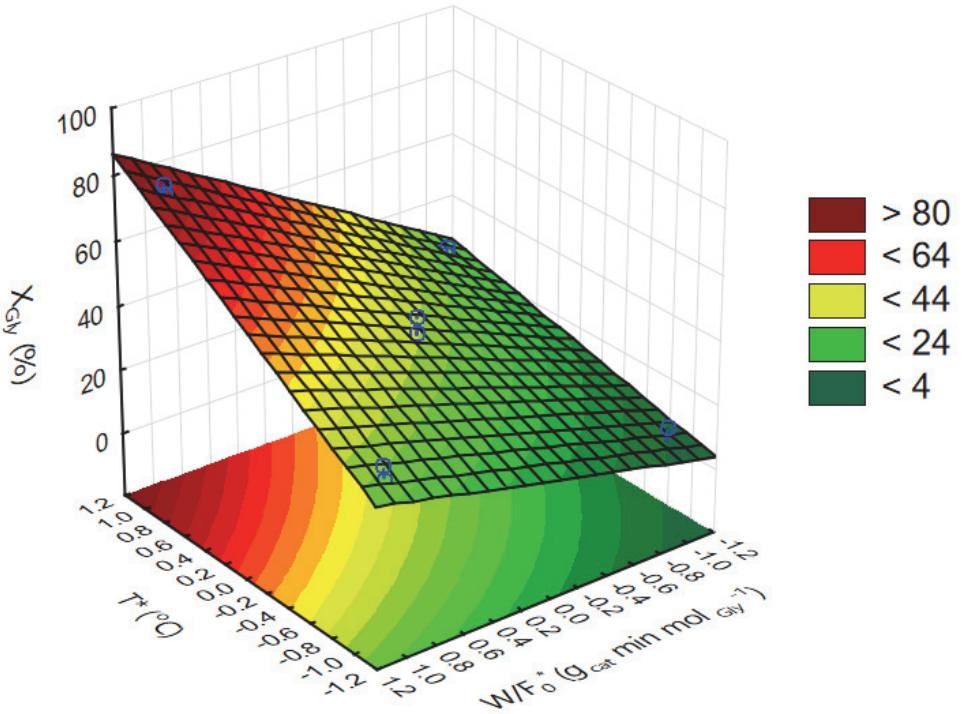

Figure 3.6. Response surface of X_{Gly} (P*= 0, fixed).

From Table 3.3 one can notice that the curvature significance is negligible (p-value= 0.46 > α_s). Thus, a first-order response surface model is obtained. X_{Gly} data was fitted to a first-order model, with pressure fixed at the centre point (42.5 bar) and not considering the T-P-W/F_0 interaction. The three-dimensional response surface obtained is shown in Figure 3.6.

The regression parameters of the equation model are presented in Table 3.4. The table presents: the coefficient of multiple determination (R^2), the regression coefficients for each factor and the two-factor interaction, their standard error (Std. Error) and confidence intervals, as well as their statistical significance including the t-test and p estimations.

Table 3.4. Regression analysis of the factorial model for X_{Gly}.

Factor	Regr. Coefficients; Var.:X_{Gly}; R^2=.99401; Adj:.97306 2**(3-0) design; MS Pure Error=12.6505 DV: X_{Gly}					
	Regressn Coeff.	Std.Err. Pure Err	t(1)	p	-95.% Cnf.Limt	+95.% Cnf.Limt
Mean/Interc.	36.3613	1.2575	28.9155	0.0220	20.3832	52.3393
Curvatr.	3.1737	2.8119	1.1287	0.4616	-32.5543	38.9018
(1)T* (°C)	16.3913	1.2575	13.0348	0.0487	0.4132	32.3693
(2)P* (bar)	0.1012	1.2575	0.0805	0.9489	-15.8768	16.0793
(3)W/F_0^*	17.7937	1.2575	14.1501	0.0449	1.8157	33.7718
1 by 2	1.2263	1.2575	0.9751	0.5080	-14.7518	17.2043
1 by 3	6.1388	1.2575	4.8817	0.1286	-9.8393	22.1168
2 by 3	1.6937	1.2575	1.3469	0.4066	-14.2843	17.6718

The optimal region for maximum X_{Gly} is found in between 230 to 250 °C, and 1600 to 2400 g_{cat}·min·mol_{Gly}^{-1}, which indicates that high temperature and space time favour the glycerol conversion. Similar results were obtained by Garcia et al. [132].

The subtle curvature of the X_{Gly} response surface attends to the inclusion of the two-factor interaction coefficients in the model. In this line, the equation 3.1 has been proposed for the estimation of X_{Gly} in the glycerol ARP using NiAl:

$$X_{Gly} = 36.3613 + 16.3913 \times T^* + 17.7937 \times W/F_0^* \quad (3.1)$$

Finally, from the observed vs. predicted values plotted in Figure 3.7, one can notice that the model accurately predicts X_{Gly} as no relevant deviation of the predicted values is noticed.

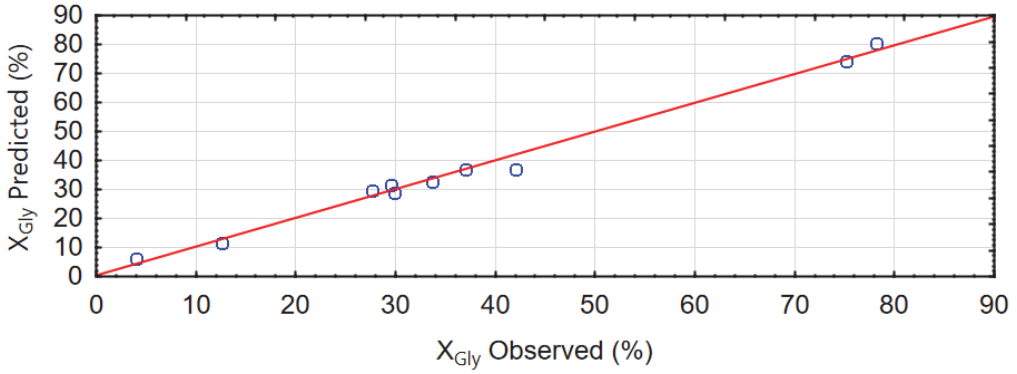

Figure 3.7. Parity plot for X_{Gly} model.

3.2.2 Conversion to gas (X_{Gas})

The ANOVA table of the effect of the factors on X_{Gas} is shown in Table 3.5. The ANOVA evidences that T* has the highest effect in the variation of X_{Gas} followed by the W/F_0*.

Table 3.5. Analysis of variance of X_{Gas}.

	ANOVA; Var.:X_{Gas}; R^2=.99848; Adj:.9863 2**(3-0) design; MS Pure Error=2.3328 DV: X_{Gas}				
Factor	SS	df	MS	F	p
Curvatr.	9.45	1	9.45	4.05	0.2936
(1)T* (°C)	670.15	1	670.15	287.27	0.0375
(2)P* (bar)	8.69	1	8.69	3.73	0.3043
(3)W/F_0^*	641.89	1	641.89	275.16	0.0383
1 by 2	0.61	1	0.61	0.26	0.7001
1 by 3	181.64	1	181.64	77.86	0.0718
2 by 3	9.42	1	9.42	4.04	0.2940
1*2*3	7.26	1	7.26	3.11	0.3283
Pure Error	2.33	1	2.33		
Total SS	1531.44	9			

The important effect of the temperature and space time over gas production in the APR process has also been reported by other authors [26, 75]. Consequently, p-values for T* and W/F_0* (0.03) are lower than α_s evidencing their significant effect on X_{Gas}. On the

contrary, no significant influence on X_{Gas} is observed for P* (p= 0.3). None of the joint factor interactions presents significant influence on X_{Gas}.

The SS-Curvatr. is 9.45, and the ANOVA indicates no evidence of second-order curvature (p= 0.29). Thus, data has been fitted to a first-order model with pressure fixed at the centre point (42.5 bar). Figure 3.8 shows the three-dimensional response surface plot obtained by regression modelling.

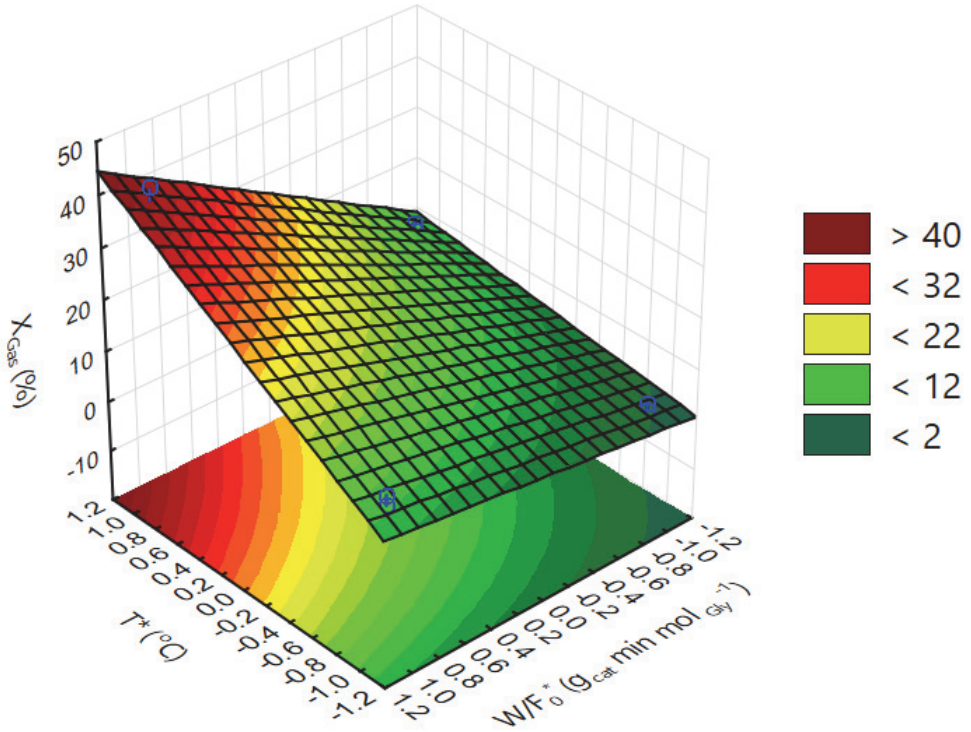

Figure 3.8. Fitted surface for X_{Gas} (P*= 0, fixed).

One can notice from the response surface that the optimal region for X_{Gas} is reached when the values of the temperature and space time are set in the higher values of the region explored (230-250 ºC and 1600-2400 g_{cat}·min·mol_{Gly}^{-1}, respectively). The regression coefficient for each factor and interactions, as well as their confidence intervals are presented in Table 3.6.

The model of equation 3.2 is proposed for the estimation of X_{Gas}:

$$X_{Gas} = 15.6400 + 9.1525 \times T^* + 8.9575 \times W/F_0^* \quad (3.2)$$

Table 3.6. Regression analysis of the factorial model for X_{Gas}.

Factor	Regr. Coefficients; Var.:X_{Gas}; R^2=.99374; Adj:.97182 2**(3-0) design; MS Pure Error=2.3328 DV: X_{Gas}					
	Regressn Coeff.	Std.Err. Pure Err	t(1)	p	-95.% Cnf.Limt	+95.% Cnf.Limt
Mean/Interc.	15.6400	0.5400	28.9630	0.0220	8.7786	22.5014
Curvatr.	-2.4300	1.2075	-2.0125	0.2936	-17.7724	12.9124
(1)T* (°C)	9.1525	0.5400	16.9491	0.0375	2.2911	16.0139
(2)P* (bar)	1.0425	0.5400	1.9306	0.3043	-5.8189	7.9039
(3)W/F_0^*	8.9575	0.5400	16.5880	0.0383	2.0961	15.8189
1 by 2	0.2750	0.5400	0.5093	0.7001	-6.5864	7.1364
1 by 3	4.7650	0.5400	8.8241	0.0718	-2.0964	11.6264
2 by 3	1.0850	0.5400	2.0093	0.2940	-5.7764	7.9464

The model fits experimental values well. Accordingly, no important deviation of predicted values is observed from Figure 3.9, regardless of X_{Gas} being high or low.

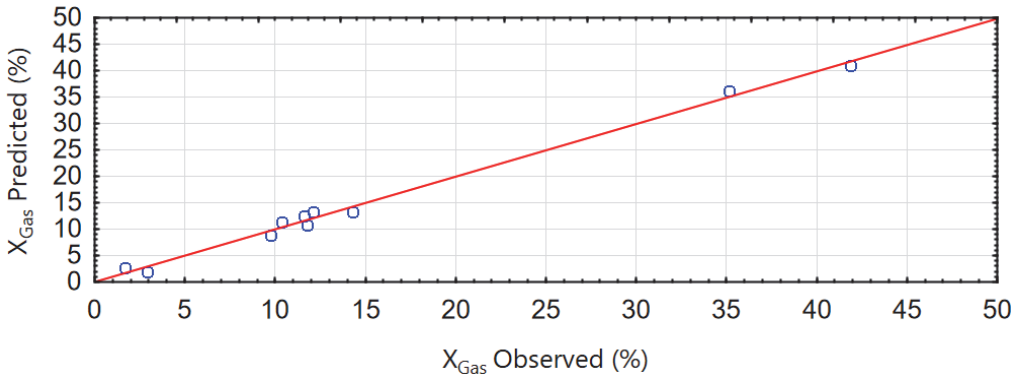

Figure 3.9. Parity plot for X_{Gas} model.

3.2.3 Hydrogen yield (YH_2)

The ANOVA is displayed in Table 3.7. T*, P* and W/F_0* present significant influence in the YH_2, with lower p-values than 0.05. It seems that the temperature is the main factor of influence, following by the space time, and consequently, T-W/F_0 interaction. The

pressure factor along with joint T-P interaction also present influence. Contrary, P-W/F_0 and the three-factor interaction do not influence YH_2.

Table 3.7. Analysis of variance for YH_2.

Factor	ANOVA; Var.:YH_2; R^2=.99993; Adj:.9994 2**(3-0) design; MS Pure Error=.00712 DV: YH_2				
	SS	df	MS	F	p
Curvatr.	6.40	1	6.40	899.54	0.0212
(1)T* (°C)	47.53	1	47.53	6679.74	0.0078
(2)P* (bar)	5.31	1	5.31	745.87	0.0233
(3)W/F_0^*	20.85	1	20.85	2929.37	0.0118
1 by 2	4.92	1	4.92	690.83	0.0242
1 by 3	19.59	1	19.59	2753.26	0.0121
2 by 3	0.77	1	0.77	108.64	0.0609
1*2*3	0.65	1	0.65	90.89	0.0665
Pure Error	0.01	1	0.01		
Total SS	106.03	9			

The H_2 production in the APR reaction involves multiple reactions. The complex set of side reactions involved could be the origin of the second-order interactions. In fact, the p-value for the pure quadratic effect (0.02) evidences second-order curvature in the region explored. Even though, the consideration of quadratic terms in the model is not allowed within the proposed design, due to the minor number of independent runs (9) of the unknown parameters (β= 10) in the second-order model [133]. Therefore, the response surface of YH_2 (Figure 3.10) was approximately calculated, assuming a model where P is fixed at the centre point and neither the T-P-W/F_0 interaction and quadratic effects are taken into consideration.

The surface plot (Figure 3.10) indicates that to obtain high YH_2, at pressure near the centre point, the optimum working ranges for the temperature and the space time are 230-250 ºC and 1600- 2400 g_{cat} min·mol_{Gly}^{-1}, respectively.

The multiple regression analysis (Table 3.8) indicates that except for the P-W/F_0 interaction, all other factors have a significant effect on the variance of YH_2.

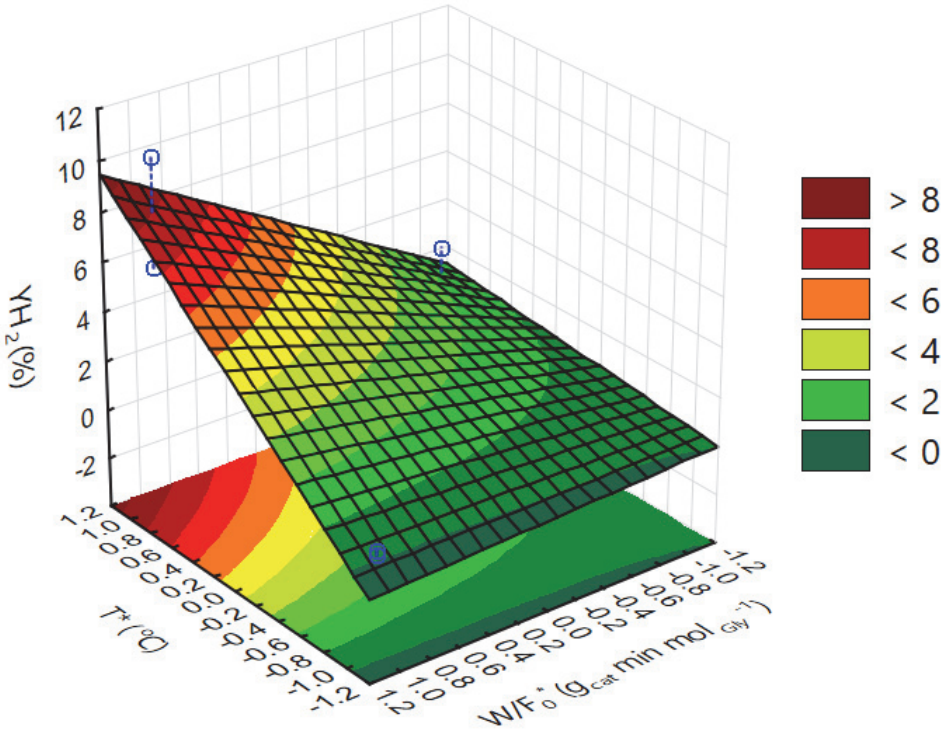

Figure 3.10. Response surface and contour plot of YH_2 (P*= 0, fixed).

Table 3.8. Regression analysis of the factorial model for YH_2.

Factor	Regr. Coefficients; Var.:YH_2; R^2=.9938; Adj:.9719 2**(3-0) design; MS Pure Error=.02 DV: YH_2					
	Regressn Coeff.	Std.Err. Pure Err	t(1)	p	-95.% Cnf.Limt	+95.% Cnf.Limt
Mean/Interc.	2.5075	0.0500	50.1500	0.0127	1.8722	3.1428
Curvatr.	-2.0075	0.1118	-17.9556	0.0354	-3.4281	-0.5869
(1)T* (°C)	2.4425	0.0500	48.8500	0.0130	1.8072	3.0778
(2)P* (bar)	-0.8200	0.0500	-16.4000	0.0388	-1.4553	-0.1847
(3)W/F_0^*	1.6050	0.0500	32.1000	0.0198	0.9697	2.2403
1 by 2	-0.7800	0.0500	-15.6000	0.0408	-1.4153	-0.1447
1 by 3	1.5450	0.0500	30.9000	0.0206	0.9097	2.1803
2 by 3	-0.3175	0.0500	-6.3500	0.0994	-0.9528	0.3178

Thus, model equation 3.3 is proposed to estimate the hydrogen yield in the glycerol APR:

$$YH_2 = 2.5075 + 2.4425 \times T^* - 0.8200 \times P^* + 1.6050 \times W/F_0^* - 0.7800 \times T^* \times P^* + 1.5450 \times T^* \times W/F_0^* \quad (3.3)$$

The model predicts the experimental YH_2 well despite neither the pressure variable nor second-order curvature being considered. Accordingly, Figure 3.11 shows that the observed YH_2 are located near the diagonal in the observed vs. predicted values plot.

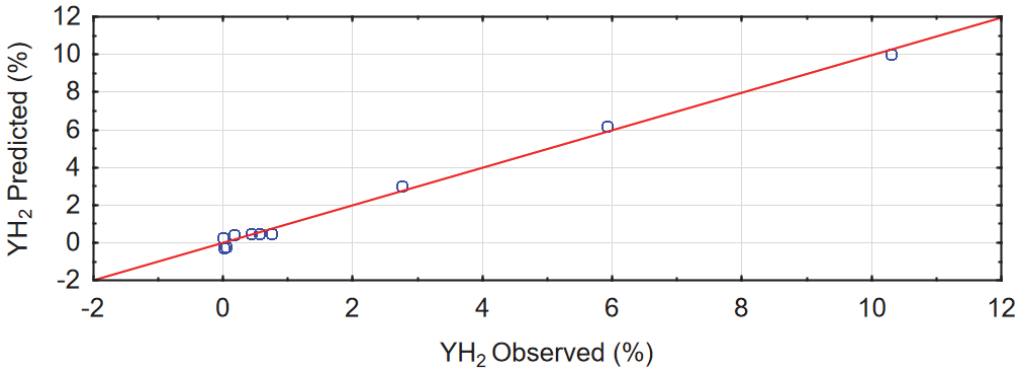

Figure 3.11. Parity plot for YH_2 model.

Therefore, the first-order model fitting can be considered valid for YH_2.predictions in the region explored.

3.2.4 Selectivity to hydrogen (SH_2)

The ANOVA for SH_2 is shown in Table 3.9. It was found that the three operative variables have a significant effect on SH_2 in the following order: T*> P*> W/F_0*. Besides, the T-P and T-W/F_0 interactions also have a significant effect. On the contrary, P-W/F_0 and the three-factor interactions have no significant effect on SH_2.

The curvature test indicates second-order curvature (p-value curvatr.< α_s). As occurred with YH_2, the second-order fitting could not be done, due to under sampling. As an approximation, the SH_2 response has been fitted to a first-order model. The three-dimensional response surface plot is shown in Figure 3.12.

The model excludes the three-factor interaction, and the space time is the factor fixed in the centre point, as changes in the temperature or pressure generate more important variations in SH_2 than changes in W/F_0 does.

Table 3.9. Analysis of variance of SH_2.

Factor	ANOVA; Var.:SH_2; R^2=.99995; Adj:.99957 2**(3-0) design; MS Pure Error=.0936579 DV: SH_2				
	SS	df	MS	F	p
Curvatr.	135.62	1	135.62	1448.08	0.0167
(1)T* (°C)	1221.31	1	1221.31	13040.13	0.0056
(2)P* (bar)	222.34	1	222.34	2373.93	0.0131
(3)W/F_0^*	100.30	1	100.30	1070.96	0.0194
1 by 2	193.85	1	193.85	2069.75	0.0140
1 by 3	76.28	1	76.28	814.50	0.0223
2 by 3	1.02	1	1.02	10.88	0.1874
1*2*3	3.03	1	3.03	32.39	0.1107
Pure Error	0.09	1	0.09		
Total SS	1953.86	9			

According to Figure 3.12, SH_2 increases with the temperature and with the decreased in pressure. The optimal region is at high temperature (235-250 ºC) and low pressure (30-40 bar), while the space time is kept at about 1275 $g_{cat}\cdot min\cdot mol_{Gly}^{-1}$.

The enhancement of SH_2 could be associated to the suppression of hydrogen-consuming glycerol hydrogenolysis and methanation side reactions [130], at high temperature and low pressure operating conditions of APR reaction. The regression coefficients shown in Table 3.10 confirm that the P-W/F_0 interaction has no effect on SH_2.

The following model equation is proposed for SH_2 predictions.

$$SH_2 = 12.92 + 12.36\times T^* - 5.26\times P^* + 3.53\times W/F_0^* - 4.92\times T^*\times P^* + 3.09\times T^*\times W/F_0^* \quad (3.4)$$

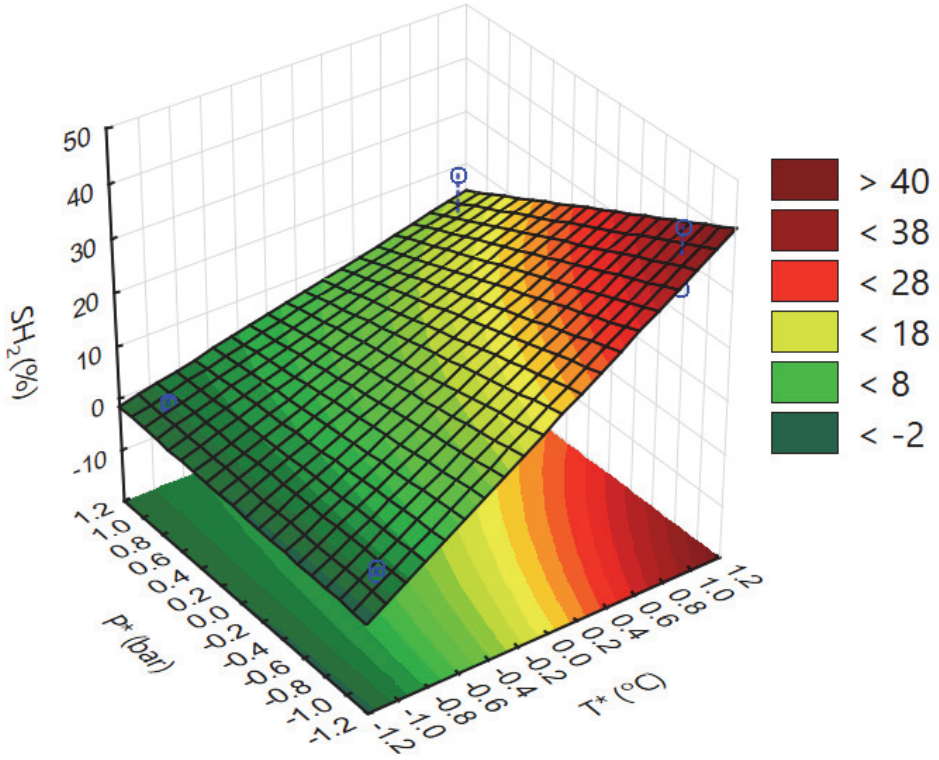

Figure 3.12. Fitted surface and contour plot of SH_2. (W/F_0= 1275 g_{cat}·min·mol_{Gly}^{-1}, fixed).

Table 3.10. Regression analysis of the factorial model for SH_2.

Factor	Regr. Coefficients; Var.:SH_2; R^2=.9984; Adj:.9928 2**(3-0) design; MS Pure Error=.09 DV: SH_2					
	Regressn Coeff.	Std.Err. Pure Err	t(1)	p	-95.% Cnf.Limt	+95.% Cnf.Limt
Mean/Interc.	12.9150	0.1000	129.1500	0.0049	11.6444	14.1856
Curvatr.	-9.2150	0.2236	-41.2107	0.0154	-12.0562	-6.3738
(1)T* (°C)	12.3600	0.1000	123.6000	0.0052	11.0894	13.6306
(2)P* (bar)	-5.2600	0.1000	-52.6000	0.0121	-6.5306	-3.9894
(3)W/F_0^*	3.5350	0.1000	35.3500	0.0180	2.2644	4.8056
1 by 2	-4.9150	0.1000	-49.1500	0.0130	-6.1856	-3.6444
1 by 3	3.0900	0.1000	30.9000	0.0206	1.8194	4.3606
2 by 3	0.3600	0.1000	3.6000	0.1725	-0.9106	1.6306

The parity plot for the SH_2 model shown in Figure 3.13 indicates that it accurately predicts the response variable, as no deviation of the predicted values are observed.

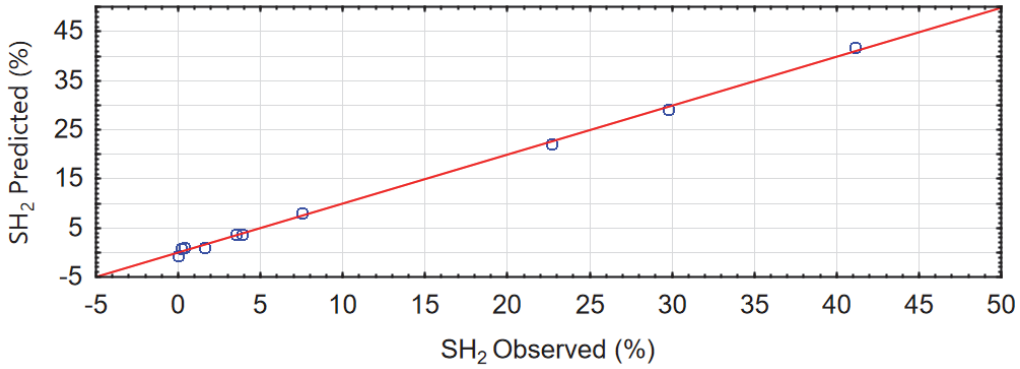

Figure 3.13. Parity plot for SH_2 model.

3.3 GENERAL OVERVIEW AND CONCLUSIONS

Given the different matter of study in this chapter (catalysts screening and optimization of operation variables) the conclusions are given separately.

Regarding the selection of the most suitable catalyst from the screening results, and according to APR performance, bulk catalysts derived from spinels are more advantageous than supported ones (both supported on γ-alumina and Na-Y zeolite). It is recognized that both the metal and the support play an essential role in the glycerol Aqueous-Phase Reforming over Ni-based catalysts.

The use of a nickel aluminate as catalyst precursor leads to obtaining catalysts that achieve high glycerol conversion and conversion to gas. The synthesis procedure notably affected the catalysts physicochemical properties, and therefore, APR activity. Nickel aluminate spinel synthesized by co-precipitation allows incorporating high Ni loadings and obtaining solids with good textural and morphological properties. Chapter 4 delves into the influence of the $NiAl_2O_4$ structure in the stabilization of small metallic nickel particles.

Cobalt-containing CoNiAl also presents physicochemical properties that accomplish notable APR performance, nevertheless, the stability is compromised. The

hydrogen yield can be tailored by the Ni content and the degree of reducibility. It can be deduced that small metallic Ni particles are crucial for achieving active catalysts for the APR; thus, the detriment of the reducibility of nickel species in the Mg-doped MgNiAl catalyst (even in very low Mg loadings) worsens its catalytic behaviour. Furthermore, this solid shows huge Mg leaching, though lessens Ni leaching. Based on these results, $NiAl_2O_4$ doping with a third metal by co-precipitation does not seem to be an effective approach for improving catalytic behaviour.

In this line, co-precipitation synthesis leads to good physicochemical characteristics, with promising stability that might be confirmed with long duration runs. Besides, a superior catalytic behaviour in terms of glycerol conversion, conversion to gas and hydrogen yield was exhibited by NiAl, compared with the other catalysts selected for the screening. Additionally, NiAl shows better stability than CoNiAl, the second more active catalyst. Based on both characterization and catalytic test results, the catalyst derived from stoichiometric $NiAl_2O_4$ precursor, synthesized by co-precipitation, has been chosen as an optimal formulation for the glycerol APR. In the following chapters, this catalyst will be thoroughly studied, with the aim of optimizing its catalytic performance, through improvements in the structure and morphology regarding the accessible Ni^0 surface, Ni^0 size, and the surface acid-base properties, among other key characteristics.

The factorial experimental design 2^3+2 for the glycerol APR to produce H_2 was done for the NiAl catalyst, derived from $NiAl_2O_4$ catalytic precursors. It has been found that the operation variables temperature, pressure, and space time influence the APR outputs differently. The optimal intervals of the operation variables are: 235-250 ºC for temperature, 30-42.5 bar for pressure, and 1600-2400 g_{cat}·min·mol_{Gly}^{-1} for the space time.

The response variables were analysed independently, so that the optimal operating intervals for each of them were found. Concerning the glycerol conversion, results evidenced that high temperature and high space time could enhance it, being the optimal regions for the temperature and space time 230-250 ºC, and 1600-2400 g_{cat}min·mol_{Gly}^{-1}, respectively. The only factors influencing the conversion of glycerol are temperature and space time.

In the case of the conversion to gas, it has been found that increasing temperature and space time, higher X_{Gas} are obtained. Besides, the optimal operation region for high X_{Gas} is 230-250 ºC for temperature and 1600-2400 $g_{cat}min \cdot mol_{Gly}^{-1}$ for space time, regardless of the operating pressure.

In the case of the hydrogen yield, the three operation variables presented a significant influence. Also, the interactions T-P and T-W/F_0 affect YH_2. The optimal operation regions for this response variable are similar to that of X_{Gas}: 230-250 ºC for temperature, and 1600-2400 $g_{cat}min \cdot mol_{Gly}^{-1}$ for space time, for pressure of about 42.5 bar.

Accordingly, T, P and W/F_0 evidenced a significant effect on the selectivity to hydrogen, and the interactions T-P and T-W/F_0 also have a significant influence. Increasing temperature while decreasing pressure enhance SH_2. The optimal operating intervals predicted, in terms of temperature and pressure, are: 235-240 ºC and 30-40 bar, with the space time set at about 1275 $g_{cat} \cdot min \cdot mol_{Gly}^{-1}$.

The statistical analysis has determined that the joint interaction of the three factors (T-P-W/F_0) does not influence conversion, nor the hydrogen production (YH_2 or SH_2).

The results observed confirm that the catalyst obtained by reduction of $NiAl_2O_4$ precursor performs adequately in the glycerol APR for the operation conditions stated above, achieving X_{Gly}= 75%, X_{Gas}= 35%, YH_2= 10%, and SH_2= 41% at 240 ºC, 35 bar and 2100 $g_{cat} \cdot min \cdot mol_{Gly}^{-1}$.

The response variables have been fitted to a first-order model. Although evidence of second-order curvature was identified for YH_2 and SH_2, the obtained R^2 and parity plots indicate that the regression models are expected to be good predictors for X_{Gly}, X_{Gas}, YH_2 and SH_2. Futhermore, the regression models represent the experimental results properly.

Chapter 4

Nickel aluminate spinel as catalyst precursor: effect of the reduction temperature

Bulk stoichiometrich nickel aluminate ($NiAl_2O_4$) was synthesised by co-precipitation at a Ni/Al mole ratio of 1:2. The prepared solid was reduced at different temperatures, in the 300 °C to 850 °C range. The obtained assays were analysed by a wide range of analytical techniques including XRF, XRD, H_2 chemisorption, H_2-TPR, UV–vis-NIR DRS, FTIR, ^{27}Al MAS NMR, NH_3 chemisorption, CO_2- TPD, and TPO, in order to gain knowledge in their physicochemical characteristics, which could influence the catalytic performance. The spinel precursor allowed the formation of small and stable Ni^0 particles (< 14 nm) after reduction. The strong interaction of the metal nanoparticles with the surroundings promotes their dispersion in the catalysts obtained upon reduction.

4. NICKEL ALUMINATE SPINEL AS CATALYST PRECURSOR EFFECT OF THE REDUCTION TEMPERATURE

Suitable nickel speciation and nickel-support interactions were sought to attain good catalytic performance towards hydrogen production by glycerol APR. This chapter aims to characterize the stoichiometric nickel aluminate spinel, that was activated at different reduction temperatures, in order to gain knowledge on the structural changes upon reduction treatment. For this purpose, a wide number of characterization techniques was employed, such as XRD, UV–vis–NIR DRS, FTIR, ^{27}Al MAS NMR, H_2-TPR, H_2 chemisorption, CO_2-TPD, NH_3 chemisorption and TPO.

Reduction can alter the structural properties of the nickel aluminate spinel. In the reduction process of spinel, oxygen vacancies move through the spinel to the particle surface. As a consequence, changes in the surface microstructure occur, with a major fraction of the metallic nickel particles forming on the surface. Thus, if the metal-support interaction is improved, a better catalytic behaviour could be obtained. For example, the creation of a nickel aluminate layer between the metallic nickel particles and the alumina could prevent sintering [78, 83, 89, 91].

For this study, $NiAl_2O_4$ precursor was synthesized by co-precipitation at a nickel to alumina mole ratio of 0.5, as Figure 4.1 shows in a schematic way. Actual nickel loading, evaluated by ICP-AES analysis was 32 wt.%, close to the stoichiometric value (33%), which gave a Ni/Al ratio of 0.49. The as-prepared precursor was divided into six parts. Five were subjected to different reduction temperatures (300, 450, 600, 700 and 850 ºC) and the remaining part was modified no further. The reduced solids are labelled NiAl-T, where T indicates the reduction temperature to which it has been submitted. The calcined, non-reduced solid is labelled NiAl-C. Reduction was done under 20% H_2/He atmosphere with a 5 ºC·min^{-1} heating ramp up sustained for 30 min. For comparative purposes, bare NiO and γ-Al_2O_3 were synthesized. NiO was obtained by direct calcination from the nickel acetate and γ-alumina by calcination of aluminium nitrate precursors, both at 850 ºC for 4 h, with a heating rate of 10 ºC·min^{-1}. The solids obtained were characterized as either calcined and reduced, and the results are discussed in the following sections.

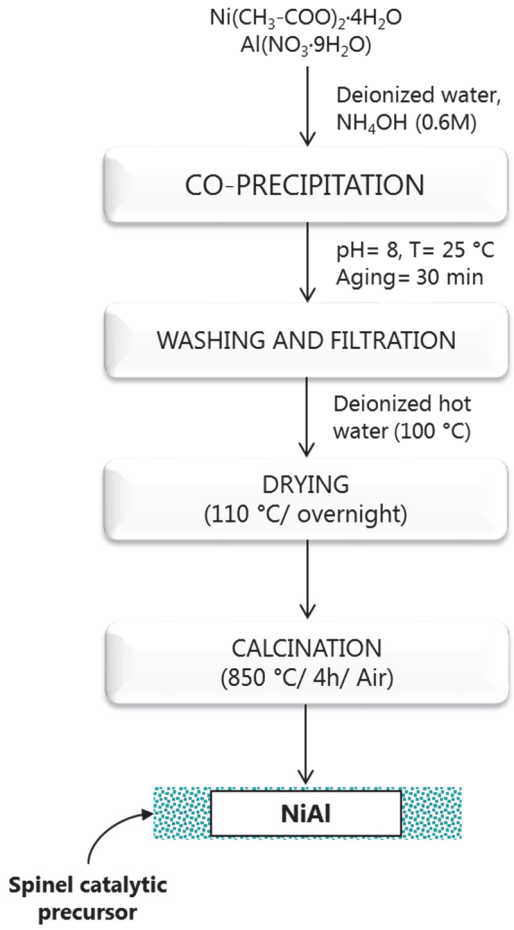

Figure 4.1. Scheme of the $NiAl_2O_4$ co-precipitation synthesis.

4.1 TEXTURAL PROPERTIES

The solids were analysed by N_2-physisorption. The adsorption-desorption isotherms are shown in Figure 4.2, and the textural properties are given in Table 4.1. Irrespective of the reduction temperature, very similar Type IV (IUPAC classification) isotherms are observed for all the solids. This type of isotherms are characteristic by mesoporous solids. In addition, all solids show H2-type hysteresis loop, related to disordered porous materials.

Textural properties, obtained from BET formalism, are detailed in Table 4.1. The specific surface area of the calcined nickel aluminate (NiAl-C) is similar to that of bare γ-alumina (101.6 $m^2 \cdot g^{-1}$). S_{BET} slightly decreased upon reduction, monotonically with

reduction temperature, which could be associated with a $NiAl_2O_4$ phase transition by reduction. Nonetheless, a partial blockage of pores cannot be discarded. Overall, this behaviour points to the notable structural stability of the stoichiometric $NiAl_2O_4$, as S_{BET} decreases only 22% after reduction at 850 ºC.

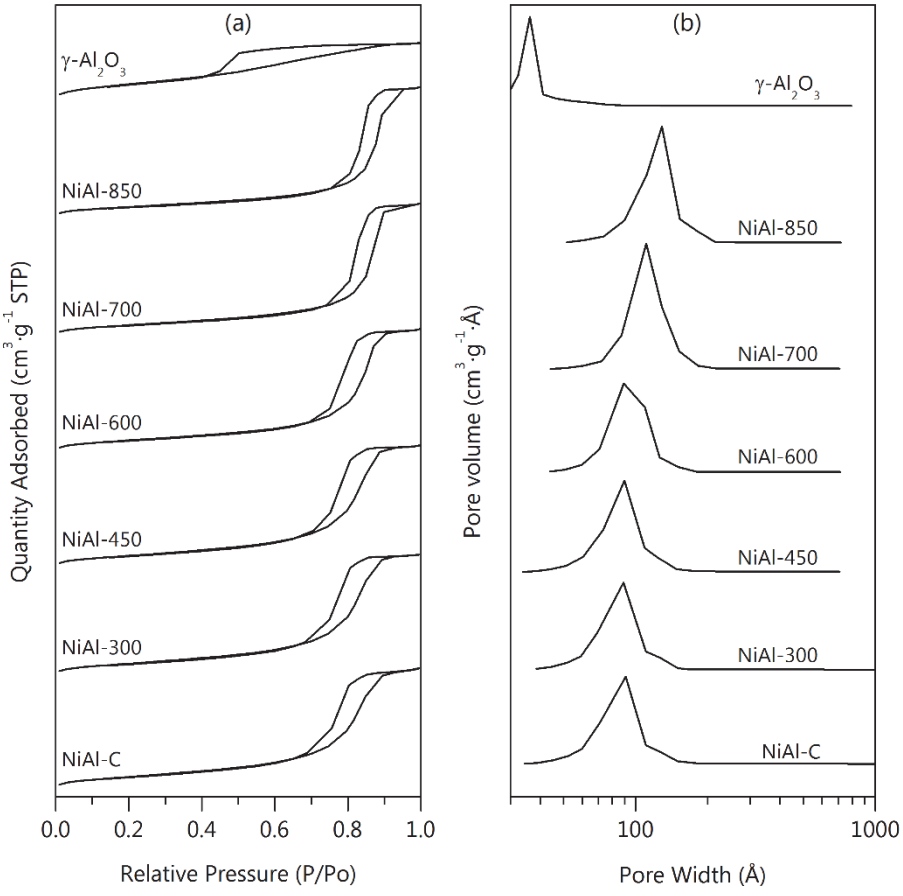

Figure 4.2. (a) N_2 physisorption isotherms and (b) pore size distribution for NiAl-T and NiAl-C solids.

Regarding the pore size distribution, all solids show an unimodal structure as depicted in Figure 4.2 (b). It is noticed that the pore volume (Vp) and the average pore size (Dp), determined from BJH formalisms, increases more than twofold after the incorporation of Ni. In addition, with higher reduction temperatures, a slight increase in Vp and Dp were observed for NiAl-T solids. Reduction at above 450 ºC shifted the main

average pore diameter to larger values, likely caused by the collapse of the smallest pores at high temperatures.

Table 4.1. Textural characteristics of the nickel aluminate spinel calcined (-C) and reduced at different temperatures (NiAl-T).

Catalysts	S_{BET} ($m^2 \cdot g^{-1}$)	Vp ($cm^3 \cdot g^{-1}$)	Dp (nm)
γ-Al_2O_3	101.6	0.13	3.6
NiO	0.3	0.0013	n.d.
NiAl-C	98.0	0.27	8.3
NiAl-300	94.9	0.27	8.3
NiAl-450	93.5	0.28	8.4
NiAl-600	89.8	0.28	9.1
NiAl-700	83.1	0.29	10.8
NiAl-850	76.6	0.29	11.8

4.2 REDUCIBILITY AND PHASE IDENTIFICATION

The reducibility of the nickel aluminate spinel precursor (NiAl-C) and the solids reduced at different temperatures (NiAl-T) was studied by H_2-TPR. The obtained profiles are shown in Figure 4.3, and those for bare NiO and Al_2O_3 are also included for comparison purposes.

Noteworthy that H_2-TPR was carried out for NiAl-C, NiO, and γ-Al_2O_3 samples up to 950 ºC and kept for 30 min (H_2-TPR_{950}). Also H_2-TPR was done for the partially reduced samples (NiAl-T), with the aim of calculating the fraction of reduced nickel (f_{red}). As explained in detail in Chapter 2, each sample was reduced at temperature T for 30 min. The amount of H_2 consumed in this stage was defined as H_2-TPR_{Tred}. Then, after cooling down to room temperature, a subsequent TPR run, up to 950 ºC, was carried out and the amount of H_2 consumed there is H_2-$TPR_{Tred\text{-}950}$ (see Figure 2.1). The value f_{red} for each NiAl-T sample is the fraction of H_2-TPR_{Tred} consumption with regard to the NiAl-C consumption in the H_2-TPR_{950}. The H_2 consumptions of the samples are given in Table 4.2.

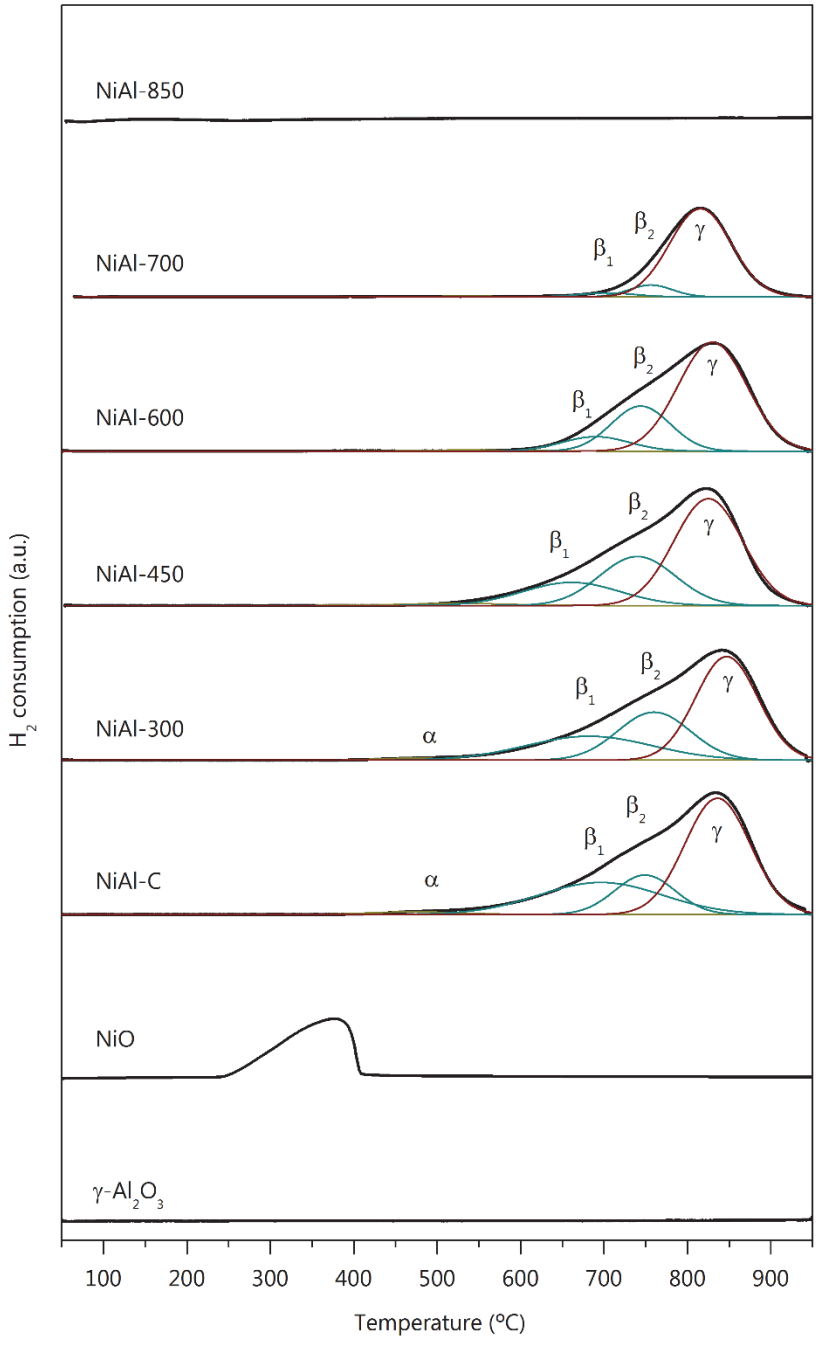

Figure 4.3. Reduction profiles for the calcined nickel aluminate spinel and reduced at different temperatures ($TPR_{T\text{-}950}$).

Bare NiO exhibits a relatively narrow reduction peak in the 240 ºC to 410 ºC range, with its maximum at 377 ºC in line with literature [78]. All NiO is reduced at below 410 ºC, since the experimental hydrogen consumption (13.4 mmol $H_2 \cdot g^{-1}$) and the theoretical value (13.3 mmol $H_2 \cdot g^{-1}$) are the same, within the experimental error. Bare γ-Al_2O_3 shows null H_2 consumption in the studied temperature range, indicating it is hardly reducible. Therefore, only nickel species will be reduced in the NiAl-C and -T samples. Reduction profile of NiAl-C sample indicates that the incorporation of aluminium significantly modified the reduction profile of nickel species. The observed peaks shift toward higher temperatures in the reduction profile of NiAl-C and NiAl-T, with respect to bare NiO, evidencing the intimate interaction of Ni species with alumina, accomplished by the co-precipitation synthesis.

Note that profiles of NiAl-T solids in Figure 4.3 correspond to the so-called $TPR_{Tred\text{-}950}$, that is, the hydrogen consumption profile of the samples that have previously been reduced at temperature T, for 30 min. Recall that the TPR_{950} profile for NiAl-C sample was already discussed in Chapter 3.

All reduction profiles present a left tail, which suggestes the existence of several nickel species with different degrees of interaction with the surroundings, i.e. NiO and $NiAl_2O_4$, as depicted by the following reactions:

$$NiO + H_2 \rightarrow Ni^0 + H_2O \quad (4.1)$$

$$NiAl_2O_4 + H_2 \rightarrow Ni^0 + Al_2O_3 + H_2O \quad (4.2)$$

The reduction profile was deconvoluted into three peaks, namely α, β and γ for the low (~460 ºC), medium (~680 ºC) and high (~850 ºC) temperature centered maxima of consumption. Similar findings have been reported by other authors [85, 127, 134, 135]. The α peak is ascribed to surface nickel oxide of easy reduction. The reduction of these nickel species is according to reaction 4.1. The medium temperature β peak is ascribed to Ni^{2+} species in a defective $Ni_{1-X}Al_2O_{4-X}$ phase. Finally, the high temperature γ peak, centred at approximately 830 ºC, is related to the reduction of Ni^{2+} species in the $NiAl_2O_4$ spinel lattice [127], according to stoichiometry in reaction 4.2.

Free nickel oxide (α peak) is reduced around 150 ºC above that of bare NiO, which evidenced the interaction between NiO particles and the surroundings [136]. The peak β was split into two contributions, namely β_1 (at a lower temperature) and β_2 (at a higher temperature). The molar ratio β_1/β_2 for the non-reduced sample was 1.1, which in turn, decreased with the reduction temperature, as shown in Table 4.2. This suggested that the composition of defective $Ni_{1-X}Al_2O_{4-X}$ depends upon reduction treatment, likely β_1 referred to Ni-rich solid and β_2 referred to Ni-lean solid [137].

Hydrogen consumption of β and γ species scarcely vary upon reduction below 450 ºC, causing a relative contribution to overall Ni species of around 45% and 52%, respectively. Reduction at 600 ºC decreases the hydrogen consumption of the defective spinel phase (β peak) to half, and the Ni^{2+} species in the NiAl-700 resultant catalyst were mainly $NiAl_2O_4$. Eventually, at 850 ºC, all Ni is fully reduced (Figure 4.3, Table 4.2).

Regarding the fraction of reduced nickel, it can be interpreted by Ni^{2+} exudation from the spinel matrix towards the surface during the nickel reduction [138]. It is found that very low values of f_{red} at lower temperatures than 600 ºC are obtained (Table 4.2), owing to the good stability of the spinel phase. Nonetheless, the fraction of reduced nickel for NiAl-T greatly increased at higher temperatures. The reduction at 600 ºC accomplishes f_{red}= 21%, while at 700 ºC, f_{red} shows a more than two-fold increase. Besides, it reaches almost a total fraction of nickel reduced within the NiAl-850 sample. It is worth mentioning that the support role in NiAl-T is played by a mixture of γ-alumina and remaining $NiAl_2O_4$ and related phases (Ni-Al-O). These results could lead to the interpretation of the slight decrease in S_{BET} upon reduction by the phase transformation from $NiAl_2O_4$ to Ni/support (Table 4.1) [78, 139].

The speciation in Table 4.2 evidences the amount of Ni^0 in the calcined NiAl-C and NiAl-T reduced solids. It can be directly associated with f_{red}, thus showing similar trends. Solids reduced at T ≥ 600 ºC present a higher Ni^0 content, of 1.10, 2.90 and 5.19 mmol $Ni \cdot g^{-1}$ for NiAl-600, NiAl-700 and NiAl-850, respectively.

Table 4.2. Results from H_2-TPR for the stoichiometric nickel aluminate spinels, calcined and reduced at different temperatures.

	H_2 consumption (mmol $H_2 \cdot g^{-1}$)		**Ni^0 extent**	**Distribution of Ni (mmol Ni·g^{-1})**				
Sample	H_2-TPR_{950}	H_2-$TPR_{Tred-950}$	f_{red} (%)	As Ni^0	As Surface NiO (α peak)	As $Ni_{1-X}Al_2O_{4-X}$ (β peak)	As $NiAl_2O_4$ (γ peak)	β_1/β_2 molar ratio
NiAl-C	5.2	-	-	~0	0.08 (1.5)	2.32 (44.7)	2.79 (53.8)	1.10
NiAl-300	-	5.0	3.8	0.20 (3.8)	0.10 (1.9)	2.32 (44.5)	2.59 (49.7)	0.90
NiAl-450	-	4.9	5.8	0.30 (5.9)	~0	2.19 (42.8)	2.63 (51.4)	0.72
NiAl-600	-	4.1	21.1	1.10 (21.4)	~0	1.30 (25.3)	2.74 (53.3)	0.47
NiAl-700	-	2.3	55.8	2.90 (56.2)	~0	0.30 (5.8)	1.96 (38.0)	0.44
NiAl-850	-	0.01	99.8	5.19 (99.8)	~0	~0	0.01 (0.2)	~0

Values in parentheses are molar percentages (%).

It has been suggested that reduction of α-type nickel species (free NiO) produces large metallic Ni particles [85, 97, 136, 137]. The quantitative results of the TPR profiles (Table 4.2) show that α-type species are less than 2% for the $NiAl_2O_4$ catalyst precursor. Thus, the small average crystallite size of Ni^0 particles obtained (Table 4.3), could be partially attributed to the low amount of surface nickel oxide species and the fact that the catalyst precursor contained mainly Ni^{2+} species in a spinel-like structure. In addition, the spinel phase of remaining $NiAl_2O_4$ or related phases at the interface between the metal nanoparticles and the oxide support in NiAl-T samples, could act as a fixer [138], thus inhibiting the coalescence of metallic nickel particles in the surface, which favours dispersion of the metallic nickel phase formed upon reduction.

To determine the accessible metallic nickel to reactants of the APR reaction, H_2 chemisorption has been carried out over NiAl-T catalysts and the obtained results are given in Table 4.3. As expected, the accessible metallic nickel surface ($A_{S\text{-}Ni^o}$) increased with the reduction temperature from 0.07 $m^2_{Ni^o}\cdot g^{-1}$ for NiAl-300 to 3.47 $m^2_{Ni^o}\cdot g^{-1}$ for NiAl-850. In terms of exposed Ni^0 atoms, it increased from $1.14x10^{18}$ for NiAl-300 to $53.4x10^{18}$ $at_{Ni^o}\cdot g^{-1}$ for NiAl-850, due to the migration of nickel from spinel phase to the catalyst surface (exudation). The onset in the surface enrichment in Ni^0 starts at 600 ºC.

4.3 CRYSTALLINE PHASES AND MORPHOLOGY

The morphological study and the identification of crystalline phases of NiAl-C and NiAl-T solids was carried out by X-ray diffraction analysis, for each solid previously reduced at the evaluated T_{red}, for 30 min. Details of ex-situ reduction are found in Chapter 2. The obtained diffractograms are presented in Figure 4.4. XRD of bare γ-alumina is also included.

The calcination at high temperature of aluminium nitrate leads to aluminium oxide with nominal formula $Al_{2.144}O_{3.2}$ (JCPDS 01-079-1558). The diffractogram of this solid presents wide peaks and elevation of the background, indicating its amorphous characteristics.

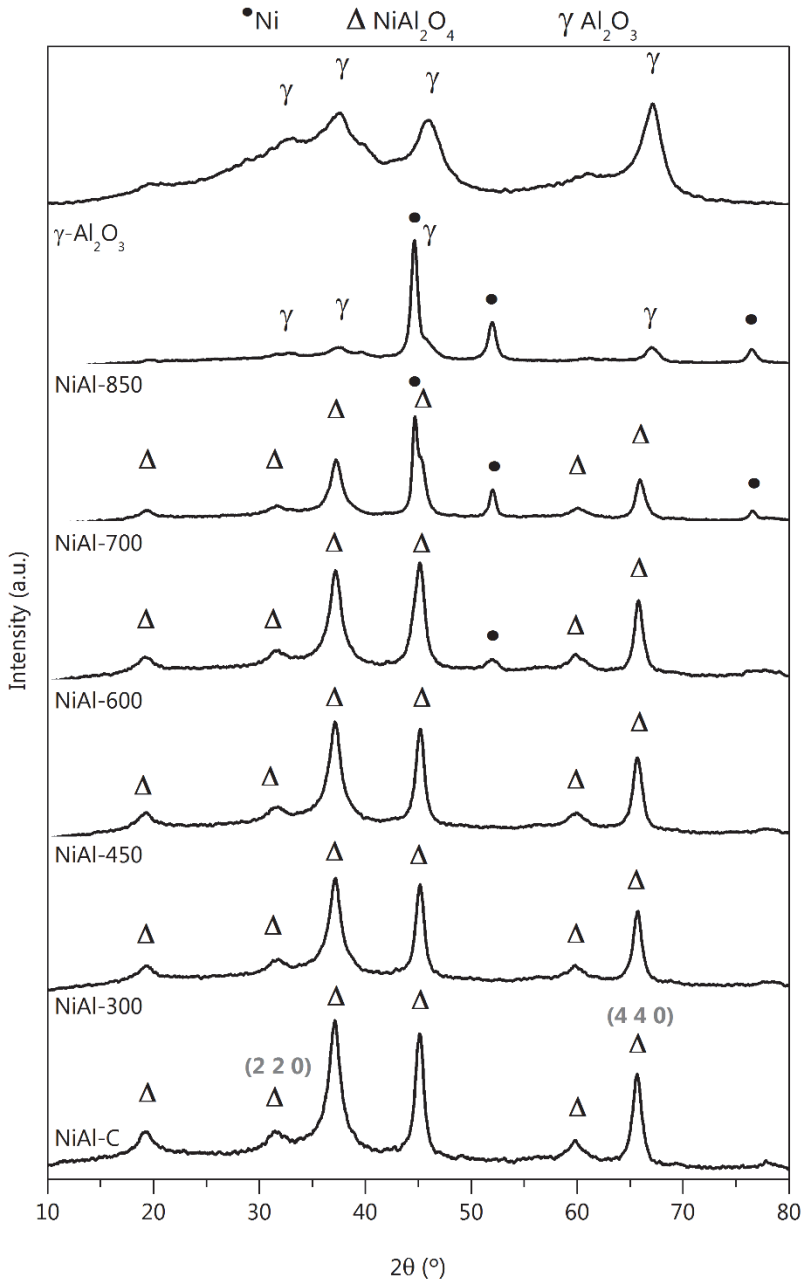

Figure 4.4. XRD spectra of the nickel aluminate spinel, calcined and reduced at T_{red}.

Table 4.3. Structural characteristics and H_2 chemisorption results for NiAl-C and NiA-T.

Sample	$d_{NiAl2O4}$[a] (nm)	d_{Ni^o} [a] (nm)	Phases detected[a]	$a_{NiAl2O4}$ [a] (Å)	a_{Ni^o} [a] (Å)	I_{220}/I_{440} [a]	$Ni^{2+}{}_{Td}/Ni^{2+}{}_{Oh}$[b]	$A_{S\text{-}Ni^o}$ [c] ($m^2{}_{Ni^o}{\cdot}g_{cat}{}^{-1}$)	Exposed Ni^0 [c] ($at_{Ni}{\cdot}g_{cat}{}^{-1}$)
NiAl-C	8.9	n/a	$NiAl_2O_4$	8.044 ±0.0063	n/a	0.25	1.44	~0	~0
NiAl-300	9.9	n/a	$NiAl_2O_4$	8.040 ±0.0060	n/a	0.25	1.35	0.07	$1.14x10^{18}$
NiAl-450	9.2	n/a	$NiAl_2O_4$	8.036 ±0.0088	n/a	0.24	1.31	0.10	$1.53x10^{18}$
NiAl-600	9.8	7.7	Ni^0 + $NiAl_2O_4$	8.028 ±0.0053	3.520 ±0.0026	0.22	n.d.	0.48	$7.37x10^{18}$
NiAl-700	9.1	13.6	Ni^0 + $NiAl_2O_4$	8.010 ±0.0061	3.519 ±0.0032	0.21	n.d.	1.63	$25.1x10^{18}$
NiAl-850	7.0*	11.6	Ni^0 + γ-Al_2O_3	7.879*	3.522 ±0.0021	n/a	n.d.	3.47	$53.4x10^{18}$

[a] from XRD. [b] from DRS UV-vis NIR. [c] from H_2 chemisorption.* γ-Al_2O_3

For NiAl-C and NiAl-T solids, the most prominent features of XRD patterns are ascribed to cubic spinel structure (JCPDS 78-1601). The diffraction peak at 2θ= 65.7º corresponding to the plane (4 4 0) confirms the formation of $NiAl_2O_4$ spinel, together with the peaks at 19.1º, 31.6º, 37.1º, 45º, and 60.1º 2θ. Contrary, XRD peaks related to NiO structure are not detected, despite the presence of NiO (α-phase) in NiAl-C (1.5%) and NiAl- 300 (1.9%), as confirmed by TPR. The absence of NiO signals could be associated with a low concentration and a smaller crystallite size than XRD detection limit (≈2-4 nm). Characteristic features for metallic nickel at 44.5º, 51.8º, and 76.4º 2θ (JCPDS 01-087-0712) appear upon reduction at 600 ºC and above. Although TPR analysis confirmed that about 6% of the nickel in the spinel precursor is reduced at 450 ºC, its absence in the XRD spectra highlighted an adequate dispersion of the metal. Metallic Ni diffraction signals increase in intensity at higher reduction temperatures. It is observed that reduction at ≤ 600 ºC hardly alters the XRD spectra peaks shape and position (i.e. 2θ= 19.0º, 37.0º, and 59.6º) remain almost constant, reflecting the high stability of the $NiAl_2O_4$ phase. The formation of the γ-alumina phase can be recognized upon reduction at 850 ºC.

The crystallite size of each identified specie was calculated using the Scherrer equation and results are presented in Table 4.3. The crystallite size of spinel and metallic nickel (in reduced catalysts) varies in the 9-10 nm and 8-14 nm range, respectively. In both cases, no clear trend in crystal growth is observed with the reduction temperature. The relatively small size of the formed metallic nickel nanoclusters, despite the high reduction temperature used, reflects the strong interaction of nickel with the Al-Ni-O support, which stabilizes Ni^0 particles and decreases their surface mobility, protecting against sintering under a reductive atmosphere. Similar findings are reported in literature [85, 136, 137].

The unit cell parameter (a) of the nickel-containing phases was also calculated from the XRD diffractograms, and the results are shown in Table 4.3. Spinel crystallizes into Fd-3m cubic system and metallic nickel into Fm-3m cubic system. The experimentally measured lattice parameter for the unreduced sample is 8.044 Å ± 0.0063, very close to that of stoichiometric nickel aluminate spinel (a= 8.0480 Å) (JCPDS 00-010-0339). Similar cell parameters were found by others [79]. Exposition to hydrogen atmosphere notably decreases the unit cell parameter of the spinel phase, more pronounced with the

increase of the reduction temperature (from 8.044 Å for NiAl-C to 8.010 Å for NiAl-700). According to Halevy et al. [140], this could be explained in terms of the compressive residual stresses generated during the reduction of the mixed oxide. The lattice compression reflected the exudation of the nickel ions from the nickel aluminate lattice to the surface, suggesting that the solid bulk is progressively enriched in alumina, approaching to the alumina lattice parameter (7.911 Å, JCPDS 01-079-1558). The unit cell parameter of the metallic nickel was almost unaffected (around 3.52 Å).

Shifts in the diffraction peak (4 4 0) are detailed Figure 4.5. Notably, the (4 4 0) peak position from NiAl-C shifted toward higher 2θ values (given as Δθ). The Δθ boosted for reduction temperatures above 600 °C. For the highest reduction temperature of 850 °C, 2θ position for plane (4 4 0) shifts to 67.3°. This fact reinforces the idea that nickel was drawn towards Ni^0 clusters and matrix composition tended to γ-Al_2O_3 [78].

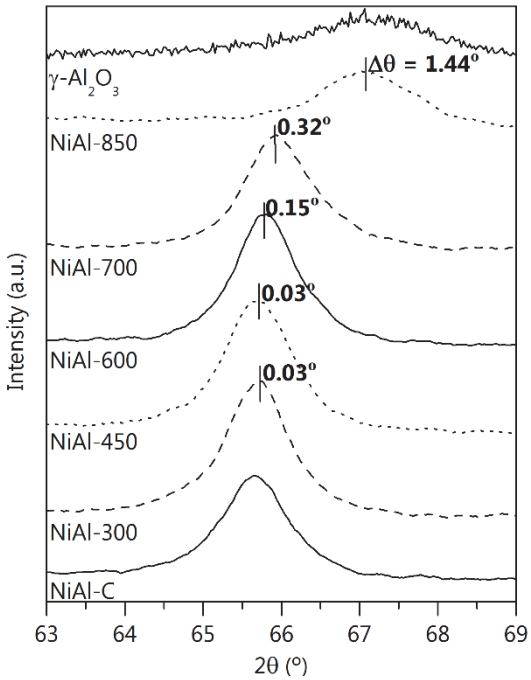

Figure 4.5. Shift of the peak at 2θ= 65° with T_{red} for the (4 4 0) plane respect to NiAl-C.

The intensity ratio of peaks corresponding to (2 2 0) and (4 4 0) reticular planes (I_{220} / I_{440}), is usually related to cation distribution [141]. I_{220} / I_{440} for NiAl-C and NiAl-T are shown in Table 4.3, which differ among the catalysts. As the ionic radius of Ni^{2+}

(0.69 Å) exceeds that of Al^{3+} (0.54 Å), I_{220} / I_{440} increases with increasing Ni^{2+} cations on tetrahedral sites (Td), and the ratio decreases with increasing occupancy of Ni^{2+} cations on octahedral sites (Oh). For "normal" spinel this ratio would approximate 0.33 [141]. NiAl-C sample shows an I_{220} / I_{440} of 0.25, and a decreasing trend with reduction temperature is observed (e.g. I_{220} / I_{440}= 0.21 for sample NiAl-700). This could be associated with a slight enrichment of the reduced system in Ni^{2+} hosted in octahedral sites. This points out that tetrahedral Ni^{2+} is more readily reduced as compared to octahedral Ni^{2+} sites. Presumably, the lattice oxide ions of the trigonal prism stabilize the Ni^{2+} rather effectively.

Further evidence on the exudation of Ni^0 from the spinel lattice with the reduction treatment are observed from the thermodifractometric analysis in Figure 4.6.

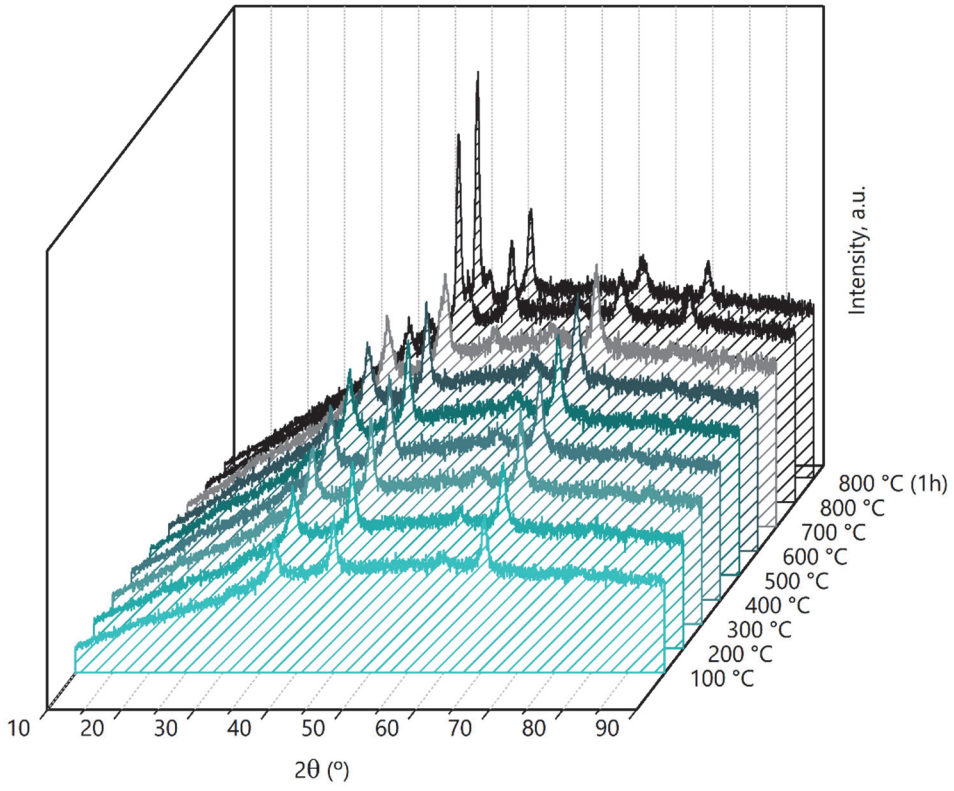

Figure 4.6. Effect of reduction temperature on the structure of the nickel aluminate spinel: thermodiffractometric reductive analysis (from ambient to 800 °C).

Under reductive conditions, the XRD pattern for NiAl-C presents characteristic signals of $NiAl_2O_4$ at 100 ºC, the intensities of which significantly drop with the increase of temperature (T>100 ºC). When the reduction temperature reaches 800 ºC, $NiAl_2O_4$ signals disappear giving rise to γ-Al_2O_3 diffraction peaks (37.6º, 45.6º, and 66.5º 2θ), at slighty higher positions of 2θ than those for the spinel phase. On the other hand, the presence of the Ni^0 crystalline phase at 700 ºC is evidenced by the appearance of a shoulder and a peak at 44.7º and 51.6º 2θ, respectively. The XRD intensity of Ni^0 peaks clearly rises with temperature up to 800 ºC, mainly due to an increase in the fraction reduced Ni (f_{red}). Then, the total diffusion of nickel from the spinel lattice to the surface requires rising temperature to 800 ºC or even above, as is confirmed by the thermos-diffractometric results.

4.4 SPECIATION ANALYSIS BY FTIR AND UV-vis-NIR DRS

The speciation of nickel cations (coordination and oxidation states) was analysed by FTIR and UV-vis-NIR DRS spectroscopy. The recorded FTIR spectra for NiAl-C and NiAl-T, in the 400- 4000 cm^{-1} range, are presented in Figure 4.7. Spectra for γ-Al_2O_3 and NiO have also been included for comparison.

For the γ-alumina the broad peak at around 3410 cm^{-1} (with three peaks at 3415, 3454 and 3542 cm^{-1}) is associated to the presence of surface hydroxyl groups (OH stretching–Al–OH). Peaks at 1619 and 1637 cm^{-1} are due to OH^- bending. The absorption bands below 1000 cm^{-1} correspond to the vibrational modes of coordinated aluminium oxides i.e., bending modes of O-Al-O (484 cm^{-1}) and stretching modes of Al-O-Al (607 cm^{-1}) [142].

Substantial differences are found in the spectrum of the NiAl-C solid, in comparison to NiO. Similarly to γ-alumina, the broad band at 3422 cm^{-1} is assigned to the O-H stretching mode of water, while bands at 1382, 1505 and 1638 cm^{-1} are related to the vibration mode of the adsorbed water, clearly appreciated in NiAl-C [143]. The intense bands at 725 cm^{-1} and 492 cm^{-1} observed for NiAl-C are characteristic of spinel structure [144, 145].

The FTIR spectra significantly vary with reduction temperature. For instance, the bands characteristic for spinel remained for catalysts treated at low temperatures

(NiAl-300 and NiAl-450). Upon treatment above 600 ºC, these bands disappear and characteristic features of γ-alumina could be observed (484 cm^{-1} from O-Al-O bending mode, 607 cm^{-1} from Al-O-Al stretching mode) and a single OH bending at 1631 cm^{-1} [142].

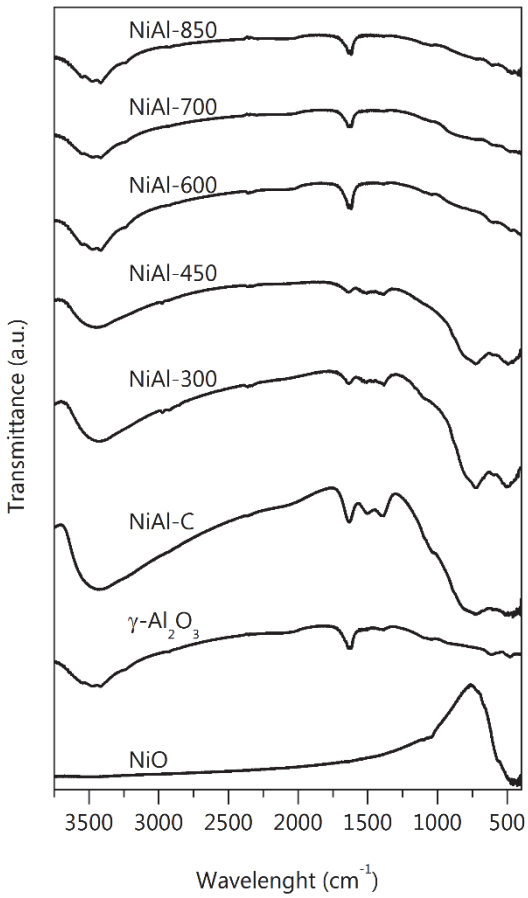

Figure 4.7. FTIR spectra for nickel aluminate spinel in the calcined and reduced at T_{red} forms. Spectra from nickel oxide and γ-alumina are included.

The FTIR analysis confirmed the presence of the spinel structure in the calcined sample and evidences its transformation into γ-alumina under H_2 flow. Besides, alumina could be detected upon reduction above 600 ºC.

Further structural characterization was carried out by diffused reflectance, and obtained spectra are shown in Figure 4.8. The UV-vis-NIR DRS spectra of NiO reference sample shows main features including a broad band in the 900-1400 nm region ascribed

to $O^{2-} \rightarrow Ni^{2+}$ charge transfers and bands at 377, 414 and 720 nm corresponding to $^3A_{2g} \rightarrow {}^3T_{1g}$ (F) transition [146]. All these features are characteristic of octahedral Ni^{2+} in NiO lattice [147]. For catalyst NiAl-C, the intensity in the $O^{2-} \rightarrow Ni^{2+}$ charge transfer region increases whereas it was attenuated in the visible range, at around 720 nm, as compared to bare NiO, which suggests that Ni^{2+} is in a different electronic environment. The intense doublet, with maxima at 605 and 638 nm, observed for catalyst NiAl-C, was attributed to the $^3T_1 \rightarrow {}^3T_2$ (^3P) spin-allowed transition of Ni^{2+} ions in tetrahedral symmetry (Ni^{2+}_{Td}). Moreover, absorption bands centred at 550 and 760 nm characteristic of Ni^{2+}_{Td} were observed. Thus, these results reflected that Ni^{2+} ions are embedded in the alumina lattice to form the $NiAl_2O_4$ phase in the non-reduced NiAl-C sample, consistent with XRD data.

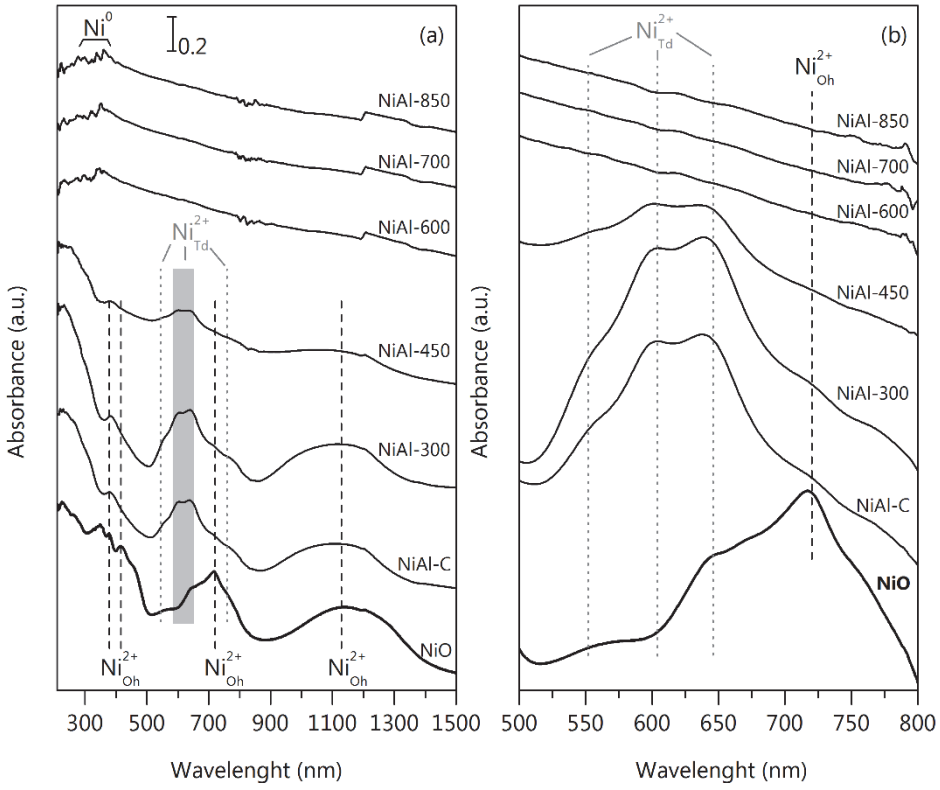

Figure 4.8. (a) UV-vis-NIR DRS spectra for NiAl-C, NiAl-T and NiO; (b) detailed spectra in the 500-800 nm region.

The UV-vis-NIR DRS spectra of partially reduced samples (i.e. ≤450 ºC) are qualitatively similar to NiAl-C. Reduction at 600 ºC removes typical features of NiO and

nickel aluminate and only some complex bands at around 330 nm are observed, ascribed to metallic nickel nanoparticles [148]

The intensity ratio of the doublet at 600-650 nm to peak at 1100 nm is related to the nickel in tetrahedral over octahedral coordination ($Ni^{2+}_{Td}/Ni^{2+}_{Oh}$) [149]. $Ni^{2+}_{Td}/Ni^{2+}_{Oh}$ ratios were estimated from the bands' intensities, and are shown in Table 4.3. The experimentally measured values reflect that the highest $Ni^{2+}_{Td}/Ni^{2+}_{Oh}$ corresponds to sample NiAl-C, and decreases upon reduction, which supports the XRD results.

Therefore, UV-vis-NIR DRS results confirm the presence of spinel lattice in the NiAl-C solid, where Ni^{2+} is both tetrahedrically and octahedrically coordinated ($Ni^{2+}_{Td}/Ni^{2+}_{Oh}$=1.44). Upon reduction, the relative content of Ni^{2+}_{Td} with respect to Ni^{2+}_{Oh} decreases indicating Ni^{2+}_{Td} easier reducibility. The spectra evidenced that nickel is exudated and thus, extracted from the spinel phase at temperatures above 600 ºC.

4.5 ^{27}Al MAS NMR

The ^{27}Al chemical shift was measured by solid-state ^{27}Al MAS NMR. Figure 4.9 shows the spectra of the prepared samples. The spectrum of γ-Al_2O_3 consists of two peaks at 3.7 and 60 ppm (i.e. octahedral and tetrahedral aluminium, respectively), with an intensity ratio of 73 : 27, similar to others [150].

The non-reduced NiAl-C solid shows a broad peak centred at -33 ppm, reflecting the predominant existence of Al_{Oh}. The subtle peak at around 70 ppm denotes the presence of Al_{Td}, characteristic of partially inverted spinels. Reduction at below 600 ºC hardly vary ^{27}Al-NMR spectra, and Al^{3+} mainly occupy the octahedral sites. However, reduction at above 600 ºC increases the amount of Al_{Td}, as deduced from the enlarged signal at around 60 ppm.

This is consistent with the departure of Ni^{2+} to octahedral sites to ensure neutrality. Indeed, Figure 4.10 shows that Al_{Oh} chemical shift linearly increases with the reduction temperature, which is limited by NiAl-C (-33.3 ppm) at the bottom and by the γ-alumina (+3.8 ppm) at the top. For NiAl-850 sample, δ_{AlOh} is +0.8 ppm, close to that of γ-alumina. Accordingly, these results corroborate the partial inversion of the spinel, as well as the enrichment in γ-alumina of the solids as an effect of the reduction temperature. These observations correlate fairly well with the above characterization results.

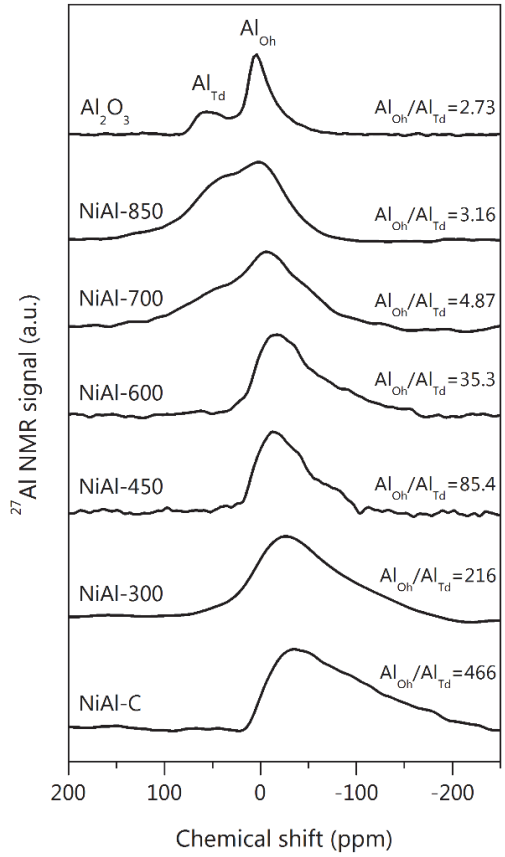

Figure 4.9. The NMR spectra of NiAl-C, NiAl-T and γ-Al_2O_3 samples.

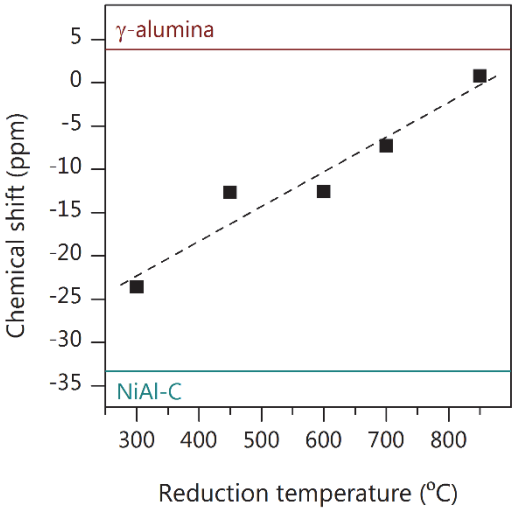

Figure 4.10. Variations of Al_{oh} chemical shift with reduction temperature.

4.6 SURFACE ACID-BASE CHARACTERISTICS

Aqueous-Phase Reforming of glycerol involves, among others, dehydration reactions [75], which are very sensitive to the catalysts surface acid-base properties [151]. Therefore, the study of the total amount of such functionalities could help the interpretation of the activity and selectivity data. Results from CO_2-TPD and NH_3 chemisorption are given in Table 4.4.

Table 4.4. Acid-base properties of the prepared samples and calcined parent oxides.

Sample	Acid sites density (μmol $NH_3 \cdot m^{-2}$)	Basic sites density (μmol $CO_2 \cdot m^{-2}$)	Acid/basic ratio
NiO	(4.17) 12.25	(10.03) 29.17	0.0045
γ-Al_2O_3	(240.45) 2.37	(53.06) 0.52	4.5
NiAl-C	1.57	0.66	2.4
NiAl-300	1.57	0.59	2.7
NiAl-450	1.93	0.39	4.9
NiAl-600	1.82	0.73	2.3
NiAl-700	1.95	1.12	1.7
NiAl-850	2.13	1.03	2.0

Values in parentheses are acidity per mass unit (μmol $NH_3 \cdot g^{-1}$).

Activation under hydrogen flow increases the density of acid sites up to 35% (highest value for NiAl-850: 2.13 μmol $NH_3 \cdot m^{-2}$). As revealed by XRD, FTIR and ^{27}Al MAS NMR, with the reduction treatment the surface of the solids enriches in γ-Al_2O_3, being almost completely exposed with the reduction at 850 ºC. The acidity of the catalysts is mainly assigned to the γ-Al_2O_3 present in the sample. However, the slight decrease of the acid sites density for NiAl-850 comparing with that of the γ-Al_2O_3, can be explained by the high temperatures used during calcination (850 ºC) and reduction treatment, which could diminish alumina acidity [152].

The study of the strength of the basicity can explain to some extent the performance of the catalysts in the glycerol APR. CO_2-TPD was used to characterize the basic strength distribution, assuming that the desorption peak temperature could be related to the strength of basic sites. The CO_2-TPD profiles and the estimated density of the basic sites are presented in Figure 4.11 and Figure 4.12, respectively.

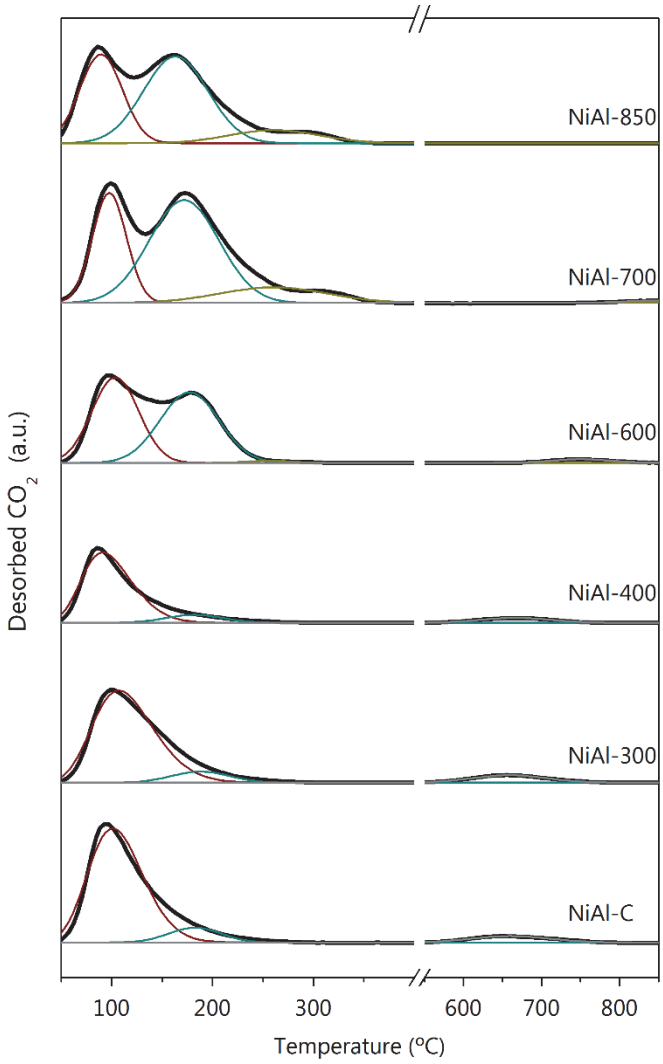

Figure 4.11. CO_2-TPD profiles for NiAl-C and NiAl-T solids.

Related low, medium and strong basic peaks are depicted in patterns of CO_2 desorption. Desorption peaks can be indexed at three different temperature intervals: weak basic sites below 120 ºC, ascribed to the decomposition of bicarbonates on surface hydroxyl groups; medium strength basic sites, located at 130-200 ºC, associated to bidentate carbonates on Ni – O; and a third peak at high temperature, reaching maximum desorption at 240-320 ºC, which is associated with strong basic sites as unidentate carbonates [104]. Moreover, the unidentate and bidentate carbonates can be formed on surface oxygen atoms in different coordination degrees, the former over

oxygen ions showing low coordination number, and the latter over adjacent cationic sites [153]. NiAl-C and those reduced a T< 600 ºC eventually present very small desorption peaks above 650 ºC, associated to the possible formation of carbonates during calcination steps and dehydroxylation processes [154].

The distribution of the basic strength presented in Figure 4.12 was obtained by deconvolution of CO_2-TPD profiles, assuming gaussian peaks. Treatment under hydrogen flow causes an increase in medium strength sites, which could be assigned to the progressive dehydroxylation of the surface and the increase of exposed γ-alumina on the surface. The observed complexity in the medium strength desorption region as reduction temperature increased (Figure 4.11) could be ascribed to modification of the oxygen coordination on the catalyst surface. Besides, strong surface basic sites increase with higher reduction temperatures.

The increase in the total surface basicity is even more marked, up to a two-fold increase, especially at the most severe reduction conditions. Overall, based on the APR selectivity data discussed later, it could be deemed that these differences in the acid-base properties are sufficient to change the catalyst performance.

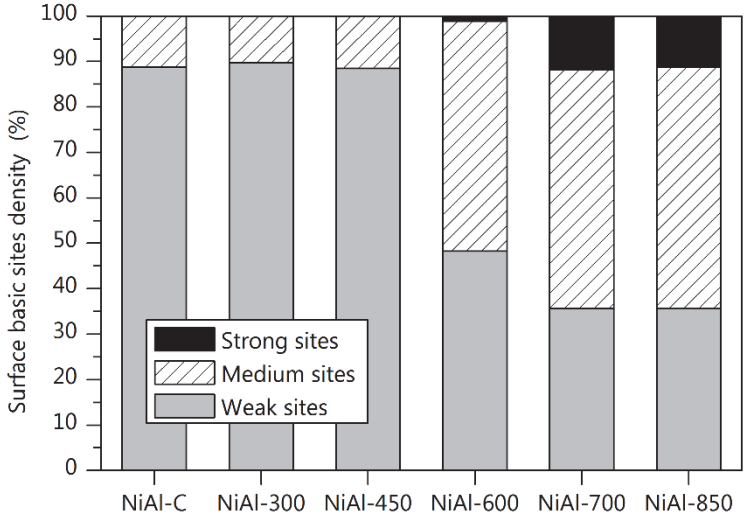

Figure 4.12. Distribution of the strength of the surface basic sites density for NiAl-C and NiAl-T.

4.7 GENERAL OVERVIEW AND CONCLUSIONS

Nickel species of different reducibility were found in the nearly stoichiometric $NiAl_2O_4$, prepared by co-precipitation:

(i) a small fraction of surface free nickel oxide (α), without interaction with the support, which vanishes after reduction above 300 ºC.

(ii) two kinds of Ni^{2+} species in defective $Ni_{1-X}Al_2O_{4-X}$, β (one in Ni-rich and the other in Al-rich environment), the contribution of which decreased upon reduction at above 600 ºC.

(iii) nickel in spinel phase (γ), which can only be completely reduced at 850 ºC, or above.

Based on H_2-TPR data, it was found that Ni^{2+} species in the Ni-rich mixed oxide phase (peak β_1), were more reducible [78]. Reduced Ni^{2+} species exudates, i.e., migrated from the spinel lattice to the solid surface, leading to a framework composed by less and less Ni^{2+} species embedded into an Al-rich mixed oxide phase (β_2), as suggested by the decrease of the β_1/β_2 ratio (Table 4.2).

Under H_2 atmosphere, nickel diffused through the lattice of the non-stoichiometric spinel to form metallic Ni. Ni diffusion continued until $Ni_{1-X}Al_2O_{4-X}$ was completely reduced, at around 700 ºC. Above that temperature, further Ni exudation proceeded from stoichiometric $NiAl_2O_4$. Similar behaviour was observed by Braidy et al. [137], with Ni-doped alumina spinels synthesized by IWI method. They proposed that under a reductive atmosphere, a continuous transition between $Ni_{1-X}Al_2O_{4-X}$ towards γ-alumina occured as Ni left the matrix to form $NiAl_2O_4$ and, eventually, Ni^0. The intermediate formation of $NiAl_2O_4$ before metallic Ni could explain the upturn observed in the contribution of $NiAl_2O_4$ in the NiAl-T series (Table 4.2). Previous research based on H_2-TPR analysis concluded that Ni located in tetrahedral sites could be more difficult to reduce than Ni located in octahedral sites. [78, 127]. Nevertheless, based on XRD, UV-vis-DRS and ^{27}Al NMR data of our stoichiometric nickel aluminate spinels, a different behaviour could be evidenced. That is, upon reduction, the number of tetrahedral nickel atoms diminished and increased in octahedral sites. Regarding surface acid-basic

properties, treatment under hydrogen flow caused the increase in the acidity of the samples and also the surface enrichment in medium and strong strength basic sites.

Chapter 5

Effect of the reduction temperature of $NiAl_2O_4$ precursor on the glycerol APR performance

Bulk nickel aluminate ($NiAl_2O_4$) synthesized by co-precipitation at a Ni/Al mole ratio of 1:2 (stoichiometric ratio) was used as catalysts precursor for the APR reaction. The synthesized solid was subjected to different reduction temperatures, in the 300 °C to 850 °C range, prior to the APR reaction. The spinel precursor allows the formation of small and stable metallic Ni particles (< 14 nm) upon reduction with good performance in the APR of glycerol. APR test at different coupled T/P conditions were carried out and the activation energy was estimated. Hydrogen was the main gaseous product, and the activation temperature does not substantially alter selectivity to gaseous products; however, selectivity to intermediate oxygenated liquids is substantially modified. Overall, glycerol dehydrogenation predominates at higher reduction temperatures. The adequate stability of the spinel-derived catalysts leads to stable H_2 yield during the long-term runs (50 h) and proven potential to be used in the APR of glycerol.

5. EFFECT OF THE REDUCTION TEMPERATURE OF $NiAl_2O_4$ PRECURSOR ON THE GLYCEROL APR PERFORMANCE.

Catalytic tests of glycerol APR were performed at 250 ºC/45 bar in a bench scale fixed-bed up-flow reactor, operating at a WHSV= 24.5 h^{-1} (0.5 g catalysts, feed rate= 0.2 mL/min, 10 wt.% glycerol in water mixture). The catalytic performance results are reported for 2 h steady state. A blank test with the reactor bed filled with quartz wool showed no glycerol conversion, which suggests that homogeneous APR made no contribution to the conversion of glycerol. In addition, experiments with bare γ-alumina and NiAl-C showed almost null activity, which indicates the pivotal role of the metallic function. As a reference, the activity of bare metallic Ni, obtained by reduction of NiO at 850 ºC for 1 h and labelled Ni-850, was also evaluated. Glycerol conversion (X_{Gly}) and carbon conversion to gas (X_{Gas}) of NiAl-T catalysts are displayed in Figure 5.1.

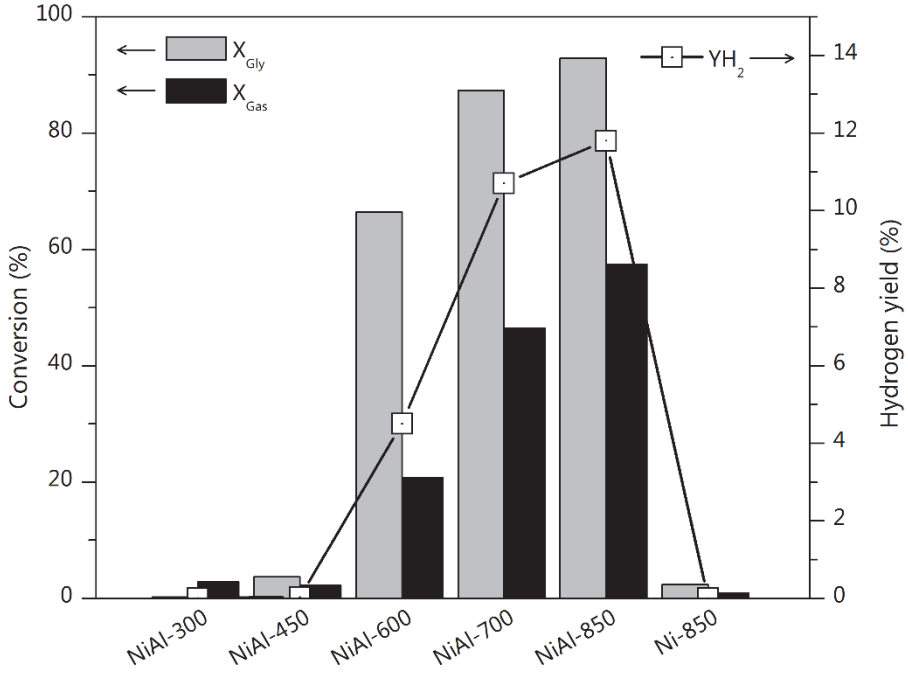

Figure 5.1. Glycerol conversion, conversion to gas and hydrogen yield for NiAl-T catalysts in the glycerol APR. Reaction conditions: 250 ºC/45 bar, WHSV= 24.5 h^{-1}. Reaction time: 2 h.

Metallic nickel (Ni-850 catalysts) shows very low activity in glycerol APR, with X_{Gly} and X_{Gas} below 3% and 1%, respectively. Despite Raney-Ni having been reported to be active for APR [102], the very low performance of Ni-850 (in terms of X_{Gly} and X_{Gas}) could be ascribed to its very low surface area (less than 5 $m^2 \cdot g^{-1}$) and a possible sintering of Ni^0 particles during the reduction step. Similarly, X_{Gly} and X_{Gas} for NiAl-350 and NiAl-450 catalysts remain below 5%. However, catalytic activity boosted for NiAl-600 catalyst. For instance, glycerol conversion increased by a factor of 20 from NiAl-450 to NiAl-600 (NiAl-600: X_{Gly}= 66%). The most active assay was that reduced at 850 ºC, with X_{Gly}= 93% (i.e., X_{Gly} increased by a factor of 1.4 with respect to NiAl-600). Regarding the conversion to gas, results evidenced an increasing tendency of X_{Gas} with higher reduction temperatures, reaching values of 21%, 46% and 57% for NiAl-600, NiAl-700 and NiAl-850, respectively.

The hydrogen yield for NiAl-300 and NiAl-450 is negligible, as shown in Figure 5.1, and correlated with the low conversion. Similar to X_{Gly} and X_{Gas}, YH_2 boosted for catalysts reduced at 600 ºC and above. For instance, NiAl-600 presents YH_2= 5%, which increases to ~12% for NiAl-850 catalyst.

The site time yield (STY), defined as the overall rate within reactor normalized by the total number of active sites, is shown in Figure 5.2. STY for the overall glycerol conversion (STY_{XGly}) and STY for the molar flow of H_2 produced (STY_{FH2}) follow the same trend with $A_{S\text{-}Ni^o}$, with STY_{XGly} being higher than STY_{FH2} for all catalysts.

The role of the available Ni^0 in the reforming activity seems evident. NiAl-600 shows the highest STY for both, glycerol conversion and H_2 production (1538 h^{-1} and 728 h^{-1}, respectively), though not having the highest accessible metallic nickel surface (86% less Ni^0 area than NiAl-850 assay). Further increase on the reduction temperature decrease both STY. For instance, in the case of NiAl-850 catalyst, a decrease of STY_{XGly} by ~5 and by 2.5 in the case of STY_{FH2}, are found. It seems that H_2 production is less sensitive than overall glycerol conversion to accessible metallic nickel surface. The smallest Ni^0 size in NiAl-600 catalysts (d_{Ni^o}= 7.7 nm) could be involved in this behaviour, suggesting superior intrinsic activity of small particles (Table 4.3).

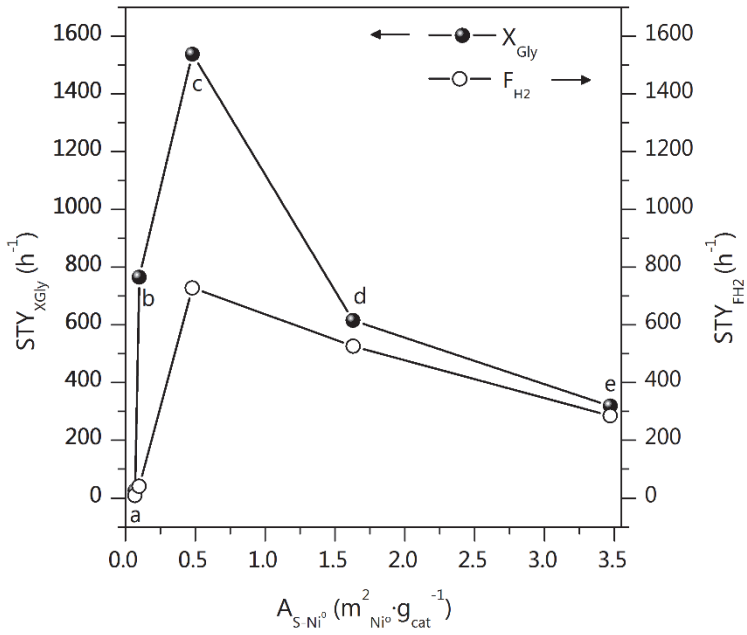

Figure 5.2. STY for glycerol conversion (left axis) and for H_2 production (right axis) in function of accessible metallic surface. (a) NiAl-300, (b) NiAl-450, (c) NiAl-600, (d) NiAl-700 and (e) NiAl-850 catalysts. Reaction conditions: 250 ºC/45 bar, WHSV= 24.5 h^{-1}. Reaction time: 2 h.

Worthy of mentioning is that a small particle size would enhance close proximity between Ni^0 and the surroundings, thus promoting both reforming and WGS reactions, which involve activation of water molecule. This can be associated to the ability of nickel and alumina to activate water by forming NiO and hydroxyl groups, respectively [155, 156]. This fact could affect the catalyst durability, since nickel oxidation leads to a decrease in accessible metallic surface.

5.1 GAS PRODUCTS FROM GLYCEROL APR

The gas products of the reaction were analysed on-line by *Micro GC* and the experimental results are depicted in Figure 5.3, and expanded in Table 5.1. The X_{Gas} ranges between 3% and 60%, for NiAl-300 and NiAl-850 respectively.

The molar flow of gaseous products of NiAl-300 and NiAl-450 catalysts is very low, in line with their low activity. A noticeable increase in gas flow is shown by catalysts reduced at temperatures ≥ 600 ºC, being NiAl-850 the catalyst with a maximum flow of

0.9 mmol·min^{-1}·g_{cat}^{-1}. These results pointed to the active role of metallic sites in the production of gas, since $A_{S\text{-}Ni^0}$ increases with reduction temperature.

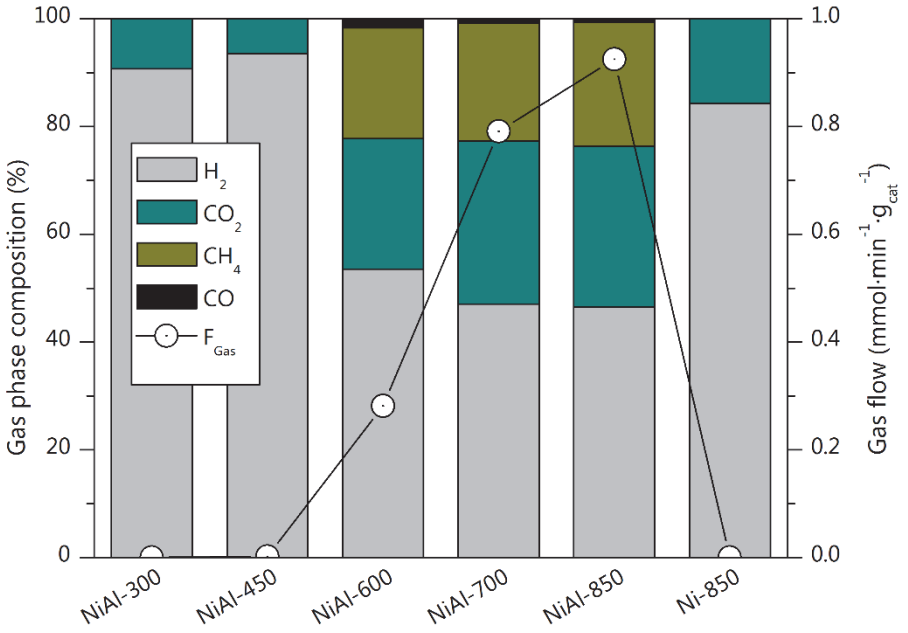

Figure 5.3. Gas composition (bars) and total gas flow (line) of glycerol APR over NiAl-T. Reaction conditions: 250 ºC/45 bar, WHSV= 24.5 h^{-1}. Reaction time: 2 h.

In addition, selectivity to gas (S_{Gas}), which has been defined as the percentage of carbon moles converted into gas phase per converted glycerol moles, is doubled in this temperature range: NiAl-600 (31%) vs NiAl-850 (62%) (Table 5.1). Concomitantly, the accessible metallic nickel surface increases by a factor of 7 (NiAl-850/ NiAl-600= 3.47/ 0.48) (Figure 5.2, Table 4.3).

For all NiAl-T catalysts, the main products are, in decreasing order: hydrogen, carbon dioxide and methane, which account for more than 97% (mol %) of the reaction products in the gas phase (Figure 5.3). Other minor compounds in the gas phase are: other alkanes (ethane, propane and C4+), and carbon monoxide, all of them in very low quantities. In contrast to the Steam Reforming of glycerol at atmospheric pressure, in which CO and H_2 are the main products (CO/H_2= 0.5) [157, 158], the glycerol APR only generates trace amounts of CO (CO/H_2<0.04), and it can be associated to its lower operation temperature, which is beneficial for the WGS equilibrium.

Table 5.1. Gas phase characteristics for the glycerol APR at 250 ºC/45 bar over NiAl-T catalysts (2 h).

Catalyst	S_{Gas} (%)	YH_2 (%)	SH_2 (%)	SCH_4 (%)	SC2 (%)	SC3 (%)	H_2/CO_2	CO_2/CH_4
NiAl-300	n/a	~0	13.5	~0	~0	~0	9.7	n/a
NiAl-450	61.3	~0	2.2	~0	~0	0.02	14.4	n/a
NiAl-600	31.2	4.5	20.3	22.2	0.58	0.32	2.2	1.2
NiAl-700	53.1	10.7	36.6	39.7	1.71	0.97	1.6	1.4
NiAl-850	61.9	11.8	38.3	44.2	1.75	0.93	1.6	1.3
Ni-850	38.0	~0	0.8	~0	~0	~0	5.4	n/a

Catalysts reduced at low temperatures produce a H_2-rich gas stream (80-90% H_2). Nonetheless, their hydrogen yield is rather low (YH_2< 0.1%). This can be associated to their low amount of metallic nickel sites (Figure 5.2, Table 4.3), which are known to be the active sites. Note that very low concentration of gases could lead to further analysis error. The H_2 concentration (%) in the gas stream for the catalyst reduced at 600 ºC or above, decays and levels-off at around 45-55% while CH_4 concentration does not vary so much, remaining at around 22%. Regarding YH_2, it is doubled for NiAl-700 and NiAl-850 with respect to NiAl-600 (4.5%). Despite X_{Gly} and X_{Gas} increase with reduction temperature in the 600 ºC to 850 ºC interval, the gas phase composition remains similar (Figure 5.3), which suggests that the reaction mechanism does not vary substantially among the most active assays.

The ability of Ni^0 for the C-C scission is evidenced based on the large differences found between the selectivity of C1 (methane), C2 (ethane) and C3 (propane) alkanes in those catalysts reduced at high temperatures, which present high $A_{S\text{-}Ni^o}$ values. In fact, NiAl-600 catalyst (0.48 $m^2_{Ni^o} \cdot g^{-1}$) shows 22% selectivity to C1 alkane, with negligible formation of C2 and C3 alkanes. NiAl-700 and NiAl-850 catalysts also show similar trends for SC1, SC2 and SC3. The C-C bond cleavage implies the formation of CO (via decarbonylation). However, only trace amounts of CO are detected for our catalysts, especially those reduced above 600 ºC, despite high glycerol conversions. This suggests that CO readily reacts through side reactions, such as WGS (to give CO_2) and methanation (to give CH_4). Not in vain, Ni has been recognized as very active metal for both said reactions [159, 160].

On the other hand, as revealed by data in Table 5.1, H_2/CO_2 ratio remains below 7/3 (stoichiometric ratio in APR of glycerol) for catalyst reduced at 600 ºC or above (H_2/CO_2 ratio ranged between 1.6 and 2.2). This result supports that hydrogen is readily used in side reactions. Despite the low glycerol conversion for NiAl-300 and NiAl-450 catalysts, the high H_2 content in their gas phase led to higher H_2/CO_2.

NiAl-300, NiAl-450 and Ni-850 catalysts present negligible CH_4 formation (Figure 5.3), thus the CO_2/CH_4 ratio could not be calculated accurately for these assays. However, the CO_2/CH_4 ratio for the catalysts reduced at 600 ºC or above present similar values among them (between 1.2 and 1.4). The CO_2/CH_4 ratio has been taken as an indicator of the selectivity to hydrogen, as the formation of methane involves H_2 consumption. Dietrich et al. [157] presented theoretical values of CO_2/CH_4 ratio for catalysts with different selectivities and they stablished a lower limit on CO_2/CH_4= 0.71 for reforming with zero H_2 selectivity. Thus, any ratio above this will lead to a net production of H_2 as in the case of the NiAl-T catalysts reduced at 600 ºC or above. Results in Table 5.1 suggest that both glycerol reforming and WGS reactions are favoured over methanation reaction. Further evidence is discussed in Chapter 6. It proves that $NiAl_2O_4$-derived catalysts favoured WGS reaction. Indeed, Ni-based catalysts are reported to be active for the WGS reaction.

Selectivity to H_2 is conditioned by the reforming stoichiometry, thus, it is not directly comparable to SCH_4. Similar values of SH_2 are observed for NiAl-700 and NiAl-850 catalysts (37-38%) (Table 5.1), the highest among NiAl-T catalysts. Nonetheless, it seems that the higher activity presented by NiAl-850 catalyst could enhance methane formation, as it present higher SCH_4 (44%).

Table 5.2 shows a comparison between our results with NiAl-850 catalyst, and other works reported in the literature. In general terms, the high performance shown by the nickel aluminate-derived catalysts is remarkable when compared to other nickel-based catalysts, in spite of the high space velocity employed in this work (WHSV= 24.5 h^{-1}). The performance in terms of activity of our NiAl-T catalysts is even comparable to Pt-based catalysts, despite, lower selectivity to hydrogen, due to the inherent methanation activity of Ni [49].

Table 5.2. Comparison of the performance of nickel aluminate spinel-derived catalysts with other reported for APR of glycerol.

T/P (ºC/bar)	Reactor type	Catalyst	Feed, WHSV or Gly/cat	X_{Gly} (%)	X_{Gas} (%)	SH_2 (%)	YH_2 (%)	S_{Gas} (%)	Ref.
250/50	Fixed-bed	5%Ni/Al_2O_3, CP	10 wt.% Gly/H_2O, 2.45 h^{-1}	67	87	-	-	43	[161]
250/50	Fixed-bed	10%Ni/Al_2O_3, IMP	10 wt.% Gly/H_2O, 2.6 h^{-1}	40	10	-	-	25	[162]
250/20	Fixed-bed	15%Ni/$LaAlO_3$, DP	15 wt.% Gly/H_2O, 5.2 h^{-1}	23	-	61	-	-	[163]
240/40	Fixed-bed	6%Ni/3%CeO_2/Al_2O_3, IMP	1 wt.% Gly/H_2O, 12 h^{-1}	26	-	49	12	-	[63]
250/35	Fixed-bed	20%Ni/HTLC, CP, Al/Al+Mg= 0.24	10 wt.% Gly/H_2O, 5.1 h^{-1}	30	16	31	10	18	[67]
250/40	Fixed-bed	1%Cu-12%Ni/MWNT, IMP	1 wt% Gly/H_2O, 20 h^{-1}	84	-	86	65.4	-	[164]
250/25	Fixed-bed	10%Ni/$Ce_{0.3}Zr_{0.7}O_2$, CP	10 wt.% Gly/H_2O, 2.5 h^{-1}	90	99	-	-	37	[165]
240/42	Batch	2%Pt/Al_2O_3, SC	10 wt.% Gly/H_2O, Gly/cat= 34	34	-	-	2.5	-	[166]
225/28	Fixed-bed	$Pt_1Fe_{0.75}$/Al_2O_3, SC	5 wt.% Gly/H_2O, 3.7 h^{-1}	-	63	36	22	-	[167]
225/28	Microreactor Fixed-bed	3%Pt-3%Re/AC, IMP	10 wt.% Gly/H_2O, 5.0 h^{-1}	88	58	25	-	22	[168]
250/45	Batch	1%Pt-2.8%K/HT, IMP	10 wt.% Gly/H_2O, Gly/cat= 0.1, 4 h	88	87	-	48	33	[169]
225/28	Fixed bed	0.79%Pt/MgO, IMP	5 wt.% Gly/H_2O, 3.6 h^{-1}	-	38	60	28	-	[58]
250/45	Fixed bed	$NiAl_2O_4$, CP, 33% Ni	10 wt.% Gly/H_2O, 24.5 h^{-1}	93	57	38	12	62	This work

Gly/cat: glycerol to catalyst weight ratio in the feed, batch reactor
HTLC: hydrotalcite-like compound
MWNT: multiwalled carbon nanotubes
AC: activated carbon
IMP: impregnation
DP: deposition-precipitation
CP: co-precipitation
SC: synthesis of colloids

5.2 LIQUID PRODUCTS FROM GLYCEROL APR

The X_{Gas} of NiAl-T catalysts is lower than 100%, which indicates that carbon fed as glycerol is being converted to either gas and liquid-phase products. The produced liquid phase was analysed by liquid chromatography, and the results are shown in Figure 5.4. The main liquid compounds identified are hydroxyacetone (HA), 1,2-propylene glycol (1,2-PG), ethylene glycol (EG), ethanol (EtOH), methanol (MeOH) and acetaldehyde (MeCHO), the composition of which account for more than the 98% of the liquid-phase compounds. Others liquid compounds such as propionaldehyde, 1-propanol and 2-propanol are also found in trace amounts.

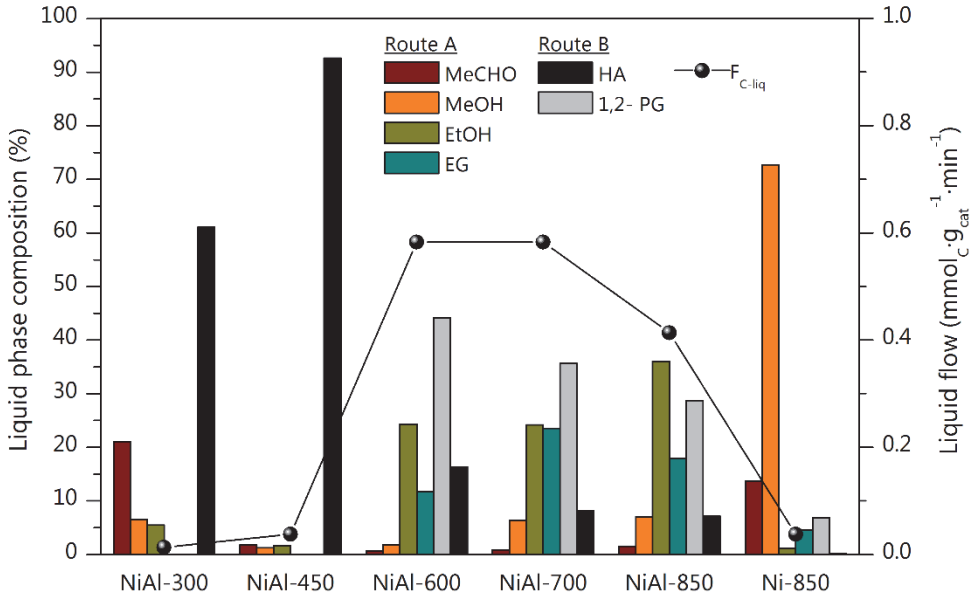

Figure 5.4. Molar composition of the main liquid products. Reaction conditions: 250 ºC/45 bar, WHSV= 24.5 h^{-1}. Reaction time: 2 h.

The molar flow of liquid products is negligible for NiAl-300 and NiAl-450 catalysts, as well as for Ni-850, as due to their very low catalytic activity. Catalysts reduced at 600 ºC and 700 ºC produce the highest quantity of liquid products, with around 0.6 $mmol_C \cdot g_{cat}^{-1} \cdot min^{-1}$. Then, it slightly decreases by increasing the reduction temperature to 850 ºC (0.4 $mmol_C \cdot min^{-1} \cdot g_{cat}^{-1}$). This decline in the liquid products flow is confirmed by the simultaneous increase in the gas flow, and the conversion to gas, ascribed to further reforming of the formed intermediate oxygenated hydrocarbon

species. Those reforming reactions are catalysed by metallic sites, which are more available in NiAl-850 catalyst (Figure 5.2, Table 4.3). Similar findings were reported by others [35].

Liquid-phase product distribution is notably affected by the catalyst activation temperature, as evidenced by Figure 5.4. Catalysts reduced at low temperature (NiAl-300 and NiAl-450) mainly produce HA and very low amounts of small chain mono-alcohols (EtOH, MeOH), suggesting that these catalysts favour both dehydration and hydrogenation reactions, which can be associated to the scarcity of accessible nickel surface (Table 4.3) and thus, acid sites taking advantage. The acid function was dominant in these catalysts, as revealed by the high ratio of acid/basic sites Table 4.4. As a consequence, HA is hardly hydrogenated to 1,2-PG. In contrast, Ni-850 catalyst, with only metallic function, produced a liquid stream mainly composed of MeOH (73%), and a H_2-rich gaseous stream.

For catalysts reduced at 600 ºC or above, the main liquid products are glycols (1,2-PG and EG), small chain mono-alcohols (EtOH and MeOH), HA and MeCHO, the latter in a much lesser concentration. The observed liquid products distribution points to a complex reaction network, where dehydrogenation, dehydration and hydrogenolysis reactions take place in the glycerol APR, as also suggested by others [49, 71]. It should be noted in Figure 5.4 that large number of glycols (sum of EG and 1,2-PG) are produced, in the 47-59% range, by all the active assays. This indicates C-O (i.e. 1,2-PG), C-H and C-C (i.e. EG) bond scission, which occurs over acidic (C-O) and metallic (C-H and C-C) sites. Low amounts of 1-propanol and 2-propanol are also detected (less than 2%). Gandarias et al. [170] reported that these can be produced by additional dehydration and hydrogenation of 1,2-PG in the presence of H_2. Production of 1,2-PG and HA decreased as reduction temperature increased. For NiAl-600 and NiAl-850 catalysts 1,2-PG concentration decay from 44% to 29% and the HA from 16% to 7%, respectively. In contrast, the production of MeOH and EtOH increased.

5.3 REACTION NETWORK

The gas and liquid product distribution evidences the occurrence of multiple side reactions. With the observed products distribution for glycerol APR, a plausible reaction pathway, with two main reaction paths, is proposed and depicted in Figure 5.5.

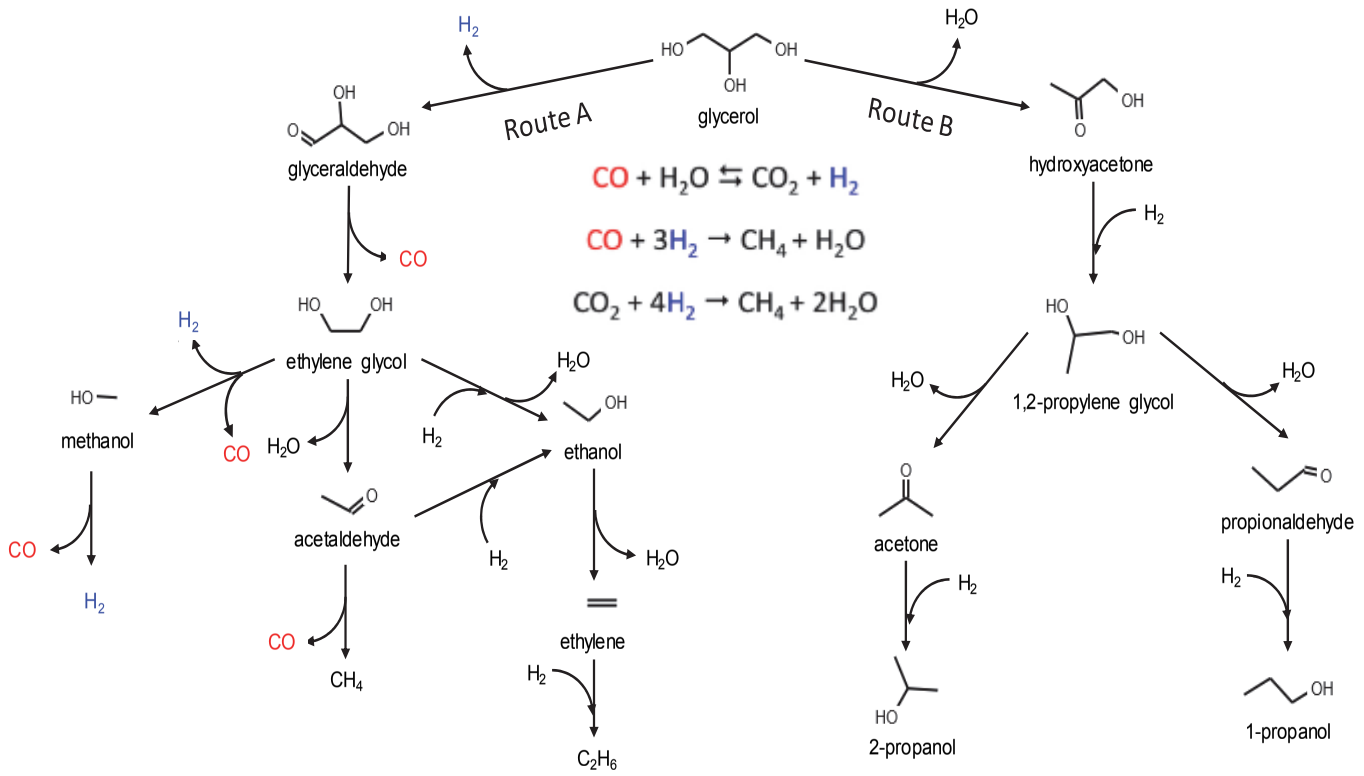

Figure 5.5. Scheme of the reaction pathway proposed for the glycerol APR over nickel aluminate spinel-derived catalysts.

The glycerol APR over bifunctional NiAl-T catalysts comprises two main routes in the first stage: route A, over metallic sites with dehydrogenation to glyceraldehyde; and route B, over acid sites with dehydration to hydroxyacetone. It is widely accepted that HA is formed by elimination of primary hydroxyl group of glycerol, while 3- hydroxypropanal is formed by elimination of secondary hydroxyl group. The fact that the latter was not detected, could be ascribed to the preponderant Lewis type acidity of NiAl-T catalysts [171]. This is further discussed in Chapter 6.

On the one hand, the obtained gas-phase composition above discussed (Table 5.1) together with the proposed reaction network indicate that methane is formed by CO hydrogenation, which requires the presence of metallic sites. In fact, this reaction is thermodynamically favoured at the APR operation conditions (low temperature) due to its exothermic character ($\Delta H^0_{CO\ methanation}$= -206 kJ·mol^{-1}). In this line, much higher SCH_4 with respect to SC2 and SC3 is noticed, which implies that C-C scission activity is higher than dehydration/hydrogenation of the intermediate liquid compounds over NiAl-T catalysts reduced at 600 ºC or above.

It can be deduced that a low amount of metallic Ni is required on catalyst surface to drive hydrogenolysis reactions. Metallic sites ensure sufficient in-situ produced H_2 for hydrogenation of the liquid intermediate hydroxyacetone molecule. For instance, catalyst NiAl-450, with 0.1 $m^2_{Ni^o}·g^{-1}$, produced trace amounts of C3 alkanes, being SC3 lower than 0.1%. This sample presents the highest acid to basic sites ratio of 4.9 (Table 4.4), which is beneficial for cleavage of C-O bonds [172].

It is worth mentioning that C2 and higher alkanes could be formed through Fischer-Tropsch [49] and other reactions. For example, dehydration/hydrogenation of light alcohols can produce ethane and propane, while condensation reactions of intermediate liquid products can yield butane [173].

On the other hand, liquid products distribution points to the prevalence of the mechanism of formation of Ni-C bond (route A) over the NiAl-T catalysts reduced at 600 ºC or above, which requires a previous dehydrogenation of glycerol in order to be adsorbed on Ni^0 [174]. In contrast, NiAl-300 and NiAl-450 catalysts show major proportion of HA in the liquid product (Figure 5.4), indicating prevalence of the glycerol

dehydration pathway (route B). Their behaviour can be associated to the low accessible metal surface and consequential low YH_2.

Route B is favoured by the H_2 partial pressure increase (i.e. due to in-situ formation), allowing adsorption of both hydrogen and glycerol on Ni^0 sites. After protonation of hydroxyl group by acidic sites [175], cleavage of the C-O bond would proceed followed by hydrogen transfer from Ni^0 to the carbon, resulting in 1,2-PG formation, which is observed for catalysts reduced at 600 ºC or above. The occurrence of this pathway (route B) is also supported by the presence of 1-propanol and 2-propanol, which are formed through the dehydration/hydrogenation of 1,2-PG (Figure 5.5). Note that small amounts of propanol and acetone (less than 1%) reflected that 1,2-PG is the main final liquid product of route B, since further decomposition would require more acidic sites for dehydration to acetone or propionaldehyde. Experimental data points to the predominance of metallic function over acid function in the investigated catalytic system.

According to Figure 5.5, MeOH (minor product of route A) is formed through decarbonylation reactions (route A), with concomitant CO (and H_2) release, which would be subsequently converted by WGS to yield more hydrogen and CO_2. EtOH (main product) may be formed through the dehydration/hydrogenation of EG or by hydrogenation of MeCHO molecule [176]. The low amount of MeCHO produced by the active catalysts reveals a major feasibility of the latter route. By increasing reduction temperature above 600 ºC, the yield to EtOH increases, leading to a slight decrease of H_2/CO_2 ratio, as shown in Table 5.1 and Figure 5.4, respectively. Nonetheless, catalysts reduced at the highest temperatures (700 ºC and 850 ºC) present the highest YH_2 due to their enhanced catalytic activity, despite that another fraction of the in-situ formed H_2 is consumed in hydrogenolysis reactions.

Figure 5.6 shows the evolution of the overall reaction liquid products of route A with respect to all reaction liquid products of route B, i.e., the ratio between the atomic carbon liquid flow of main products of dehydrogenation (EG, MeOH, EtOH and MeCHO) to dehydration-hydrogenation products (HA and 1,2-PG). A clear trend to enhance the production of dehydrogenation products is confirmed with the increase of

Route A/Route B ratio by increasing the reduction temperature. This also endorses the relevant role of metallic sites in determining the dominant route in the APR of glycerol.

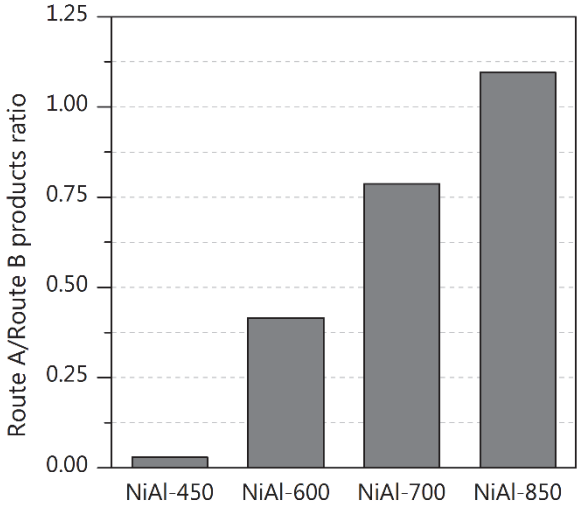

Figure 5.6. Effect of the reduction temperature in the dehydrogenation (route A) to dehydration-hydrogenation (route B) liquid products ratio.

The fact that route A (dehydrogenation-decarbonylation) is the main pathway reflected that C-H and C-C scission by hydrogenolysis is favoured, in detriment of C-O cleavage, as it is also reported elsewhere [174]. Gandarias et al. [177] studied the effect of the incorporation of Cu into Ni/Al_2O_3 catalysts and they concluded that the reduction in size of the Ni^0 ensembles inhibited the C-C bond cleavage capacity. This effect should not be discarded in the glycerol APR with $NiAl_2O_4$-derived catalysts reduced at high temperatures.

5.4 EFFECT OF THE COUPLED TEMPERATURE AND PRESSURE

The set of different reactions involved in the APR makes the global process significantly influenced by operation conditions [75]. In Chapter 3, it was found that temperature specifically influenced the reforming activity towards hydrogen production of NiAl catalysts. To further study this effect on NiAl-T catalysts, tests were performed at 235 ºC/35 bar, 250 ºC/45 bar and 260 ºC/52 bar over NiAl-T catalysts, and experimental results are depicted in Figure 5.7, and expanded in Table 5.3.

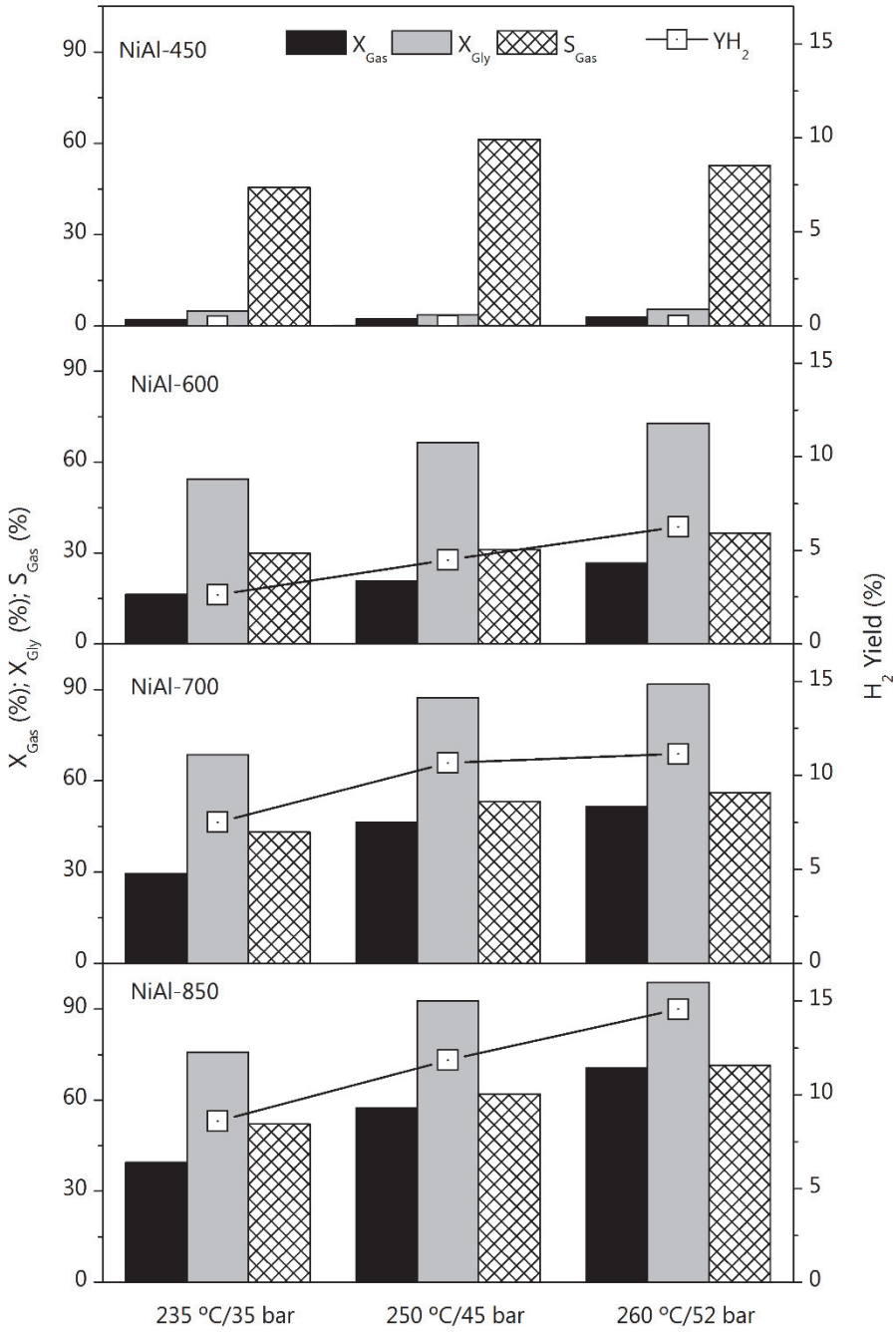

Figure 5.7. Effect of T/P on the catalyst performance. Data at 2 h of APR reaction.

Table 5.3. Gas-phase composition, selectivities and hydrogen yield for the different T/ P operation conditions (2 h).

Catalyst	T(ºC)/P(bar)	H_2 (%)	CH_4 (%)	S_{Gas} (%)	SH_2 (%)	YH_2 (%)	SCH_4 (%)	H_2/ CO_2	CO_2/CH_4
NiAl-300	235/35	~0	~0	n/a	0	0.00	~0	0	n/a
	250/45	90.7	~0	n/a	13.5	0.01	~0	9.7	n/a
	260/50	90.4	~0	n/a	9.9	0.01	~0	9.4	n/a
NiAl-450	235/35	93.6	~0	45.5	3.1	0.05	~0	15.8	n/a
	250/45	92.6	~0	61.3	2.2	0.03	~0	14.4	n/a
	260/50	94.5	~0	52.6	1.4	0.03	~0	24.0	n/a
NiAl-600	235/35	54.2	20.4	30.0	14.5	2.62	12.7	2.5	1.1
	250/45	52.7	20.3	31.2	20.3	4.49	18.2	2.2	1.2
	260/50	51.8	20.2	36.5	25.8	6.26	23.4	2.1	1.2
NiAl-700	235/35	52.5	19.4	43.1	32.9	7.50	28.3	2.1	1.3
	250/45	46.1	21.4	53.1	36.6	10.66	39.7	1.6	1.4
	260/50	45.0	23.5	56.2	36.5	11.14	44.4	1.6	1.2
NiAl-850	235/35	48.0	19.7	52.1	34.0	8.60	32.6	1.6	1.5
	250/45	45.6	22.5	61.9	38.3	11.85	44.2	1.6	1.3
	260/50	43.4	25.0	71.5	44.2	14.57	59.5	1.5	1.2
Ni-850	235/35	73.5	~0	62.2	0.3	~0	~0	2.8	n/a
	250/45	84.3	~0	38.0	0.8	0.01	~0	5.4	n/a
	260/50	90.4	~0	25.5	0.8	0.01	~0	9.4	n/a

In order to ensure liquid phase of the APR reaction, the system pressure was normally maintained about 4 bar above the saturation pressure at the experimental temperature, established by simple simulation of the system. Therefore, the effect of coupled temperature and pressure variables (T/P), was studied.

Independent of T/P, activity in glycerol APR is negligible for NiAl-300 catalyst, as well as for Ni-850, specially for X_{Gas} (< 2%) (data not shown in Figure 5.7 for the sake of simplification). Similarly, NiAl-450 presents X_{Gas}< 5% for all the T/P studied conditions. The catalytic behaviour, in terms of conversion of glycerol and gasification activity improves with T/P increase, in agreement with literature [67, 178]. For example, X_{Gly} reached 99% at 260 ºC/52 bar for NiAl-850 catalysts. Regarding the conversion to gas, it can be noticed that X_{Gas} increases by 31% (NiAl-450), 63% (NiAl-600), 74% (NiAl-700) and 79% (NiAl-850) by changing from 235 ºC/35 bar to 260 ºC/52 bar. Concomitantly, S_{Gas} increases by 22% (NiAl-600), 30% (NiAl-700) and 37% (NiAl-850). The enhancement of X_{Gly} and X_{Gas} with higher temperatures can be associated to the endothermic characteristics of both reactions, the C-C cleavage, and the global glycerol reforming [52].

Notice that with the increase on T/P, the hydrogen yield also increases for the most active assays. For example, NiAl-700 passes from 7.5 to 11.1% by changing from 235 ºC/35 bar to 260 ºC/50 bar. Similar outputs were reported by others [50, 179]. These findings corroborate that the operation temperature promotes both C-C and C-H bond cleavage. Likewise, the selectivity to hydrogen increases with T/P conditions (Table 5.3). It is noticed that NiAl-600 catalyst presents the major increase in SH_2 (by 78%) with the change of T/P from 235 ºC/35 bar to 260 ºC/52 bar. On the other hand, the selectivity to methane was also enhanced at 260 ºC/52 bar, with respect to the other T/P conditions. This could be associated to the consumption of H_2 in side reactions of methanation or hydrogenation of intermediate liquids, being favoured at those operation conditions. Interesting, NiAl-700 catalyst presents the lowest increase of SCH_4 among the most active catalysts (NiAl-600, NiAl-700 and NiAl-850), which indicate a possible restraint of methanation reaction.

5.4.1 Effect on the gas products distribution

Regarding the gas products distribution presented in Table 5.3, it is seen that the concentration of H_2 and CH_4 in the gas stream slightly varies with T/P conditions, and a trade-off could be deduced between both species. This way, as T/P changed from 235 ºC/ 35 bar to 260 ºC/ 52 bar, H_2 concentration in the gas stream vaguely decreases from 54% to 52% (NiAl-600); 53% to 45% (NiAl-700); 48% to 43% (NiAl-850). Meanwhile, CH_4 concentration increases more significantly for NiAl-T reduced at high temperatures (e.g. CH_4 concentration passes from 20% to 25%, for NiAl-850 catalyst).

In this line, the decrease of H_2/CO_2 ratio with T/P suggests that operating at high T/P conditions, hydrogen is more intensively consumed in side reactions, such as CO methanation, as indicated by the increase of the selectivity to methane. The decreasing trend of the CO_2/CH_4 ratio indicates that methanation reactions are favoured for NiAl-850, as this catalyst presents a decrease by 23% in CO_2/CH_4 ratio. However, the decrease in CO_2/CH_4 ratio for NiAl-700 is minor (only 7%), in agreement with its SCH_4 minor increase tendency in comparison to NiAl-600 and NiAl-850 assays. Thus, these results suggest that CO methanation reaction is not in equilibrium, i.e., it is kinetically controlled.

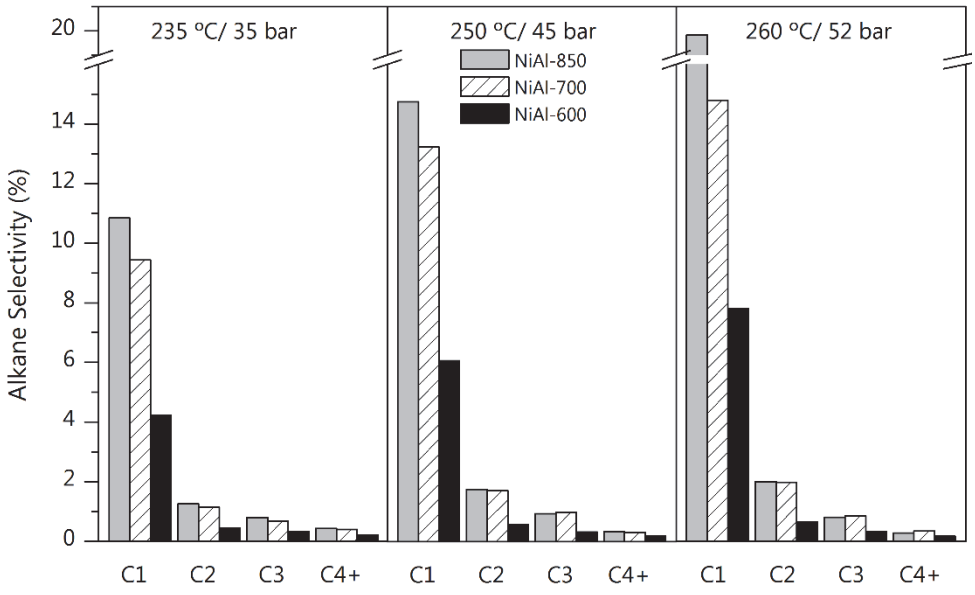

Figure 5.8. Effect of T/P on the alkane selectivity, in function of Carbon numbers.

The alkane selectivity as a function of C number is presented in Figure 5.8. It was calculated in terms of the flow of carbon atoms produced in the gas phase with respect to converted carbon atoms (equation 2.27). S_{Alkane} follows a similar distribution with reaction T/P, the highest selectivity by far for C1 alkanes (methane) at the three T/P operation conditions. For all catalyst (except NiAl-300 and NiAl-450, which are not included due to their very low conversion to C-products), at most severe conditions, the selectivity to methane increases, especially at the highest reduction temperature, confirming the C-C scission promotion by temperature.

5.4.2 Effect on the liquid products distribution

Liquid-phase composition of active catalysts also varied with the reaction T/P conditions, as displayed in Figure 5.9.

A kind of trade-off between small chain alcohols (which increase) and glycols (which decrease) is observed with the increase of T/P, with an almost constant production of hydroxyacetone. The noticeable increase of EtOH production for NiAl-700 and NiAl-850 catalysts could be associated to the enhancement of the catalytic performance, in terms of X_{Gly} and X_{Gas}, at higher T/P conditions, which enable high availability of H_2 for the EG hydrogenation.

The evolution of the main reaction products obtained by dehydrogenation (route A: EG, MeOH and EtOH), with respect to the main reaction products of dehydration-hydrogenation (route B: HA and 1,2-PG) was analysed. Route A/Route B product ratio (in terms of atomic carbon liquid flows), depicted in Figure 5.10, shows that for NiAl-700 and NiAl-850 catalysts, the ratio is above 0.5, and below 0.5 for the rest of catalysts. In addition, it increases with reaction T/P conditions, except for NiAl-450 catalysts which follow a non-defined trend. For example, changing from 235 ºC/ 35 bar to 260 ºC/ 52 bar, the ratio increases from 0.34 to 0.47 for NiAl-600, and boosted for NiAl-850 (from 0.74 to 1.83).

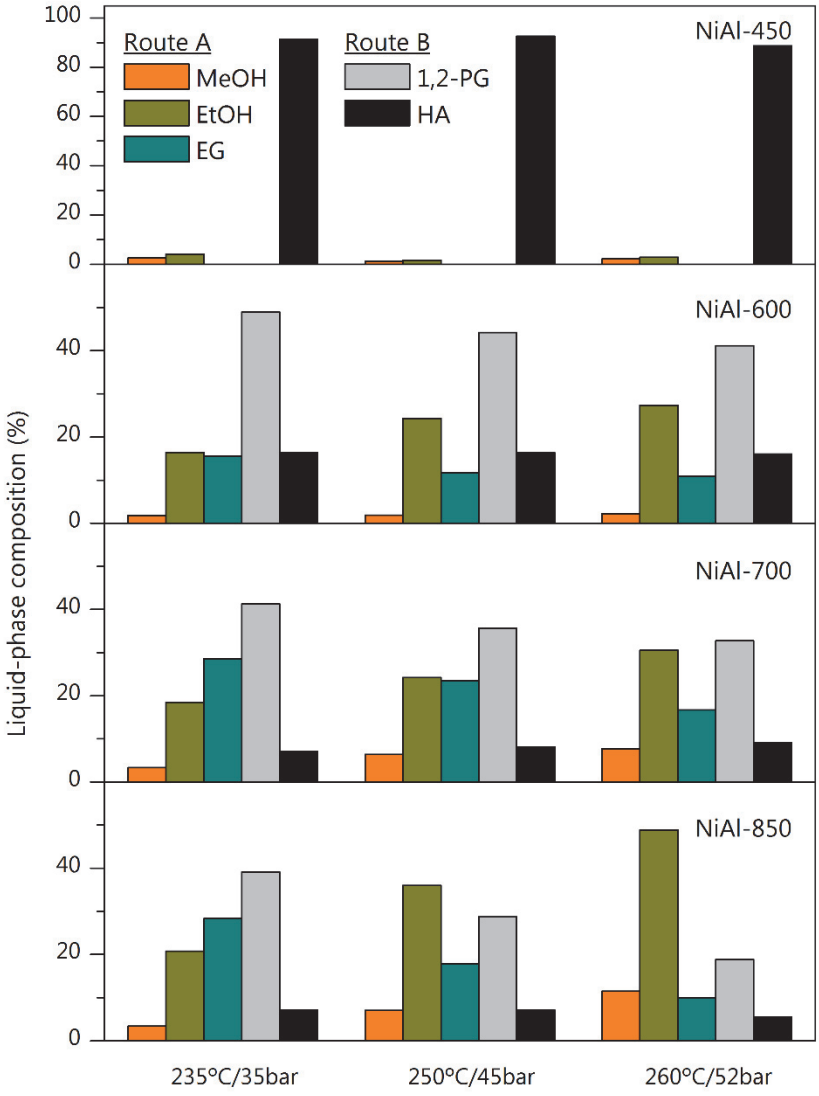

Figure 5.9. Effect of T/P on the composition of the liquid phase.

At the most severe conditions, both decarbonylation and C-C scission are promoted over C-O scission. Similar findings are reported in literature [180]. These results agree with the obtained aforementioned tendency of liquid products at higher T/P conditions, with EG diminishing to produce higher amounts of small chain monoalcohols while the HA production is almost invariable.

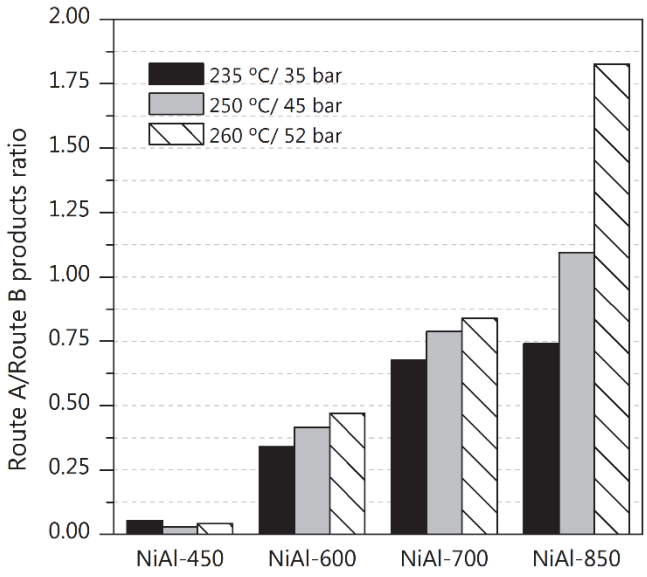

Figure 5.10. Dehydrogenation (Route A)/ Dehydration-hydrogenation (Route B) products ratio for different T/P conditions.

5.4.3 Activation energy for glycerol APR

An attempt was made to estimate the apparent activation energy (E_{app}) for glycerol conversion. For this purpose, first order kinetics was assumed [181, 182]. Equation 5.1 presents the reaction rate in form of power law equation, where $-r_{Gly}$ is the rate of glycerol reforming reation, C_{Gly} is the glycerol concentration, C_{Gly}^0 is the initial glycerol concentration, and k_{app} is the apparent reactions rate constant:

$$-r_{Gly} = kC_{Gly} = kC_{Gly}^0\left(1-X_{Gly}\right) = k_{app}\left(1-X_{Gly}\right) \tag{5.1}$$

As the following design equation shows, plug-flow reactor was assumed:

$$\frac{W}{F_{Gly}^0} = \int_0^{X_{Gly}} \frac{dX_{Gly}}{-r_{Gly}} \tag{5.2}$$

After replacement of $-r_{Gly}$ and the respective integration of the design equation, the apparent rate constant is calculated as follows, for isothermal reactor:

$$k_{app} = -\ln\left(1 - X_{Gly}\right) \times \frac{F^{0}_{Gly}}{(W * A_{S\text{-}Ni^{o}})} \tag{5.3}$$

With the logarithmic Arrhenius expression (equation (5.4), E_{app} is determined from the slope of the linear plot of $\ln(k_{app})$ vs 1/T, as shown in Figure 5.11. The obtained E_{app} are also displayed in the figure.

$$\ln\left(k_{app}\right) = \ln\left(A_0\right) - \frac{E_{app}}{R}\left(\frac{1}{T}\right) \tag{5.4}$$

The E_{app} range between 46-102 kJ/mol for catalysts reduced at 600 ºC or above. Those values of the reforming are similar to that reported in by Coronado et al. [183] on the Aqueous reforming of C1-C4 alcohols. The coefficient of determination (R^2) is >0.95 for all estimated E_{app}.

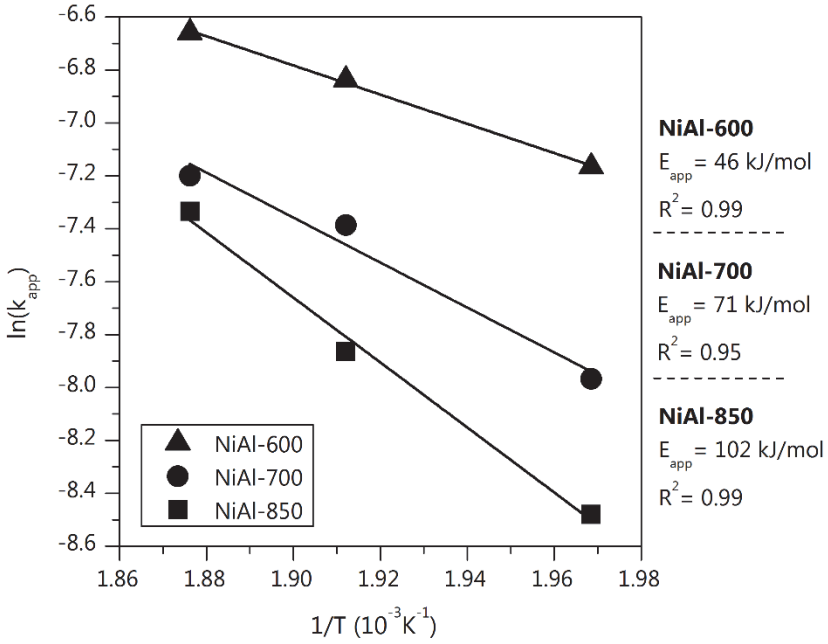

Figure 5.11. Apparent activation energy and fitted curves for NiAl-T most active assays.

The influence of the reduction extent of NiAl-T catalyst on the reaction mechanism is reflected in their E_{app} values, and the increasing trend suggests that the reactions over metallic nickel sites are characterized by a higher activation energy than those occurring over the acid sites, characteristic of catalysts with higher acid/base ratio

(e.g. NiAl-600= 2.3). Furthermore, E_{app} values evidenced that the effect of T/P becomes more intense as the reduction temperature increases.

5.5 CATALYSTS STABILITY STUDY

Among NiAl-T catalysts, those reduced at higher temperatures (NiAl-700 and NiAl-850) presented notable catalytic activity and good performance in the glycerol APR, thus their stability at the hydrothermal conditions of the APR reaction was studied. Catalysts performance (i.e. X_{Gly}, X_{Gas}, S_{Gas}) as a function of time-on-stream (TOS) was investigated for NiAl-700 and NiAl-850, under mild operation conditions (235 ºC/35 bar) for a period of 50 h operating at WHSV of 24.5 h^{-1}. Results are shown in Figure 5.12.

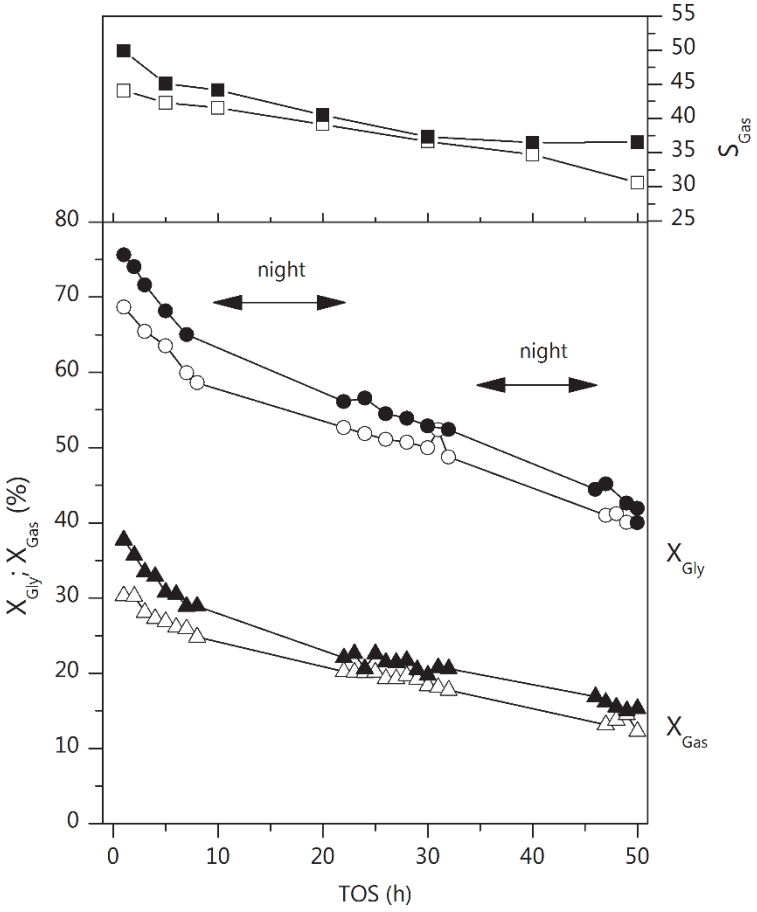

Figure 5.12. Evolution with TOS of X_{Gly} (circles) X_{Gas} (triangles) and S_{Gas} (squares). Filled symbols: NiAl-850; Open symbols: NiAl-700.

The activity (in terms of X_{Gly} and X_{Gas}) follows a similar trend for both catalysts, with sustained decay throughout the catalytic test, being more pronounced during the first hours of operation (i.e. 8 h TOS). An overall decay of around 37% and 45% is observed in the glycerol conversion and conversion to gas, respectively, for NiAl-700 catalyst. In this line, the S_{Gas} also decreases with TOS, and after 50 h, it levels-off at around 31% for NiAl-700. Similarly, NiAl-850 catalysts presents a drop, in 50 h TOS of 39% and 50% for X_{Gly}, and X_{Gas} respectively. Its overall selectivity to gas decrease (by 27%) is much less than that of NiAl-700, which decreases by 36%.

In order to evidence more differences among the samples, the deactivation rate constant was estimated for both catalysts assuming a first order deactivation kinetics [184], as follows:

$$\ln\left(X'_{Gly}\right) = -\beta_d t \tag{5.5}$$

where X'_{Gly} is the relative conversion of glycerol respect to the initial conversion, at time t (TOS). The deactivation rate constants β_d are depicted in Figure 5.13.

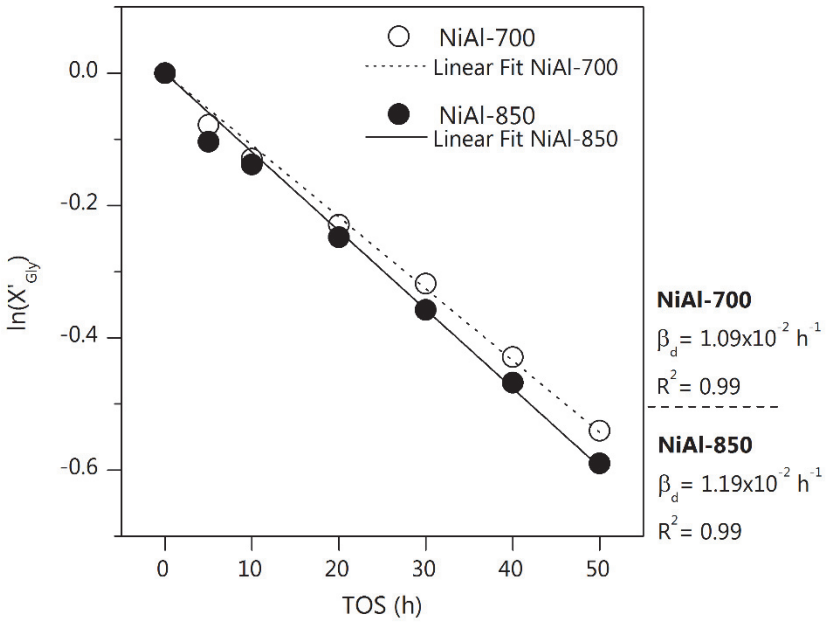

Figure 5.13. Deactivation rates and fitted curves for NiAl-700 and NiAl-850.

Note that NiAl-700 catalyst has lower β_d than NiAl-850 does ($1.09 \cdot 10^{-2}$ h^{-1} vs $1.19 \cdot 10^{-2}$ h^{-1}), which confirms the observations mentioned previously. Optimal coefficients of determinations are found for the stability test studied of $R^2 = 0.99$ for both estimated β_d.

Once again, the fraction of reduced nickel seems to play a key role in the deactivation rate, possibly by being affected by the hydrothermal conditions of the reaction, suffering changes that could be associated to sintering, oxidation and/or lixiviation. In this line, the obtained deactivation rate constants evidenced that the effect of the TOS in the glycerol APR is slightly more intense for NiAl-850 catalyst, than with the highest accessible metallic surface (3.47 $m^2_{Ni^o}$ g_{cat}^{-1}).

Figure 5.14 depicts the evolution, with TOS, of several reaction parameters related to the selectivity of the APR reaction, for NiAl-700 and NiAl-850 catalysts. Despite the selectivity to hydrogen suffering an initial drop for NiAl-700, it increases after 10 h TOS, reaching a value of 34% after 50 h TOS. Meanwhile, SCH_4 decreases in the same period. This could be associated to a suppression of methanation reaction due to less H_2 availability, in line with the hydrogen yield tendency observed for NiAl-700. Note that this catalyst suffers just a slight decrease to 4.9% at 30 h TOS and then remains almost stable from 30 h to 50 h TOS of reaction.

Similar trends for SH_2 and SCH_4 are observed for NiAl-850 catalysts. However, the increase of SH_2 in the 20 h to 50 h TOS period, is less pronounced than that for NiAl-750 (14% vs 22%). A decrease in the selectivity to methane of NiAl-850 also proceeds but less marked than that for NiAl-700 catalyst. Regarding the hydrogen yield, it notably decreases from 7% to 4% (from 1 to 50 h TOS).

The total molar flow of gaseous products dropped-off by around 45% for both catalysts after 50 h of operation, in agreement with the observed evolution of X_{Gas}. Nonetheless, the gas stream enriched in hydrogen with TOS, as revealed by the H_2/CO_2 ratios (Figure 5.14), which is more pronounced for NiAl-700. The CO_2/CH_4 ratio remain constant with TOS for both catalysts, confirming the detriment of the methanation reaction evidenced by the SCH_4 results. On the other hand, the H_2/CO ratio decreased by around 36% for NiAl-850 and down to 65% for NiAl-700 catalysts, which indicates that WGS occurrence is being limited as the APR proceed, generating less CO_2.

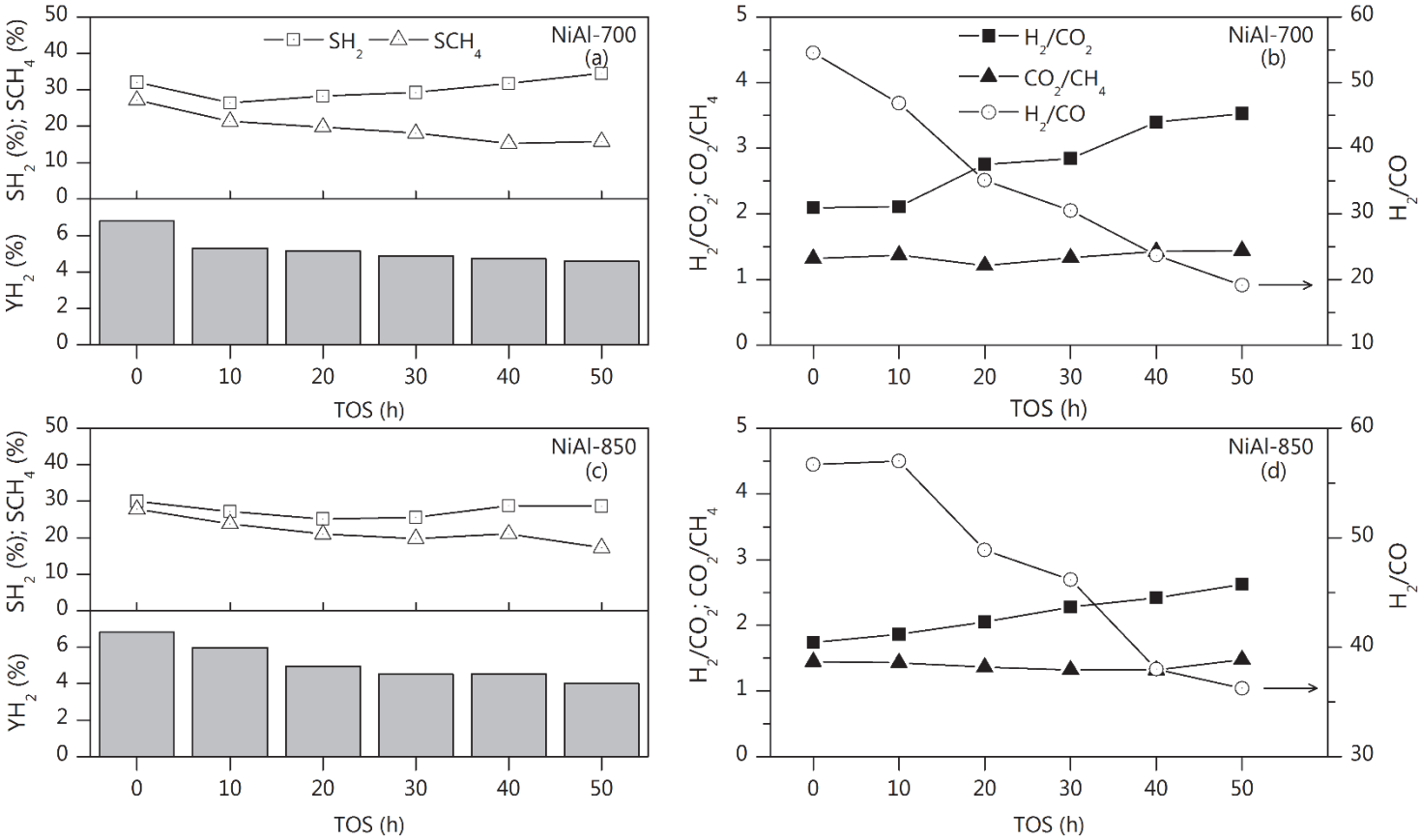

Figure 5.14. Variation of the reaction indices with TOS (WHSV= 24.5 h^{-1}). Selectivities and hydrogen yield (a) NiAl-700, (c) NiAl-850. Ratios from the gas-phase composition (b) NiAl-700 (d) NiAl-850.

The observed results for the reaction parameters related to the selectivity of the APR (Figure 5.14) pointed out that both methanation and WGS reaction are partially inhibited with TOS. As mentioned above, CO as well as CO_2 methanation and WGS reactions take place on metallic Ni [156, 185]. Therefore, the stability results suggest that the severe hydrothermal conditions of APR inhibit the C-containing molecule activation capacity of metallic Ni, necessary to catalyze both reactions.

The changes related to the liquid-phase composition with TOS are presented in Figure 5.15.

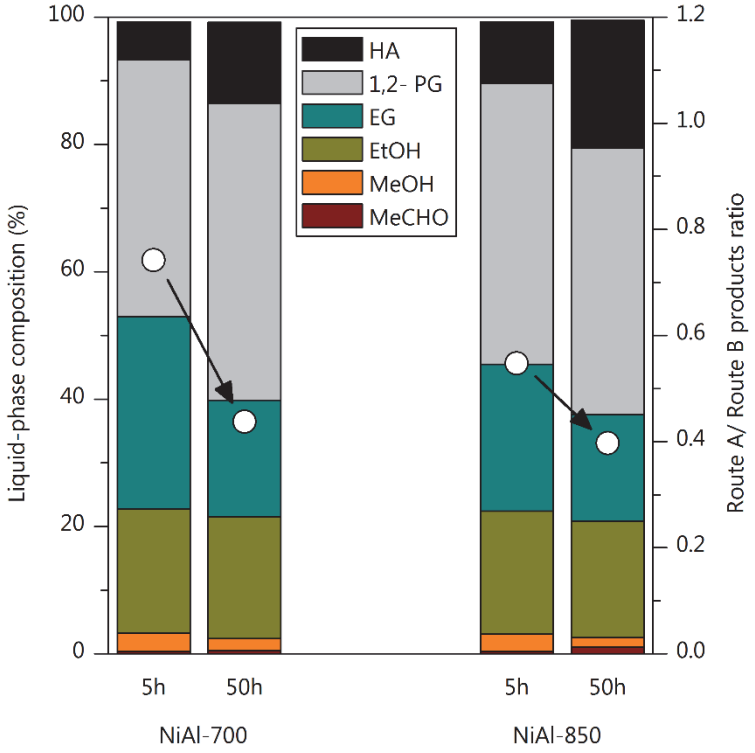

Figure 5.15. Variations in the liquid-phase distribution with TOS and Route A/Route B products ratio (open circles).

Regarding intermediate liquid products, both NiAl-700 and NiAl-850 catalysts showed a similar trend, according to which hydroxyacetone formation increases and ethylene glycol, ethanol and methanol decrease with TOS. This behaviour revealed a drop in the Route A/ Route B product distribution, which varies from 0.74 to 0.44 for NiAl-700 and from 0.55 to 0.40 for NiAl-850, i.e., the amount of

dehydration-hydrogenation product becomes more abundant than those products from dehydrogenation path. This could indicate of a loss of metal function.

Shabaker et al. [72] reported 90% of initial activity decay during 48 h of APR of ethylene glycol over Ni supported on different supports, among them γ-alumina (due to metal sintering). Comparing those results with the ones for NiAl-700 and NiAl-850 catalysts, one can see that, in general, stability of NiAl-T catalysts, synthesized by co-precipitation, can be deemed as promising as compared to other supported nickel catalysts, though there are still characteristics with room for improvement. The characterization of used catalysts will help to identify those properties.

5.6 CHARACTERIZATION OF USED CATALYSTS

The catalysts were analysed by multiple techniques, after being used in consecutive APR reactions 2 h at each condition (235 ºC/35 bar → 245 ºC/45 bar → 250 ºC/52 bar), as well as after the stability test (50 h TOS). This aims to elucidate the catalyst changes with the hydrothermal conditions of APR reaction. The possible nickel oxidation and lixiviation, the textural and structural changes in the catalysts, and the possible formation of carbonaceous deposits were analysed by means of N_2 physisorption, H_2-TPR, FTIR, XRD, TG-TPO techniques on the exhausted catalysts, and ICP-AES on the overall collected liquid product. Variation (in %) with respect to the fresh reduced solids are shown (ΔS_{BET} and Δd_{Ni^0}). A summary of the results is presented in Table 5.4.

5.6.1 Leaching of metals

Leaching of both Ni and Al was considered given the acidity of the reaction medium, since the pH decreased from around 8 to 3, in 50 h TOS. The ICP data (Table 5.4) revealed that, on the one hand, leaching of Al from the support is negligible. This could be associated to the capacity of hydrated alumina to leach-off and re-deposit on the catalysts surface [186], generating an overcoating-like effect on the metallic nickel particles. On the other hand, leaching of Ni occurs at higher rate during the APR reaction. It can be promoted by the phase transformation of the support (γ-alumina-rich solid) at hydrothermal conditions, conducing to a detachment of the supported metal particles supported on. In addition, Ni could also be detached by the formation and posterior elution of Ni by chelation mechanism [187]. These phenomena agree with the worsening

activity of the catalysts in WGS and methanation reactions, and with the decreasing trend of Route A/Route B products, with TOS.

The average Ni leaching rate, defined as the percentage of the initial nickel on the catalyst that is removed in a reaction period, has been calculated for NiAl-700 and NiAl-850 catalysts at 2 h (steady state) and 50 h TOS. For both catalysts, the nickel leaching rate remained almost unaltered in the whole reaction time (NiAl-700: 0.135-0.130 $\%Ni \cdot h^{-1}$; NiAl-850: 0.095-0.108 $\%Ni \cdot h^{-1}$), independent of the TOS. Therefore, it can be concluded that Ni leaching is proportional to TOS, at least in the studied reaction time. In the same way, the lower rate of Ni leaching for NiAl-850 can be related to the higher amount of boehmite detected, of bigger Ni^0 crystallite size, which could facilitate the coating of nickel. The over-coating of nickel ensembles by the re-deposited layer could increase the catalysts' lifetime [188-190].

The adsorption-desorption isotherms are shown in Figure 5.16. The isotherms of NiAl-300-U and NiAl-450-U are quite similar to those of fresh reduced samples, type IV of mesoporous materials. NiAl-600-U catalyst presents a slightly different shape of the hysteresis loop, as it starts at slightly lower P/P_0 and the desorption branch is separated from higher relative pressure ($P/P_0 \approx 1$). This profile can be associated to changes in the pore morphology, which can be due to one (or more) of the following events: (i) generation of additional porosity by the alumina-phase change [191]; (ii) deposition phenomenon on the catalysts' surface; (iii) oxidation of the active metal, with inherently low S_{BET}; and (iv) carbonaceous deposits. Note that those differences are more marked for NiAl-700 and Ni-Al-850, especially after 50 h TOS.

Table 5.4. Textural and structural characteristics of the NiAl-T catalysts used in the glycerol APR.

Sample	S_{BET} ($m^2 \cdot g^{-1}$)	ΔS_{BET} (%)	$d_{Ni}{}^{0}$ [a] (nm)	$\Delta d_{Ni}{}^{0}$ (%)	$d_{boehmite}$ [a] (nm)	Leached Ni[d] (%)	Leached Al[d] (%)	C[e] ($mmol_C \cdot g^{-1}$)
NiAl-300	102.6	n/a	33.9	n/a	n.d.	0.65	<0.025	n/a
NiAl-450	87.0	n/a	30.0	n/a	n.d.	0.78	<0.025	n/a
NiAl-600	110.2	23	45.9	+496	8.1	0.72	<0.025	n/a
NiAl-700	97.4 (92.6)	18 (12)	44.5 (32.0)	+227 (+132)	15.0 (8.0)	0.27 (6.5)	<0.025 (<0.025)	(1.12)
NiAl-850	109.9 (102.9)	44 (34)	41.5 (44.0)	+258 (+279)	17.4 (8.0)	0.19 (5.4)	<0.025 (<0.025)	(0.16)

[a]: from XRD. [b] from NH_3-TPD. [c] from CO_2-TPD. [d] from ICP-AES. [e] carbonaceous deposits by TPO-TG-MS. In parenthesis, data for experiments with TOS= 50 h.

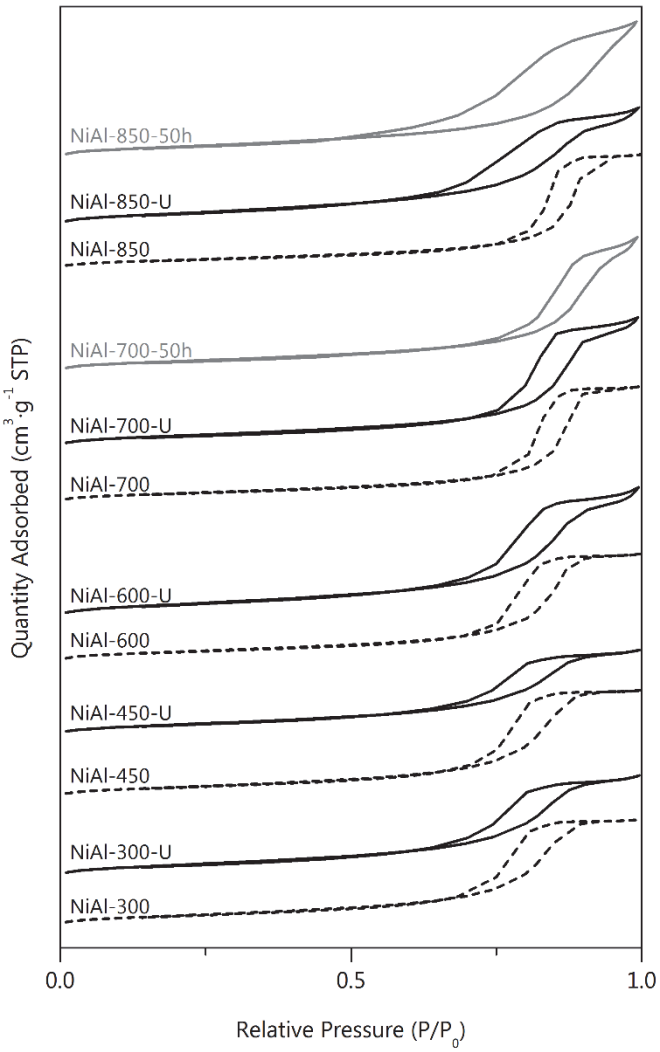

Figure 5.16. N_2 physisorption isotherms for used catalysts. Black continuous line: used in consecutive APR reactions (235 ºC/35 bar → 245 ºC/45 bar → 250 ºC/52 bar), 2 h at each condition, labelled –U; gray line: 50 h TOS, labelled -50h; dashed line: fresh reduced catalyst.

The pore size distributions of the exhausted catalysts are presented in Figure 5.17. After use in APR reaction, all catalysts show almost identical main pore size to those of their parent fresh reduced solids. Nonetheless, a bimodal pore size distribution is observed, with a low intensity peak emerging at <50 Å. No clear tendency in the changes of the pore width with higher TOS are found, since NiAl-700-50h presents a slight increase of average pore width, while NiAl-850-50h, shows a decrease.

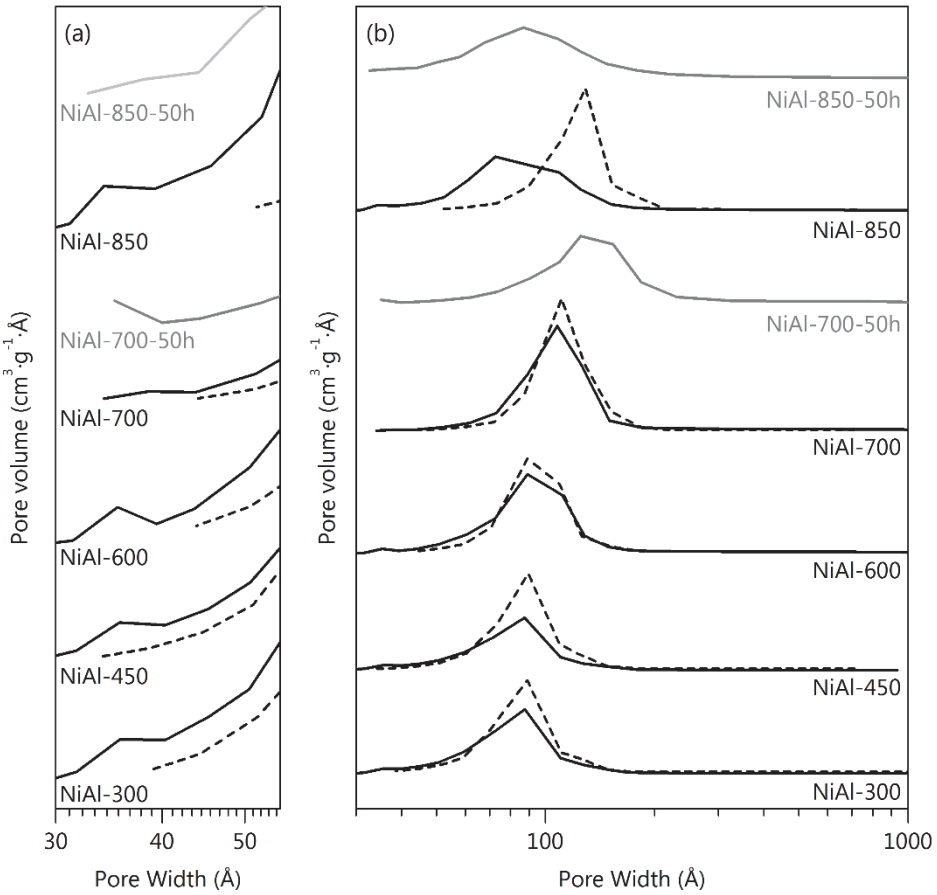

Figure 5.17. Pores size distribution for NiAl-T: (a) in 30-50 Å range; (b) in the whole pore width range. Black continuous line: used in consecutive APR reactions (235 ºC/35 bar → 245 ºC/45 bar → 250 ºC/52 bar), 2 h at each condition; gray line: 50 h TOS, labelled -50h; dashed line: fresh reduced catalyst.

The specific surface area of the spent catalysts increases with respect to that of fresh reduced solids. The total change with respect to the fresh reduced catalysts (ΔS_{BET}) is shown in Table 5.4. A positive ΔS_{BET} is notable for catalysts reduced at higher temperatures, e.g., 12% and 34% for NiAl-700 and NiAl-850, respectively, after 50 h TOS. NiAl-700 catalysts show an increase of 17% in the average pore size after 50 h TOS, while NiAl-800 presents a decrease of 30% (Figure 5.17).

5.6.2 Phase transitions and crystallinity

XRD diffractograms of the used catalysts are displayed in Figure 5.18. Diffractograms reveal the presence of boehmite (an aluminium oxide hydroxide) phase (JCPDS 01-083-2384) for spent catalysts reduced at 600 ºC or above. The characteristic peak intensity increased with reduction temperature, probably due to increasing content of boehmite-precursor (γ-Al_2O_3) in fresh catalyst (as seen in previous sections) and its transformation into boehmite. Moreover, the acidity of the reaction medium increases with time (feedstock pH: 8; collected liquid product after 6 h steady state pH: 4). This could enhance the hydration of γ-alumina. On the other hand, NiO diffraction peaks are also detected for the solids reduced at 700 ºC and 850 ºC, which indicates the oxidation of nickel surface, in agreement with TPR results. Nonetheless, the presence of intense Ni^0 peak, for all samples, suggests that Ni^0 oxidation to NiO is limited to the outermost layers of Ni^0 clusters. Besides, the bimodal pore size distribution observed for the used samples (Figure 5.17) could support the coexistence of both boehmite and nickel aluminate phases.

XRD analysis demonstrated the metallic nickel particle sinterization occurs in the first periods of reaction. For example, after 6 h TOS at the three different coupled T/P reaction conditions abovementioned, Ni^0 particle size increased from around 8-14 nm to 42-46 nm (230-260% increase, Table 5.4). Thereafter, it does not substantially increase until 50 h of usage (for example, for NiAl-850 catalyst, metallic nickel crystallite size stabilised at 44.0 nm, i.e., 279% increase). The opposite trend is observed for NiAl-700 catalyst, where the Ni^0 crystallite size after 50 h TOS (32 nm) is even smaller than that of the catalysts used for only 6 h (44.5 nm). This can be explained by the preferential leaching of larger particles, what contradicts the results from other authors. According to them, small particles are main sources of leached species [192]. Metallic nickel particles from NiAl-600 catalyst, with the initial smallest size, outgrow those from NiAl-700 and NiAl-850 catalysts, and all the spent catalysts ended up with similar particle size. This is consistent with theories on particle migration, where the initial particle growth rate is larger for smaller particles, and the rates decrease as the average particle size increases [192]. It appeared that the average Ni^0 particle size of used catalysts is not significantly affected by the activation temperature. However, a subtle decreasing trend

could be deduced with the reduction temperature increase, what could be ascribed to stronger interaction of Ni^0 particles with the support.

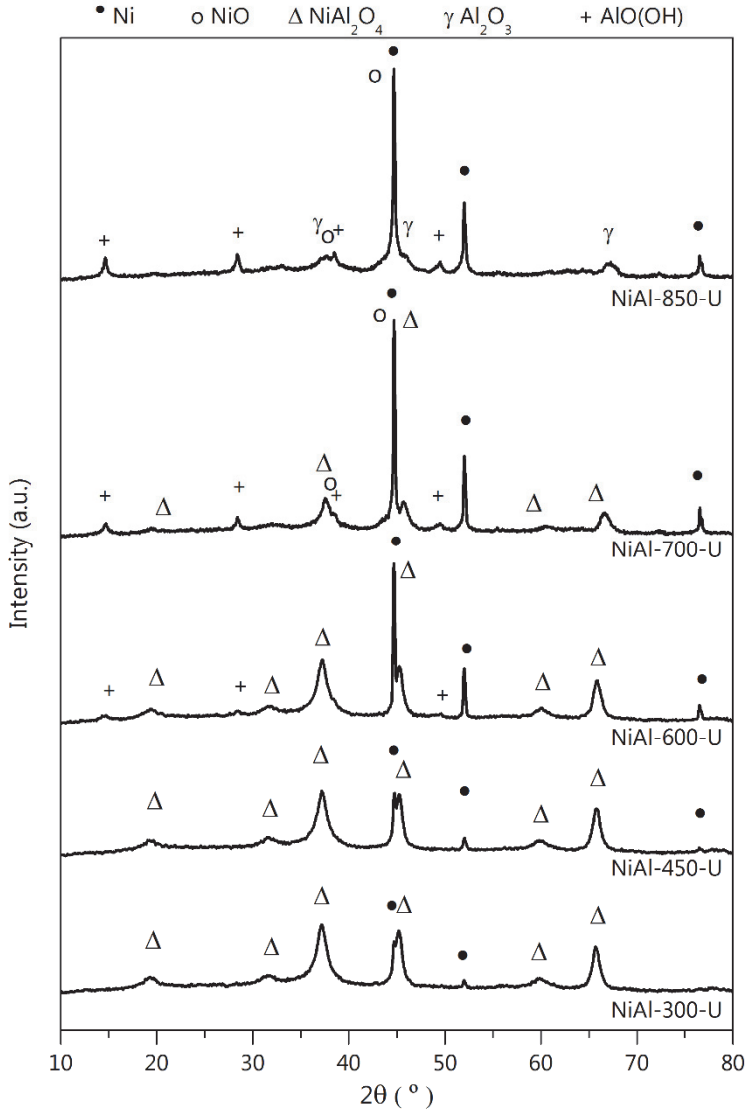

Figure 5.18. XRD spectra of the catalysts used in consecutive APR reactions: 235 ºC/35 bar → 245 ºC/45 bar → 250 ºC/52 bar, 2 h at each condition.

Formation of boehmite is further confirmed for NiAl-700 and NiAl-850 used catalysts after 50 h TOS by FTIR, as displayed in Figure 5.19. The transmittance bands at 611, 1068, 1631 and 3089 cm^{-1} are characteristic of boehmite phase.

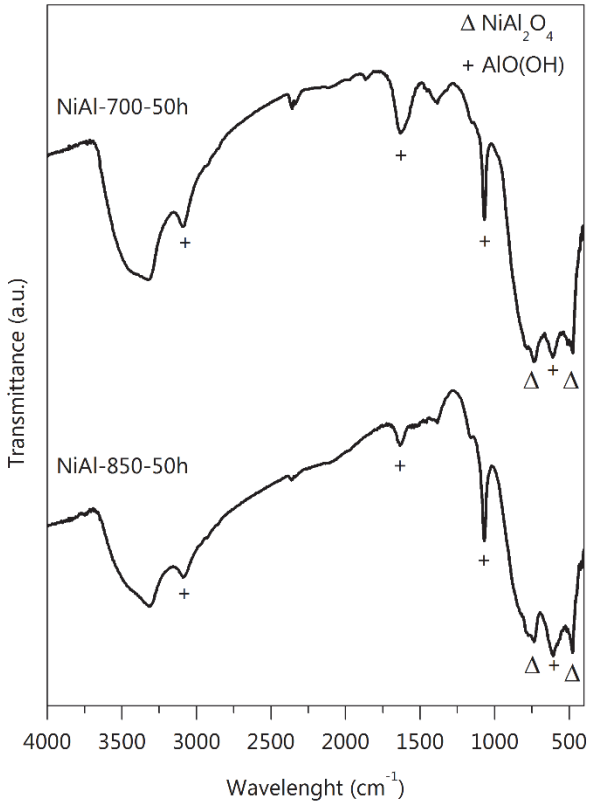

Figure 5.19. FTIR spectra of spent catalysts after 50 h TOS of APR.

The strong, broad band at 3400 cm^{-1} corresponds to stretching vibration of OH group of adsorbed water, and the band at 3089 cm^{-1} is associated to υ_s(Al)O–H stretching vibration. The band at 1631 cm^{-1} is thought to be featured for the bending mode of absorbed water. The intense band at 1068 cm^{-1} is attributed to the δ_sAl–O–H mode of boehmite, and the bands at 611 cm^{-1} is believed to be the vibration mode of AlO_6 [193].

5.6.3 Reducibility and speciation

H_2-TPR profiles of spent NiAl-T catalysts (named as NiAl-T-U) are shown in Figure 5.20. The reduction profiles of catalysts used for 50 h in glycerol APR (NiAl-700-50h and NiAl-850-50h) are qualitatively similar to those used for 6 h (2 h in the consecutive reactions at 235 ºC/35 bar, 250 ºC/45 bar and 260 ºC/52 bar).

All used catalysts show an incipient hydrogen uptake peak below 500 ºC, indicative of both nickel oxidation and reduction of C-containing liquids, which are adsorbed into the catalysts pores, and they have not been eliminated by water treatment. The peak at 250 ºC suggests coalescence of oxidized nickel species into large NiO particles.

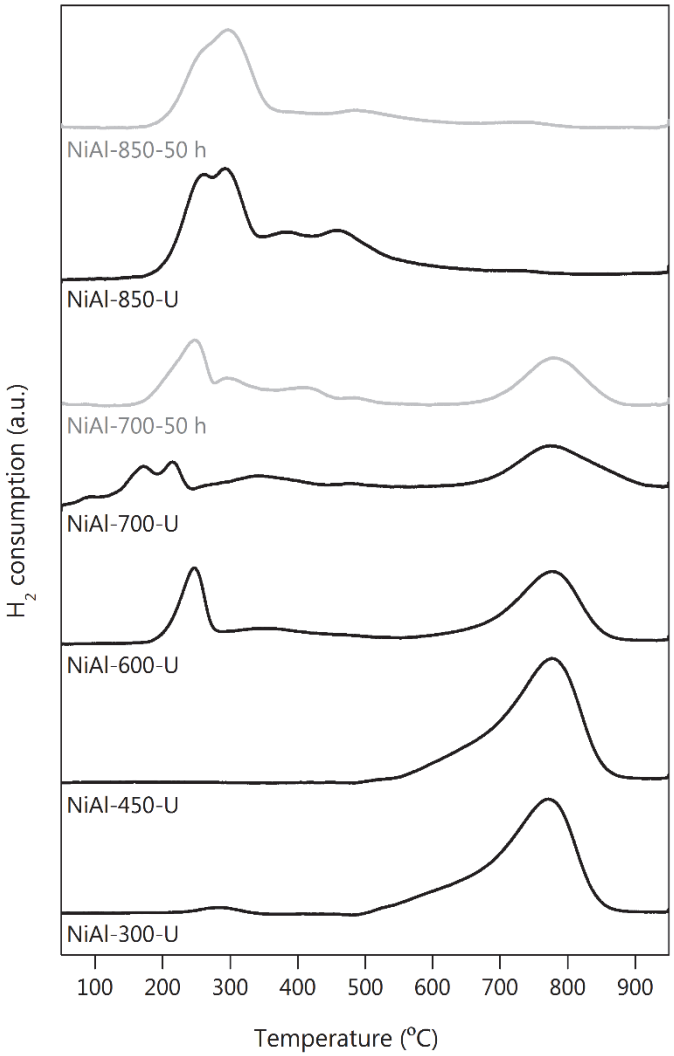

Figure 5.20. H_2-TPR profiles for catalysts used in glycerol APR reaction. NiAl-T-U: used in consecutive reactions (235 ºC/35 bar → 245 ºC/45 bar → 250 ºC/52 bar), 2 h at each condition. NiAl-T-U-50h: used for 50 h at 235 ºC/ 35 bar (stability test).

Notable differences in the reduction profiles of NiAl-T catalysts are found. Samples reduced at T≥ 600 ºC show larger low-temperature peaks, which reflects oxidation of

metallic Ni taking place to a greater extent. In addition, NiAl-700-U and NiAl-850-U catalysts show less intense, unresolved peaks in the 300-600 ºC range, which could be ascribed to the reduction of smaller NiO particles interacting with the support or to nickel defective spinel compounds. In contrast, the high-temperature peak, associated to Ni^{+2} in the spinel phase is higher for catalyst reduced at below 600 ºC. Nonetheless, the subtle reduction peak of catalyst NiAl-850-U at about 750 ºC indicates that a small part of the Ni is oxidized to the original spinel structure, facilitated by the open spinel structure of γ-alumina that hosted the Ni^{2+} species [194].

The obtained H_2 consumptions are given in Table 5.5. The high temperature hydrogen uptake (at around 775 ºC) of NiAl-700-U suggests the existence of a fraction of nickel as spinel, yet unreduced in the fresh catalyst. Overall, for these most active catalysts, the hydrogen consumption under 750 ºC is ascribed either to oxidation of the metallic Ni and hydrogenation of the adsorbed organic species. Yet, we have no clear evidence to explain the over 100% oxidation measured for catalyst NiAl-600-U, except for the presence of CH_4 in the MS registers during the TPR analysis, which evidences that the surface of catalysts retain C-containing liquids that are reduced by hydrogen. Van Haasterecht et al. [192] also acknowledged the nickel oxidation as the main cause of deactivation, employing Ni/alumina (synthesized by wetness impregnation) for the ethylene glycol reforming.

Table 5.5. TPR data for NiAl-T catalysts used in glycerol APR.

Catalyst	H_2 consumption (mmol $H_2 \cdot g^{-1}$)			
	Total	Interval 50 – 600 ºC	Interval 600 – 750 ºC	> 750 ºC
NiAl-300	4.46	0.12	1.92	2.42
NiAl-450	4.49	0.03	1.89	2.57
NiAl-600	3.33	1.36	0.43	1.54
NiAl-700	2.41 (1.85)	1.24 (0.99)	0.12 (0.26)	1.05 (0.60)
NiAl-850	2.56 (1.89)	2.34 (1.78)	0.22 (0.11)	n/a

In parenthesis, data for catalysts used during 50 h (TOS).

For the catalyst used for 6 h (steady state), around 34% of the initial Ni is oxidized (assuming that the H_2 consumption peak only corresponds to Ni^0 oxidation), while NiAl-700-50h and NiAl-850-50h present similar H_2 consumption. This indicates that the metallic Ni in the fresh reduced catalyst is mainly oxidized during initial stages of APR. This would explain the fast activity decay in the initial 10 h (Figure 5.12). Thereafter, these species progressively are leached out, and around 6.5% of the Ni loaded was lost during the long-term catalytic run, as can be seen in Table 5.4.

5.6.4 Carbonaceous deposits

TPO-TG-MS analysis was carried out to estimate the number of carbonaceous deposits (C-deposits) on the surface of the catalysts. A known amount of calcium carbonate was added to the sample and used as C-deposits content reference. Results are reported in Table 5.4.

NiAl-700-50h and NiAl-850-50h catalysts contain small amounts of carbonaceous deposits (in the range 0.2-1.0 $mmol_C \cdot g^{-1}$), one order of magnitude less than typical values reported in the literature (up to 10 $mmol_C \cdot g^{-1}$) [35, 195]. Moreover, XRD of used catalysts (Figure 5.18) showed the absence of diffraction peaks of graphitic carbon, reflecting its low content. These results, with remarkable resistant to deactivation by coke, make the nickel aluminate spinel-derived catalysts a good candidate for the APR applications.

Based on the characterization of spent catalysts, it seems that the main causes of activity decay are nickel oxidation and sintering, while metal leaching and coke formation have subtle effects.

5.7 GENERAL OVERVIEW AND CONCLUSIONS

Stoichiometric bulk nickel aluminate spinel was synthesized by co-precipitation, and then calcined at 850 ºC for 4 h. The effect of reduction temperature, between 300 ºC and 850 ºC, on the catalytic performance in the APR of glycerol was investigated. It is remarkable the high performance shown by nickel aluminate catalysts in glycerol APR, in spite of the high space velocity used (WHSV 24.5 h^{-1}). The most active assay was NiAl-850, yielding 93% glycerol conversion, 57% conversion to gas, and 62% selectivity to gas (at 250 ºC/45 bar). The maximum specific hydrogen production rate was achieved upon reduction at 600 ºC, due to an adequate balance between Ni^0 cluster size,

accessible metallic nickel surface and acidic/basic properties. Nonetheless, high selectivity to liquids of dehydration-hydrogenation is evidenced for this sample. NiAl-700 presents the best balance between conversion, selectivity to hydrogen, and stability. This catalyst shows 87% glycerol conversion, 46% conversion to gas, and 53% selectivity to gas (at 250 ºC/45 bar).

For all the prepared assays, hydrogen was the main compound in the gaseous stream, followed by carbon dioxide and methane. The low formation of CO suggested that WGS was also favoured by the $NiAl_2O_4$-derived catalysts, in which CO is oxidized by water to CO_2 giving additional H_2. Other small chain alkanes were hardly detected which evidenced the high C-C scission ability of the investigated catalysts.

Reduction temperature had a more marked effect on the liquid phase product distribution. Results suggested a key contribution of accessible metallic sites and medium strength acidic sites to the overall reaction scheme, with the glycerol reforming occurring through both the dehydrogenation to glyceraldehyde, and through dehydration of terminal hydroxyl groups, and subsequent hydrogenation to yield 1,2-propylene glycol. Activation at 700 ºC or above favoured a dehydrogenation path, whereas the dehydration-hydrogenation path was dominant for catalysts reduced at 600 ºC and below. Thus, the obtained results point to the preponderance of metallic function with respect to acid function in the investigated catalytic system.

It could be concluded that the catalyst reduced at the highest temperature consumed more H_2 in side reactions. It would be of interest to gain knowledge on the properties required to improve the intrinsic activity of the catalyst reduced at high temperature. It is likely that adequate surface acid-base properties of the nickel aluminate catalyst could allow tuning the selectivity towards dehydrogenation reactions rather than hydrogenation-hydrogenolysis reaction.

Long term catalytic runs revealed the good durability of catalysts derived from nickel aluminate spinel, where deactivation occurred mainly though nickel oxidation and sinterization, which, indeed, modified the distribution of gas and intermediate liquid products with TOS.

Chapter 6

Mg and Ce promoters for $NiAl_2O_4$ precursor to improve the APR performance

This chapter includes the study of six nickel-based catalysts which were synthesized and characterized. Their performance in the aqueous phase reforming (APR) of glycerol was evaluated at 235 °C and 35 bar, in a fixed-bed up-flow reactor. Catalysts were synthesized by co-precipitation to form stoichiometric spinel (NiAl) following by Ce and Mg doping on NiAl support (XCe/NiAl and XMg/NiAl). It was confirmed that the spinel catalyst allowed a better dispersion of the metallic Ni, and led to a more APR active and more hydrogen-selective catalyst. 5% of Mg and 5% of Ce doping further increased the nickel dispersion and increased basicity, which could be related to an enhancement of the WGS reaction. In addition, Mg doping hindered nickel reduction due to Ni-Mg interactions. Both promoters improved the stability of the textural properties under APR conditions by minimizing the formation of bohemite. Leaching of Ni was found at lesser extent after Mg doping.

6. Mg AND Ce PROMOTERS FOR $NiAl_2O_4$ PRECURSOR TO IMPROVE THE APR PERFORMANCE

In the previous chapter, the good performance in the hydrogen production by the glycerol APR of $NiAl_2O_4$-derived catalysts have been demonstrated. Nonetheless, the best catalyst (NiAl-700) presents challenges regarding its hydrothermal stability and selectivity to hydrogen, which is compromised by the methane formation. This chapter aims to evaluate the improvement of those characteristics by the addition of surface-promoters, specifically Mg and Ce, by impregnation.

The strategy followed to optimize the catalyst formulation is to add basic oxides as promoters. Among non-noble metals, Cu, La, Co, Zn, Br, Mg and Ce have been used to modify the surface properties of Ni/Al_2O_3 catalysts with the aim to improve the glycerol conversion by APR [29, 196]. Basic oxides such as MgO, CeO_2, La_2O_3 and CaO, are commonly employed to modify or neutralize the acidic nature of γ-Al_2O_3 [34, 197, 198]. In this thesis work, the first two compounds have been chosen as promoters. On the one hand, magnesium oxide, which has been reported to prevent the sintering of the supported nickel clusters [161]. On the other hand, cerium oxide, which is widely used in catalysis due to its good redox properties, which can promote the reducibility of nickel species. Besides, Ce-Ni interactions can also promote the catalytic behaviour by the creation of new species [152]. Other consideration for the choice of Mg and Ce promoters is the enhancement of the WGS reaction by basic surfaces [58].

Addition of Mg and Ce promoters on the $NiAl_2O_4$ surface, and its effects on the glycerol APR performance is the matter of study in this chapter, aiming to present novel results of the impregnation strategy of modifiers to the bulk nickel aluminate catalytic precursor.

6.1 SYNTHESIS OF MODIFIED CATALYSTS

The nickel aluminate spinel with nominal Ni/Al molar ratio of 0.5 (Ni/Al), synthesized by co-precipitation method, was subjected to a metal promotor addition (*Md*), being either Mg or Ce. Three different nominal loadings of the promoters (3%, 5% and 10%,

by weight) were incorporated to $NiAl_2O_4$ by Wetness Impregnation (WI) method, using rotary evaporator equipment, at 2 mbar, as detailed in Figure 6.1.

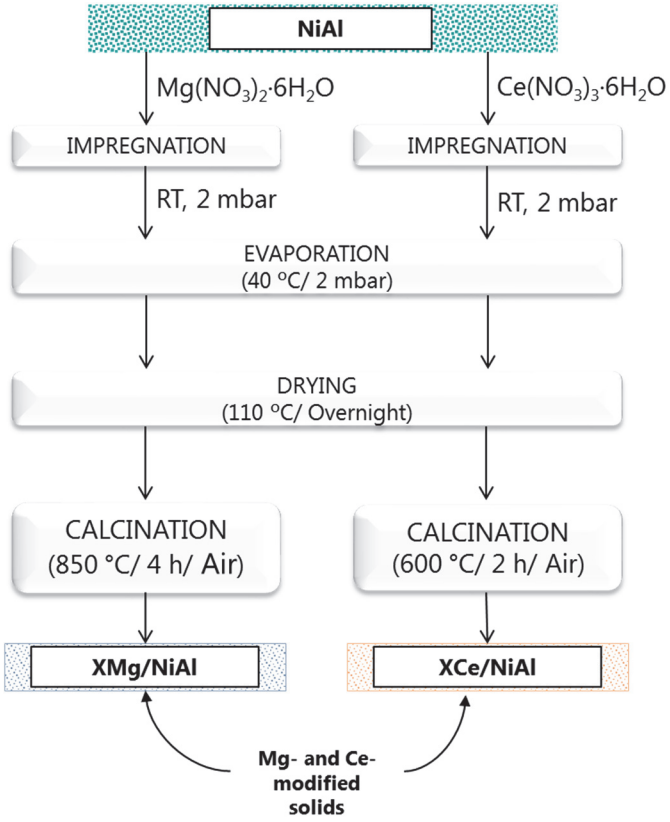

Figure 6.1. Scheme of the synthesis of Mg- and Ce-modified nickel aluminate spinel.

Aqueous solutions of cerium(lll) nitrate hexahydrate and magnesium nitrate hexahydrate were used as metal precursors. After impregnation, the solvent was evaporated at the same pressure at 40 ºC, for 5 h. The obtained solids were dried overnight at 110 ºC in an oven and finally calcined in a muffle. Catalysts modified with Ce were calcined at 600 ºC for 2 h, with a heating rate of 5 ºC·min^{-1}, while those modified with Mg were calcined at 850 ºC for 4 h, with a heating rate of 10 ºC·min^{-1}. The calcination temperature for Ce promoter assured the elimination of nitrates without deteriorating the promotion effect of ceria, as reported in the literature [152, 199]. Samples were pelletized at 0.04-0.16 mm. The solids are labelled X*Md*/NiAl, where *Md* corresponds with the employed metal promoter (Mg or Ce) and X with the nominal loading, in wt.%.

Before their use in the glycerol APR, X*Md*/NiAl catalysts were reduced in-situ at 700 ºC for 1 h, with a ramp of 5 ºC·min^{-1}, in a reducing atmosphere (20% H_2/He), as determined in previous chapters. For some surface characterization analysis (where in-situ reduction of the solid was not possible), the solid reduction was carried out ex-situ, followed by a passivation step as detailed in Chapter 2. Spend catalysts were recovered for their physicochemical characterization, after being used in the glycerol APR.

For comparative purposes, bare MgO and CeO_2 were also synthesized by direct calcination of their respective precursors. MgO was obtained by calcination of magnesium nitrate at 850 ºC for 4 h, with a heating rate of 10 ºC·min^{-1}. Meanwhile, CeO_2 was obtained by calcination of cerium(III) nitrate at 600 ºC for 2 h, using 5 ºC·min^{-1} ramp. Besides, the unpromoted nickel aluminate spinel (NiAl) is included in both characterization and activity analysis as the reference catalyst.

6.2 Mg-MODIFIED NiAl SPINEL

MgO was chosen as promoter with the aim to increase the surface basicity of $NiAl_2O_4$, which is known to help the selective dehydrogenation of glycerol in the APR [58]. For this purpose, Mg was impregnated on $NiAl_2O_4$ at 3%, 5% and 10% loadings, namely 3Mg/NiAl, 5Mg/NiAl and 10Mg/NiAl, respectively. The most relevant physicochemical characteristics of the obtained solids, and their performance in the glycerol APR are discussed in the following sections.

6.2.1 Characterization of Mg-modified samples.

The actual bulk composition of XMg/NiAl solids are presented in Table 6.1, which were measured by the ICP-MS technique. The actual Mg loadings are close to nominal, with a systematic shortage by 5-9% with respect to the nominal. Regarding the Ni/Al molar ratio, close values to the stoichiometric (0.5) were obtained.

In general, the surface promoter is expected to be dispersed forming a monolayer. Jiang et al. [200] found that the threshold loading to achieve MgO monolayer coverage over γ-alumina (S_{BET}= 220 m^2·g^{-1}) is 17%. This corresponds to 0.077 gMgO/ 100 m^2Al_2O_3 of maximum metal surface density, beyond which MgO 3D crystals begin to grow. Thus, assuming similar textural properties between NiAl and γ-alumina, the theoretical

monolayers for XMg/NiAl was estimated, and results are presented in Table 6.1. Recall that the S_{BET} of NiAl is 98 $m^2 \cdot g^{-1}$.

Table 6.1. Chemical composition of XMg/NiAl modified spinels and MgO monolayer coverage.

Catalyst	Ni/Al [a]	Mg (%)	g MgO/100 m^2 NiAl	Monolayers
NiAl	0.49	n/a	n/a	n/a
3Mg/NiAl	0.46	2.8	0.05	0.65
5Mg/NiAl	0.47	4.6	0.08	1.08
10Mg/NiAl	0.47	9.5	0.18	2.35

[a] bulk mole ratio (ICP)

Note that 10Mg/NiAl dispersion exceeds by far the monolayer coverage, indicating extra Mg content, whereas catalysts with lower Mg contents are closer to the monolayer coverage.

6.2.1.1 *Textural properties of Mg-modified samples*

The textural properties were studied by means of N_2 physisorption, and the obtained isotherms and pore size distributions, are shown in Figure 6.2. Mg-promoted solids, like parent NiAl catalyst, display isotherms type IV according to IUPAC classification, ascribed to monolayer-multilayer adsorption followed by pore condensation in mesopores. The H1 hysteresis loop, suggests pores of wider diameter than 4 nm [107]. XMg/NiAl solids, both in calcined and reduced form, present a pore size distribution with unimodal characteristics, with a narrow range of pore width (Figure 6.2 (b)), similar to NiAl. Slight differences are found between XMg/NiAl and NiAl. On the one hand, the hysteresis loop of NiAl closes at higher P/P_0 and on the other hand, Mg-modified solids show higher average pore width than that of NiAl, indicating Mg location in the tiniest pores.

The textural properties are given in Table 6.2, for calcined and reduced XMg/NiAl solids. In their calcined form, Mg addition decreases monotonically both the specific surface area and the pore volume, with respect to NiAl counterpart. Therefore, 10Mg/NiAl shows the sharpest decrease in S_{BET} by 40%. Such a monotonic decrease in S_{BET} and Vp with the increased of Mg loading suggests that Mg is partially blocking the pores of the Ni/Al, also related to the inherent low S_{BET} of MgO. Besides, upon Mg

addition, the average pore size increases indicating MgO is deposited into the smaller pores.

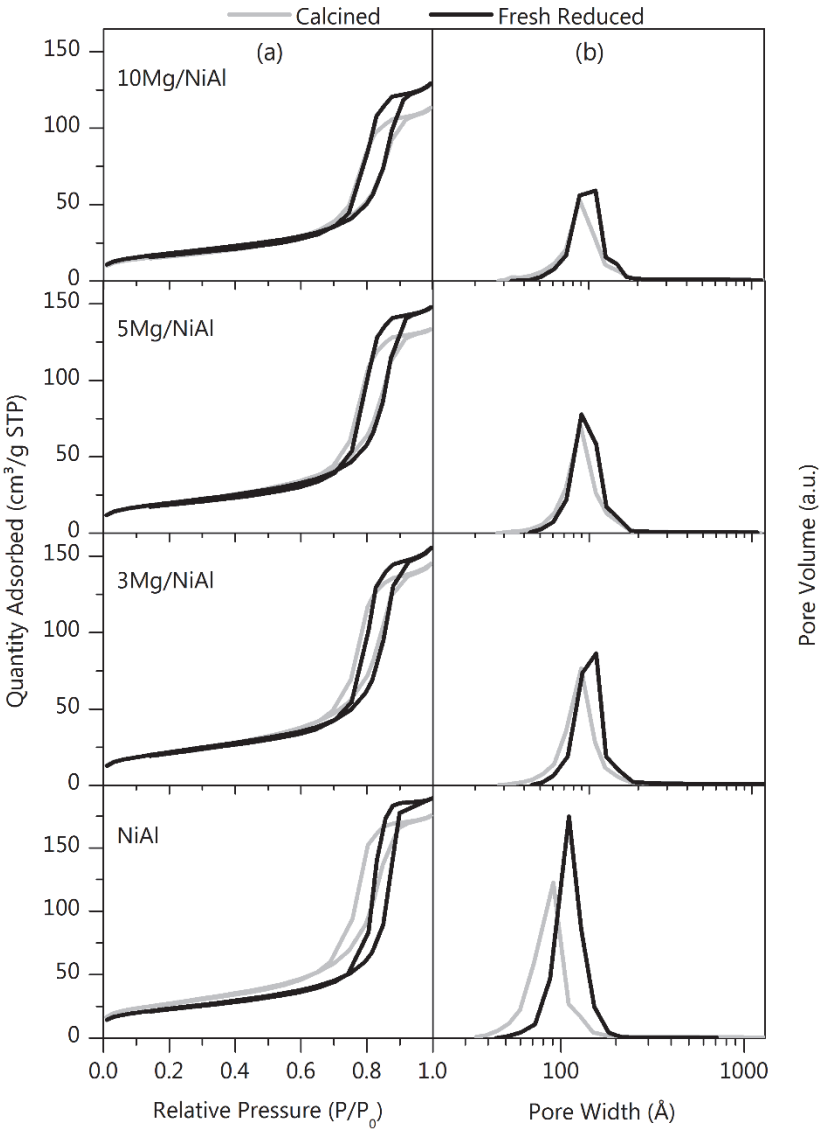

Figure 6.2. (a) N_2 isotherms; and (b) pore size distributions for calcined and fresh reduced Mg-modified solids.

Table 6.2. Textural properties for Mg-modified solids.

	Sample	S_{BET} ($m^2 \cdot g^{-1}$)	Vp ($cm^3 \cdot g^{-1}$)	Dp (nm)
CALCINED	NiAl	98.0	0.27	8.3
	3Mg/NiAl	78.8	0.23	8.7
	5Mg/NiAl	69.5	0.21	8.7
	10Mg/NiAl	59.2	0.18	8.7
	MgO	3.4	0.01	48.5
FRESH REDUCED	NiAl	83.1	0.29	10.8
	3Mg/NiAl	78.6	0.24	10.1
	5Mg/NiAl	70.9	0.23	9.6
	10Mg/NiAl	65.1	0.20	9.8

The same S_{BET} tendency is held among reduced samples, decreasing as follows: NiAl> 3Mg/NiAl> 5Mg/NiAl> 10Mg/NiAl. Interestingly, reduced Mg-modified solids keep, or even increase, their S_{BET} with respect to those in the calcined form. The increase in S_{BET} correlate with Mg loading (~0%, 2% and 10% increase for 3%, 5% and 10% Mg, respectively). These results indicate that Mg acts as a promoter of surface area upon reduction treatment, especially at 5% loadings, or above. Similar findings are reported by others [201]. Finally, the total pore volume is vaguely modified upon reduction while the average pore size slightly increases.

6.2.1.2 *Phases and morphology of Mg-modified samples*

XRD spectra of the calcined and fresh reduced solids are displayed in Figure 6.3. In their calcined form, all samples present diffraction peaks at 37º, 45º and 66º 2θ corresponding to cubic $NiAl_2O_4$ (JCPDS 01-079-1558). In the XRD diffractograms of Mg-modified samples peaks emerge at 37º, 43º and 63º 2θ which can be assigned to MgO (JCPDS 00-045-0946). Taking into account that 3%Mg loading is less than monolayer, the appearance of this peak must be related to the high calcination temperature employed. The contribution of NiO-MgO solid solution ($MgNiO_2$) to this diffraction peak cannot be discarded, as the high calcination temperature used (850 ºC) could promote its formation [202]. Since MgO and $MgNiO_2$ (JCPDS 00-024-0712) crystallize in the same crystal structure and space group, distinguishing between both phases is difficult [203]. The crystal size for that phase increases monotonically with Mg loading, from 3.5 nm to 10.4 nm, for increasing Mg loading (Table 6.3).

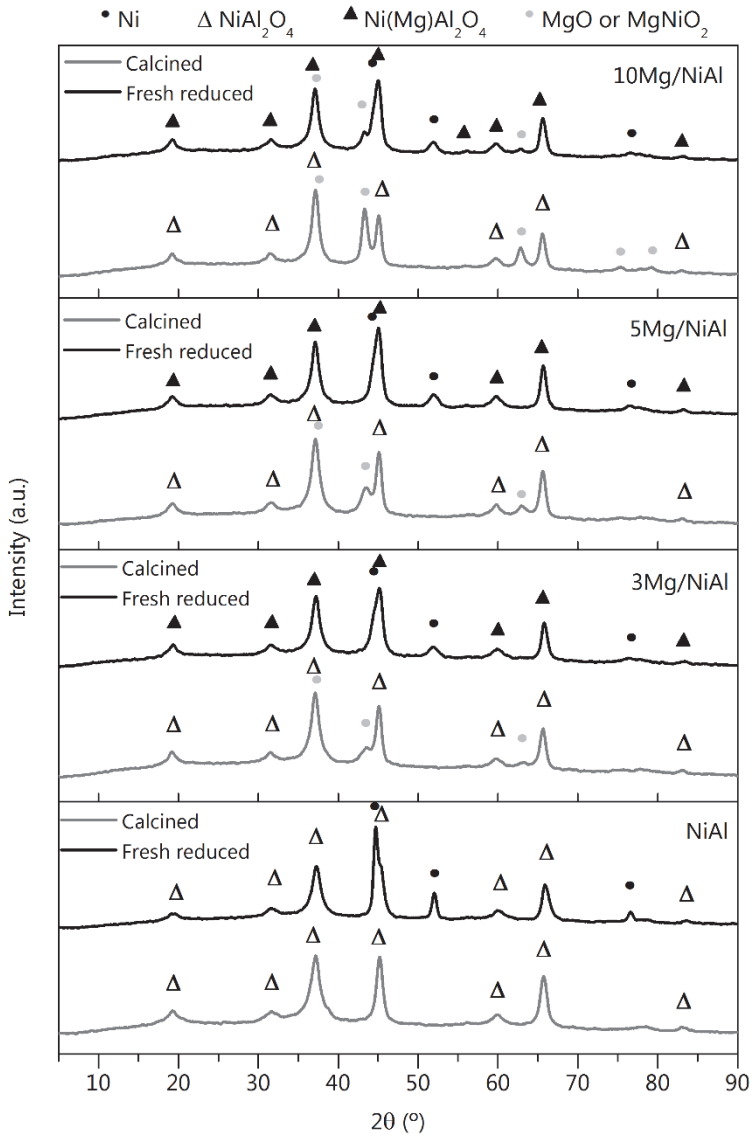

Figure 6.3. XRD patterns of calcined and fresh reduced Mg-modified solids.

After reduction, peaks related to metallic nickel are visible at 45º, 52º and 77º 2θ positions (JCPDS 01-078-0712) for all samples. Among the Mg-modified fresh reduced solids, only 10Mg/NiAl assay presents diffraction peaks corresponding to MgO/$MgNiO_2$. Nevertheless, those signals are not detected for 5Mg/NiAl or 3Mg/NiAl, in spite of the difficult reducibility of that phase [204]. These results indicate that this phase has very small crystal size and high dispersion, in agreement with the lower than monolayer coverage estimations for 3Mg/NiAl, and near monolayer for 5Mg/NiAl (Table 6.1).

The diffraction peaks of the remaining spinel phase from Mg-modified solids, downshift in 2θ (with respect NiAl) upon reduction, as shown in Figure 6.4. This effect can be ascribed to structural changes of the spinel phase, likely to the formation of the $MgAl_2O_4$ spinel. The formation of such a new phase is due to the diffusion of non-reducible Mg^{2+} ions (ionic radius 0.72 Å) towards sites in the spinel, originally occupied by Ni^{2+} ions (ionic radius 0.69 Å). As discussed in Chapter 4, upon reduction nickel exudates from the spinel lattice. The substitution of Ni^{2+} ions by Mg^{2+} ions in the spinel structure results in an increase of the lattice parameter of the spinel. Besides, the intimate contact between surface Mg and the alumina-rich phase resultant from reduction, could enhance the formation of $MgAl_2O_4$. According to literature, low Mg/Al molar ratio and high temperature promote $MgAl_2O_4$ formation [34].

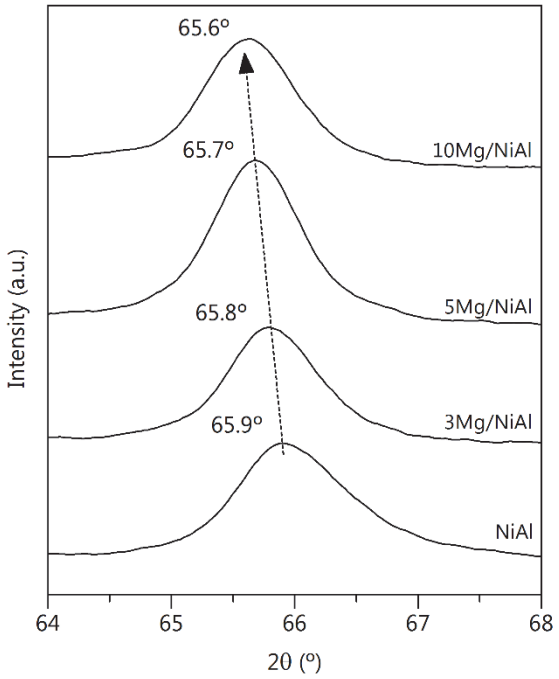

Figure 6.4. Diffractogram extract of the spinel peak at 64 – 68º 2θ region, for fresh reduced samples.

In order to confirm the formation of $MgAl_2O_4$ in the reduction stage, additional experiments were conducted over 10Mg/NiAl solid, by reducing at 1000 ºC for 60 min using a heating rate of 5 ºC/min, in 5% H_2/Ar flow. Insight into the phase evolution is obtained by XRD, as depicted in Figure 6.5. The XRD pattern of that solid downshifts in

the diffraction angle in comparison with the parent $NiAl_2O_4$ as detailed in the inserted graph. Therefore, the presence of a solid solution of Ni-Mg aluminate spinel ($Ni(Mg)Al_2O_4$) in fresh reduced samples has been confirmed.

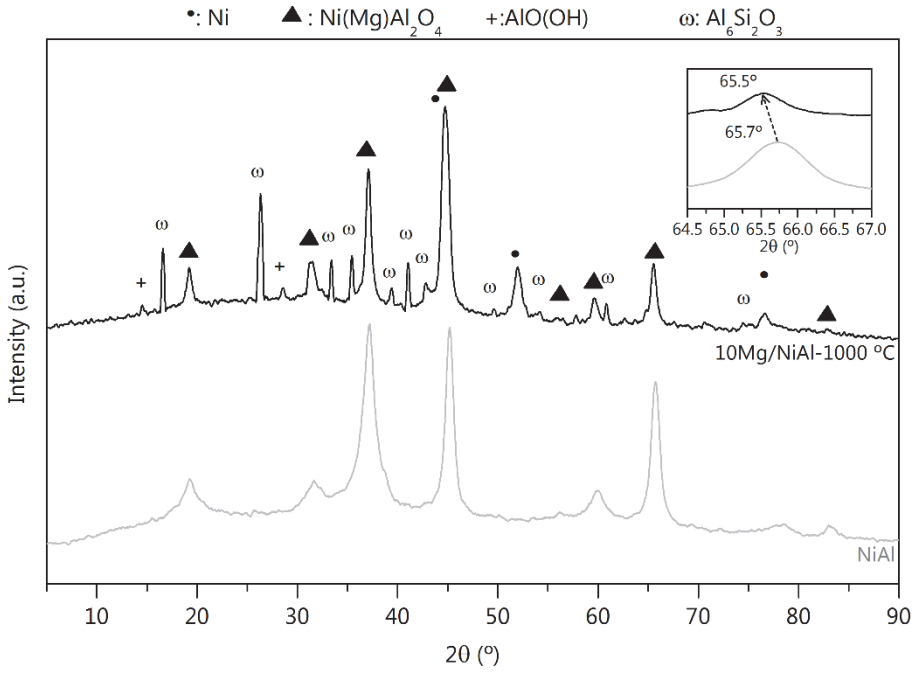

Figure 6.5. XRD analysis of 10Mg/NiAl solid after reduction at 1000 ºC.

The crystal size of the metallic nickel was calculated using Scherrer equation from the XRD peak broadening. Results for the fresh reduced samples are displayed in Table 6.3. According to the obtained results, Mg hinders the coalescence of metallic nickel upon reduction, achieving Ni^0 entities of smaller size, especially at low Mg content. A similar effect is also reported by Zhan et al. [203] for Ni-Mg-Al catalysts. The promotional effect of Mg weakens for higher Mg contents. For instance, Ni^0 cluster size decreases (with respect to the parent NiAl solid) by 58% for 3Mg/NiAl, and only 29% for 10Mg/NiAl solid.

6.2.1.3 *Reducibility and nickel speciation of Mg-modified samples*

Reducibility analysis of the Mg-modified nickel aluminate solids was carried out by H_2-TPR. The obtained reduction profiles of calcined samples are depicted in Figure 6.6,

while the total H_2 consumption and the deduced nickel speciation, are summarized in Table 6.3.

Similar to parent NiAl, reduction profiles of calcined Mg-modified samples show a large and intense reduction event, starting at ~225 ºC. The left tail indicated again the existence of different nickel species, those are ascribed to temperature range at low (<480 ºC), medium (500-620 ºC; 620-770 ºC) and high (>770 ºC), associated to the nickel species namely α, β and γ, as aforementioned (Chapter 4). Moreover, contributions of two peaks are found for the medium temperature reduction zone: β_1, owning to Ni^{2+} interacting with the surroundings (500-620 ºC); and β_2, associated to nickel defective spinel (620-770 ºC).

Bare MgO does not show reduction peaks in the evaluated temperature range. From Figure 6.6, one can notice an upshift in temperature of the non-resolved γ peak, for 10Mg/NiAl and 5Mg/NiAl assays, with respect to parent NiAl. This suggests the presence of the $MgO/MgNiO_2$, as observed in the XRD diffractograms.

Deconvolution of the peaks allows the study of the nickel speciation, and the obtained results are shown in Table 6.3. For 3Mg/NiAl and 5Mg/NiAl samples, free NiO (α peak) accounted for less than 7%, while NiO interacting with the surroundings (β_1 peak) for ~20% of the total Ni, being higher than that in parent NiAl solid. The contribution of β_2 species slightly increases with the Mg content, while that of the γ species decreases. The complete reduction of 10Mg/NiAl solid is impeded, as can be noticed from the non resolved γ peak in the TPR_{950} profile. It can be ascribed to the close interactions MgO-NiO [203], and to the less reducible $MgAl_2O_4$ phase, formed during the reduction, as confirmed by XRD.

Prior to the APR runs, the solids are reduced at 700 ºC, for 1 h. In order to measure the fraction of reduced nickel (f_{red}), i.e., the amount of metallic Ni out of the spinel lattice, the so-called $TPR_{700\text{-}950}$ procedure were used, as described in the experimental section. The obtained $TPR_{700\text{-}950}$ profiles of fresh reduced samples are also shown in Figure 6.6.

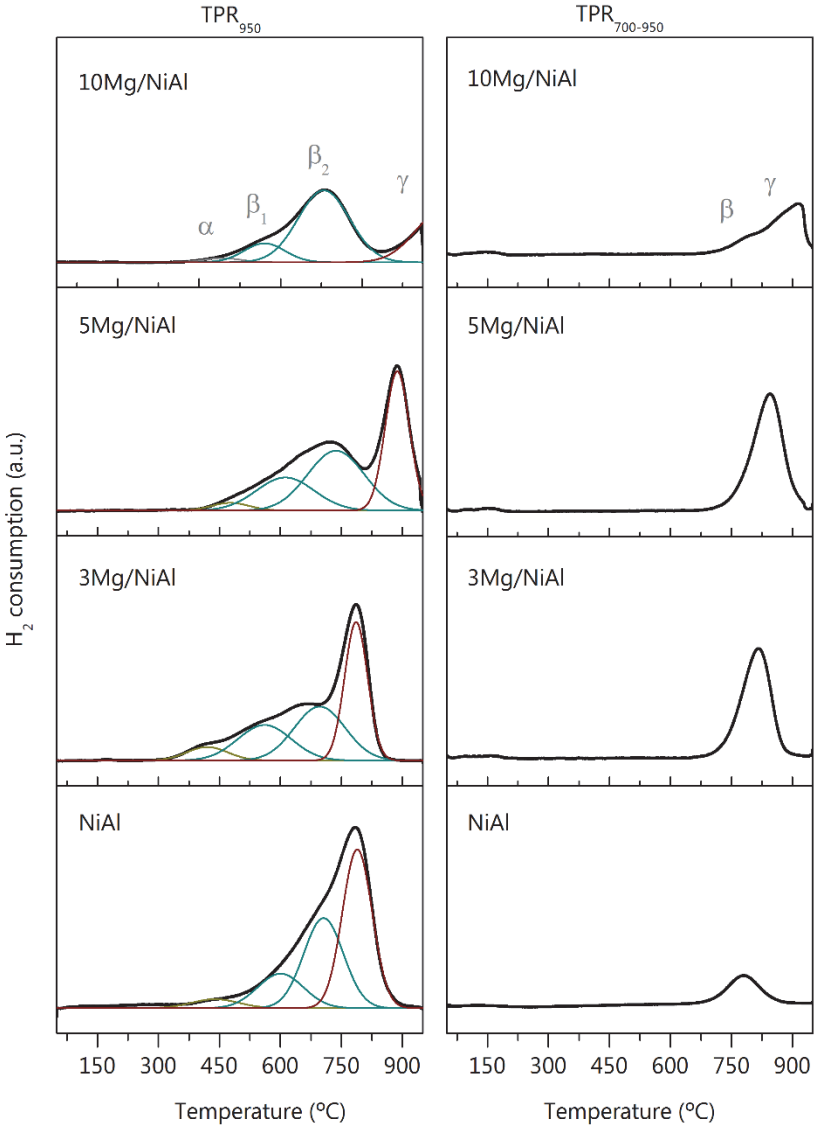

Figure 6.6. H_2-TPR profiles of Mg-modified solids. TPR_{950}: profiles of calcined samples; and $TPR_{700-950}$: profiles of fresh reduced catalysts.

Table 6.3. H_2-TPR results for Mg-modified solids and crystallites size.

Sample	Calcined						Fresh reduced		
	$d_{MgO/MgNiO2}$[a] (nm)	H_2-TPR_{950} consumption (mmol $H_2 \cdot g^{-1}$)	Nickel speciation				d_{Ni^0}[a] (nm)	H_2-$TPR_{700-950}$ consumption (mmol $H_2 \cdot g^{-1}$)	f_{red} (%)
			α (%)	β_1 (%)	β_2 (%)	γ (%)			
NiAl	n/a	5.57	4.1	15.4	34.7	45.9	16.0	0.56	79
3Mg/NiAl	3.5	4.75	6.6	22.6	32.8	38.0	6.7	1.79	64
5Mg/NiAl	5.4	4.94	3.3	21.5	38.1	37.2	7.5	2.05	60
10Mg/NiAl	10.4	3.60	2.2	11.4	54.7	31.8	11.4	1.77	72

[a] from XRD line broadening

The $TPR_{700-950}$ reduction profiles are characterized by the absence of low temperature peaks, and the presence of a peak at above 700 ºC (γ peak). The upshift in γ-peak temperature with the increase of Mg content suggests the hardening of reduction of Ni species by the interaction with MgO. The insignificant hydrogen consumption, below 700 ºC in the $TPR_{700-950}$ run, indicates that γ and β nickel phases are readily reduced in all catalysts (except in 10Mg/NiAl), by the established pre-reaction reduction treatment. Large amount of the nickel from the non-stoichiometric phase has been reduced. However, that found in the spinel phase remains unreduced. For 10Mg/NiAl sample the γ peak is accompanied by a shoulder at 785 ºC, associated to the reduction of β_2 species. In the literature it is also reported that the strong Mg-Ni interaction hinders the reducibility of nickel in $Ni(Mg)Al_2O_4$ spinels [205].

In $TPR_{700-950}$ analysis of fresh reduced samples, higher H_2 uptakes are found for Mg-modified samples, compared to that of NiAl. Mg-modified samples present f_{red} values of 9%, 24% and 20% lower than that of NiAl, for 10Mg/NiAl, 5Mg/NiAl and 3Mg/NiAl, respectively (Table 6.3). This could be associated not only to the aforementioned formation of Mg-Ni solid composites, but also to the strengthening of the Ni-O bond in the close vicinity of Mg^{2+} cations [202].

6.2.1.4 *Surface acid-base properties of Mg-modified samples*

The acid and base characteristics were evaluated by NH_3-pulse chemisorption and CO_2-TPD, respectively. An increase in the basic sites density of the catalyst could lead to an improvement in the APR selectivity, as it promotes the chemical pathway to Route A towards glycerol dehydrogenation. Besides, limitation of the acid sites density of the catalyst prevents Route B, with the corresponding limitation of hydrogenation side reactions. The results obtained are shown in Table 6.4 for fresh reduced catalysts.

The total acid sites density increases with Mg addition. Samples 3Mg/NiAl and 5Mg/NiAl present 25% and 30% higher acid sites population than NiAl, respectively. Nevertheless, higher content of Mg tends to diminish it, reaching the lowest value for 10Mg/NiAl, which is 0.88 times that for 3Mg/NiAl. The replacement of Ni^{2+} by Mg^{2+} ion in the 10%Mg loaded sample could be the reason [202].

Regarding the basic sites density, it increases with the addition of Mg (Table 6.4). A 5% loading of Mg significantly increases the total basic density (1.6 times the density of 3Mg/NiAl). However, further increase in Mg content to 10%, leads to a decay in the basic sites density. This could be due to the worsening in MgO dispersion for the highest Mg content.

Note from Table 6.4 that 3Mg/NiAl presents the highest acid/base ratio among Mg-modified solids, nevertheless, the ratio decays for higher Mg loadings. The lowest acid/base ratio is that of 5Mg/NiAl catalysts, being 50% lower than that of the parent NiAl sample.

Table 6.4. Acid-base properties for fresh reduced Mg-modified solids

Sample	Acid/ base ratio	Acidity	Basicity	Basic Strength (%)			
		μmol $NH_3 \cdot m^{-2}$	μmol $CO_2 \cdot m^{-2}$	Weak	Medium (Mg-O)	Medium (Ni-O)	Strong
NiAl	1.8	2.0	1.1	29.2	n/a	56.3	13.3
3Mg/NiAl	1.6	2.5	1.6	26.6	14.3	35.3	19.3
5Mg/NiAl	1.0	2.6	2.6	20.8	18.6	41.0	19.2
10Mg/NiAl	1.4	2.2	1.6	5.7	40.1	45.2	7.7

The distribution of the basic sites strength was obtained by Gaussian deconvolution of the CO_2-TPD profiles. The contribution of each strength sites is given in Table 6.4. Related peaks of low, medium, and strong basic strength are depicted in Figure 6.7. Desorption peaks can be indexed at three different temperature intervals. Weak basic sites at lower temperatures than 110 ºC. Medium strength basic sites located at 130-200 ºC, in this temperature range two kind of bidentate carbonates species are seen: (i) bidentate carbonates adsorbed on Mg-O pairs (MB_{Mg-O})(<155 ºC). (ii) bidentate carbonates on Ni-O pairs (MB_{Ni-O}) found at 160-200 ºC. A third peak, reaching a maximum desorption in the 240-320 ºC interval, is associated to the strong basic sites [104]. Finally, the very small desorption peak above 800 ºC is associated to the carbonates, formed in the calcination step, and to dehydroxylation processes [154].

Some relevant features can be observed. First, the addition of Mg decreases the contribution of weak base sites, and the higher the Mg content, the higher the decrease.

Second, the addition of Mg leads to new medium-strength basic sites, related to Mg-O pairs, which are more evident for higher Mg loadings (see orange peak in Figure 6.7). Nonetheless, the contribution of medium strength sites remains almost invariable, except for 10Mg/NiAl, which boosted to 85.3%, in detriment of the strong sites contribution. Finally, higher contribution of strong basic sites are found for 3Mg/NiAl and 5Mg/NiAl, with respect to NiAl.

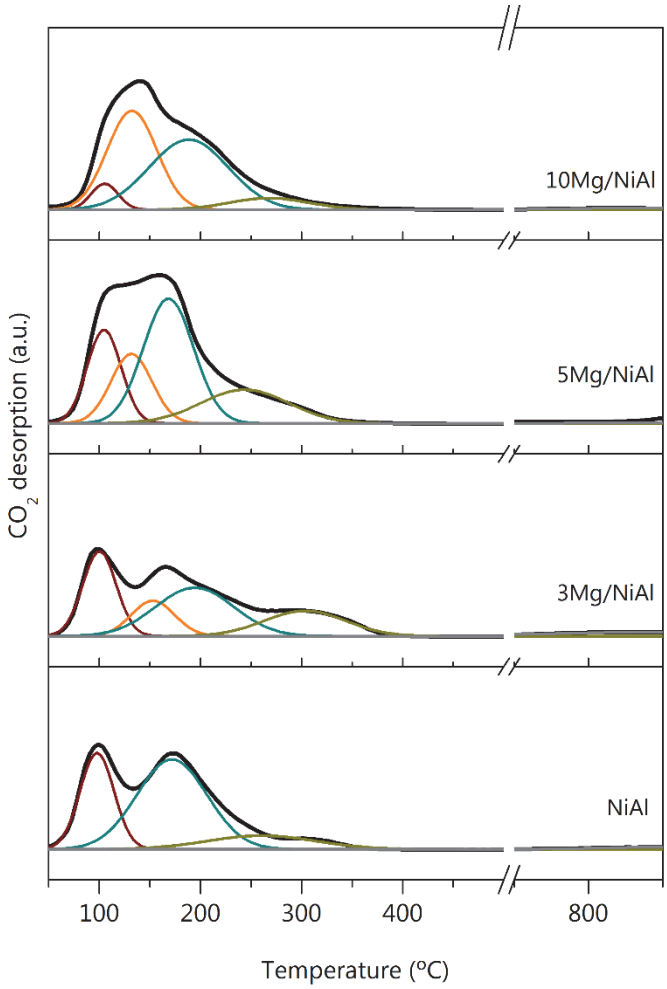

Figure 6.7. CO_2 desorption profiles of Mg-modified solids and their Gaussian deconvolution. Colour code: red (weak basic sites); orange (intermediate strength basic sites by MB_{Mg-O}); blue (intermediate strength basic sites by MB_{Ni-O}); green (strong basic sites).

A priori, Mg-modified catalysts present good structural, morphological, and surface characteristics. For them, remarkably very small metallic nickel clusters are observed, with low acid/base ratio, properties that could be beneficial for H_2 production by glycerol APR. Nonetheless, availability of metallic nickel is restricted.

6.2.2 Glycerol APR with Mg-modified catalysts

In the previous section, it has been shown that the Mg improves the physicochemical characteristics of the nickel aluminate spinel. Thus, XMg/NiAl catalysts have been tested in the glycerol APR, to determine if a performance enhancement towards H_2 production is also accomplished (with respect to NiAl). The APR test was carried out in a continuous fixed-bed up-flow reactor, at 235 ºC/35 bar, testing 0.5 g of XMg/NiAl catalyst, and feeding 0.2 mL·min^{-1} of 10 wt.% glycerol solution (WHSV= 24.5 h^{-1}). Before the APR, catalysts were subjected to reduction (700 ºC, 1 h). Results for gas and liquid products are reported at 2 h steady state, and the obtained conversions (X_{Gly} and X_{Gas}), and the YH_2 are shown in Figure 6.8.

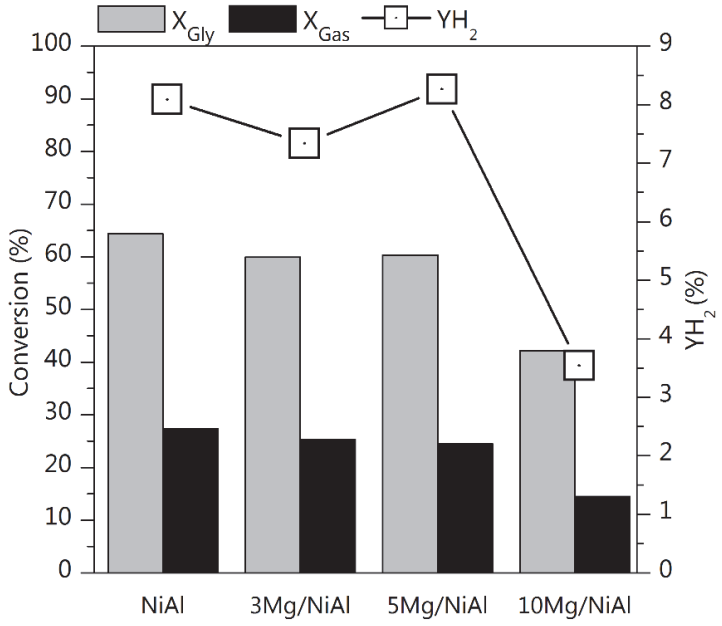

Figure 6.8. Glycerol conversion, conversion to gas and H_2 yield of Mg-modified samples. Reaction conditions: 235 ºC/35 bar, WHSV= 24.5 h^{-1}. Reaction time: 2 h.

3Mg/NiAl and 5Mg/NiAl catalysts present conversion values near to those presented by NiAl counterpart (X_{Gly}= 64%; X_{Gas}= 27%), showing null improvement of the catalytic behaviour. In this line, a marked detrimental effect on the APR performance is observed for 10Mg/NiAl assay, which only achieves 42% of X_{Gly} and 14% of X_{Gas}. Among Mg-modified catalysts, 5Mg/NiAl catalyst presents a slightly better hydrogen yield, though it is still similar than that of the parent NiAl (8.3% vs 8.1%).

The distribution of the gaseous products displayed in Figure 6.9 reveals that for XMg/NiAl catalysts the main products of the gas stream are those of reforming and methanation reactions.

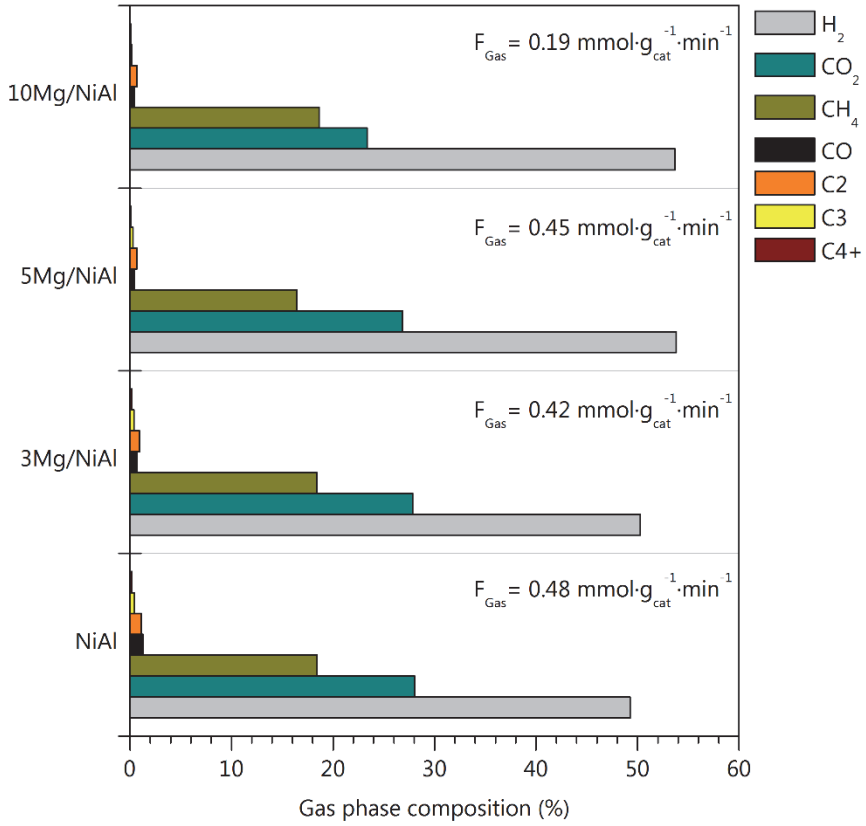

Figure 6.9. Gas-phase composition of Mg-modified products stream (dry basis). Reaction conditions: 235 ºC/35 bar, WHSV= 24.5 h^{-1}. Reaction time: 2 h.

On the one hand, XMg/NiAl produces gas streams with more than 50% H_2, in volume. The following most abundant gas compound is CO_2, its composition accounting for

more than 20%, but always lower than that by NiAl (28%). Interestingly, all the Mg-modified catalysts produced slightly lower H_2/CO_2 ratio than NiAl, which anticipates that less hydrogen is consum in side reactions with those catalysts. CH_4 concentration in the gas phase is almost the same for all catalysts, including NiAl (~18%). Mg-modified catalysts and NiAl counterpart show rather low CO concentration, <0.7% and 1.2% respectively. Other gas compounds are detected in the gas phase like ethane (C2), propane and propylene (C3), iso-butane, butane, and others not identified (compiled as C4+), all of them in remarkably low concentration (C2< 1%, C3< 0.4% and C4< 0.2%). Only 5Mg/NiAl catalyst approaches to the H_2 production rate of NiAl (23.9 vs 23.5 mmol $H_2 \cdot g^{-1} \cdot min^{-1}$).

Although 5Mg/NiAl presents slightly lower X_{Gly} and X_{Gas} than those of NiAl counterpart, it shows slightly higher hydrogen yield (YH_2= 8.3%) and selectivity to H_2 (SH_2= 41%) (Figure 6.10).

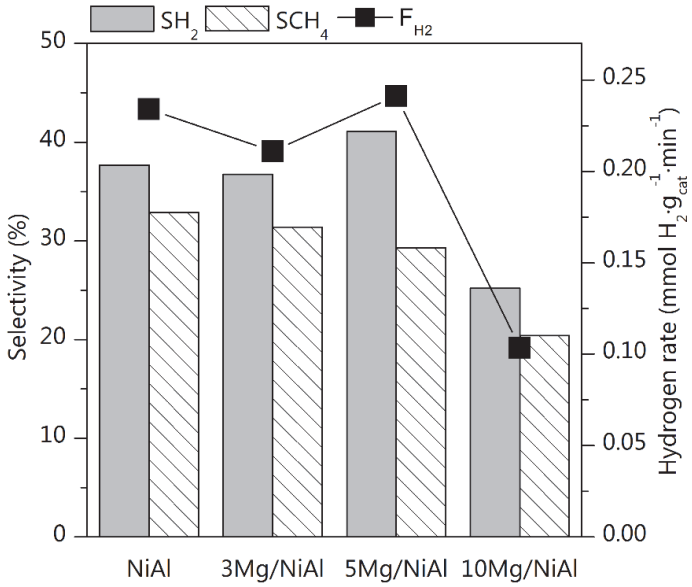

Figure 6.10. Selectivity to H_2 and to CH_4, and hydrogen production rate of Mg-modified catalysts. Reaction conditions: 235 ºC/35 bar, WHSV= 24.5 h^{-1}. Reaction time: 2 h.

Contrarily, the remarkably low H_2 production rate (F_{H2}) for 10Mg/NiAl (0.1 mmol $H_2 \cdot g^{-1} \cdot min^{-1}$) can be associated to the bigger Ni^0 clusters and to the worsened

reducibility of this catalyst. Interestingly, lower CH_4 selectivity is featured with the increase in Mg content, in agreement with the higher H_2/CO_2 ratios.

The obtained X_{Gas} (below X_{Gly}) denotes that a fraction of the reacted glycerol is converted into liquid compounds. All XMg/NiAl catalysts presented similar distribution of the liquid products. Thus, representative results are depicted in Figure 6.11 comparing the liquid-phase compounds of 5Mg/NiAl with those of NiAl. It is observed that the liquid products flow, measured in terms of carbon molar flow in the liquid stream ($F_{C\text{-}Liq}$), is almost equal (≈ 0.4 $mmol_c \cdot min^{-1} \cdot g_{cat}^{-1}$), regardless the catalyst.

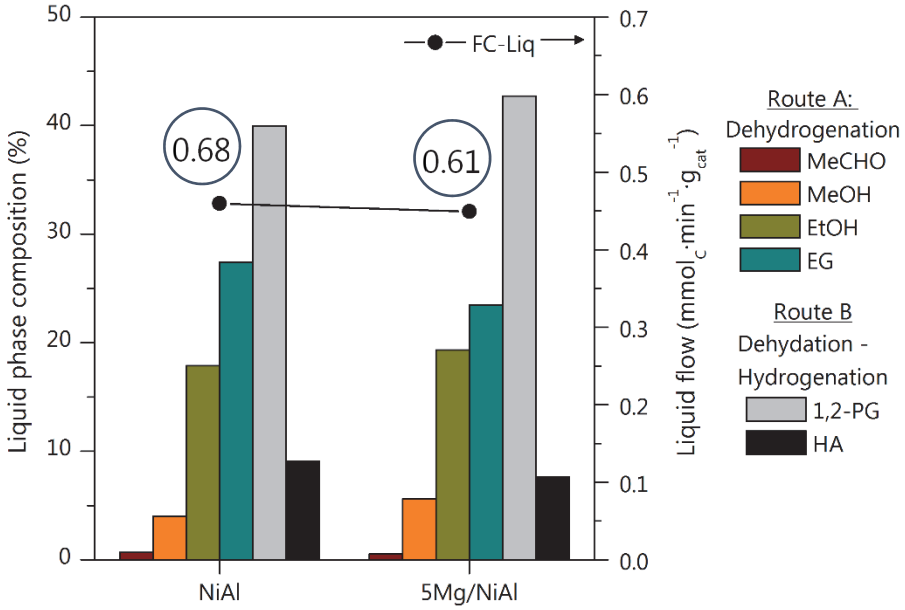

Figure 6.11. Molar composition of the main liquid products and total produced liquid flow for Mg-modified catalysts. In circles: Route A/Route B products ratio. Reaction conditions: 235 ºC/35 bar, WHSV= 24.5 h^{-1}. Reaction time: 2 h.

The main liquid compounds for both catalysts are, in decreasing order 1, 2-PG> EG> EtOH, with molar composition of 43%, 24% and 19% respectively, for 5Mg/NiAl catalyst. Very similar compositions are observed for parent NiAl. This is also reflected by the similar Route A/Route B products ratio from both catalysts. Other liquid compounds detected, in composition decreasing order, are: HA> MeOH> MeCHO.

NiAl and 5Mg/NiAl catalysts present 40% and 43% of 1, 2-PG, respectively, in the liquid stream. Lower content of HA is also seen (< 10%). 5Mg/NiAl shows rather low

concentration of 1-propanol and acetone, other compounds related to dehydration route. However, no propionaldehyde, nor 2-propanol are evidenced.

As indicated by the reaction pathway afore proposed in Chapter 5 (Figure 5.5), the primary product of glycerol dehydration (Route B) is HA, which can be forward hydrogenated to 1, 2-PG. Interestingly, 1, 2-PG is the main liquid compound produced, which is a well-known commodity chemical.

Dehydrogenation of glycerol is the chemical pathway of interest for H_2 production by the APR of oxygenated compounds. With Mg-modified catalyst, most of the liquid products entailed in the proposed reaction pathway are detected, as can be seen in Figure 6.11. EtOH accounts for 19% in the liquid composition by both catalysts. In the same line, MeOH shows low concentrations (5Mg/NiAl: 5.6%; NiAl: 4%). MeCHO production is even lower for Mg-modified and the parent NiAl catalysts (<0.7%). This could indicate that the decarbonylation of MeCHO can contribute to the high methane concentrations obtained, as also reported by others [121].

6.3 Ce-MODIFIED NiAl SPINEL

Ceria was impregnated on NiAl support at three nominal loadings, namely 3%, 5% and 10% (by Ce wt.%), and then calcined at 600 ºC. For the glycerol APR test, each catalyst was in-situ reduced at 700 ºC. In the following sections, the main physicochemical properties and the APR performance indices will be discussed.

6.3.1 Characterization of Ce-modified solids

The ICP-MS analysis confirms that the actual composition of XCe/NiAl are close to nominal (Table 6.5). Besides, Ni/Al ratio remains at the value for NiAl, within the experimental error.

Similar than for XMg/NiAl solids, the nominal monolayer for XCe/NiAl was estimated from bulk compositions, and results are presented in Table 6.5. For these calculations, the monolayer dispersion capacity of CeO_2 on NiAl was assumed to be 0.03 $gCeO_2/100\ m^2$ NiAl [206] Note that the Ce loading in all XCe/NiAl solids surpasses the monolayer capacity.

Table 6.5. Chemical composition XCe/NiAl modified spinels and CeO_2 monolayer coverage.

Catalyst	Ni/Al molar ratio	Ce (%)	g CeO_2/100 m^2 NiAl	Monolayers
NiAl	0.49	n/a	n/a	n/a
3Ce/NiAl	0.50	3.2	0.04	1.4
5Ce/NiAl	0.47	5.5	0.07	2.5
10Ce/NiAl	0.46	9.6	0.14	4.5

6.3.1.1 *Textural properties of Ce-modified samples*

Similar to XMg/NiAl, XCe/NiAl solids, both in calcined and fresh reduced forms, display isotherms type IV, with hysteresis loops (Type H1), pointing to a mesoporous nature, like the parent NiAl catalysts (Figure 6.12). In addition, unimodal pore size distribution is found for all the solids, which remains almost invariable after the reduction treatment at 700 ºC. Slightly lower pore widths are presented for Ce-modified samples, as compared to NiAl.

The textural properties are shown in Table 6.6. Ce addition does not affect, to a great extent, the specific surface area of the parent NiAl catlaysts.

Table 6.6. N_2 physisorption analysis results for Ce-modified solids.

	Catalyst	S_{BET} ($m^2 \cdot g^{-1}$)	Vp ($cm^3 \cdot g^{-1}$)	Dp (nm)
CALCINED	NiAl	98.0	0.27	8.4
	3Ce/NiAl	95.4	0.26	8.7
	5Ce/NiAl	91.8	0.24	8.4
	10Ce/NiAl	87.3	0.22	8.0
	CeO_2	49.3	0.18	11.5
FRESH REDUCED	NiAl	83.1	0.29	10.8
	3Ce/NiAl	74.7	0.23	9.8
	5Ce/NiAl	85.3	0.25	9.5
	10Ce/NiAl	77.5	0.22	9.2

In the calcined form, S_{BET} and Vp values slightly decreased monotonically with Ce loading, although to a lesser extent than Mg solids do (maximum decreased: 11% vs 40%), due to the inherently higher S_{BET} of CeO_2 as compared to MgO.

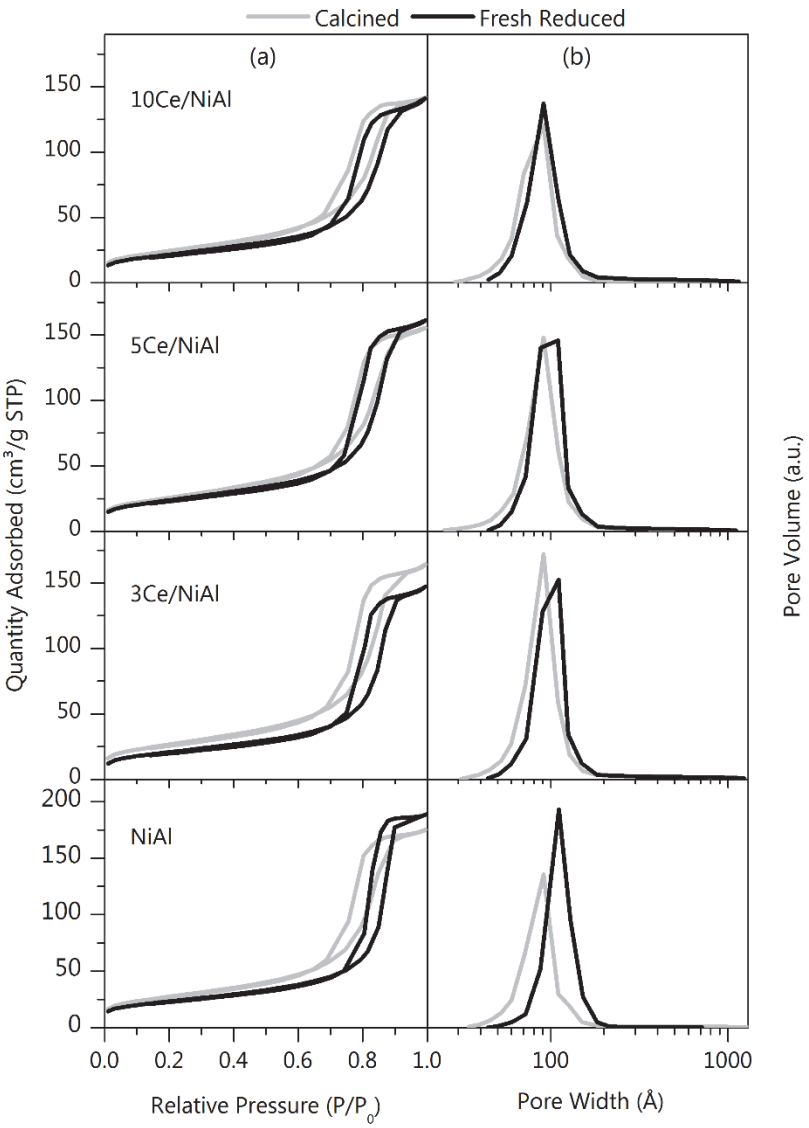

Figure 6.12. (a) N_2 isotherms; and (b) pore size distributions for calcined and fresh reduced Ce-modified solids.

The reduction treatment tends to diminish S_{BET}, being 5Ce/NiAl solid the less affected sample, with 7% decrease, by the reduction treatment. One can notice from Figure 6.12 (b) that a partial filling of NiAl pores is happening, nonetheless S_{BET} of 3Ce/NiAl, 5Ce/NiAl and 10Ce/NiAl are almost unchanged in comparison to NiAl, owing to the formation of porous CeO_2 as responsable for this offset of surface.

6.3.1.2 *Phases and morphology of Ce-modified samples*

The XRD diffractograms from Ce-modified spinels are shown in Figure 6.13. As expected, all the calcined solids display signals from cubic $NiAl_2O_4$.

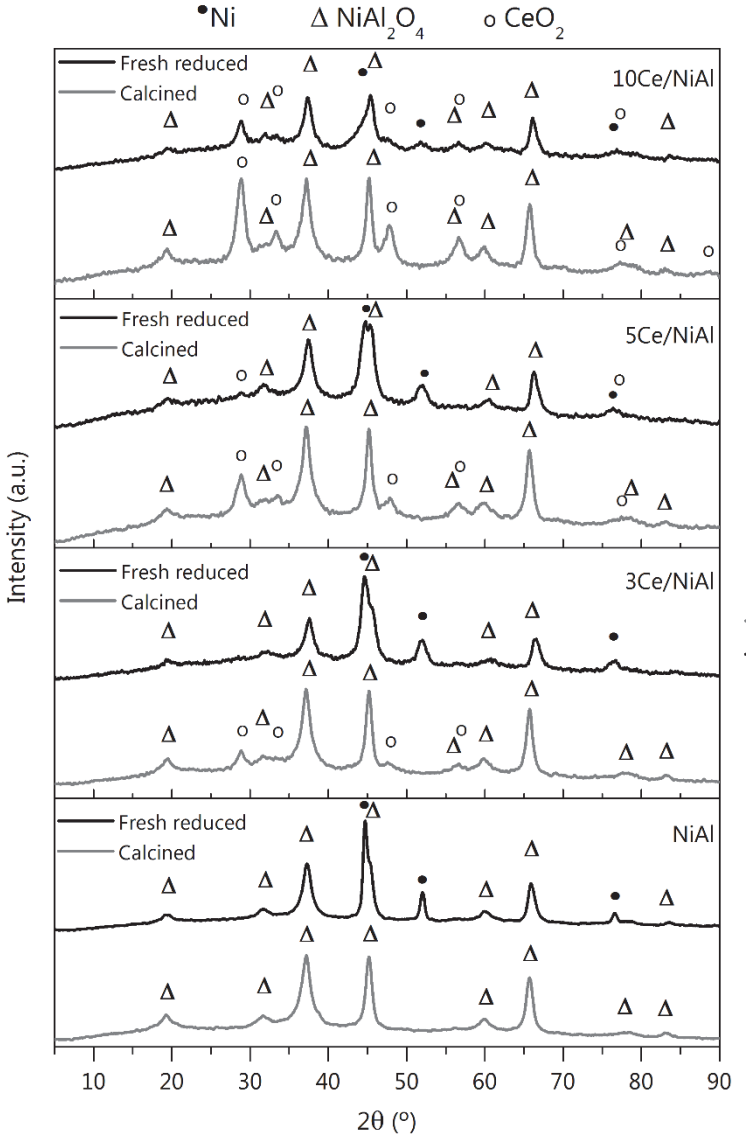

Figure 6.13. XRD patterns for calcined and fresh reduced Ce-modified solids.

Diffraction signals at 28.7º, 33.3º, 47.7º and 56.6º 2θ, from all XCe/NiAl solids, are ascribed to the cubic CeO_2 with fluorite structure (JCPDS 00-034-0394). It can be noticed that CeO_2 signals intensify while increasing Ce loading, in agreement to its

4.5 monolayers. The crystal size of ceria is around 7 nm (Table 6.7). No evidence of other cerium-containing crystalline phases (Ce_2O_3 or $CeAl_2O_3$) are observed.

XRD results also confirms that the reduction treatment (700 ºC, 1 h) results in the formation of metallic Ni (JCPDS 01-087-0712). Concomitantly, signals from $NiAl_2O_4$ weaken. In addition to $NiAl_2O_4$ phase, the presence of γ-Al_2O_3 in the fresh reduced solids is highly probable, nonetheless γ-alumina has a defective spinel structure, thus a slight upshift in 2θ on spinel lines is seen. Diffraction peaks ascribed to the fluorite structure are still visible for 5Ce/NiAl and 10Ce/NiAl fresh reduced solids, while absent for 3Ce/NiAl one. Nonetheless, the XRD intensity of ceria phase peaks weaken as compared to the calcined precursor. This suggests that CeO_2 reduction is limited to the outmost layers, and the bulk remain as Ce^{4+} oxide phase.

The average crystallite size of the metallic nickel is indexed in Table 6.7. Noteworthy Ni^0 crystallite size decrease with Ce addition by around two-fold, as occurred with Mg addition. This evidences the CeO_2 capacity to hinder the coalescence of bigger Ni^0 particles, which makes CeO_2 a structural promoter.

6.3.1.3 *Reducibility and Ni speciation of Ce-modified samples*

The reduction profiles from Ce-modified solids are shown in Figure 6.14. Calcined XCe/NiAl present similar TPR_{950} profiles to that of parent NiAl.

Peaks of H_2 consumption can be indexed within three temperature ranges, similar to those of NiAl catalysts: below 550 ºC, named α peak; β peak, in between 550-750 ºC; and γ peak, above 750 ºC. All solids present low intensity γ peak corresponding to well dispersed and free surface NiO. On the other hand, Ce-containing samples present an additional, small peak, namely α' (around 250 ºC), which can be associated to reduction of Ni-oxide species promoted by the Ce^{3+}/Ce^{4+} pair, enabling the electron transfer to the neighbouring nickel species [154]. Withn the medium temperature range, peaks β_1 and β_2 emerge, the first related to reduction of Ni^{2+} interacting with remnant phases ($NiAl_2O_4/\gamma$-Al_2O_3), and the second, located at a higher temperature, ascribed to reduction of Ni^{2+} species in defective $Ni_{1-x}Al_2O_{4-x}$. Finally, the γ peak is due to bulk $NiAl_2O_4$ reduction. Independent, separated peaks associated to CeO_2 reduction cannot be distinguished, and probably overlapped to β_2-peak [34, 207]. Nevertheless, ceria

contribution to total hydrogen uptake is expected to be very low, in accordance with Iriondo et al. [208].

It is noteworthy that TPR of Ce-modified solids in their calcined form present differences, in temperature positions of the peaks, with respect to parent NiAl sample. On the one hand, the high temperature peak slightly shifts to lower temperatures by 9 ºC and 14 ºC for 3Ce/NiAl and 5Ce/NiAl solids, respectively. Nonetheless, by increasing Ce to 10%, the γ peak upshifts by 35 ºC (up to 824 ºC). This fact indicates that the addition of low amounts of Ce (≤ 5%) promotes the $NiAl_2O_4$ reduction, while higher loading hinders it.

The total H_2 consumption and the contribution of the abovementioned α, β and γ phases in the TPR_{950} profiles, is indexed in Table 6.7.

The contribution of α peaks is higher for XCe/NiAl samples, especially for 5Ce/NiAl, which indicate a promotion in reduction of superficial NiO species. This promotional effect can be associated to the smaller size of nickel in the presence of Ce. In the Ce-containing solids, about 16% of the free Ni^{2+} species are in close contact with ceria, as indicated the $\alpha'/(\alpha'+\alpha)$ ratio. In comparison to NiAl, Ce-modified samples presented a similar contribution of β_1 nickel species, and smaller contribution of β_2 nickel species, as compared to those from NiAl. However, among the Ce-modified samples, contribution of β_2 tends to increase with higher Ce loading (10%), this high proportion of Ce^{+4} reduction is contributing to this peak area, as abovementioned. The γ-peak contribution is higher in 5Ce/NiAl and 3Ce/NiAl solids.

H_2-TPR was also carried out for catalysts reduced at 700 ºC for 1 h ($TPR_{700-950}$). Addition of Ce influences the fraction of nickel reduced (f_{red}), as displayed in Table 6.7. Note that for Ce-modified samples, f_{red} is ascribed not only to the fraction of metallic Ni, but to the Ce_2O_3 obtained. 5Ce/NiAl has the same f_{red} than its NiAl counterpart, while 3Ce/NiAl and 10Ce/NiAl catalysts present lower f_{red}, indicating that 5% of Ce is the optimum loading that prevents a worsening of the reducibility.

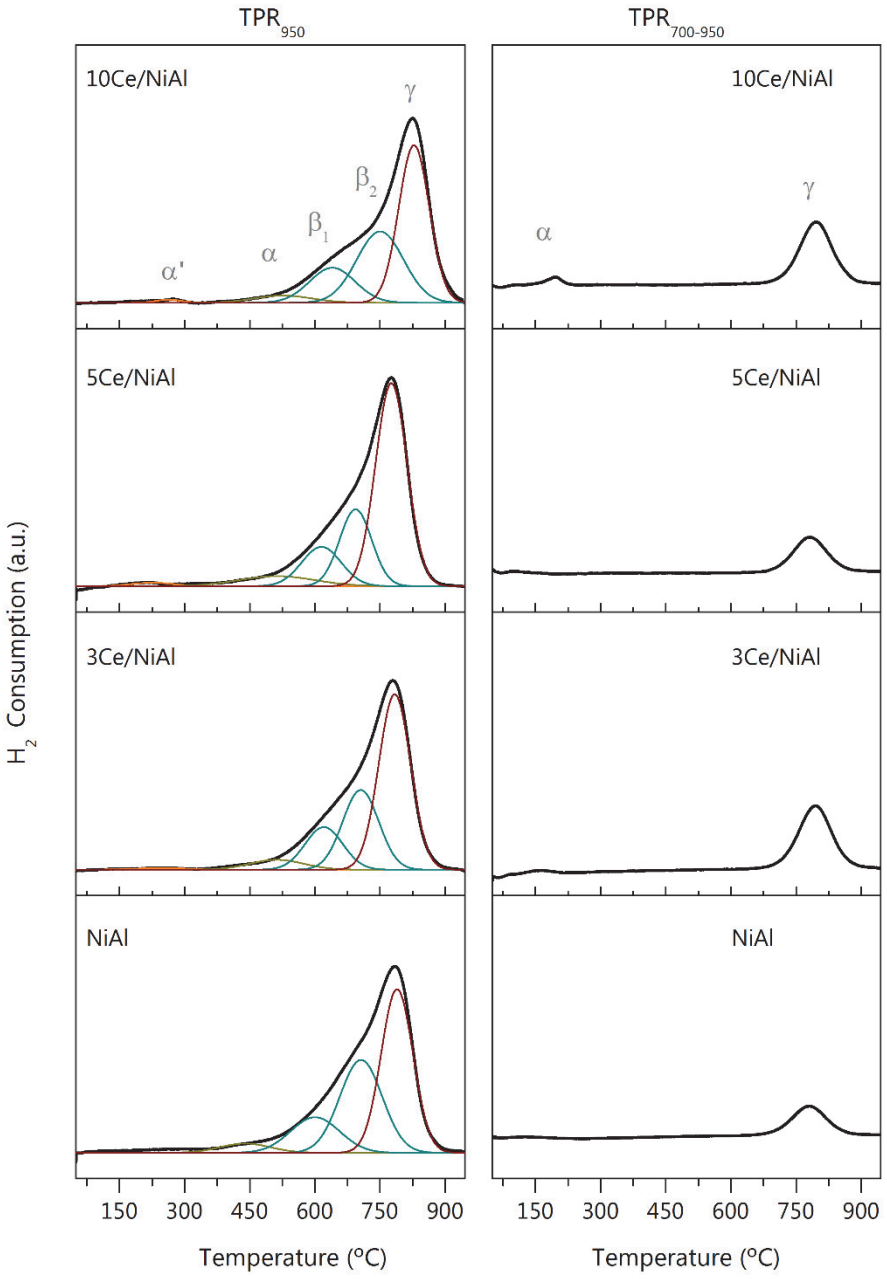

Figure 6.14. H_2-TPR profiles of Ce-modified samples: TPR_{950}: reduction profile of the calcined samples; $TPR_{700-950}$: reduction profile of fresh reduced catalysts.

Table 6.7. H_2-TPR results for Ce-modified solids and crystallites size.

Sample	Calcined							Fresh reduced		
	d_{CeO2}[a] (nm)	H_2-TPR$_{950}$ consumption (mmol $H_2 \cdot g^{-1}$)	Nickel speciation					d_{Ni^o}[a] (nm)	H_2-TPR$_{700-950}$ consumption (mmol $H_2 \cdot g^{-1}$)	f_{red} (%)
			α′ (%)	α (%)	β_1 (%)	β_2 (%)	γ (%)			
NiAl	n/a	5.57	n/a	4.1	15.4	34.7	45.9	16.0	0.56	79
3Ce/NiAl	7.3	6.00	0.9	5.0	15.0	27.0	52.3	5.8	1.12	70
5Ce/NiAl	6.7	5.58	1.3	6.7	13.7	21.8	56.5	7.5	0.65	80
10Ce/NiAl	7.1.	5.27	0.8	4.0	15.6	32.6	47.0	4.7	1.14	70

[a] from XRD line broadening

6.3.1.4 *Surface acid-base properties of Ce-modified samples*

The surface acid and base characteristics are given in Table 6.8. Ce-modified solids show a notable increase in the surface acid sites density. 3Ce/NiAl presents the highest acid density (3.5 μmol $NH_3 \cdot m^{-2}$), which represents an increase of 75% with respect to that of NiAl. Further addition of Ce decreases the acid density to ~2.5 μmol $NH_3 \cdot m^{-2}$, regardless of Ce loading, nevertheless, still higher in comparison with NiAl. Similar findings are reported by others [152].

In addition to NH_3-pulse chemisorption, IR-pyridine analysis was done in order to discriminate between Lewis (LAS) and Brønsted (BAS) acid sites. NiAl and 5Ce/NiAl were chosen as representative solids to study the effect of Ce-modification. The obtained IR spectra are shown in Figure 6.15.

Two peaks are observed for both solids in the IR-Pyr spectra: one band, centred at 1540 cm^{-1}, is related to BAS type; and the other, small band, centred at 1445 cm^{-1}, corresponding to LAS type. The latter band seems even smaller for 5Ce/NiAl. After integration of these absorbance bands, the density of the respective acid sites was calculated, and data is reported in Table 6.8.

The low BAS density can be related to a low number of Ni^{2+} cations present in the fresh reduced samples. In addition, it seems that Ce reinforces neutralization of BAS sites. On the other hand, the BAS/LAS ratio for both solids is very low (0.14 and 0.3, for NiAl and 5Ce/NiAl, respectively). These results indicated the Lewis acid sites are dominant with respect to Brønsted ones, which can be ascribed to the penta-coordinated aluminum generated γ–Al_2O_3 reduction [209, 210]. Thus, the reduction treatment is indeed the determining factor in the density of surface acid sites, and its nature is affected to a lesser degree by Ce addition.

Table 6.8. Acid and base properties for fresh reduced Ce-modified solids.

		Acidity[a]	Density of acid sites[b] (μmol·g^{-1})			Basicity[c]	Basicity Strenght[c] (%)			
Sample	Acid/base ratio	mmol NH_3·m^{-2}	BAS/LAS ratio	BAS	LAS	mmol CO_2·m^{-2}	Weak	Medium (Ce-O)	Medium (Ni-O)	Strong
NiAl	1.7	2.0	0.14	14.2	105.1	1.12	29.2	n/a	56.3	13.1
3Ce/NiAl	1.7	3.5	n.d.	n.d.	n.d.	2.00	22.7	2.2	56.1	18.3
5Ce/NiAl	1.2	2.5	0.03	2.9	83.4	2.03	18.2	21.7	39.4	20.1
10Ce/NiAl	0.9	2.5	n.d.	n.d.	n.d.	2.67	20.2	4.3	35.0	40.0

[a] from NH_3 pulse chemisorption, [b] from IR-pyridine chemisorption, [c] from CO_2–TPD.

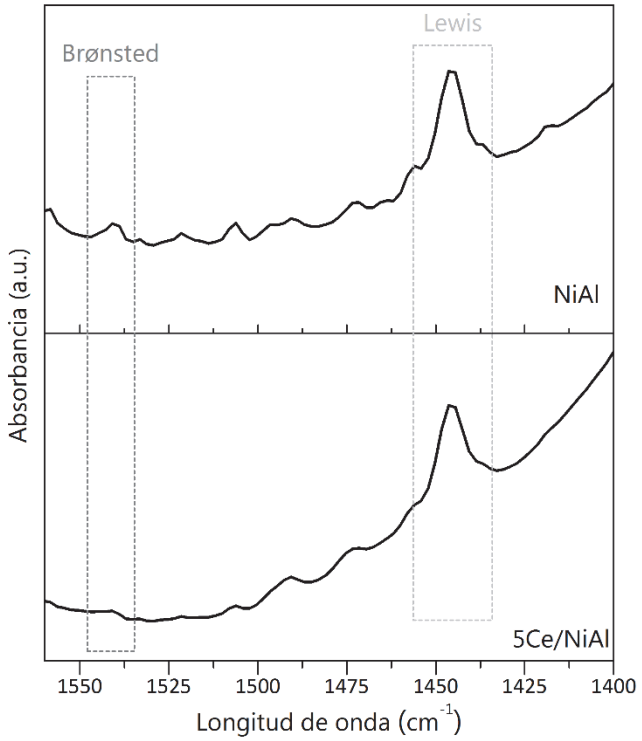

Figure 6.15. IR spectra of pyridine adsorption for fresh reduced NiAl and 5Ce/NiAl solids.

Regarding the surface basicity of the Ce-modified samples, a proportional increase is observed in total basic sites density with Ce loading. Accordingly, 10Ce/NiAl solid presents the highest density of basic sites, around 2.4 times higher than that of NiAl. This indicates that more basic sites are created on the solid's surface by Ce addition.

CO_2-TPD profiles are shown in Figure 6.16. XCe/NiAl samples evidence some differences with respect to the parent NiAl. First, a new maxima of CO_2 desorption from medium strength basic sites appears at ~130 ºC, which is associated with bidentate carbonates species adsorbed on Ce-O pairs (MB_{Ce-O}), together with the CO_2 adsorption peak on Ni-O pairs (MB_{Ni-O}) (155-175 ºC). Second, Ce-modified solids present a shift of MB_{Ni-O} and strong strength desorption peaks to the left.

Deconvolution of the desorption peaks indicates that Ce-modified samples present higher density of medium and strong strength basic sites, as indexed in Table 6.8. This can be associated to the excellent oxygen storage capacity of Ce, due to its large number of oxygen vacancies and the Ce^{3+}/Ce^{4+} redox potential, as reported by Abou Rached et

al. [211]. 5Ce/NiAl presented a remarkable density of medium basic sites (21.7%), which seems to decrease with 10% of Ce addition; this can be associated to a worsening in the dispersion with loadings above 5%, which can contribute to a breakage of metal-oxygen bond. Regarding the density of unidentate carbonates binding oxygen anions with low coordination (strong basic sites), those increase monotonically with Ce content.

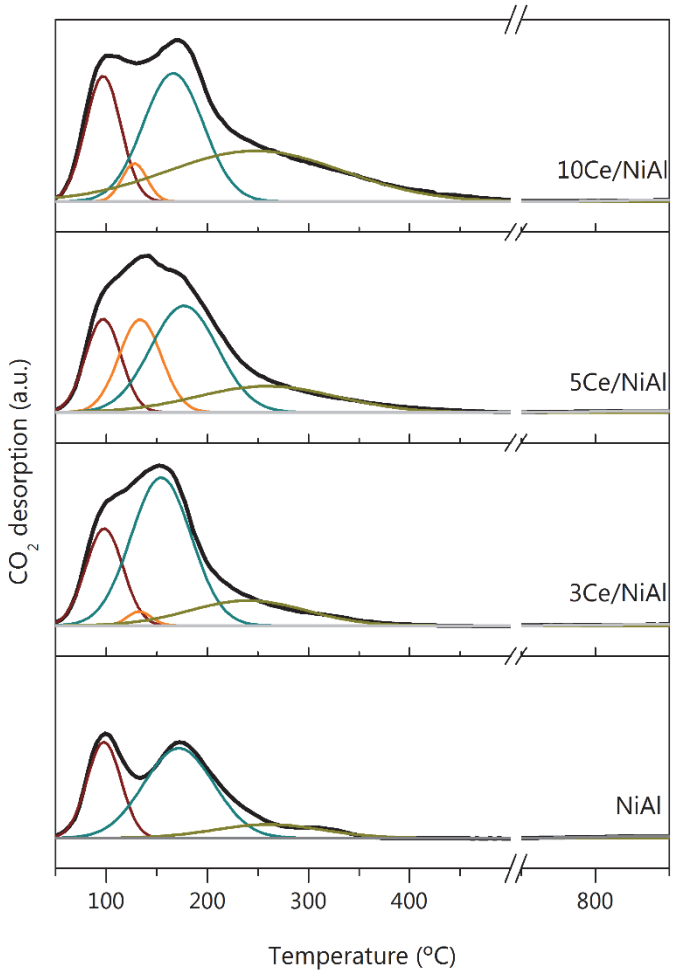

Figure 6.16. CO_2 desorption profiles of Ce-modified solids. Colour code: red (weak basic sites); orange (intermediate strength basic sites by MB_{Ce-O}); blue (intermediate strength basic sites by MB_{Ni-O}); green (strong basic sites).

In summary, TPD-CO_2 results suggested that the addition of cerium increased the total density of the basic sites of the samples, and resulted in the generation of new medium and strong strength basic sites. The acid/base ratio decreased with higher

loading of Ce, being 30% lower for 5Ce/NiAl with respect to NiAl, and 45% lower for 10Ce/NiAl.

So far, it has been observed that, in general, Ce addition enhances some physicochemical properties of the solid. More favourable surface characteristics are achieved, such as lower acid-to-base ratio and an increase in medium and strong basic sites). As well, morphological properties alike significantly smaller Ni^0 particles. On the contrary, the specific surface area and the nickel reducibility do not vary or slightly worsen upon Ce addition.

6.3.2 Glycerol APR with Ce-modified catalysts

The physicochemical characteristics of Ce-modified solids indicated that, a priori, they can improve the catalytic performance in the production of H_2 by glycerol APR. The catalytic performance in the glycerol APR were tested in the same operation conditions as XMg/NiAl were. Next, the obtained results at 2 h (steady state) will be discussed. Conversion of glycerol and carbon conversion to gas, as well as the H_2 yield are shown in Figure 6.17.

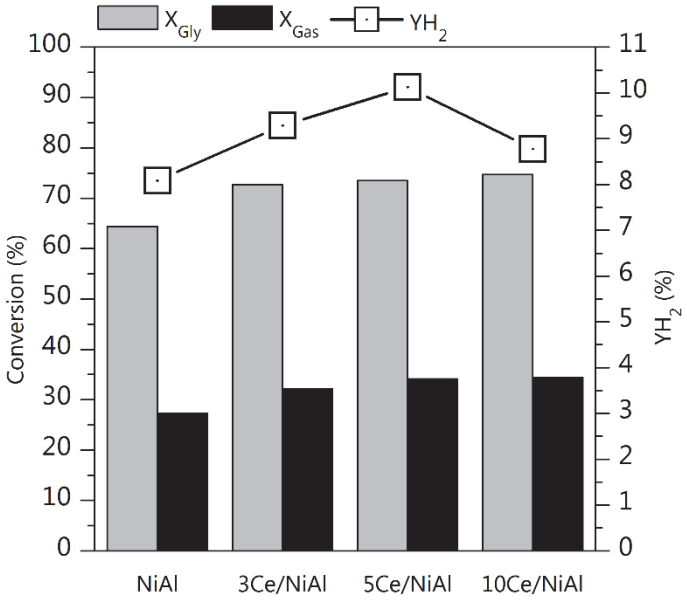

Figure 6.17. Glycerol conversion, conversion to gas and H_2 yield of Ce-modified samples. Reaction conditions: 235 ºC/35 bar, WHSV= 24.5 h^{-1}. Reaction time: 2 h.

Both X_{Gly} and X_{Gas} (Figure 6.17) slightly increase with Ce loading. Ce-modified catalysts present 13% to 16% higher X_{Gly} than the parent NiAl (NiAl: 64% and 10Ce/NiAl: 74.7%). Similarly, X_{Gas} also increases, even in greater proportion (by 17-26%). The gas product analysis indicates that Ce addition not only improves X_{Gly} and X_{Gas}, but also increases H_2 yield compared to NiAl. Among Ce-modified catalysts, YH_2 is maximised by 5Ce/NiAl (10.1%), being 25% higher than that of NiAl.

The distribution of the main gas products is depicted in Figure 6.18. It is seen that the gas streams are mainly composed by H_2 (>47%).

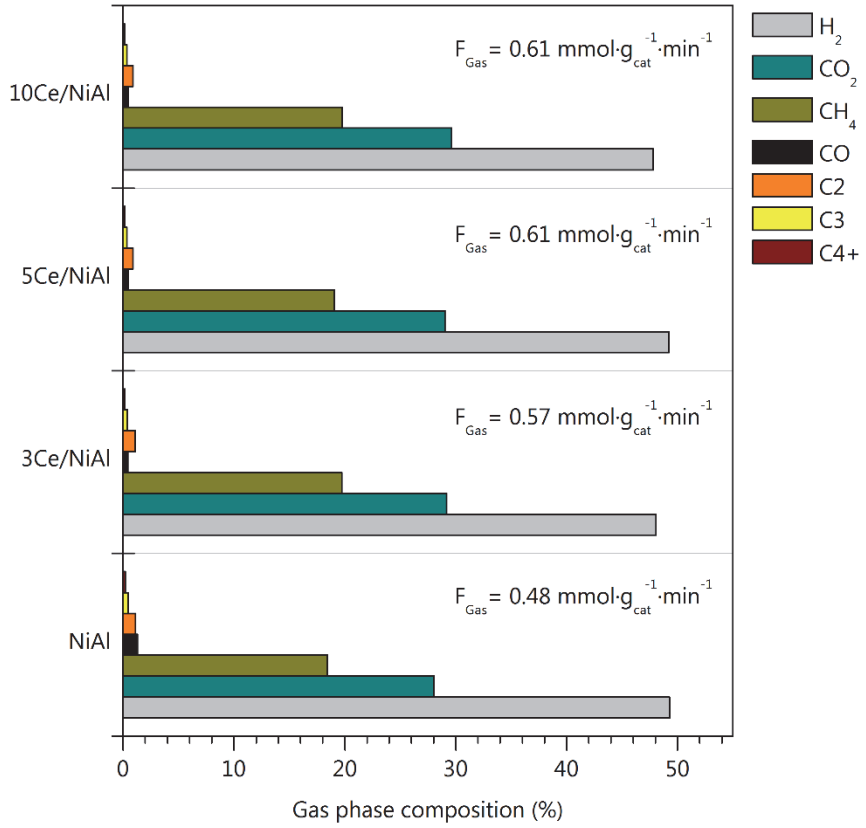

Figure 6.18. Gas-phase composition of Ce-modified catalysts (dry basis). Reaction conditions: 235 ºC/35 bar, WHSV= 24.5 h^{-1}. Reaction time: 2 h.

In decreasing order of composition, H_2 is follows by: CO_2> CH_4>> CO. It is worth noting that 5Ce/NiAl catalyst produces gas at 0.61 $mmol \cdot g_{cat}^{-1} \cdot min^{-1}$ rate (by 0.48 $mmol \cdot g_{cat}^{-1} \cdot min^{-1}$ of NiAl), both streams with similar H_2 concentration. It means that

H_2 production rate by 5Ce/NiAl is 27% higher than by NiAl. CO_2 is the second compound leading the distribution of the gas-phase products, and it is the final product of the glycerol reforming (equation 1.2). Compared to NiAl, Ce-containing catalysts produce lower H_2/CO_2 in the gas, which anticipates H_2 consumption in side reactions, such as CO hydrogenation to give CH_4, the third most abundant gas (~20%). CO contents of 1.1%, 0.9% and 0.9% for 3Ce/NiAl, 5Ce/NiAl and 10Ce/NiAl respectively, are obtained in the gas streams, which makes the stream produced feasible for further hydrogen stream purification for PEMFC. Other gas-phase compounds produced in less degree: ethane (C2), propane and propylene (C3), and finally iso-butane, butane and a small number of others not identified (C4+).

Selectivity to hydrogen (SH_2) and to methane (SCH_4) are show in Figure 6.19. SH_2 is enhanced with Ce addition (up to 38% and 41% for 3Ce/NiAl and 5Ce/NiAl, respectively), though for Ce loadings higher than 5%, SH_2 diminishes.

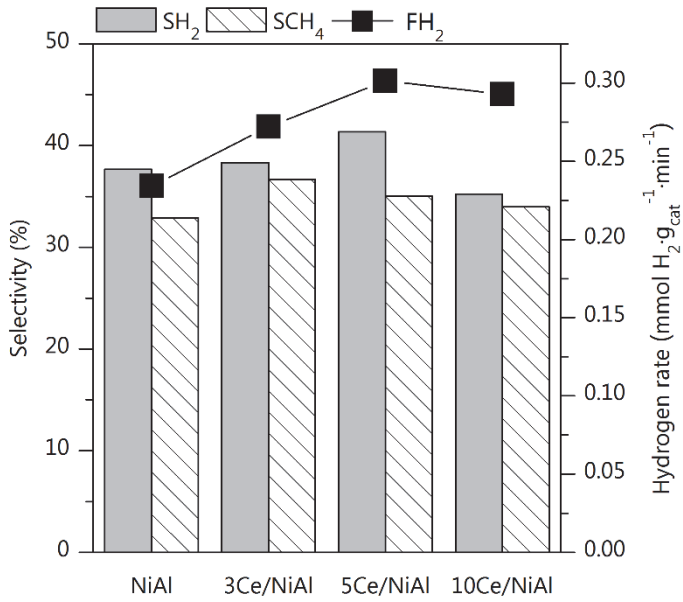

Figure 6.19. Selectivity to H_2, selectivity to CH_4 and hydrogen production rate of Ce-modified catalysts. Reaction conditions: 235 ºC/35 bar, WHSV= 24.5 h^{-1}. Reaction time: 2 h.

Methane selectivity increases, especially for 3Ce/NiAl catalysts, which agree with the lower H_2/CO_2 for these catalysts. Ce addition also favours YH_2. Interestingly, 5Ce/NiAl presented high SH_2 with minimum increase in SCH_4. It has been reported that Ce can

decorate Ni-defective sites responsible of methanation of CO or CO_2 [34]. In accordance, 5Ce/NiAl sample shows the best catalytic performance with 25% higher YH_2 than NiAl.

In addition to the improvement in SH_2, it is worth noting the production of chemical products of high value in the liquid phase, as shown in Figure 6.20. In fact, the liquid flow, in terms of C, increases for 5Ce/NiAl with respect to that produced for parent NiAl catalysts, which is due to its higher X_{Gly}.

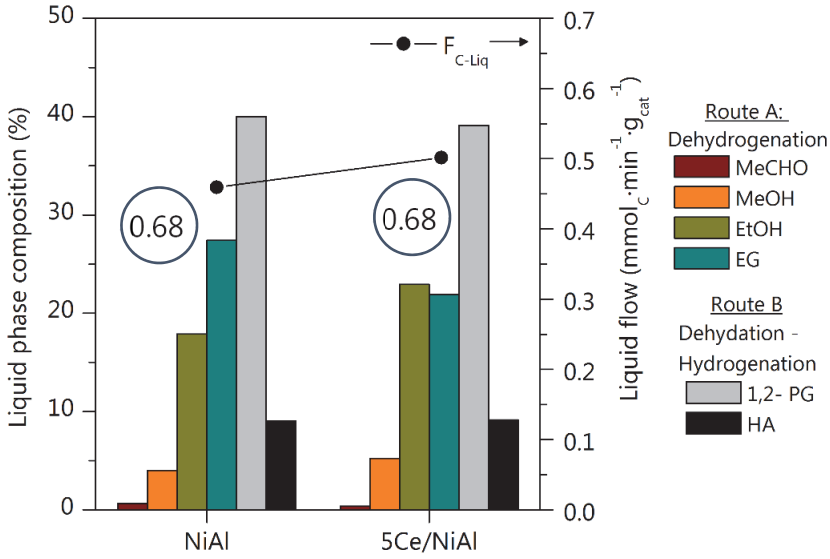

Figure 6.20. Molar composition of the main liquid products and total produced liquid flow by Ce-modified catalysts. In circles: Route A/Route B products ratio. Reaction conditions: 235 ºC/35 bar, WHSV= 24.5 h^{-1}. Reaction time: 2 h.

There are no drastic differences in the liquid products distribution between 5Ce/NiAl and NiAl, neither when compared to 5Mg/NiAl assay. In fact, the Route A/Route B products ratio is the same for both catalysts. Again, the main liquid product obtained is 1, 2-PG, with ~39%, followed by EtOH≈ EG (both around 22%). The most notable difference between 5Ce/NiAl and NiAl is in these two compounds. The EG/EtOH ratio decreases from 1.6 (for NiAl) to 0.96 by addition of 5% Ce. Since the production of both products follows the same path (Figure 5.5), the obtained results can be rationalized by the higher acid sites density and smaller Ni^0 ensembles of 5Ce/NiAl, which could promote the transformation of EG by dehydration and hydrogenation. HA, primary product of the dehydration, accounts for 9%. MeOH and MeCHO account for

5.2% and 1%, respectively. Others such as 1-propanol> 2-propanol> acetone> propionaldehyde, account for less than 0.5%.

5Ce/NiAl catalysts presented a good catalytic performance in terms of X_{Gly} and X_{Gas} (73% and 31%, respectively), in addition to high YH_2 and SH_2. APR results indicate that above 5% Ce loadings, the improvement in the catalytic behaviour is limited. An inspection of its physicochemical properties indicated that a good balance between Ce dispersion, available nickel, Ni^0 size and acid/base ratio are involved in the optimized catalytic properties of 5Ce/NiAl catalyst.

6.4 CHARACTERIZATION OF USED Mg- AND Ce-MODIFIED CATALYSTS

The harsh hydrothermal environment of the aqueous-phase operation is a challenge for the stability of the catalysts. Although the catalysts´ performance discussed in the previous sections were reported for 2 h steady state, those catalysts were left for an additional hour at the APR conditions. After being used they have been characterized to gain insight into the modifications they underwent. Here within, the results of N_2 physisorption, XRD, H_2-TPR, and ICP of the liquid product, are presented for both Mg- and Ce-modified used catalysts.

6.4.1 Leaching of metals

The ICP analysis of the reaction liquid product (Table 6.9) indicates very low Al leaching (≤ 0.05%) for all studied catalysts. As discussed in the previous Chapter, it may be due to its re-deposition as boehmite on the solid surface [186]. Low to moderate (between 0.2% and 1.6%) leaching of nickel is observed, with an average nickel leaching rate range of 0.067-0.53 $\%Ni \cdot h^{-1}$.

XCe/NiAl present the highest Ni leaching. It seems that Ce favours its detachment from their original binding sites, entailed by phase modifications at hydrothermal conditions. Remarkably lower Ni leaching rate is shown by the Mg-modified catalysts, even below NiAl. Nonetheless, it seems that the loss of the active metallic phase is not the main deactivation issue for these materials.

Regarding the modifiers used, the highest Ce leaching is for 10Ce/NiAl (0.6%), among Ce-modified solids. Mg leaches at a much higher rate than Ce does (between 13 and 66 times higher).

Table 6.9. Physico-chemical properties of XMg/NiAl and XCe/NiAl used catalysts.

Catalyst	Leaching[a]			Textural properties[b]			
	Ni (%)	Al (%)	*Md* (%)	S_{BET} ($m^2 \cdot g^{-1}$)	ΔS_{BET} (%)	Vp ($cm^3 \cdot g^{-1}$)	Dp (nm)
NiAl	0.7	0.05	n/a	114	37	0.24	6.3
3Mg/NiAl	0.1	0.01	10.9	88	12	0.24	8.9
5Mg/NiAl	0.4	0.05	13.2	81	14	0.23	9.2
10Mg/NiAl	0.1	0.02	8.3	80	23	0.24	8.9
3Ce/NiAl	1.0	0.05	0.3	100	34	0.26	8.5
5Ce/NiAl	1.6	0.03	0.2	97	13	0.27	8.9
10Ce/NiAl	1.4	0.09	0.6	94	21	0.24	7.8

Md: Mg or Ce. [a] IPC-AES, [b] N_2 physisorption.

3Mg/NiAl shows the highest leaching of Mg (13.2%). The high leaching rate of Mg at hydrothermal conditions can be associated to Mg tendency to hydration, which is the first step of the leaching mechanism [212, 213]. For the highest Mg loadings, its leaching decay to 8.3%, which may be ascribed to a better Mg attachment by the formation of $MgAl_2O_4$, as XRD results evidenced.

6.4.2 Textural properties

The N_2 physisorption isotherms of used catalysts are presented in Figure 6.21. Both spent XMg/NiAl and XCe/NiAl catalysts presented isotherms type IV with type H1 hysteresis loop, similar to that of their respective fresh reduced forms, which indicates that the mesoporous structure remains.

Few changes in the pore width distributions are perceived. An additional peak to the unimodal characteristic of the fresh reduced catalysts appears at lower pore widths. The contribution of these pores (~3.5 nm) increased for higher Mg and Ce loadings, which could be associated to the formation of new phases, as will be further confirmed by XRD results.

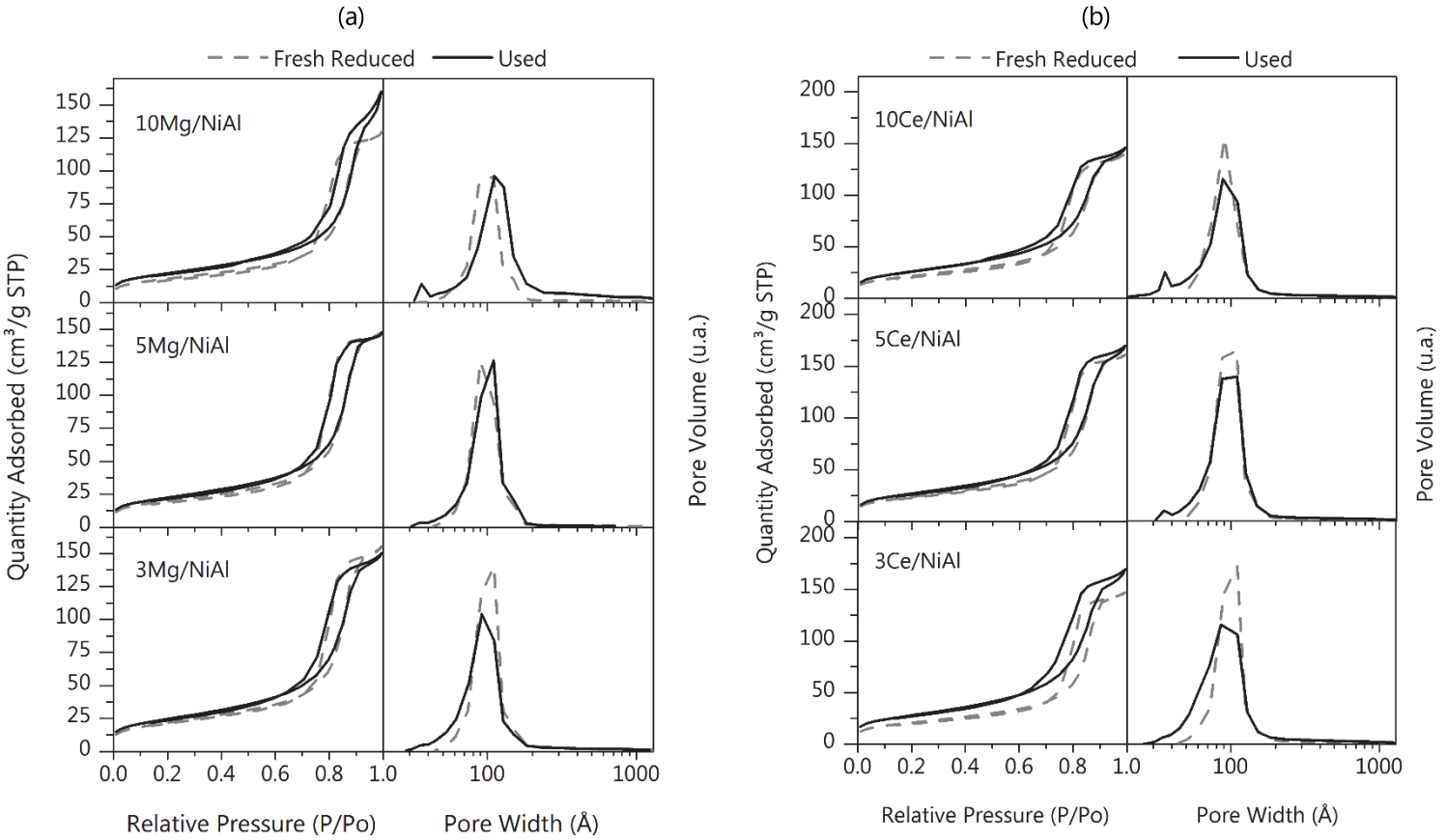

Figure 6.21. N_2 physisorption isotherms and pore size distribution of used catalysts: (a) Mg-modified catalysts; (b) Ce-modified catalysts.

Compared to fresh reduced catalysts, the specific surface area of used Mg- and Ce-modified catalysts increased after the glycerol APR reaction, that a positive ΔS_{BET} is found (Table 6.9). It can be assigned to two reasons: (i) oxidation of the outermost layers of Ni ensembles; and (ii) hydration of γ-alumina to boehmite, which could be leached off and re-deposited on the catalyst surface, generating extra porosity in the solid [186, 191]. As a general trend, the increase in S_{BET} for the modified catalysts is 1.6-3 times that for NiAl, which suggests less alumina re-deposition for the promoted catalysts. (i) and (ii) are coherent with H_2-TPR and XRD results, as is discussed further on.

6.4.3 Phase transition and crystallinity

As aforementioned, phase transitions (i.e., γ-alumina → boehmite) are favoured by the hydrothermal conditions of APR. By means of XRD analysis, the crystalline structures of used catalysts have been analysed, and the obtained diffractograms are shown in Figure 6.22 for XMg/NiAl and XCe/NiAl used catalysts.

Reflections from spinel phase are still exhibited for all used catalysts. Noteworthy; peaks from boehmite are not seen for any of the spent catalysts containing Ce or Mg, as opposed to NiAl. Another common observation for XMg/NiAl and XCe/NiAl used samples is that metallic Ni is present. Since the presence of metals hinders the hydration of γ–alumina to boehmite [214], it seems that both Ni^0 and the promoters prevent the phase transition of alumina. As S_{BET} indicate, less Al is re-deposited on the catalyst surface, which could result in a thinner layer of boehmite, invisible for XRD.

For the used XMg/NiAl catalysts (Figure 6.22 (a)), spinel diffraction lines indicate the presence of both $NiAl_2O_4$ and $MgAl_2O_4$, based on the downshift from peaks in the XRD results of fresh reduced catalysts (Figure 6.4). New peaks with respect to the fresh catalysts at 12º, 23º, 35º, 40º and 47º 2θ emerge. Those peaks can be assigned to hydrotalcite, $Mg_6Al_2(CO_3)(OH)_{16}{\cdot}4H_2O$ (JCPDS 01-070-2151). The formation of this phase could be promoted by the hydrothermal conditions of the reaction. In accordance with its highest Mg loading, 10Mg/NiAl exhibits the most intense peaks for hydrotalcite. Interestingly, 5Mg/NiAl does not show hydrotalcite signals, those being very week for 3Mg/NiAl assay. In fact, the diffractogram of 5Mg/NiAl used is quite similar to its fresh reduced form, suggesting that enhanced Mg-Ni interaction was obtained by 5% Mg loading, better stabilizing the catalyst structure.

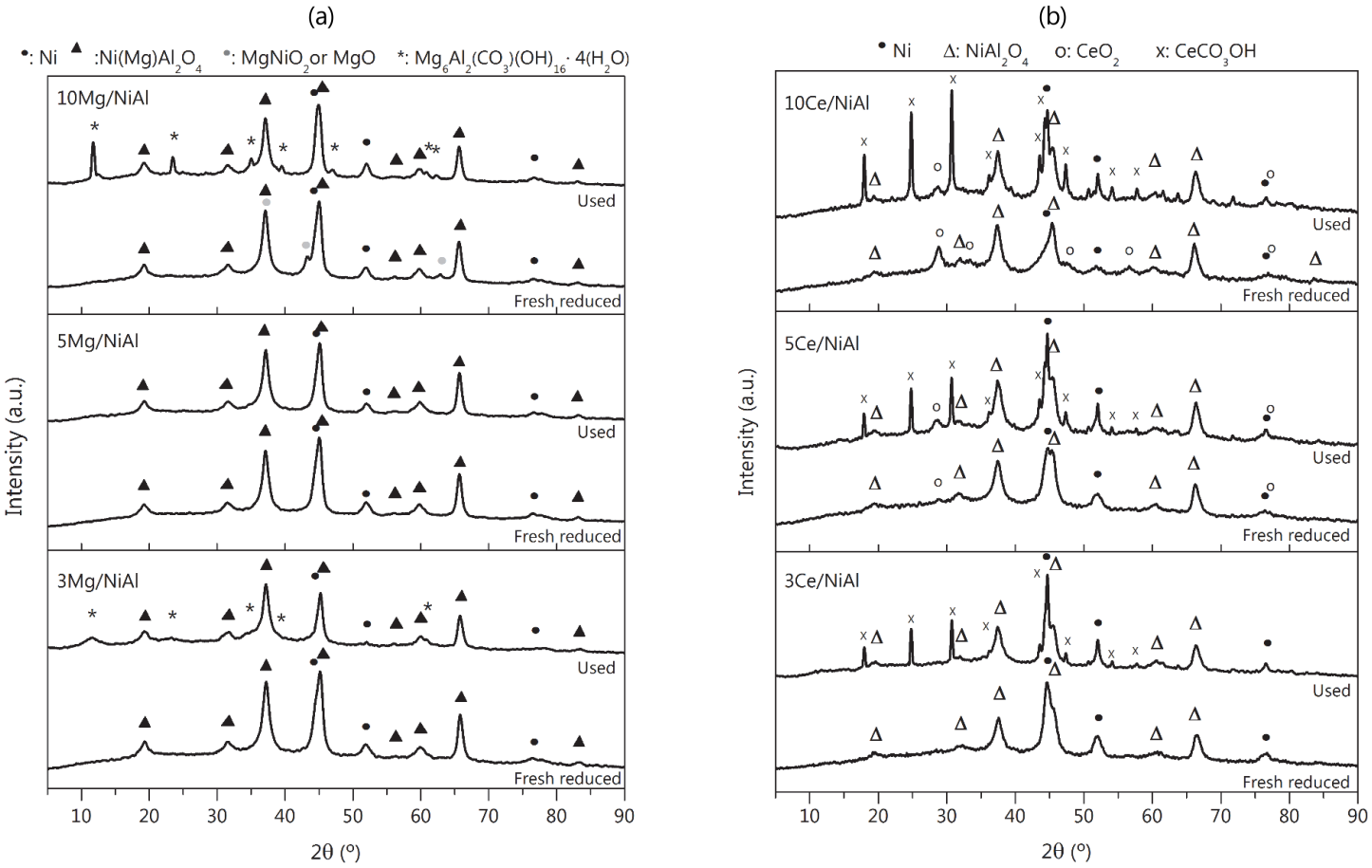

Figure 6.22. XRD patterns of used catalysts in APR: (a) Mg-modified catalysts; (b) Ce-modified catalysts.

Spent XCe/NiAl catalysts display a more complex XRD spectra, with several phases identified. Apart from the ubiquitous spinel, also metallic Ni is found. Peaks from Ni^0 are sharper than those in fresh reduced samples, indicating some grade of sintering of the active phase, which is further confirmed by the obtained Ni^0 crystallite sizes (Table 6.10). A sort of narrow and intense peaks emerged at 17.8º, 24.8º, 30.5º and 50.1º 2θ, which are due to the hexagonal cerium carbonate hydroxide, $CeCO_3OH$ (JCPDS 00-032-0189). This evidences that the harsh hydrothermal APR conditions favours carbonation of ceria with CO formed by decarbonylation [215]. Other authors have also identified the $CeCO_3OH$ phase in ceria-based catalysts subjected to APR reaction [216]. Spent 10Ce/NiAl and 5Ce/NiAl present weak XRD peaks from ceria, unlike their fresh reduced forms.

Similar to NiAl, Mg-modified catalysts preserve, even slightly decrease, the Ni^0 crystallite size. Oppositely, Ce-modified catalysts present a considerable increase, indicating Ni^0 coalescence in used catalysts.

Table 6.10. Crystal sizes of the identified phases of used Mg- and Ce-modified catalysts.

Catalyst	Ni^0 (nm)	Hydrotalcite (nm)	$CeCO_3OH$ (nm)
NiAl	14.6 (16)	n/a	n/a
3Mg/NiAl	n.f. (6.7)	2.8	n/a
5Mg/NiAl	6.9 (7.5)	n.f.	n/a
10Mg/NiAl	10.9 (11.4)	44.3	n/a
3Ce/NiAl	42.7 (5.8)	n/a	79.5
5Ce/NiAl	18.6 (7.5)	n/a	n.f.
10Ce/NiAl	54.0 (4.7)	n/a	48.1

n.f.: phase not found. In parenthesis (d_{Ni^0}): crystal size (nm) in the fresh reduced catalysts.

Among the Ce-modified used catalysts, 5Ce/NiAl shows the most stable behaviour, with a moderate coalescence (size increased from 7.5 to 18.6 nm). It can be inferred that the Ni^0 sintering is mainly promoted by Ce, in spite of the pressure and temperature conditions of APR, which are the main factors associated to sintering [197]. It can be ascribed to a wakening effect of Ni-support interaction in the proximity of Ce particles, which favours Ni^0 mobility.

6.4.4 Reducibility and speciation

Spent catalysts were also submitted to H_2-TPR analysis to enlighten the modification of the reducible species. The obtained reduction profiles TPR_{used} are shown in Figure 6.23. Two main hydrogen consumption events are identified for both Mg- and Ce-modified spent catalysts: one, at low-intermediate temperature range (200-600 ºC), and another, at high temperature (>600 ºC). Taking into account that the catalysts have been reduced at 700 ºC before APR, the presence of those H_2-consumption peaks at temperatures below 700 ºC suggest the presence of oxidised species (Ni species and, in much lesser extent, Ce species). According to XRD, bulk metallic Ni is preserved, which suggests that such oxidation of nickel is restricted to the outermost layers of the particle. Besides, hydrogenation of carbonaceous materials (unreacted glycerol and other APR liquid products) accumulated in the pores of the catalyst could contribute to the relatively large intensity of those peaks [191]. The high temperatures peaks are associated to the reduction of the remained spinel phase. For XMg/NiAl assay, this high temperature peak upshifts in temperature with increasing Mg loading (Figure 6.23 (a)), while for XCe/NiAl catalyst, the temperature does not significantly vary (Figure 6.23 (b)).

The total H_2 consumption of the used catalysts is depicted in Table 6.11. Oxidation of the active metal can be anticipated, based on the higher H_2 uptake of the used samples in comparison with the parent fresh reduced forms. Oxidation of the active metal has been identified as one of the deactivation causes in aqueous-phase reactions [102, 212]. The H_2 consumption of the unpromoted NiAl catalysts is 4.1 mmol $H_2 \cdot g^{-1}$. Both Ce- and Mg-modified catalysts uptakes H_2, to a different extent. As a general trend, Mg decreases and Ce increases H_2 consumption, with respect NiAl. According to Van Haasterecht et al. [192], the smaller Ni^0 particle is more susceptible to oxidation. As shown before (Table 6.10), Ce-modified catalysts have smaller Ni^0 than those Mg-modified ones. Accordingly, nickel oxidation is more prone in the Ce-modified catalysts. In other words, Mg hinder the oxidation of nickel. In the Ce-modified solids, nickel oxidation promoted by ceria cannot be ruled out.

Table 6.11. Results from H_2-TPR_{used} of Mg- and Ce-modified used catalysts.

Catalyst	TPR_{used} H_2 consumption (mmol $H_2 \cdot g^{-1}$)	NiO species H_2 consumption (mmol $H_2 \cdot g^{-1}$)	Ni oxidized[a] (%)
NiAl	4.1 (0.6)	2.64	60
3Mg/NiAl	3.0 (1.8)	1.18	39
5Mg/NiAl	2.6 (2.0)	0.36	13
10Mg/NiAl	3.1 (1.8)	1.15	44
3Ce/NiAl	4.0 (1.1)	0.94	22
5Ce/NiAl	4.3 (0.7)	1.11	25
10Ce/NiAl	5.1 (1.1)	1.72	46

[a]oxidized percentage, with respect to fresh reduced catalyst (TPR_{700}). In parenthesis, uptake at fresh reduced form.

An attempt was made to estimate the amount of nickel oxidized in the spent catalysts. Thus, the evolved gases in the TPR_{used} were analysed by mass spectrometry for 5Mg/NiAl, 5Ce/NiAl and the parent NiAl used catalysts, aiming to discriminate the H_2 consumption related to the oxidation of the metallic phase and that related to the hydrogenation of carbonaceous material, which produce CH_4. The obtained profiles are shown in Figure 6.24. The fact that methane release peak at high temperature is rather small (with much less intensity than hydrogen peak) suggests that solely the reduction of the spinel is taking place in that temperature range. Once the hydrogen uptake required for the methane formation ($Meth_{H2}$) (assuming 2 moles of H_2 per mole of CH_4 produced) was subtracted, the H_2 uptake ascribed to reduction of NiO (200-600 ºC range) was calculated. In decreasing order, the values of $Meth_{H2}$ are $1.70 < 0.63 < 0.39$ mmol $H_2 \cdot g_{cat}^{-1}$ for 5Ce/NiAl, NiAl and 5Mg/NiAl, respectively. It is assumed that same number of carbonaceous materials is accumulated on the surface of all catalysts. Data in Table 6.11 suggest that a significant amount of metallic Ni has been oxidised in APR (ca. 13-60%). These results evidenced that modified catalysts are more resistant to oxidation than NiAl counterpart. Addition of 5% Mg seems to limit nickel oxidation (13% nickel oxidized).

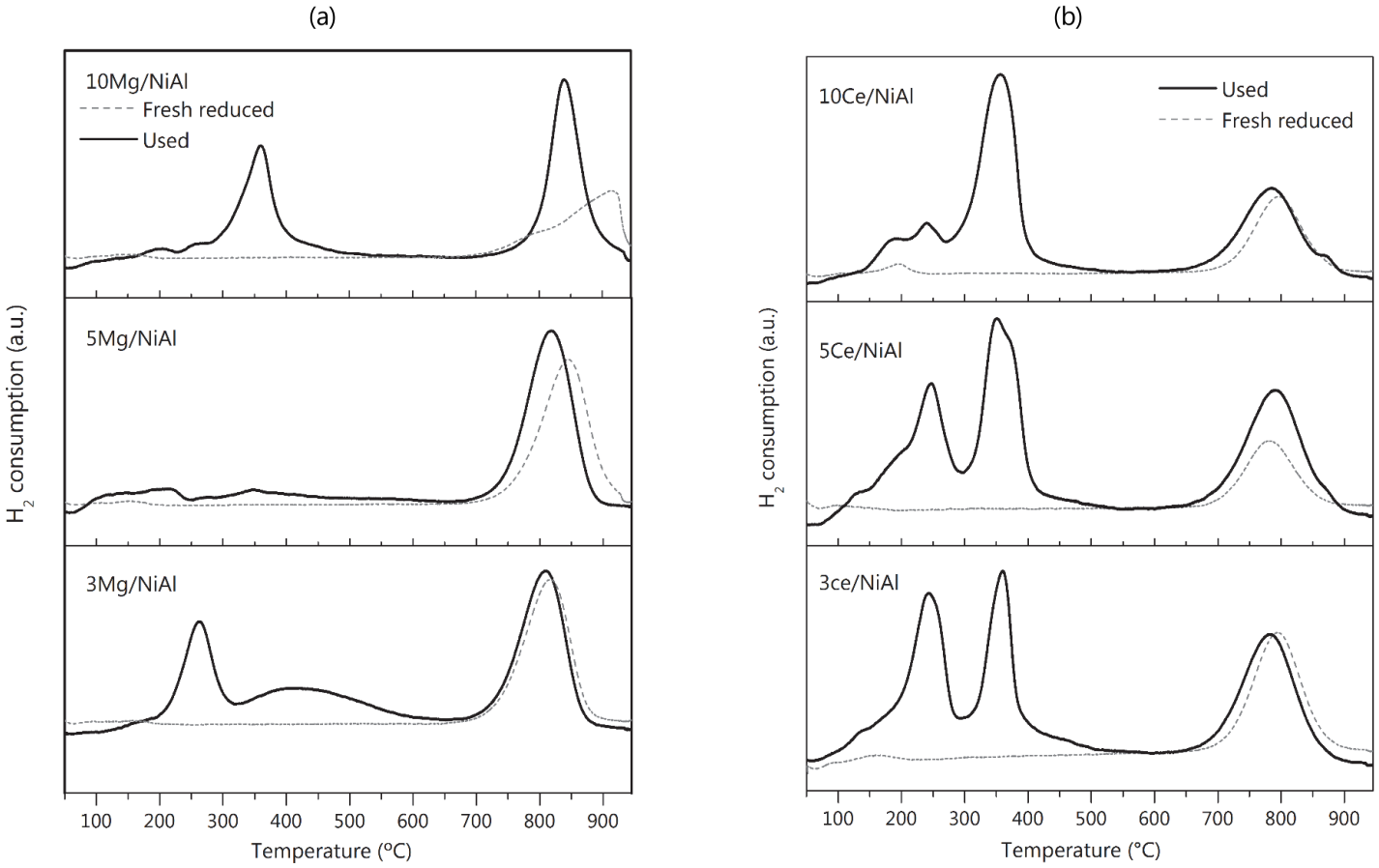

Figure 6.23. H_2-TPR profiles of used catalysts: (a) Mg-modified solids; and (b) Ce-modified solids.

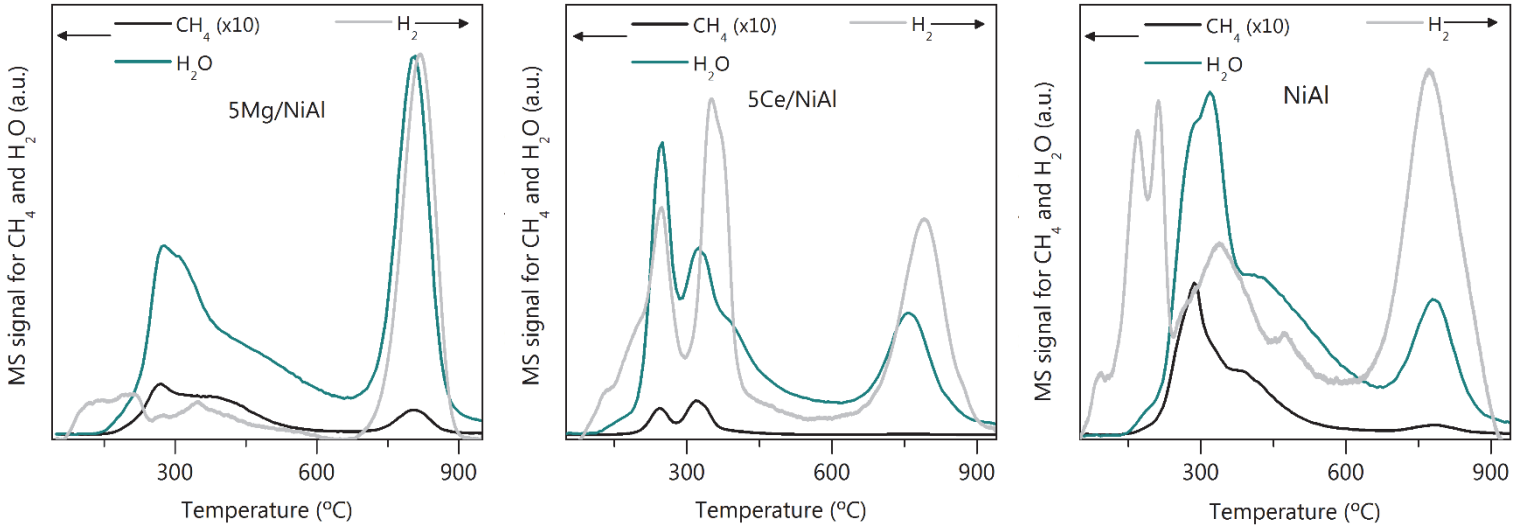

Figure 6.24. TPR coupled to MS profiles for 5Mg/NiAl, 5Ce/NiAl and NiAl used catalysts. Grey lines: H_2; blue lines: H_2O; Balck lines: CH_4 (10x magnification).

Although it is accepted that metal leaching mechanism proceeds firstly by oxidation, and then hydration to form hydroxide [102], Ni^0 oxidation results cannot explain the leaching of nickel in Mg- and Ce-modified catalysts. Nonetheless, it seems that particle size can also be involved, as suggested by the trend observed in the leached nickel and the average Ni^0 particle size in the fresh catalyst (Table 6.10). It is known that smaller Ni^0 particles are more susceptible to be oxidized and leached [192]. This behaviour would explain the increase in the average size of Ni^0 in the spent XCe/NiAl catalysts. Indeed, Ce-modified catalysts are the ones with the highest leaching rate of nickel. Mg-modified catalysts suffer from less oxidation and leaching rate of Ni^0 in comparison to that of NiAl (i.e. from 0.7% to 0.4%, in NiAl and 5Mg/NiAl, respectively). It seemed that Mg plays a kind of protection role in the leaching of Ni particles.

Based on the TPR analysis, it is seen that XCe/NiAl used catalysts could present a deactivation issue. This can be associated to the gradual change of nickel oxidation state under reaction conditions, from metallic to oxidized state (disperse NiO and surface nickel aluminate). Similar findings are reported in literature [34]. Nonetheless, oxidation of nickel in Ce-loaded catalysts is lower than that in NiAl parent assay, especially for loading <5% of Ce.

Signals from carbonaceous deposits are not found in the XRD of used catalysts, which may be ascribed to the short reaction time of the runs. Besides, the strong basic character of these modified spinel aluminates could also prevent the formation of structured carbonaceous deposits [217]. The addition of Mg and Ce enhanced the resistance of alumina transformation to boehmite, favouring the morphological properties of the samples.

The characterization results of Mg- and Ce-modified solids evidenced some deactivation issues. Regarding Ce-modified catalysts, the main probable deactivation phenomena could be Ni^0 sintering and leaching. Nonetheless, 5% Ce loading seems the optimum load to prevent both oxidation and Ni^0 sintering phenomena. In the case of Mg-modified catalysts, those present higher Mg leaching and Ni^0 oxidation rate, thought it seems that Mg stabilised the catalyst structure better than Ce, by avoiding not only Ni sintering but formation of hydrotalcite with the optimum load (5% of Mg), in addition to the low Ni^0 oxidation and leaching.

6.5 COMPARATIVE ANALYSIS OF Mg AND Ce MODIFIERS FOR NiAl

Glycerol APR results indicate that Mg partially improves the catalytic behaviour of NiAl, especially 5Mg/NiAl. It is known that magnesium can help to prevent the sintering of the nickel particles, as well as to increase the population of basic sites in the catalyst surface, and modify basic sites strength [161, 201]. Among XMg/NiAl catalysts, the 5Mg/NiAl presents slightly higher YH_2 and hydrogen molar flow than the parent NiAl. Nonetheless, loadings higher than 5% of Mg lead to a sharp drop in the activity (X_{Gly} and X_{Gas}), assigned to promotion in the formation of species like $MgNiO_2$ and $Ni(Mg)Al_2O_4$ that would obstruct the reduction of Ni^{2+} species even more, which has been attributed to the smaller surface area and the strong Mg – Ni interactions. The consequential detriment in the reducibility limited f_{red} in fresh reduced catalysts, lowering the available nickel metal sites.

Regarding Ce-modified catalysts, a synergetic effect is evidenced between Ce and Ni, which leads to the improvement of morphological properties, whilst protecting from specific surface area loss, as well as preventing sintering of metallic Ni after reduction treatment (700 ºC), in agreement to others [32, 34]. In general, Ce-modified catalysts achieved higher X_{Gly} and X_{Gas} than 5Mg/NiAl and the parent NiAl. Besides, an enhancement of YH_2 and SH_2 is accomplished with Ce addition. It is worth mentioning that 5Ce/NiAl presents the highest YH_2 (10.1%) among all the catalysts. Above 5% Ce loading, the improvement in the catalytic behaviour is limited.

The APR results point out that 5Mg/NiAl and 5Ce/NiAl catalysts present the better catalytic performance among the promoted samples. In this line, additional TEM analysis was carried out for NiAl, 5Mg/NiAl and 5Ce/NiAl catalysts in order to establish additional comparison between their morphology. It is expected that the availability of metallic nickel could better explain the observed differences in the glycerol APR activity of those samples. In addition, catalytic runs were carried out to elucidate the activity of the catalysts in the CO hydrogenation and the gas-phase WGS reactions. In the following sections the obtained results are discussed.

6.5.1 Nickel dispersion and size distribution

The morphology of the nickel particles was studied by TEM. The obtained micrographs are shown in Figure 6.25. The images revealed that unpromoted catalysts contained agglomerates of nickel particles of a nearly spherical-shape. A homogeneous particle size distribution was observed in the parent NiAl catalysts. The average metallic Ni particle size of fresh reduced samples (Table 6.12) indicate that, for modified catalysts, Ni^0 particles observed by TEM consisted of metallic crystallite agglomerates.

Table 6.12. Active metal properties of fresh reduced NiAl and Mg- and Ce-modified catalysts, estimated from TEM microscopy.

Catalyst	Ni^0 Crystal Size (nm)	Dispersion (%)	$A_{S\text{-}Ni^o}$ ($m^2_{Ni^o}\cdot g^{-1}$)
NiAl	12 (16.0)	10.0	14.1
5Mg/NiAl	11 (7.5)	11.3	9.1
5Ce/NiAl	15 (7.5)	11.2	14.7

In parenthesis, results from XRD.

The NiAl catalysts shows a narrow size distribution of Ni^0 particles, with an average size of 12 nm. This resulted in a 10% nickel dispersion. The metallic surface area (14.1 $m^2_{Ni^o}\cdot g^{-1}$) is significantly larger to values reported for impregnated Ni/γ-Al_2O_3 catalysts [218].

In the case of Mg- and Ce-modified catalysts, EDS mapping shows the formation of nearly spherical-shape metallic Ni particles. The Ni^0 size distribution in catalyst 5Ce/NiAl presents a bimodal distribution with maxima at 10 and 15 nm. This catalyst has the largest percentage of surface NiO, with the α peak in TPR being 8% of the total nickel phase distribution. The fact that α-NiO crystallites are expected to produce, upon reduction, larger metallic Ni particles than those from spinel, would explain the observed bimodal distribution. In line with the above mentioned, catalyst 5Mg/NiAl, with the least amount of free NiO, shows smaller size Ni^0 particles (11 nm), with a homogenous distribution. Regarding $A_{S\text{-}Ni^o}$, 5Ce/NiAl equals the parent NiAl area while Mg/NiAl has notable less value (35% less). The lower metal surface area and the limited reducibility (in terms of f_{Ni}) of Mg-modified catalyst are important constraints affecting its catalytic behaviour.

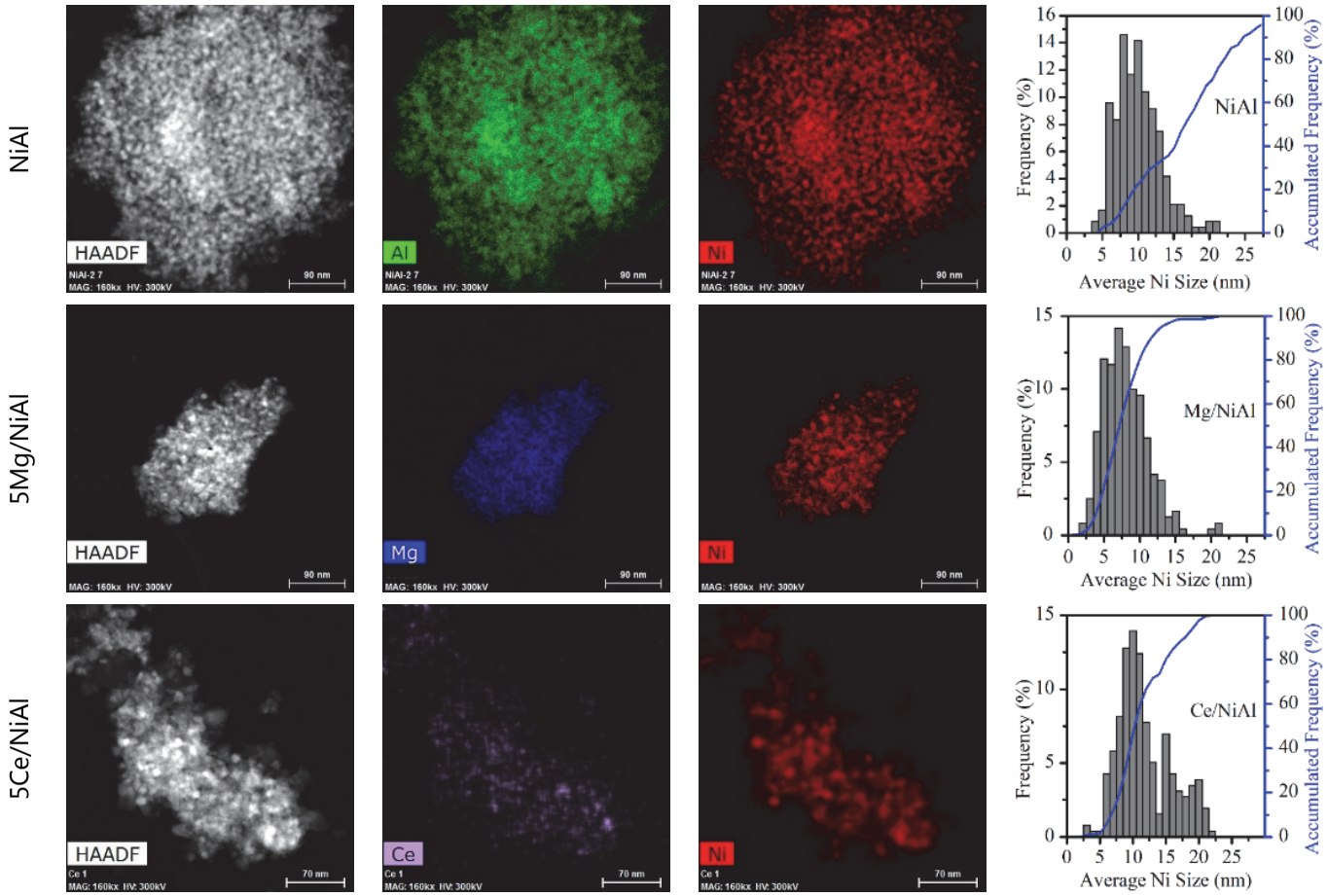

Figure 6.25. STEM, EDS mapping images, and Ni^0 particle size distribution of fresh reduced catalysts.

6.5.2 CO hydrogenation and Water-Gas Shift activity

According to the proposed APR reaction pathway, decarbonylation of aldehydes would produce CO, which could further react with other gaseous species to give either CO_2 or CH_4, through the WGS or CO hydrogenation, respectively [54]. WGS and CO hydrogenation activity was investigated in the gas phase, and catalytic runs were carried out at a CO/H_2 mole ratio of 7.5/10 in the feed stream. Additional runs were carried out by adding 25% H_2O to the feed stream in order to check the WGS activity. The obtained CO conversion and selectivities to CO_2 and CH_4, are presented in Table 6.13. Methane is the only product in the absence of water, reflecting negligible Fischer-Tropsch activity for all the catalysts. On the other hand, under WGS conditions, both CO_2 and CH_4 are formed.

For the feed stream containing only CO and H_2, modified catalysts show around ten-fold increase in CO conversion with respect to NiAl (i.e. X_{CO}> 30% vs X_{CO}= 3%). Under WGS conditions, these differences further increased as X_{CO} raised up to 67% by catalyst 5Mg/NiAl (vs. X_{CO}= 4.5% by the unpromoted catalyst). As a general trend, X_{CO} increases when water is added in the feed stream. Mg and Ce addition further increase the WGS activity. It is well known that basic surfaces promote WGS reaction [58]. Specifically, CeO_2 promotes the water dissociation, which is beneficial to achieve high WGS activity [219]. By means of WGS, carbon monoxide is converted into CO_2 giving additional H_2. Therefore, catalysts that promote WGS are crucial for obtaining a high hydrogen selectivity [172]. Nonetheless, high selectivity to methane is also reported, in line with the high ability of nickel for CO methanation [220].

Table 6.13. CO hydrogenation and WGS activity results.

	$CO+H_2$		**$CO+H_2+H_2O$**		
Catalyst	X_{CO} (%)	S_{CO2} (%)	X_{CO} (%)	S_{CO2} (%)	Normalized rate of H_2 production (WGS)
NiAl	3.0	100	4.5	55.1	1.16
Mg/NiAl	31.0	100	67.0	35.0	1.40
Ce/NiAl	34.6	100	45.4	30.3	1.46

It is worth mentioning that the CO/CO_2 molar ratio during the APR of glycerol (Table 6.14) is three-fold lower in Mg- and Ce-modified catalysts. This is in line with the estimated relative WGS reaction rates, which suggest that Ce and Mg can increase the CO conversion through the WGS reaction. However, it is not reflected in an increased selectivity to hydrogen, since hydrogen was consumed in subsequent CO hydrogenation reactions. The established working conditions imply that both water and hydrogen molecules competed for CO, the former to give CO_2 (and produce one molecule of hydrogen) and the latter to give CH_4, with the consumption of 3 molecules of hydrogen.

Table 6.14. Gas-phase characteristics for NiAl, 5Mg/NiAl and 5Ce/NiAl in the glycerol APR at 235 ºC/35 bar (2 h).

Catalysts	CH_4/Alkanes	CO/CO_2	$S_{H2\text{-}gas}$ (%)
NiAl	92.2	21.9	57.4
5Mg/NiAl	94.0	60.0	62.3
5Ce/NiAl	94.5	61.7	57.7

As previously noted, methane could be produced through the decarbonylation of acetaldehyde or hydrogenation of CO. However, the high hydrogenation activity and selectivity to methane observed for the promoted catalysts suggested that CH_4 was mainly produced through hydrogen consuming reactions, with the concomitant decrease in hydrogen selectivity.

These observations are in agreement with the $S_{H2\text{-}gas}$, which has been calculated, considering the moles of H_2 produced with respect to hydrogen lost in alkanes production, i.e., only considering gas-phase products. Significant differences can be appreciated regarding $S_{H2\text{-}gas}$ (Table 6.14), in favour of 5Mg/NiAl, which presents the highest $S_{H2\text{-}gas}$ (62.5%). Meanwhile, 5Ce/NiAl shows the same selectivity as NiAl.

6.5.3 General Discussion

According to the plausible reaction path for glycerol APR over Ni-based catalysts proposed in Chapter 5, both the metal and the support play an essential role in the catalytic behaviour. Indeed, the products obtained can be tailored by the fine-tuning of both functionalities [49]. On one hand, the surface acidity directly affects the activity

since glycerol could adsorb on the acid-sites to form hydroxyacetone through C-O bond cleavage (dehydration reaction) [166]. On the other hand, the surface basic sites would promote the desired WGS reaction [58], by which CO is removed in form of CO_2 and H_2, leading to free metal site for APR. In addition, the metallic Ni activates the organic molecule through the C-C bond cleavage to form ethylene glycol. This reaction route releases one mole of CO and H_2 per mole of glycerol converted. Indeed, hydrogen production will depend on whether the WGS (beneficial) or the CO hydrogenation (detrimental) reaction is promoted by metallic sites.

It was observed that both Mg and Ce promote WGS reaction. The notable low amount of CO in the APR gas-phase product can be associated to the WGS reaction, promoted by Mg and Ce high basicity, in addition to the operation at thermodynamically favourable reaction conditions [58, 121].

It could be deduced that small metallic Ni particles are crucial to achieve highly active catalysts for the APR; however, small nickel particles can also activate CO to drive hydrogenation reactions [220], which would reduce selectivity to hydrogen [221]. The observed behaviour is in contrast to the reported activity vs. metal particle size trend for Pt/Al_2O_3 catalysts, where the cleavage of C-C bonds preferably occurred on the facet Pt atoms rather than on edge and corner atoms (i.e., larger Pt particles were more active) [55].

It was observed that Ce addition improved the APR activity, whereas it was slightly decreased by Mg. Hydrogen yield and selectivity were slightly increased by both Mg and Ce, whereas no great effect on methane selectivity was found. XRD indicated that smaller metallic Ni particles were formed upon reduction of both modified catalysts (around half of those in NiAl). Others also found that magnesium, deposited by impregnation on nickel aluminate spinel, could help to prevent the sintering of the metallic nickel particles [201]. The reducibility of the nickel aluminate spinel derived catalysts has been found to increase upon Ce addition, and nickel species in the spinel phase, could be reduced at 700 ºC. Contrarily, the formation of magnesium-nickel aluminate spinel, which is a difficult-to-reduce species, led to a lower degree of reduction of the XMg/NiAl catalyst. In this case, the nickel species in the spinel phase could not be reduced. Doping of either Ce or Mg increased the density of basic and acid functionalities on the catalysts surface,

with a more marked increase of basic sites [161, 201]. Moreover, the strength of the basic sites was increased.

The presence of CO_2 and CH_4 in the gas stream during glycerol APR indicated that the catalysts researched were active for the C-C bond cleavage. According to the reaction pathway, CO_2 formation requires a first dehydrogenation step, to form glyceraldehyde, followed by decarbonylation and further conversion of the released CO by WGS. Therefore, 2 moles of H_2 are formed for each mole of CO_2 produced. However, the production of CH_4 implies hydrogen consumption. Methane could be produced by either hydrogenation of the released CO or by dehydration of intermediate liquid products (i.e., ethylene glycol) and subsequent C-C bond cleavage and hydrogenation. The higher content of CO_2, compared to that of CH_4 in the gaseous products by the spinel-derived catalysts indicates the higher H_2 selectivity of the former, likely due to a lowered acid to basic sites ratio and the high accessible metallic Ni surface. Among the promoted catalysts, the superior basicity of 5Mg/NiAl led to a more marked contribution of CO_2 than that of CH_4 in the produced gas phase. Metallic nickel dispersion and surface areas were significantly high, which would explain the enhanced hydrogenation activity of the spinel-derived catalysts, as pointed out by the composition of the liquid products, as well as their enhanced APR activity.

6.6 GENERAL OVERVIEW AND CONCLUSIONS

The physicochemical characterization of Ce- and Mg-modified solids indicated that nickel strongly anchored to the $NiAl_2O_4$ spinel structure, which improved nickel dispersion upon reduction. This could positively affect the catalytic activity of the studied samples, in terms of glycerol conversion and hydrogen selectivity. Addition of Mg and Ce limited the growth of metallic Ni particles upon reduction and increased the basicity. In general, Ce promoted the reducibility of the nickel species while Mg addition caused the opposite effect due to Ni-Mg interactions. Both modifiers slightly increased the catalyst selectivity to hydrogen. The main difference was reported in the glycerol conversion. It notably increased after Ce addition whereas it was slightly lowered after Mg addition. Furthermore, the modified catalysts achieved a gas stream with less CO and concomitant higher CO_2 concentrations, in agreement with the gas-phase WGS test where Mg and Ce showed promoted the WGS reaction. Regarding the obtained liquid-

phase products, catalysts showed a similar product distribution, being propylene glycol the most abundant product.

Characterization of the used catalysts indicated that both promoters improved the stability of the textural properties under APR conditions. Oxidation and leaching of metals are likely the main issues to be addressed in future investigations in order to seek stable catalysts that allow liquid-phase biomass upgrading.

Chapter 7

Nanocasting synthesis for the structural modification of $NiAl_2O_4$

This chapter addresses a morphological strategy for the optimization of the nickel aluminate spinel precursor, consisting in nanocasting synthesis of catalysts. In the first part of the chapter, a detailed description of the synthesis of SBA-15, supported spinel over SBA-15 (NiAl/SBA-15) and two nanocasted catalysts with different template-removal procedures (NiAl-NCF and NiAl-NCN) is reported. The second section addresses the physicochemical characterization of all the solids, examining their textural, acid-base, structural and compositional characteristics. The third section deals with the evaluation of the catalytic performance in the APR of glycerol, at 235 °C and 35 bar. Particular emphasis is put on the NiAl-NCN catalyst, including a comparison with reference NiAl catalyst over a range of glycerol conversions. Used samples are characterised to enlighten the changes that occur in APR conditions.

7. NANOCASTING SYNTHESIS FOR THE STRUCTURAL OPTIMIZATION OF $NiAl_2O_4$

Aiming acid-base properties modification in the surface of the catalyst by chemical modification leads to an improvement in H_2 production, although a limited one. Thus, a new strategy regarding the morphology and structure of the nickel aluminate is addressed by nanocasting synthesis, where an ordered mesoporous silica SBA-15 is used as hard template. Nanocasted samples could enhance the transport and diffusion of the reactants and products due to the ordered pore arrangement, providing shorter diffusion pathways and higher surface/volume ratio in comparison with coprecipitated catalysts [222]. Improvement in the catalytic performance for H_2 production with this strategy has been found by several authors [96, 123, 223, 224]. However, structured Ni catalysts have been mostly tested in the gas-phase reactions. The nanocasting synthesis of mixed oxides for Aqueous-Phase Reforming have not been reported yet. In this line, this chapter addresses the study of a novel nickel aluminate nanocasting synthesis for H_2 production by glycerol APR.

7.1 NANOCASTING SYNTHESIS

The synthesis of $NiAl_2O_4$ by nanocasting consists of several steps, as depicted in Figure 7.1. First, the siliceous hard template SBA-15 was synthesised by hydrothermal polymerization of silica. The following step entails the infiltration of the SBA-15 template with Ni and Al precursors, to obtain a solid with negative replica of the void structure of the template. Then, the target material (NiAl) was obtained by thermal treatment. Finally, the Ni-Al mixed oxide was recovered as a mesoporous replica by removal of the silica template. Two procedures were studied for SBA-15 removal in this final step: (i) basic-washing with a NaOH solution called hereafter NaOH etching; and (ii) calcination with Teflon. The followed synthesis steps are detailed below.

7.1.1 Hydrothermal synthesis of SBA-15

Hexagonally ordered mesoporous SBA-15 was synthesised by hydrothermal method [225]. An amphiphilic block copolymer (Pluronic, P123) is used as a

structure-directing agent, which provides the template for polymerization. TEOS is used as silica source (Table 2.1).

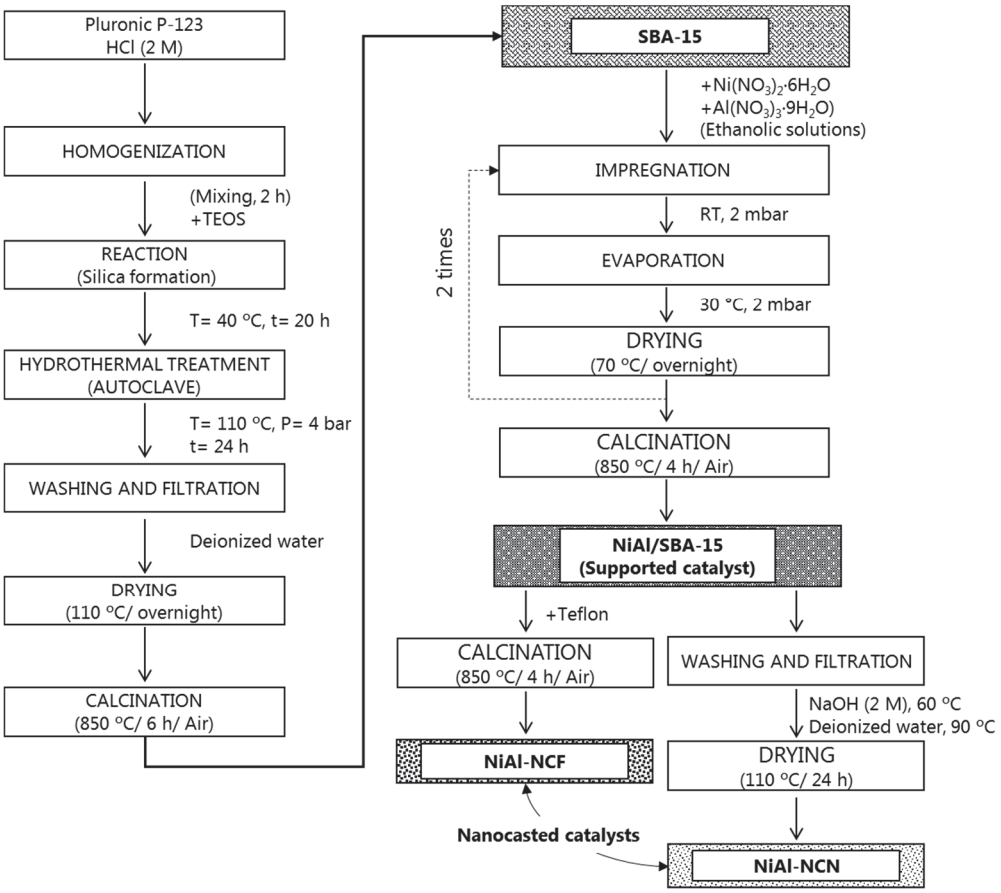

Figure 7.1. Scheme of the nanocasting synthesis of $NiAl_2O_4$.

For a typical synthesis of SBA-15, the Pluronic P123 (22.5 g) was dissolved in 700 ml of HCl solution (2 M), reaching acidic conditions to ensure ordered silica formation. The obtained solution was homogenised for 2 h by stirring. Then, TEOS copolymer (44 g) was quickly added into the solution. The mixture was stirred at 40 ºC for 20 h. The temperature employed avoided amorphous silica attainment, as well as the formation of silica gel. The mixture was transferred to a Teflon container and treated at hydrothermal conditions (110 ºC, 4 bar) for 24 h in a batch autoclave reactor (*Parr instruments*). The obtained white solid was collected by filtration and rinsed with 15 L of deionized water. Finally, the solid was dried at 110 ºC for 18 h in an oven and calcined at 850 ºC for 6 h, with a heating rate of 1 ºC·min^{-1}, in a muffle furnace. The obtained solid

is labelled hereafter as SBA-15. The chosen temperature and time were based to avoid large pores and thin walls in the obtained template [225].

7.1.2 Loading of metals over SBA-15

Both nickel and alumina precursors were incorporated to the SBA-15 template by wetness co-impregnation method using rota evaporator equipment. Ethanolic solutions of nickel(II) nitrate tetrahydrate and aluminium nitrate nonahydrate were used as metal precursors (Table 2.1), in a molar ratio 1 : 2, respectively. The mixture of SBA-15 and precursor solution were left for 1 h at 2 mbar vacuum, under rotation, to allow precursors to diffuse into SBA-15 pores by capillary motion. Then, the solvent was evaporated at the same pressure at 30 ºC for 5 h, approximately. The obtained solid was dried overnight at 70 ºC in an oven. This sequence was repeated twice in order to attain about 20% loading of the target solid over the SBA-15 template (8 g). Finally, after drying at 70 ºC, the solid was calcined in a muffle at 850 ºC for 4 h with a heating rate of 1 ºC·min^{-1}. This solid is named NiAl/SBA-15. It has been reported that a pore filling above 15% by metal oxides is enough to obtain high quality replicas [226].

Within the so-called NiAl/SBA-15 solid, the mesostructured silica template (SBA-15) is kept as support intended to provide high structural order to this catalyst. The other two parts were subjected to template removal.

7.1.3 Template removal

For the recovery of the NiAl mixed oxide, two methods were used for the SBA-15 template removal as further described in this section.

7.1.3.1 *NaOH etching*

The SBA-15 template was removed by etching the sample with 2 M NaOH aqueous solution at 60 ºC under constant stirring for 1 h. The silica removal in this procedure happens through the formation of Na_2SiO_3 in the reaction between the SBA-15 and the NaOH solution. After filtration, the remaining solid was washed twice, first with 400 mL of the NaOH solution, and subsequently with 800 mL of hot deionized water (90 ºC). Then, the wet solid was dried at 110 ºC for 24 h, to finally be pelletized at 0.04-0.16 mm. This replica is named NiAl-NCN.

7.1.3.2 *Teflon assisted removal*

A solid mixture of NiAl/SBA-15 and polytetrafluoroethylene (PTFE or Teflon) with a sample : Teflon mass ratio of 2 : 9, was thoroughly mixed by grinding in a mortar. The mixture was put under calcination in a muffle at 650 ºC for 4 h at a heating rate of 5 ºC·min^{-1}. This procedure, which eliminates the use of toxic HF, allows silica removal through the formation of SiF_4 by a reaction of silica to the in situ generated HF [222]. The replica was pelletized at 0.04-0.16 mm and labelled here as NiAl-NCF.

Before glycerol APR reaction tests and characterization, solids were reduced in-situ at 700 ºC under the same conditions as in previous chapters. For comparative purposes, the nickel aluminate spinel synthesized by co-precipitation (NiAl) is included in both, characterization, and activity analysis, as the reference catalyst.

7.2 CHARACTERIZATION OF NANOCASTED SOLIDS

7.2.1 Chemical composition

The bulk chemical composition of the solid determined by ICP/MS, is reported in Table 7.1. The Ni/Al molar ratio of NiAl/SBA-15 is higher than the nominal (0.6 vs 0.5). This ratio notably changes after template removal. On the one hand, when removal was carried out by NaOH etching, the Ni/Al ratio in NiAl-NCN solid increased by 17% (up to 0.74), associated specially to the leaching of aluminium. Apart from silica removal in NaOH solutions, aluminium can form sodium aluminate, which is soluble in water. On the other hand, the NiAl-NCF bulk Ni/Al ratio (0.48) is close to the theoretical one (0.5).

Table 7.1. Chemical composition of nanocasted solids.

Chemical composition	NiAl/SBA-15	NiAl-NCF	NiAl-NCN	NiAl
Ni/Al	0.60	0.48	0.74	0.49
Si (%)	55.80	2.93	1.17	n/a

ICP results for Si content indicate massive elimination of the hard template in NiAl-NCN and NiAl-NCF replicates, even though some residual silica remains left (< 3%). It seems that NaOH etching is more efficient that calcination with Teflon for silica removal.

7.2.2 Textural properties

N_2 adsorption-desorption isotherms and the BJH pore size distributions are shown in Figure 7.2. The SBA-15 template shows an isotherm of type IV with a well-developed hysteresis loop appearing in the 0.55-0.80 relative pressure range. The sharp adsorption and desorption branches indicate the presence of ordered and homogeneous mesopores [227]. The sharpness of the hysteresis loop ($P/P_0 \approx 0.07$) agrees with the narrow pore size distribution, which exhibits a sharp maximum between 4.2 and 7.2 nm.

The isotherms of the supported NiAl/SBA-15 solid also corresponds to type IV curves of mesoporous materials. Besides, it shows H2-type hysteresis loop characteristic of complex pore structures, in which the network effects are important [107]. Note that NiAl/SBA-15 shows hysteresis loop is less sharp than that of SBA-15 template (Figure 7.2), as well as a bulge in the desorption branch of the isotherm at about $P/P_0 \approx 0.05$, indicating a decreased homogeneity of the pores [227]. This in agreement with the lower average pore size of NiAl/SBA-15, which could result from inclusion of the metals within the porous structure of the SBA-15.

Similar to the SBA-15 template and the NiAl/SBA-15 solid, NiAl-NCN solid presents type IV isotherms characteristic of mesoporous materials with H2-type hysteresis. The isotherms of the nanocasted NiAl-NCF solid notably differs from others. It presents a type V isotherm and H3 hysteresis, related to layered material of large pore width [107], probably within the mesopores to macropores range.

Regarding the pore size distribution, a bimodal distribution of pores size for NiAl/SBA-15 solid was observed, with a new larger peak at lower pore width values than those for the unimodal distribution of the SBA-15 template, which is associated to the NiAl mixed oxide filling of SBA-15 pores. NiAl-NCN presents unimodal pore size distribution with a maximum at similar pore width to that of NiAl/SBA-15. Contrarily, NiAl-NCF shows a wide unimodal distribution at much larger pore widths.

The textural properties are presented in Table 7.2. Hydrothermal synthesis with calcination at 850 ºC yields to an SBA-15 material with a specific surface area of 459 $m^2 \cdot g^{-1}$, average pore diameter of 5.5 nm and a pore volume of 0.76 $cm^3 \cdot g^{-1}$. Co-impregnation of Ni and Al over SBA-15 diminishes the BET surface area and the pore

volume by 54% and 61%, respectively, indicating a significant pore filling of the mesoporous template within NiAl/SBA-15 solid.

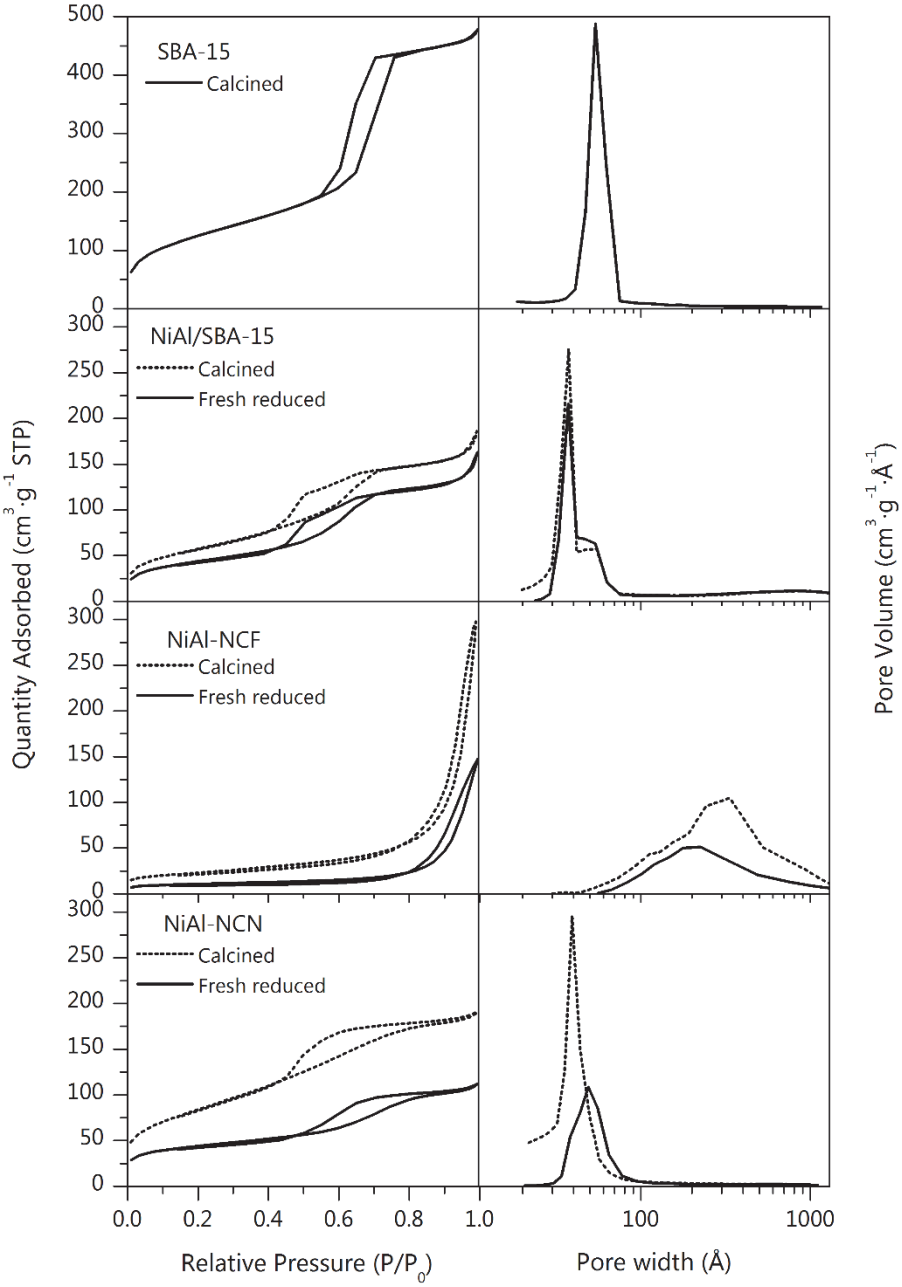

Figure 7.2. N_2 adsorption-desorption isotherms and pore size distributions of SBA-15, NiAl/SBA-15 and nanocasted catalysts in their calcined and reduced forms.

Table 7.2. Textural properties for SBA-15, NiAl/SBA-15 and nanocasted solids.

	Sample	S_{BET} ($m^2 \cdot g^{-1}$)	Vp ($cm^3 \cdot g^{-1}$)	Dp (nm)
CALCINED	SBA-15	459	0.76	5.5
	NiAl/SBA-15	210	0.30	4.7
	NiAl-NCF	81	0.46	22.1
	NiAl-NCN	306	0.33	3.9
	NiAl	98	0.27	8.4
FRESH REDUCED	NiAl/SBA-15	158	0.26	5.5
	NiAl-NCF	38	0.22	20.9
	NiAl-NCN	155	0.15	5.4
	NiAl	83	0.29	10.8

Nanocasted catalysts present different S_{BET} tendencies associated to the template removal method. Compared to the NiAl/SBA-15 supported solid, NiAl-NCF shows an important pore collapse, since its S_{BET} decreases by 62% after removal of the SBA-15. Moreover, its S_{BET} is even lower than that of NiAl catalysts. In addition, NiAl-NCF presents a big increase in the average pore diameter (22.1 vs 4.7 nm).

Regarding NiAl-NCN, it presents a S_{BET} of 306 $m^2 \cdot g^{-1}$, being almost 3 times higher than the coprecipited NiAl, and 1.5 times higher than that of NiAl/SBA-15. In NiAl-NCN solid, the pore volume and average pore width are almost preserved. These observations suggest the formation of a wormhole-like rod structure after removal of the siliceous template, which could be formed due to an incomplete filling of the pores during the impregnation step [223]. It is worth mentioning that after solvent evaporation and calcination, the volume of the obtained oxide is much smaller than that of the nitrate precursors (the shrinkage ratio of the metal nitrate solids to oxides is ~16) [228].

N_2 physisorption of fresh reduced solids (at 700 ºC, 1 h) was also measured and results are presented in Figure 7.2 and Table 7.2. In general, the N_2 physisorption capacity of fresh reduced solids is lower than that of calcined ones, indicating a decrease in S_{BET} upon reduction. However, no important differences are observed in the shape of the isotherms. Regarding the pore size, similar distributions are observed for both the calcined and reduced forms of NiAl/SBA-15 solid. Instead, the NiAl-CNF distribution is slightly shifted to the left, whereas that of NiAl-NCN shifted to the right and widened. The shift suggests changes in the pore's morphology.

After reduction, S_{BET} of the supported NiAl/SBA-15 sample decreases by 25%, while its Dp and Vp are almost unvaried respect to its calcined form. For nanocasted solids, S_{BET} decreases by 54% and 49% for NiAl-NCF and NiAl-NCN respectively, after the reduction treatment. Concomitantly, Vp decreases by ca. 50% for both nanocasted solids. The average pore size increases for NiAl-NCN and preserved for NiAl-NCF.

The parent NiAl solid seems to present higher textural stability to reduction treatment. Nonetheless, NiAl/SBA-15 and NiAl-NCN still present higher S_{BET} than NiAl.

7.2.3 Phases and morphology

The low-angel XRD patterns from the SBA-15 template and NiAl/SBA-15 supported solid are shown Figure 7.3. The 2-D hexagonal (*p6mm*) mesoporous structure of the SBA-15 is confirmed by the diffraction peaks at 1.2º, 1.8º, 2.1º 2θ, accompanied by scattered reflections in the 2.4º-3.6º 2θ region.

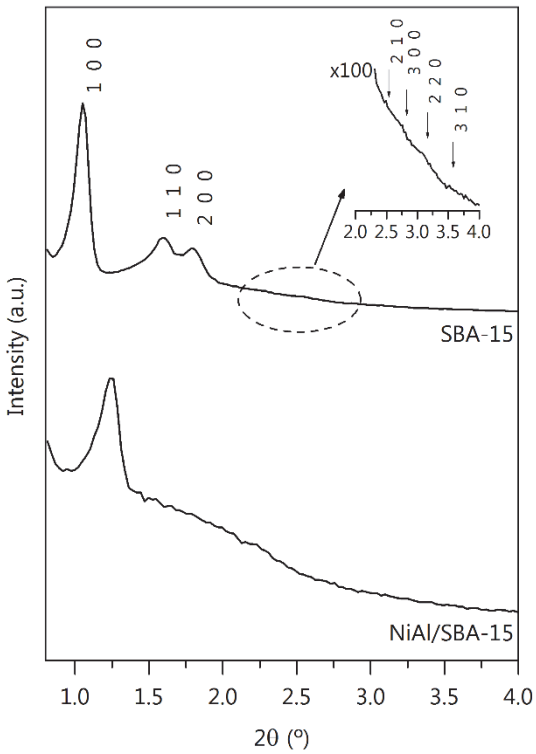

Figure 7.3. Low-angle XRD diffractogram for calcined SBA-15 and NiAl/SBA-15 solids.

The unit cell spacing a_0, which corresponds to the distance between the centres of two adjacent pores, was calculated from the cell spacing value for the (1 0 0) plane. Also, the wall thickness W_t was calculated by subtracting the average pore diameter to the unit cell spacing. The obtained a_0 and W_t are presented in Table 7.3.

Table 7.3. Structural characteristics of calcined SBA-15 and NiAl/SBA-15 solids.

Sample	$d_{(1\,0\,0)}$ (nm)	a_0 (nm)	W_t (nm)
SBA-15	7.9	9.1	3.6
NiAl/SBA-15	7.1	8.2	3.5

The intense (1 0 0) peak of SBA-15 (Figure 7.3) and the corresponding a_0 indicate a large unit-cell parameter of the template (9.1 nm), with a pore wall thickness of 3.6 nm. Nonetheless, a_0 is slightly lower than others reported in literature [229, 230], owing to the high calcination temperature employed.

The low-angle XRD pattern of NiAl/SBA-15 shows a single strong peak corresponding to (1 0 0) peak, which upshifts in 2θ (1.25º). Therefore, this solid presents even smaller unit cell spacing (8.2 nm). The wall thickness is almost the same as the SBA-15 template. The absence of well-pronounced (1 0 0) and (2 0 0) reflections for NiAl/SBA-15 suggests a lower structural ordering, which could be associated to incomplete pores filling during the decomposition of the metal nitrate precursors by the impregnation [231]. Nonetheless, the presence of the peak (1 0 0) in the diffractogram from NiAl/SBA-15 points to the thermal and structural stability of the as-synthesized SBA-15, which does not present significant structural shrinkage at the high calcination temperature treatment (850 ºC).

Wide-angle XRD diffractograms for all calcined solids are presented in Figure 7.4. All samples, except NiAl, present a large bump distributed in a wide range of 2θ values, indicating the presence of amorphous silica. Besides, these diffractograms show features of the nickel aluminate spinel at around 37.1º, 44.9º, 59.7º and 65.5º 2θ for all samples.

In the case of the NiAl/SBA-15 solid, it also shows peaks at 37.4º, 43.7º, and 63º 2θ related to cubic NiO. The formation of NiO in NiAl/SBA-15 is promoted by the interactions of both metals with the siliceous cast. The broad elevation of the background at 22.3º 2θ is associated with amorphous SiO_2.

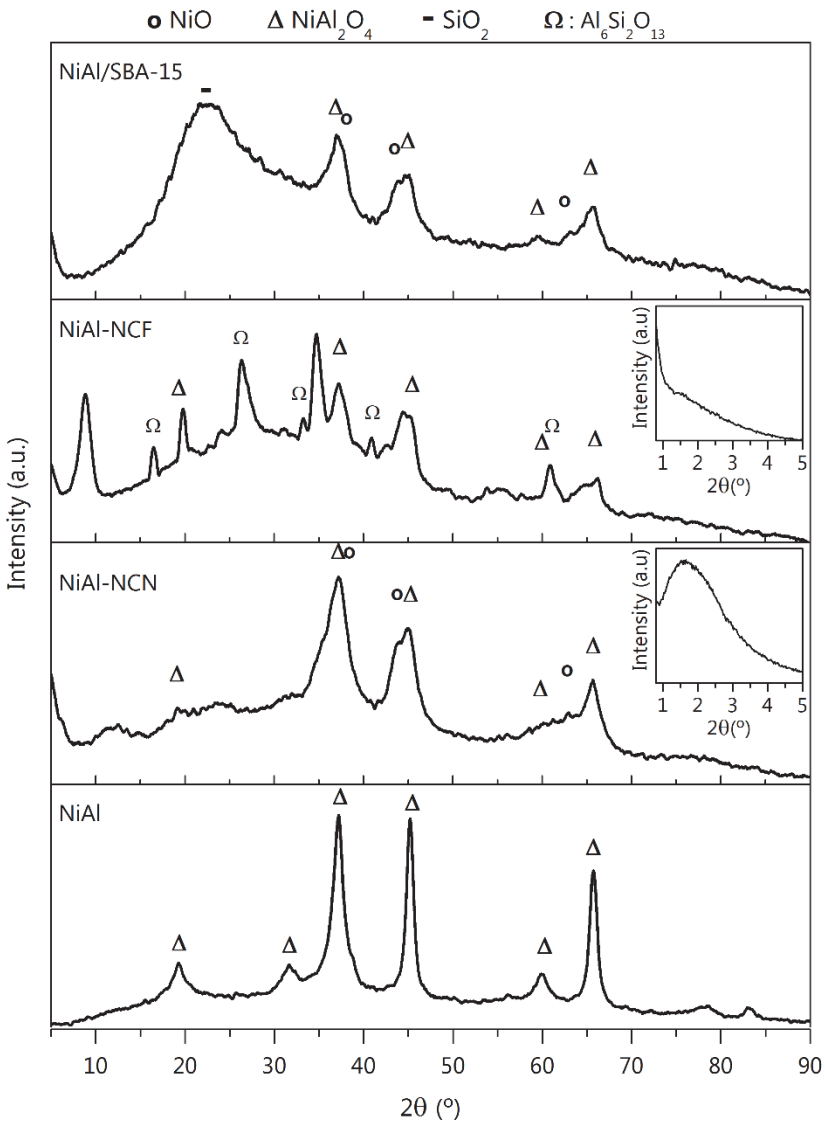

Figure 7.4. XRD diffraction patterns of calcined NiAl/SBA-15 and nanocasted solids. Insets include small angles.

Regarding the calcined nanocasting solids, NiAl-NCN solid also presents peaks from cubic NiO, which is associated to the leaching of Al, and the resulting Ni/Al ratio increase. Meanwhile, spinel characteristic features appear slightly shifted to the right in NiAl-NCF diffractogram. Formation of aluminium silicate (mullite) (JCPDS 015-0776) is suggested by the presence of intense diffraction peaks at 16.5º, 26.4º, 33.2º, 40.8º and 60.9º 2θ. Other diffraction signals at 8.72º, 34.7º, 42º, 44.3º, 64.1º 2θ could not be

identified, although the formation of new species during the calcination with Teflon is highly probable.

The low-angle XRD patterns for both nanocasted samples are also included in the inset of Figure 7.4. On the one hand, NiAl-NCN presented a peak at small angles corresponding with the 2-D structure (1 0 0), suggesting a wormhole-like rod structure replica of SBA-15 after NaOH etching. The broadness and not well resolved *p6mm* reflections, indicate hollow framework interference with the diffraction lines [223]. On the other hand, the diffractogram of low-angle of NiAl-NCF seems linear, which could be due to a structural deterioration owing to the second calcination at the high temperature with Teflon.

XRD analysis was also carried for fresh reduced solids and results are shown in Figure 7.5. Upon reduction, diffraction peaks from metallic nickel emerge in all catalysts. Nonetheless, peaks from $NiAl_2O_4$ spinel phase remain suggesting that the employed reduction temperature (700 ºC) is not high enough to take out all the Ni^0 from the spinel framework.

By comparing the intensity and the width of the spinel diffraction signals, it is concluded that the remaining spinel in NiAl/SBA-15 and nanocasted solids are less crystalline than that in the parent NiAl sample. The presence of γ-Al_2O_3 cannot be discarded. As occurs in its calcined form, peaks from mullite are still observed in NiAl-NCF fresh reduced, though with much less intensity.

Metallic nickel crystal size was calculated from the related maximum intensity peak, and results are presented in Table 7.4.

Table 7.4. Crystallite size of metallic nickel and exposed metal surface

Catalyst	Ni^0 particle size (nm)		Ni^0 Dispersion[a] (%)	Metallic surface area[a] ($m^2_{Ni^o} \cdot g^{-1}$)
	XRD	TEM		
NiAl/SBA-15	24.3	n.d.	n.d.	n.d.
NiAl-NCF	27.7	31.7	3.2	3.8
NiAl-NCN	6.7	9.0	12.0	17.9
NiAl	16.0	12.0	10.0	14.1

[a] From TEM analysis.

In general, the metallic nickel crystallite size calculated from XRD are bigger than that of NiAl, except for NiAl-NCN, which has the smallest Ni^0 (6.7 nm). The usage of the hard siliceous cast (SBA-15) in the $NiAl_2O_4$ synthesis aims to improve the structure of the samples, control crystal growth and improve dispersion of the active phase.

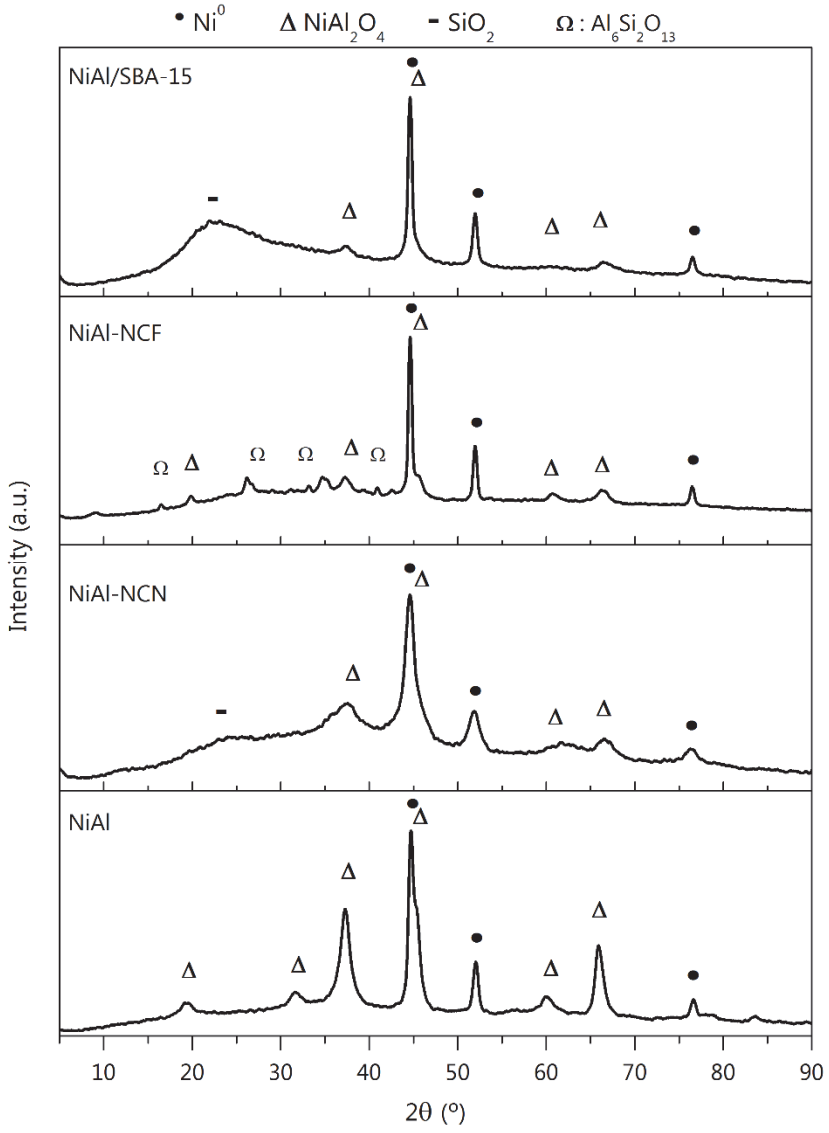

Figure 7.5. XRD patterns of fresh reduced NiAl/SBA-15 and nanocasted solids.

7.2.4 Dispersion and morphology by TEM

The morphology of the hydrothermally synthesised SBA-15 template, NiAl/SBA-15 and the nanocasted solids was analysed by TEM microscopy in their calcined form, and the obtained images are shown in Figure 7.6. Besides, micrographs from fresh reduced nanocasted solids are obtained (Figure 7.7) and the metallic nickel particle size distribution was determined by measuring the diameter of at least 240 particles. Other characteristics like the Ni^0 dispersion and metallic surface area were also estimated (Table 7.4).

An ordered mesoporous network is seen in the high resolution TEM image of SBA-15 template. It shows long-parallel channels of pores of an estimated size of 4.5 nm, measured through image analysis, in line with that from N_2 physisorption (Dp= 4.7 nm). Besides, the distance between the centres of the channels walls is 9.2 nm, in agreement with the unit cell spacing estimated from XRD (see Table 7.3).

NiAl/SBA-15 shows a partial filling of mesopores by the mixed oxide, as N_2 physisorption results also indicates. Besides, metal oxide particles of different sizes and shapes are observed. On the one hand, irregular particles with a size of about the diameter of the SBA-15 channel, corresponding to spinel formed inside the hexagonal structure, indicated controlled particle growth. On the other hand, spherical and larger particles formed outside the channels. Nevertheless, NiAl/SBA-15 micrographs indicate a good dispersion of the nickel aluminate.

After template removal, TEM micrographs of NiAl-NCF and NiAl-NCN calcined samples display closer particles, with homogeneous morphologies and approximate sizes. It confirms the wormhole-like rod structure for these samples, as also revealed by their S_{BET} and low-angle diffractograms. Besides, in Figure 7.6 one can notice clear differences of nanocasted samples with respect to parent NiAl catalysts, where NiAl shows more heterogeneous particles morphologies with less particle density and ordering.

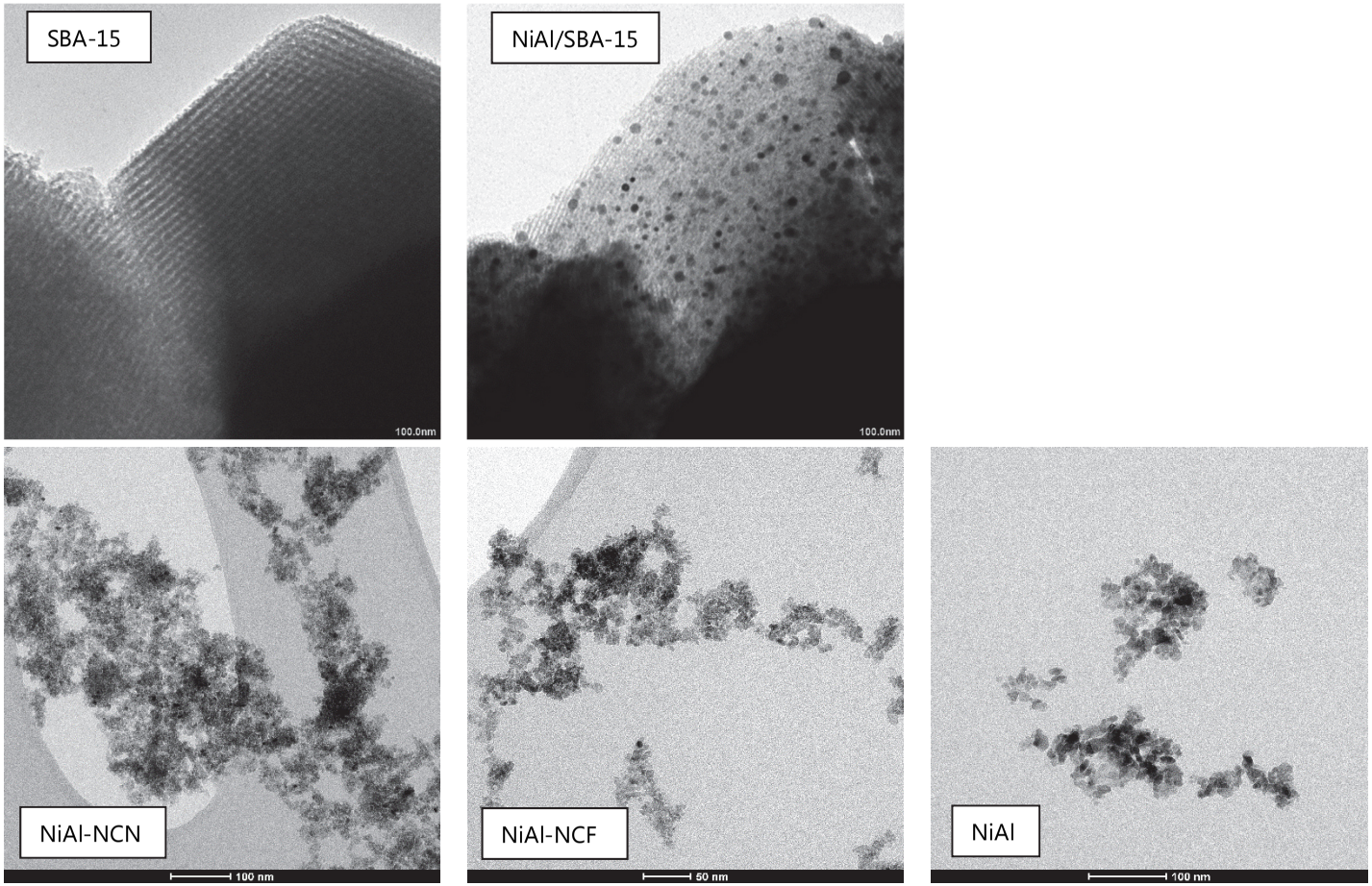

Figure 7.6. TEM images of calcined SBA-15, NiAl/SBA-15, nanocasted and NiAl solids.

Nickel particles are clearly visible in TEM images of fresh reduced nanocasted catalysts, those consist of metallic crystallite agglomerates as can be observed in Figure 7.7.

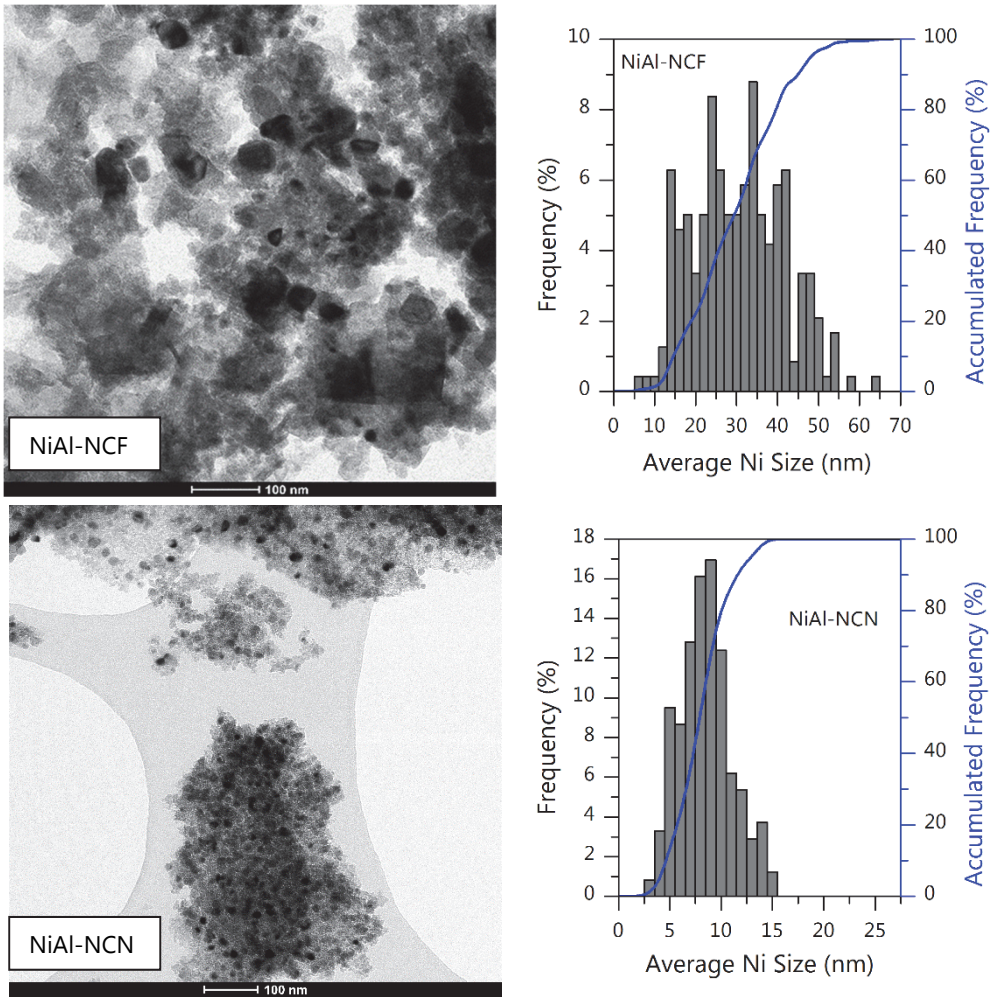

Figure 7.7. TEM images and Ni^0 particle size distribution of fresh reduced nanocasted solids.

NiAl-NCF catalysts contain agglomerates of Ni^0 particles of different shapes. Indeed, cubic Ni^0 particles are observed for those with larger sizes. Calcination with Teflon leads to a wide particle size distribution (Figure 7.7), from 11 to 50 nm, approximately. In the case of the NiAl-NCN solid, nearly spherical-shaped metallic Ni particles are observed, with a homogeneous and ordered appearance. Once again, the wormhole-like rod

structure is evidenced. The Ni^0 particle size distribution is much narrower than that of NiAl-NCF, with unimodal distribution with a maximum at 9 nm.

Among the nanocasted solids, NiAl-NCF contains the biggest metallic Ni particles with an average size of 31.7 nm (Table 7.4), in accordance with XRD results. The Ni^0 average size for NiAl-NCN is 3.5 times smaller than in NiAl-NCF. Consequently, significantly higher dispersion of Ni^0 (12% vs 3.2%) and metallic surface area (17.9 vs 3.8 $m^2_{Ni^0} \cdot g^{-1}$) are observed for NiAl-NCN as compared to NiAl-NCF.

Based on the TEM micrographs, it can be concluded that the nanocasted synthesis is highly influenced by the template removal procedure. It has been seen that the Teflon-assisted removal approach worsens the Ni^0 accessibility in the obtained catalyst. Nickel in form of phases not detected by XRD cannot be discarded.

The nanocasted NiAl-NCN solid presents higher Ni^0 surface area than NiAl. These results suggest that the nanocasted synthesis (with NaOH etching) of nickel aluminate spinel limited the surface mobility of the metallic Ni particles during the reduction stage, possibly due to the nanocasting structural input controlling particle growth, and the improved interaction of Ni with the sample environment (Ni-O-Al).

7.2.5 Reducibility and speciation

Reducibility analysis was carried out by H_2-TPR. The obtained profiles of calcined (TPR_{950}) and fresh reduced samples ($TPR_{700\text{-}950}$) are depicted in Figure 7.8. Similar to parent NiAl, all calcined solids present peaks in three temperature zones, namely α, β and γ, which are related to the H_2 consumption at low, medium and high temperatures respectively, owning to the different reducibility grade of the Ni^{2+} species, as discussed in Chapter 4.

For all the samples, the α-peak is located at below 500 ºC, indicating the existence of bulk NiO with low interaction with the surroundings and thus, easily reducible. Similar to parent NiAl, β peaks are observed at temperatures between 550-700 ºC. Recall that β_1 peak (at lower temperatures) corresponds to reduction of NiO phase with strong interaction with the support (or remaining phases), in the form of smaller NiO particles. Instead, β_2 peak (at higher temperatures) is related to NiO tied by Al-rich phase and/or to the presence of a defective spinel phase ($Ni_{1-X}Al_2O_{4-X}$). The TPR profile could also

include the reduction of Ni^{2+} interacting with silica in this region [224]. Finally, peaks above 700 ºC in the reduction profiles are related to γ-type species, confirming the presence of nickel in the spinel framework, as found in XRD.

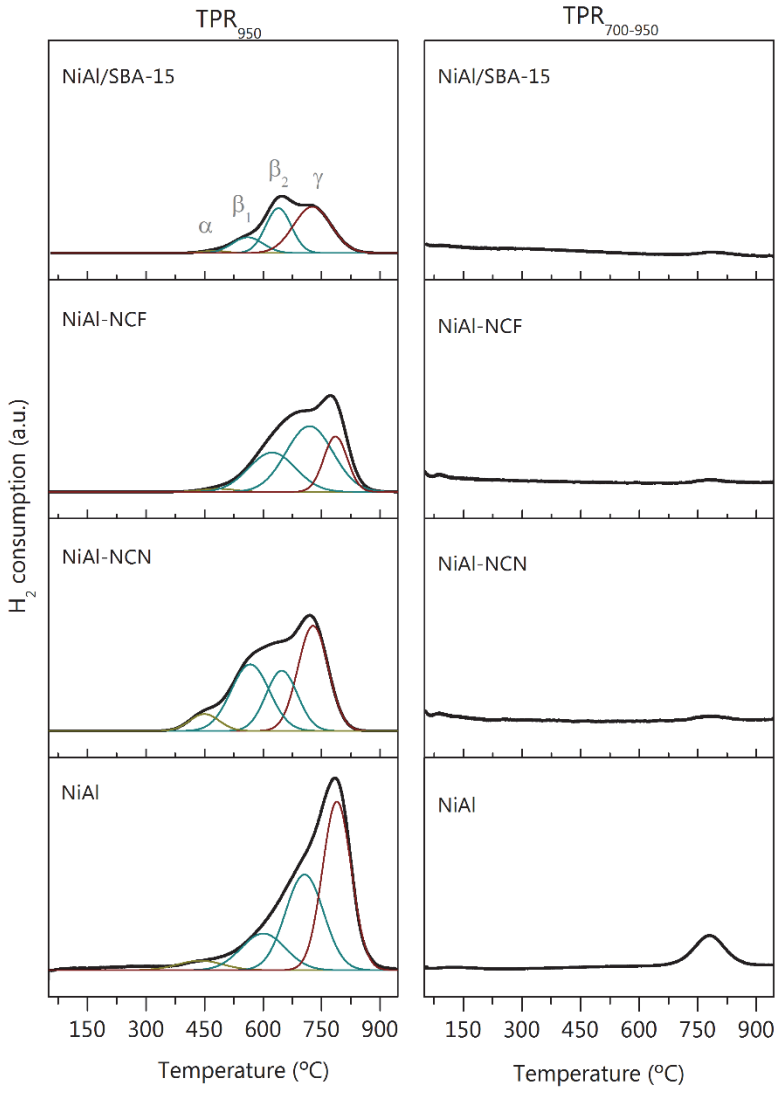

Figure 7.8. H_2-TPR profiles of NiAl/SBA-15 and nanocasted solids. TPR_{950}: reduction profile of calcined sample; $TPR_{700\text{-}950}$: reduction profile of fresh reduced catalyst.

The hydrogen consumption in TPR_{950} is reported in Table 7.5. The complete reduction of Ni species in the calcined samples are accomplished, since remarkably close

consumption values to that of theoretical values are found (within the experimental error). All the solids present the same nickel species, though differences in the left tail (below 700 ºC) points to different distribution of Ni^{2+} species, as shown in Table 7.5. NiAl/SBA-15 and NiAl-NCF calcined solids have lower α-peaks contribution than NiAl-NCN and NiAl. On the other hand, both nanocasted calcined solids (NiAl-NCN and NiAl-NCF) present higher proportion of β-type nickel species than that of the supported NiAl/SBA-15 solid.

NiAl/SBA-15 presents similar contribution of γ-type nickel species than NiAl parent sample. Nonetheless, once the template is removed the proportions of γ-type nickel fall to 20.6% and 39.1% for NiAl-NCF and NiAl-NCN, respectively. It could be directly associated to the nanocasting synthesis enhancing NiO formation due to SBA-15 interference during the formation of nickel aluminate (calcination step), as well as to the imbalance of Ni-Al stoichiometric proportion due to losses during template removal. Those factors could inhibit the total nickel transformation to $NiAl_2O_4$. NiAl-NCN presents the highest proportion of easily reducible NiO (α-type) and the smallest Ni^0 crystallites (Table 7.4). This confirms that the growth of the crystal is mastered by the SBA-15 framework and its structural input to the NiAl-NCN solid.

Compared to the reduction profile of parent NiAl, the lower temperature of the γ peak for NiAl-NCN (730 ºC vs 790 ºC) suggests an improvement of spinel reducibility, possibly being influenced by the higher amount of metallic Ni formed during reduction of those majority β species, which would enhance the spinel reduction by H_2 spillover.

As one can notice from the $TPR_{700-950}$ profile (Figure 7.8), fresh reduced solids only show weak reduction peaks at high temperatures, which is associated with remaining non-reduced $NiAl_2O_4$ after pre-reduction treatment at 700 ºC. This is in line with the f_{red} found (Table 7.5).

Table 7.5. Results of H_2-TPR for NiAl/SBA-15 and nanocasted solids.

Sample	Calcined					Fresh reduced		
	H_2-TRP$_{950}$ consumption	Nickel speciation				H_2-TPR$_{700-950}$ consumption	f_{red}	Ni^0 content
	(mmol $H_2 \cdot g^{-1}$)	α (%)	β_1 (%)	β_2 (%)	γ (%)	(mmol $H_2 \cdot g^{-1}$)	(%)	(mmol $H_2 \cdot g^{-1}$)
NiAl/SBA-15	2.0	1.7	14.2	33.6	50.6	0.22	88	1.8
NiAl-NCF	4.0	1.6	29.1	48.6	20.6	0.10	98	3.9
NiAl-NCN	5.2	6.2	31.4	23.3	39.1	0.16	97	5.0
NiAl	5.6	4.1	15.4	34.7	45.9	0.56	79	4.4

The fraction of the nickel that has been reduced (f_{red}), which was accomplished with the pre-treatment at 700 ºC (1 h), was calculated from the hydrogen consumption in both steps of the $TPR_{700-950}$ (Table 7.5). NiAl/SBA-15 and nanocasted solids present higher f_{red}, than NiAl. In decreasing order, it is: NiAl-NCF> NiAl-NCN> NiAl/SBA-15> NiAl.

In general, the nanocasted solids show better reducibility than NiAl due to the higher contribution of β-type and lower of γ-type nickel species, and thus higher reduction fraction of nickel is accomplished upon pre-reduction treatment.

7.2.6 Surface acid-base properties

The CO_2-TPD profiles for fresh reduced are shown in Figure 7.9. The basic sites strength assignation was carried according to the desorption temperature [96, 104, 232], as detailed in Chapter 4. All solids present a desorption peak below 110 ºC, due to weak basic sites. Medium-strength basic sites, in a desorption range at 130-200 ºC, are displayed only by NiAl-NCN, like NiAl. As opposed to NiAl catalysts, NiAl/SBA-15 and both nanocasted catalysts do not show strong basic sites (at around 300 ºC). Finally, low intensity peaks above 800 ºC are detected for all the solids and can be associated to either carbonates formed during calcination steps or dehydroxylation processes. The intense peak above 800 ºC displayed by NiAl/SBA-15 solid could be due to the release of decomposition gases of precursors, that have been trapped in the siliceous template.

The total basic and acid sites density for fresh reduced solids are shown in Table 7.6. Accordingly, nanocasted solids present higher basic sites density than that of parent NiAl/SBA-15, nonetheless these solids have much lower basic sites density than reference NiAl, e.g. NiAl/SBA-15 shows ~9 times lower basicity than that of NiAl.

Table 7.6. Acid-base properties of NiAl/SBA-15 and nanocasted fresh reduced solids

Sample	Acid/base ratio	Acidity μmol $NH_3 \cdot m^{-2}$	Basicity μmol $CO_2 \cdot m^{-2}$
NiAl/SBA-15	7.2	0.93	0.13
NiAl-NCF	15.7	5.64	0.36
NiAl-NCN	2.7	1.73	0.64
NiAl	1.7	1.95	1.12

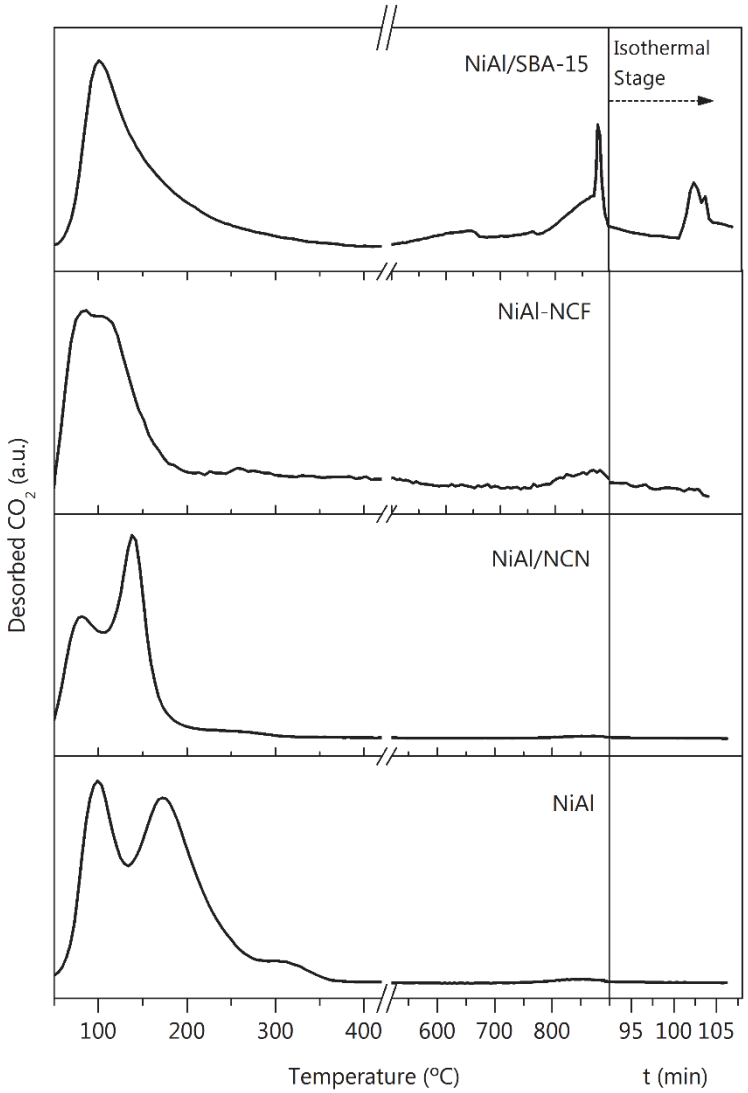

Figure 7.9. CO_2 desorption patterns of NiAl/SBA-15 and nanocasted solids.

NiAl/SBA-15 has less density of acid sites than NiAl (0.93 vs 1.95 μmol $NH_3 \cdot m^{-2}$), this is due to the two-fold higher S_{BET} of NiAl/SBA-15 (Table 7.2). In this line, NiAl-NCN also present low density of acid sites. It is well known that the acidity is mainly provided by alumina since SBA-15 is almost non-acidic [233]. Therefore, the less acidic nature of NiAl/SBA-15 and NiAl-NCN could also be related to their lower alumina content in comparison with NiAl, as found by ICP. An exception is found in NiAl-NCF, in which the acidity is distributed in the lowest specific surface area (38 $m^2 \cdot g^{-1}$).

The acid/base ratio increases for supported and nanocasted solids with respect to NiAl, especially for NiAl-NCF, which has ~9 times higher ratio than NiAl. The amphoteric nature of the Al_2O_3 affects the acidity of the samples more significantly than SiO_2 does. At the same time, the high specific area holds a dilution effect on the acid nature of the NiAl-NCN, while the presence of silica suppresses basicity in NiAl/SBA-15.

7.3 GLYCEROL APR WITH NiAl/SBA-15 AND NANOCASTED CATALYSTS

Useful physicochemical characteristics are found for catalysts synthesised by nanocasting methodology. Superior BET areas, some mesostructured order and high reducibility are in general, the improved physicochemical characteristics of these samples. Besides, control growth of Ni^0 crystals was found in the solids that present structural ordering. Thus, the influence of the followed nanocasting structural strategy on the glycerol APR is discussed in this section

7.3.1 Catalytic performance

First, the solids were reduced in-situ at 700 ºC for 1 h. The APR tests were performed at 235 ºC/ 35 bar, with a space velocity of 24.5 h^{-1}, using an aqueous feed solution of 10 wt.% glycerol. The catalytic performance results are reported for 2 h steady state.

Results for the conversions (X_{Gly} and X_{Gas}) and H_2 yield are shown in Figure 7.10. NiAl/SBA-15 and NiAl-NCF are much less active than the parent NiAl catalyst (X_{Gly} of 6% and 19%, respectively). Accordingly, both achieve very low hydrogen yield, below 2%. For NiAl-NCN catalysts both X_{Gly} and X_{Gas} boosted to 80% and 40%, respectively, higher than those for NiAl (X_{Gly}: 64%; X_{Gas}: 27%). Besides, NiAl-NCN presents the highest hydrogen yield (9.4%).

The superior performance of NiAl-NCN can be associated to its improved metallic Ni accessibility (Table 7.4). Also, its two-fold higher specific surface area, with highly open porous structure (wormhole-like rod) could facilitate the diffusion throughout the solid [223].

The large Ni^0 size and the very low metallic nickel surface area could explain the very poor performance of NiAl-NCF catalyst. In the case of supported NiAl/SBA-15 catalyst, the encapsulation of Ni^0 inside the SBA-15 channels could hinder its availability

for reactants. Moreover, NiAl/SBA-15 presents 50% bigger Ni^0 crystallites than those for NiAl.

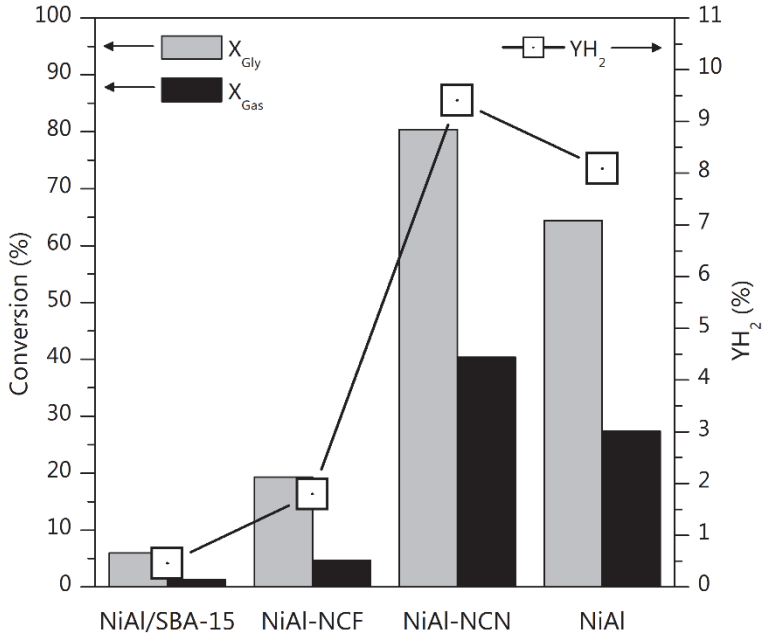

Figure 7.10. Glycerol conversion, conversion to gas and hydrogen yield for nanocasted catalysts. Reaction conditions: 235 ºC/35 bar, WHSV= 24.5 h^{-1}. Reaction time: 2 h.

The analysis of the gas stream is shown in Figure 7.11 and detailed in Table 7.7. NiAl-NCN catalyst also improves the production of gaseous products, as its F_{Gas} is 1.4 times higher than that of NiAl. In this line, the selectivity to gas in decreasing order is: NiAl-NCN> NiAl> NiAl-NCF> NiAl/SBA-15, being ~50% lower for NiAl/SBA-15 and NiAl-NCF than for NiAl.

Table 7.7. Gas-phase characteristics for nanocasted samples in the glycerol APR.

Catalyst	F_{Gas} ($mmol \cdot g_{cat}^{-1} \cdot min^{-1}$)	S_{Gas} (%)	H_2/CO_2	CO_2/CH_4
NiAl/SBA-15	0.01	21	12.9	0.6
NiAl-NCF	0.09	24	3.6	1.2
NiAl-NCN	0.66	50	1.4	1.3
NiAl	0.48	42	1.8	1.5

As observed in Figure 7.11, H_2 is the most abundant gas product for all catalysts, followed by CO_2 and CH_4. Other compounds like CO and C2+ are found in much lesser concentrations.

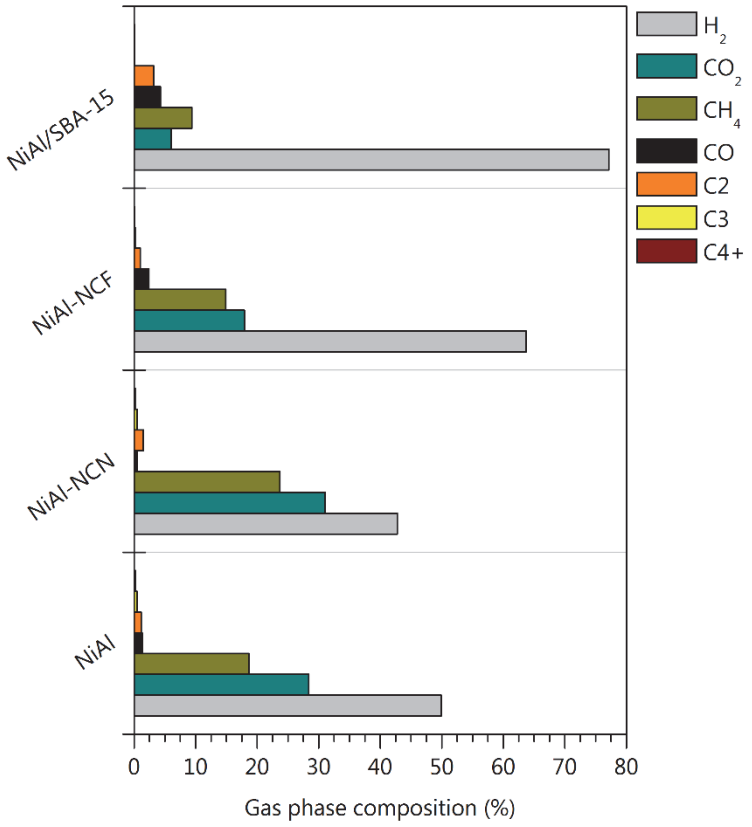

Figure 7.11. Gas-phase composition of glycerol APR over nanocasted catalysts. Reaction conditions: 235 ºC/35 bar, WHSV= 24.5 h^{-1}. Reaction time: 2 h.

NiAl achieved higher concentration in H_2 and lower in CH_4 than NiAl-NCN, indicating that the improvement in H_2 yield for NiAl-NCN catalyst also favours methanation reaction, where the produced hydrogen is consumed. Anyway, the H_2 production rate of NiAl-NCN catalyst (0.28 mmol $H_2 \cdot g^{-1} \cdot min^{-1}$) is 20% higher than that of NiAl. The gas streams from the less active catalysts are largely composed of H_2 (NiAl/SBA-15: 77%; NiAl-NCF: 65%). The H_2 production rate of both catalysts is 5-36 times lower than NiAl-NCN. Regarding the low concentration of CO in the gas stream for all catalyst tested (< 4.2%), recall that the nickel aluminate spinel precursor is effective to catalyse WGS reaction at the temperature and pressure conditions used in

the APR. Far less extent for production of other C-containing compounds, like C2 (<3%), C3 (<0.5%) or C4+ (<0.2%) is found, proving the low degree of occurrence of Fisher-Tropsch reactions.

Contrary to NiAl and NiAl-NCN, the H_2/CO_2 ratio for NiAl/SBA-15 and NiAl-NCF catalysts (3.6-15.5 range) are notably higher than the stoichiometric ratio. Despite the low conversion obtained for those catalysts, their high H_2 concentration led to higher H_2/CO_2. For NiAl-NCN catalysts, the H_2/CO_2 ratio is lower than that of NiAl (1.4 vs 1.8). Indeed, the CO_2/CH_4 for those samples suggest H_2 consumption by side reactions, such as CO hydrogenation (methanation).

Figure 7.12 depicts the H_2 and CH_4 selectivity. SH_2 increases in the order: NiAl/SBA-15< NiAl-NCF< NiAl-NCN< NiAl. On the other hand, SCH_4 shows a maximum for NiAl-NCN with 45.7% (vs 32.8% of NiAl). The two less active catalysts present SCH_4 below 15.2%.

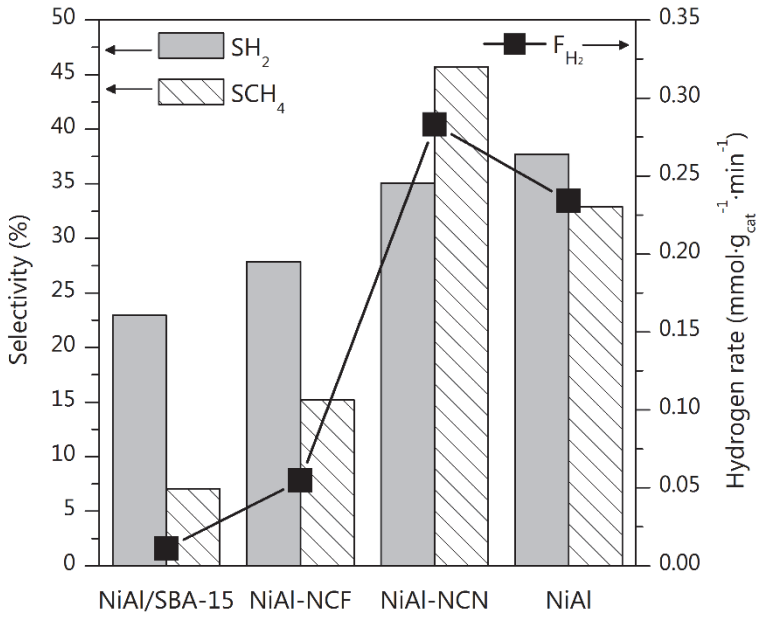

Figure 7.12. Selectivity to H_2 and CH_4, and H_2 production rate for nanocasted catalysts. Reaction conditions: 235 ºC/35 bar, WHSV= 24.5 h^{-1}. Reaction time: 2 h.

Results evidenced promotion of side reactions with H_2 consumption, by both the high availability of H_2 accomplished by NiAl-NCN catalyst and its high Ni^0 accessibility.

In addition, an increase in the H_2 partial pressure inhibits the reforming reaction; hence, the H_2 is consumed in methanation [50, 157]. As a drawback, NiAl-NCN has a 40% larger H_2 production rate than that of NiAl, and at the same time NiAl-NCN shows the highest selectivity to methane (SCH_4= 45.7%), while other catalysts present much less SCH_4 as shown in Figure 7.12.

In view of the very poor performance of NiAl/SBA-15 and NiAl-NCF catalysts, the analysis of the liquid stream was focused on the comparison of the two most active catalysts, i.e., NiAl-NCN and NiAl. Results of the liquid stream composition are shown in Figure 7.13.

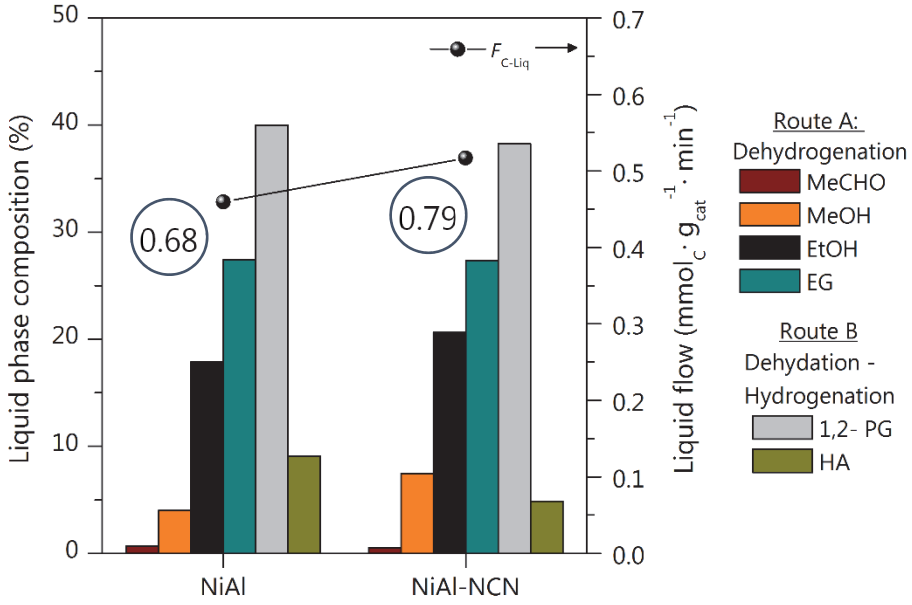

Figure 7.13. Molar composition of the main liquid products and total produced liquid flow by nanocasted catalysts. In circles: Route A/Route B products ratio. Reaction conditions: 235 ºC/35 bar, WHSV= 24.5 h^{-1}. Reaction time: 2 h.

For both catalysts, the main liquid compound is 1,2-PG, followed by EG and EtOH. There are no major differences between these catalysts, but a slightly minor concentration of route B products are obtained by NiAl-NCN, as reflected by the increase of Route A/Route B product ratio to 0.79. This can be related to the slightly lower density of the acid sites of this nanocasted catalyst (Table 7.6).

It can be inferred that for both catalysts C-O bond cleavage for liquid production is taking place. Nonetheless, NiAl-NCN molar flow of liquid products is 0.52 $mmol_C \cdot g_{cat}^{-1} \cdot min^{-1}$, being 12% higher than NiAl liquid flow.

7.3.2 Comparison of NiAl-NCN and NiAl catalysts performance over a range of X_{Gly}

Nanocasted NiAl-NCN showed an enhanced X_{Gly} and X_{Gas} as compared to the parent NiAl catalyst. NiAl-NCN also presented 12% higher H_2 yield than that of NiAl. As this study has been conducted over a single space time values, it seems of great interest to broaden the study of performance for those two catalysts over a range of X_{Gly}. This section addresses an evaluation of the effect of contact time (in form of space time) on the catalytic behaviour in the glycerol APR for the most active assays, nanocasted NiAl-NCN and bulk NiAl (coprecipitated) catalysts. Catalytic experiments were run at 6 different space times (W/F_0) varying both catalyst weight and reagent flow. Experiments were run in the afore mentioned reaction conditions (235 ºC/35 bar, feed: 10 wt.% glycerol-water solution). Samples were previously reduced in-situ at 700 ºC, 1 h. The results obtained are shown in Figure 7.14. The evaluated reaction indices are reported once the stable operation is accomplished (1-4 h).

The contact time of reactants over the catalyst has a huge impact on the glycerol APR outputs, for both catalysts. Independent of the space time employed, NiAl-NCN catalysts are more active than NiAl for both glycerol and carbon to gas conversions (Figure 7.14 (a) and Figure 7.14 (b)).

For instance, for the lower space time, the NiAl-NCN achieves 35.5% of X_{Gly} and NiAl 23.6%, while at the highest space time both catalysts convert similar percentage of glycerol (99-98%). In the case of X_{Gas}, both catalysts perform similarly at low space time and diverge at higher space time. As expected, the glycerol conversion to gas increases with space time. This indicates that at higher contact times the reforming reactions are promoted, thus higher reforming products are obtained. NiAl-NCN presents higher yield to hydrogen at those contact times, though its selectivity to methane is also enhanced. The maximum improvement with respect to NiAl catalyst is at a space time range of 37-41 $g_{cat} \cdot h \cdot mol^{-1}$, where the increase in X_{Gly}, X_{Gas} and YH_2 are more marked.

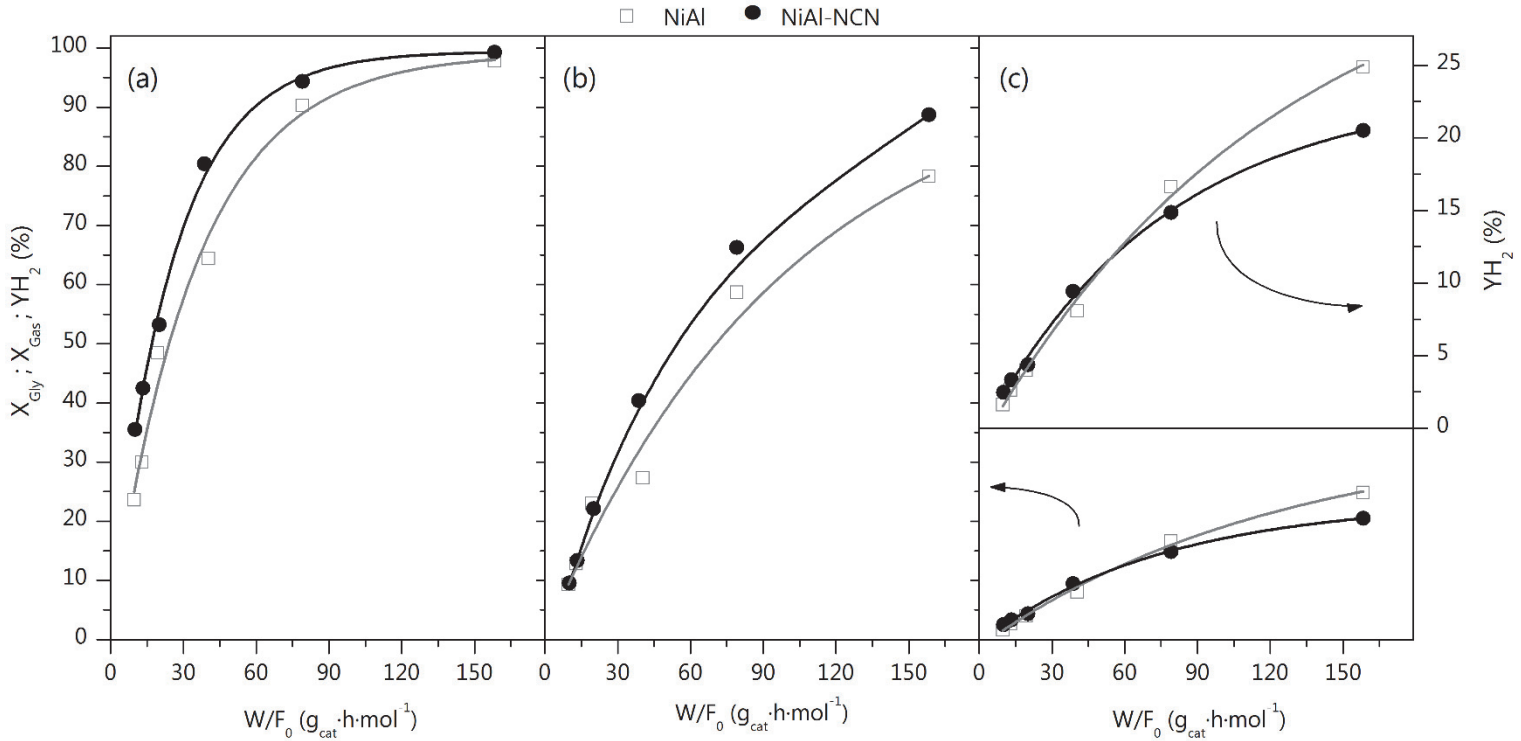

Figure 7.14. Effect of the space time on (a) X_{Gly}, (b) X_{Gas} and (c) YH_2, for NiAl-NCN and NiAl catalysts.

The NiAl-NCN improvement can be assigned to its higher metallic surface accessibility. In addition, to the wormhole-like rod porous structure of NiAl-NCN, which can enhance the reactants diffusion into the pores. Although the nanocasted catalyst accomplishes greater conversions, its YH_2 does not overcome that obtained with the NiAl sample at high contact times. It could be associated with the high selectivity to CH_4 shown by NiAl-NCN. The activity improvement led to high availability of H_2, which simultaneously favours side methanation reactions or others like hydrogenation, to produce liquids (EtOH and 1, 2- PG).

Selectivity to H_2 follows an increasing trend with X_{Gly}, in parallel to YH_2 (Figure 7.15). Similarly, CH_4 follows an increasing trend with X_{Gly}. Despite the improved conversion, in terms of X_{Gly} and X_{Gas} presented by NiAl-NCN, the selectivity to H_2 is lower at all conversions with respect to NiAl. At low X_{Gly} (<55%) the SH_2 is similar, while the differences increase at higher conversions. An inverse tendency is observed for the selectivity to methane, which is higher for NiAl-NCN at all conversions.

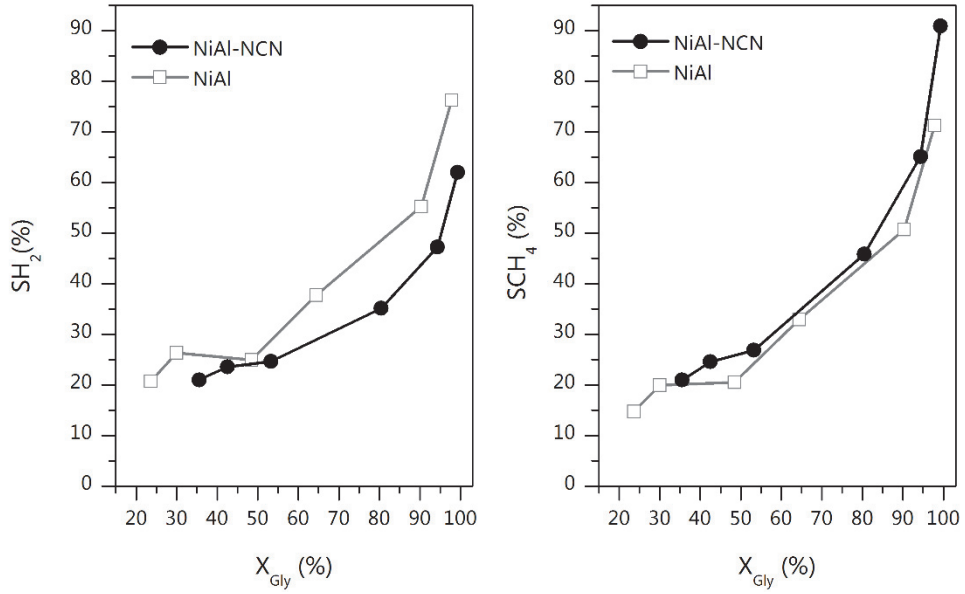

Figure 7.15. Selectivity to hydrogen and to methane as a function of glycerol conversion for NiAl-NCN and NiAl.

In order to further rationalize the results obtained, $S_{H2\text{-}gas}$ was calculated, considering the moles of H_2 produced with respect to hydrogen lost in the alkanes production (Figure 7.16).

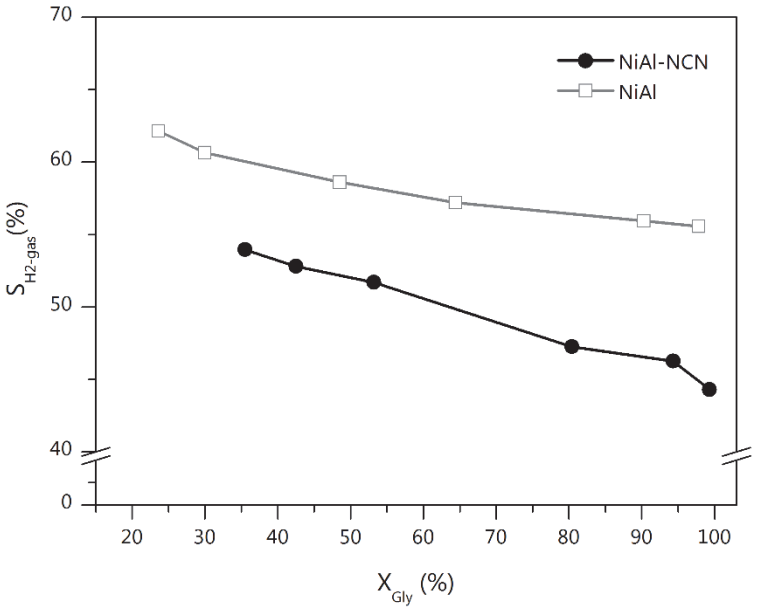

Figure 7.16. Selectivity to H_2 regarding gas products.

Notably, $S_{H2\text{-}gas}$ is lower for NiAl-NCN in the entire range of X_{Gly} studied, which agrees with its higher SCH_4. This time, the ratio follows a decreasing trend with X_{Gly}, indicating that more hydrogen is lost in alkanes formation at higher conversions. A similar trend was reported by others [121]. The decreasing trend of $S_{H2\text{-}gas}$ suggested that CO hydrogenation is lessened by the short contact times.

7.4 CHARACTERIZATION OF THE USED NiAl/SBA-15 AND NANOCASTED CATALYSTS

Catalyst performance has been discussed based on the reaction outputs at 2 h steady state. These catalysts were further left for 1 h at APR conditions, and then recovered to their physicochemical characterization. Inhere with, the results of different characterization techniques are discussed.

7.4.1 Leaching of metals

The leaching of the metals during 3 h of APR reaction is summarised in Table 7.8. Interestingly, nanocasted catalysts show less nickel leaching than that of parent NiAl. Aluminium leaching is negligible for all catalysts, except for NiAl-NCF, that accounted for 1%. Silica is also leached. In the case of NiAl/SBA-15, it accounted for 5.5%. For the nanocasted catalysts, Si leaching increased to 31% and 94% for NiAl-NCF and NiAl-NCN, respectively, exaggerated by their low Si content.

7.4.2 Textural properties

N_2 adsorption-desorption isotherms and the pore size distribution of the used catalysts are shown in Figure 7.17. NiAl/SBA-15 catalysts present a drastic change in the isotherm's form, which passes from type IV to type V. This can be attributed to a decrease in porous material in comparison to its fresh reduced form. Besides, the pore size distribution widens, evidencing a depletion of the ordered mesoporous structure

Subtle changes are observed in the isotherms of spent NiAl-NCF and NiAl-NCN catalysts. The most striking difference is the decrease in the adsorbed nitrogen volume. Regarding the pore size distribution, it slightly shifts to smaller pores in both used nanocasted catalysts, indicating a shrinkage of the pores.

Used NiAl/SBA-15 catalyst significantly loses the specific surface area, by 42% respect to that of its fresh reduced form (Table 7.8). This suggests low textural stability of SBA-15 at hydrothermal conditions, in agreement to others [234]. The incorporation of Ni-Al mixed oxide and the high calcination temperature used do not seem to stabilize enough the siliceous material, since structural collapse occurs at APR conditions. The blockage of the active phase from the reagents by the collapse of the pores could also affect the poor APR performance of this catalyst.

Regarding the nanocasted samples, S_{BET} increase after 3 h under APR conditions. For instance, NiAl-NCF catalyst doubled its S_{BET}. Instead, S_{BET} of NiAl-NCN catalyst increases by 33%, similar to that of NiAl.

Table 7.8. Physicochemical properties of used nanocasted catalysts.

Catalyst	Leaching[a] (%)			Textural properties[b]			Crystallite size[c]
	Ni	Al	Si	S_{BET} ($m^2 \cdot g^{-1}$)	Vp ($cm^3 \cdot g^{-1}$)	Dp (nm)	Ni^0
NiAl/SBA-15	0.3	0.04	5.5	91.4 (- 42%)	0.3	8.6	28.7 (+18%)
NiAl-NCF	0.4	1.02	31.0	88.7 (+137%)	0.3	10.1	36.0 (+30%)
NiAl-NCN	0.1	0.06	94.1	206.4 (+33%)	0.2	4.3	6.3 (-6%)
NiAl	0.7	0.05	n/a	114.0 (+37%)	0.2	6.3	14.6 (-9%)

[a] IPC-AES; [b] N_2 physisorption; [c] XRD. In parenthesis, variations with respect to the parent fresh reduced forms.

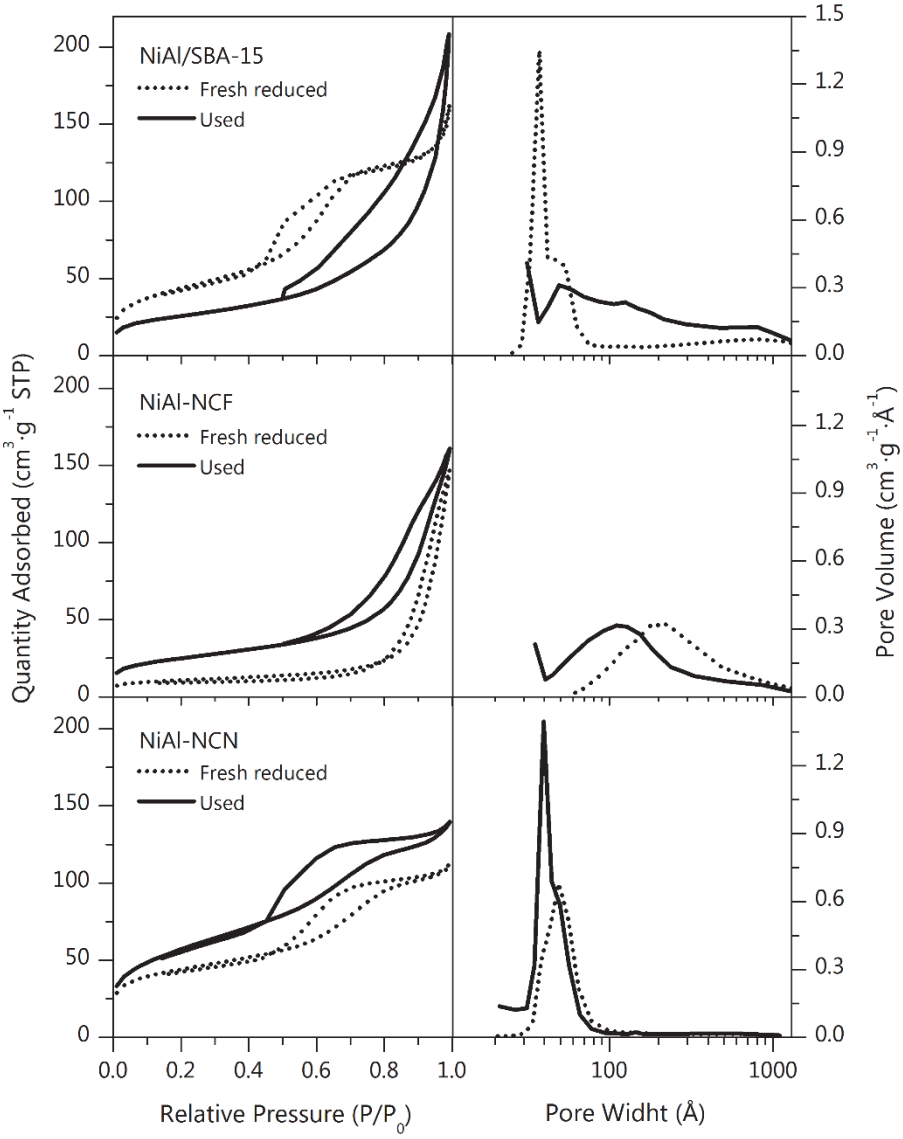

Figure 7.17. N_2 physisorption isotherms, and pore size distributions of used nanocasted catalysts.

7.4.3 Phase transition and crystallinity

XRD diffractograms of used catalysts are depicted in Figure 7.18. Similar XRD patterns to fresh reduced samples are uncovered regarding $NiAl_2O_4$ phase, suggesting that spinel phase is preserved in all used catalysts. Moreover, intense XRD features of

metallic Ni are still found for all used catalysts, denoting that bulk metallic Ni nanoparticles are also preserved.

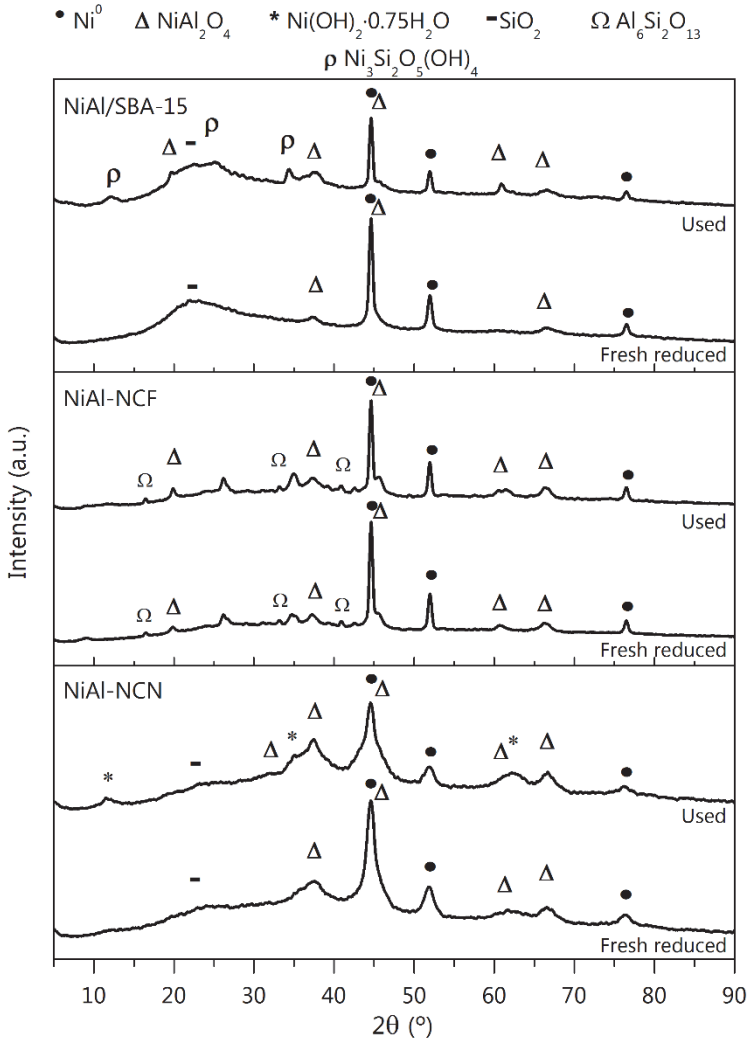

Figure 7.18. XRD diffractograms of used nanocasted catalysts.

The elevation in the spectra from NiAl-SBA-15 (broad) and NiAl-NCN (subtle) are due to SiO_2, despite the 5.5% and 94.5% silica leaches, respectively, from these catalysts.

New XRD peaks appear in the diffractograms of the used catalysts, which likely points to phase transformations under the hydrothermal conditions of the APR reaction. NiAl/SBA-15 shows peaks at 12.2°, 24.8° and 34.4° 2θ, which can be assigned to

pecoraite phase ($Ni_3Si_2O_5(OH)_4$) (JCPDS 049-1859) formed by hydroxylation reactions enhanced by the acidic aqueous medium. According to the mechanisms proposed by Park et al. [235], in hydrothermal conditions Ni^0 oxidises to nickel hydroxides, which diffuses into silica layers and react with further surface hydroxides, resulting in nickel phyllosilicates polymerization. This can explain the lower nickel leaching by this solid. However, the loss of metallic nickel in form of this new phase is detrimental to the APR performance.

Diffraction pattern from used NiAl-NCF, with no evidence of new phases, almost replicates that from the fresh reduced form. XRD from spent NiAl-NCN shows new reflections at 12.2º, 35º and 62.2º 2θ, corresponding to the formation of nickel hydroxide hydrate ($Ni(OH)_2 \cdot 0.75H_2O$) (JCPDS 038-0715). The nickel hydroxylation reaction is highly probable after oxidation of Ni^0 at the lower pH in the reaction media [236]. The absence of peaks from pecoraite could be due to the low amount of silica in this solid.

It is noteworthy that, diffraction peaks from boehmite or carbon are not evidenced in the XRD spectra of any of the spent catalysts. The first fact indicates that nanocasted approach protects alumina from hydration. The second fact suggests that solid carbonaceous deposits are not affecting the catalysts stability in the reaction times used in this work.

The crystallite size of Ni^0 (Table 7.8) varies differently after APR reaction. Certain coalescence of Ni^0 occurs on NiAl/SBA-15 and NiAl-NCF used catalyst (increase by 18-30% respect their fresh reduced forms), while Ni^0 crystallites slightly shrink for NiAl-NCN and NiAl catalysts with respect to their fresh reduced forms (by 6-9%). The structural order accomplished in the NiAl-NCN catalyst may prevent Ni sintering, as also reported by Kim et al. [223]. According to them, the large surface area and the additional mesopores of the wormhole-like rod structure (obtained by partial filling of the SBA-15 pores), prevent the growth and aggregation of metal nanoparticles.

7.4.4 Reducibility and nickel speciation

H_2-TPR analysis was carried out for the used catalysts to enlighten the chemical behaviour of the active phase during the APR. The obtained reduction profiles are presented in Figure 7.19.

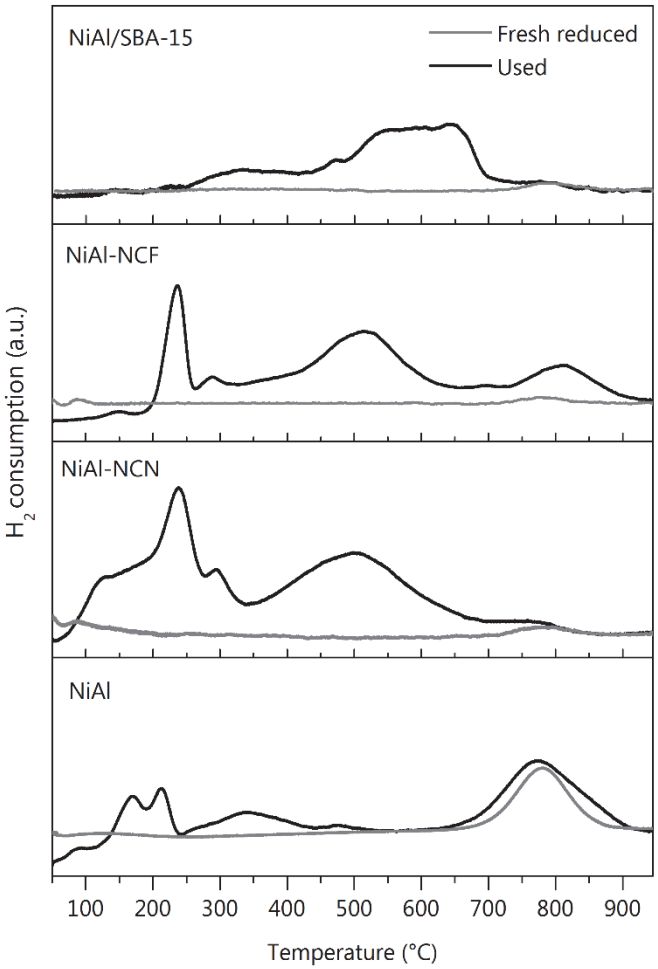

Figure 7.19. Reduction profiles of used nanocasted catalysts.

Compared to the $TPR_{700-950}$ profiles from the fresh reduced forms, all the spent catalysts showed different hydrogen consumption events. They can be grouped into low-intermediate (110-700 ºC) or high (> 700 ºC) temperature ranges. As previously mentioned, the high temperature peak is related to reduction of the Ni^{2+} in the spinel structure and its position coincides with that of corresponding fresh reduced samples, except for NiAl-NCF assay, whose peak is around 30 ºC upshifted. The low temperature peaks are associated to both, reduction of Ni^{2+} oxidized during APR and deposited organic liquids reduction.

In order to discern between different hydrogen uptake events at low-intermediate temperature, additional H_2-TPR coupled to MS experiments have been carried out. As an example, Figure 7.20 shows the evolution of H_2 and CH_4 released during the H_2-TPR-MS carried out over used spent NiAl-NCN catalyst. The CH_4 profile indicates that it only arises from the low-intermediate temperature events (200-400 ºC). This confirms that the high temperature peak corresponds to the reduction of Ni^{2+} in spinel. CH_4 is formed by the reduction of organic matter (unreacted glycerol and intermediate liquid products with a low boiling point) adsorbed into the catalysts pores [191]. The H_2O peak in the 400-700 ºC interval corresponds to the reduction of NiO.

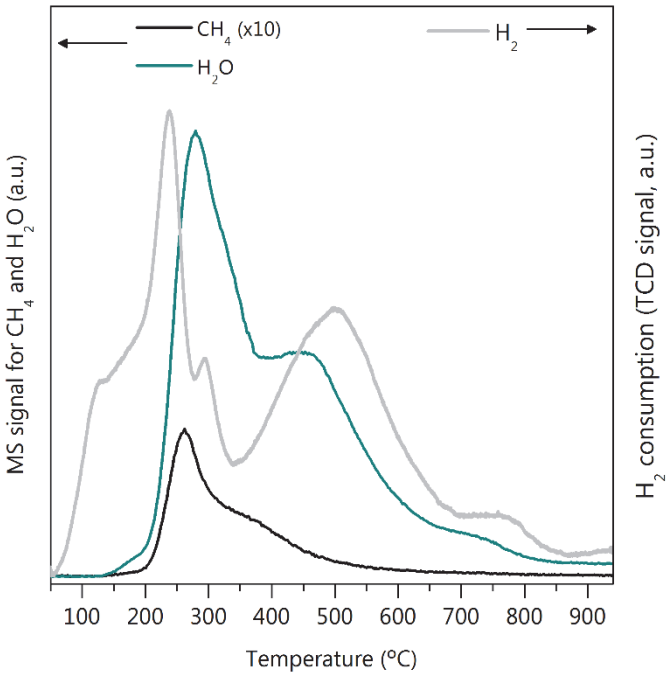

Figure 7.20. TPR_{used} profile for NiAl-NCN used catalyst, coupled to MS.

An attempt was made to calculate the hydrogen consumed in the NiO reduction exclusively. For this, an uptake of 2 mol of H_2 per mol of CH_4 released was assumed. In addition, it was assumed that the same mass of organic liquids of the same composition is adsorbed in the pores of all the spent catalysts (i.e. 0.63 mmol $H_2 \cdot g_{cat}^{-1}$). The obtained results are shown in Table 7.9. It is evidenced that Ni^0 significantly oxidizes in 3 h of APR reaction. Since signals from Ni^0 are visible in the XRD patters, it can be stated that

oxidation of nickel must be limited to the outermost layers of nickel particles. However, this strongly diminishes the available metallic surface.

Table 7.9. H_2-TPR results for spent catalysts.

Sample	H_2 consumption (mmol $H_2 \cdot g_{cat}^{-1}$)		Ni^0 oxidation
	TPR_{used}	NiO species (200-700 ºC)	%
NiAl/SBA-15-U	1.9	1.1	67
NiAl-NCF-U	2.8	1.8	44
NiAl-NCN-U	3.4	2.7	60
NiAl-U	4.1	2.6	60

Among nanocasted catalysts, NiAl-NCF is the one that better preserves nickel in its metallic form, with 44% of nickel oxidized. Interestingly, this catalyst has the lowest nickel metallic surface area, about 5 times lower than that of NiAl-NCN and NiAl. Oppositely, NiAl/SBA-15 catalyst is the one whose nickel is oxidized in higher extent (67% of Ni). The percentage of oxidized nickel in NiAl-NCN and in the reference NiAl catalysts are similar, although the crystallite size of the former is half the size than that of the latter. It can be associated to the inhibition of the oxidation by structural aspects, like nickel nanoparticles hiding in the wormhole-like rod structure.

To sum up, catalysts stability issues could be assigned to the effect of two facts, namely the oxidation of Ni^0, and transformations and creation of new phases. The first fact has also been recognized as one of the deactivation factors [192]. The effect of the deposition of carbonaceous materials seemed to be non-significant for these catalysts.

7.5 GENERAL OVERVIEW AND CONCLUSIONS

It was found that the physicochemical and the catalytic properties of the nickel aluminate spinels synthesised by nanocasting technique are highly influenced by the SBA-15 removal approach. The parent solid NiAl/SBA-15, which preserves the siliceous template, has higher Ni/Al ratio than the nominal and very high surface area. However, its reducibility is deteriorated, and the acid/basic sites density ratio increases with respect to NiAl. NaOH etching to recover the spinel in the NiAl-NCN leads to a solid with improved textural characteristics, higher than nominal Ni/Al ratio, and smaller metallic

nickel particles, improving Ni^0 dispersion. Additionally, the acid/basic sites density ratio does not vary substantially with respect to NiAl. Also, the ordering accomplished by nanocasting synthesis provided a wormhole-like rod structure that could facilitate reagents diffusion throughout the catalyst pores. Teflon-assisted template removal leads to a solid with similar to nominal Ni/Al ratio but deteriorated textural and metallic nickel dispersion characteristics. Besides, the acid/basic sites density ratio boosted in this assay.

Both NiAl/SBA-15 and NiAl-NCF catalyst show very deficient performance in glycerol APR, with less than 20% glycerol converted and 1-to-2 orders of lower hydrogen production magnitude than NiAl.

NiAl-NCN catalyst presented improved activity in the glycerol APR with respect to NiAl, with 20% higher hydrogen production rate. Nevertheless, this catalyst gives more methane and has a lower selectivity to hydrogen than NiAl. Such a performance has been attributed to its small and dispersed Ni^0 particles.

There are not relevant differences in the chemical route of the glycerol Aqueous-Phase Reforming among the catalysts, as the composition of the liquid phase remains similar for all them. A slight increase in liquid product yield from route A with respect to those from Route B is found for NiAl-NCN catalyst, in comparison to NiAl counterpart.

The analysis of the glycerol APR activity, selectivities and hydrogen yield at various spatial times indicate that the nanocasting synthesis improves the conversion of glycerol and conversion to gas. Those are accompanied by a marked enhancement of hydrogenation of carbon oxides (methanation), in detriment of H_2 selectivities and yield.

Moreover, it has been demonstrated that the nanocasted catalyst etched by NaOH presents promising stability, though changes in the oxidation state of nickel is a challenge to be addressed. It efficiently stabilizes the active phase preventing sintering. In turn, other deactivation causes extensively reported for APR, such as leaching or phase transitions related to alumina, could contribute to a lesser extent to its stability.

Chapter 8

Summary and conclusions

8. SUMMARY AND CONCLUSIONS

8.1 SUMMARY

Hydrogen, as an energy carrier, plays an important role in decarbonizing energy and fuels, contributing to world sustainability challenges. Biomass-based feedstocks have huge potential for the renewable hydrogen production, glycerol being one of the most relevant. Aqueous-Phase Reforming (APR) of glycerol is a promising method for green hydrogen production that also promotes the biodiesel industry profitability. APR is a one-step catalytic process, which operates in the liquid phase at low temperature and pressure high enough to keep the reactants in the liquid phase. The efficiency of the glycerol APR to produce H_2 depends on the proper formulation of the catalyst. To provide high H_2 selectivity and reaction rates under optimal operating conditions, the catalyst must be effective in breaking the C-C, C-H, and O-H bonds, as well as active for the WGS. At the same time, catalysts must be inactive in C-O scission and methanation. Besides, the catalyst should presents resistance to deactivation under harsh hydrothermal conditions of the APR. Noble metal-based catalysts are very active and selective to H_2, but they are expensive. Thus, alternatives that are more economically attractive must be explored. Ni-based spinel catalytic precursor constitute a more economical alternative, with notable catalytic behaviour.

In this doctoral thesis, a screening of Ni-based catalysts helps to determine the potential of the stoichiometric nickel aluminate spinel as a catalytic precursor for the H_2 production in the glycerol APR. The optimal ranges of the operation variables were determined by a factorial design of experiments. The effect of the reduction temperature on the catalytic precursor was studied establishing correlations between the physicochemical properties and the catalytic performance. Complementarily, two strategies for the $NiAl_2O_4$ catalytic precursor optimization were examined: (i) the addition of Mg and Ce surface promoters; and (ii) the synthesis by the nanocasting method. The catalytic tests were carried out for extended periods of time, and the characterization of the spent catalysts, offered insight into the main deactivation causes in glycerol APR.

As a starting point, the optimum catalyst precursor was chosen. For the screening, two families of Ni-based catalysts, bulk and supported, were synthesised by

co-precipitation, impregnation and, ion exchange methods. Basic characterization of the catalysts allowed the determination of the key role of properties such as Ni content, reducibility, metallic surface area, and surface acidity in the glycerol APR performance. Over the best catalyst formulation ($NiAl_2O_4$), the optimum ranges of the operation variables were established by a 2^k+n_c factorial design of experiments.

In the next step, the effect of reduction temperature on the nickel aluminate spinel catalytic precursor, synthesised by co-precipitation at a Ni/Al mole ratio of 1 : 2, was studied. The synthesised solid was reduced at different temperatures, in the 300 ºC to 850 ºC range. The obtained solids were analysed by several techniques examining their physicochemical properties and nickel speciation. It was found that the strong interaction of the metal nanoparticles with the surroundings promotes nickel dispersion upon reduction.

The physicochemical characteristics of the nickel aluminate reduced at different temperatures were related to the catalytic performance. APR test at different coupled temperature/pressure conditions were carried out, and the quantitative results for both the gas and the liquid products allowed the proposal of a plausible reaction pathway for the glycerol APR. Besides, the apparent activation energy was calculated for the catalytic precursor reduced at higher temperatures. The stability of those catalysts was evaluated over 50 h TOS, and the spent catalysts were characterized to determine the chemical and structural changes in APR.

Hereunder, the addition of Mg and Ce surface modifiers to the $NiAl_2O_4$ catalytic precursor as optimization strategy was analysed. Specific characterization of the obtained solids helped to determine the effect of Mg and Ce loading, which has been associated with the APR catalytic behaviour. WGS and CO hydrogenation activity in the gas phase was also investigated to elucidate the role of promoters in the gas-phase products distribution. The used catalysts were characterized, and the stabilizing role of the promoters determined.

Finally, the optimization of the synthesis method for the nickel aluminate spinel was addressed, by using nanocasting synthesis. The SBA-15 template was hydrothermally synthesised and thoroughly characterized. Overall, three precursors were studied: NiAl spinel supported over SBA-15, and two nanocasted solids, with different

template-removal procedures (NaOH etching and Teflon-assisted methods). The solids were characterized employing several methods, paying especial attention to their morphological properties. The APR performance of the nanocasted catalysts was compared with that of parent bulk nickel aluminate. The influence of the space time on the activity and hydrogen yield was examined for the optimum nanocasted catalyst. Spent catalysts were characterised to enlighten the changes that occur under APR conditions.

8.2 MAIN CONCLUSIONS

It is expected that the results obtained in this doctoral thesis contribute to future research works in hydrogen production by APR of water fractions derived from biofuel production that contain oxygenated compounds. The viability of APR technology is conditioned by the development of active catalysts, selective to the formation of reforming products (H_2, CO and CO_2), stable for long periods of operation and economically viable. The following conclusions are highlighted:

1. Catalysts derived from bulk nickel aluminate spinels are more advantageous than supported ones. Specifically, nickel aluminate spinel synthesised by co-precipitation allows incorporating high Ni loadings and obtaining solids with good textural and morphological properties. This catalyst shows superior catalytic behaviour in terms of glycerol conversion, conversion to gas and hydrogen yield. It is recognized that both the metal and the support play an essential role in the glycerol APR over Ni-based catalysts.

2. The factorial experimental design 2^3+2 for the glycerol APR to produce H_2 over $NiAl_2O_4$ reduced at 700 ºC establishes that the operation variables such as temperature, pressure, and space time influence the APR outputs differently. The optimal intervals of the operation variables are: 235-250 ºC for temperature, 30-42.5 bar for pressure, and 1600-2400 $g_{cat}{\cdot}min{\cdot}mol_{Gly}^{-1}$ for the space time.

3. Three nickel species of different reducibility are found in the stoichiometric $NiAl_2O_4$ synthesised by co-precipitation: surface free nickel oxide, Ni^{2+} in defective spinel, and nickel in stoichiometric spinel (the later with the highest contribution). The spinel structure provides stability to small metallic nickel particles. Upon reduction, Ni^0

species exudate from the spinel lattice to the solid surface, leading to a framework composed by less and less Ni^{2+} species embedded into an Al-rich mixed oxide phase. Accordingly, metallic nickel particles smaller than 14 nm are obtained. Likewise, the number of tetrahedral nickel atoms diminishes, and those in octahedral sites increase, when the reduction temperature increaseed. Regarding surface acid-basic properties, treatment under hydrogen at a higher temperature causes an increase in the acidity of the solids, and enrichment in medium-strength and strong basic sites.

4. For all the nickel aluminate-derived catalysts, regardless of the reduction temperature, hydrogen is the main compound in the gas stream, followed by carbon dioxide and methane. The low formation of CO suggests that WGS is also favoured by the $NiAl_2O_4$-derived catalysts. Reduction temperature has marked effect on the liquid-phase product distribution. Results suggest a key contribution of the accessible metallic sites and the medium-strength acidic sites to the overall reaction scheme. The gas and liquid products obtained support a reaction pathway with two paths for the glycerol APR: one, starting with dehydrogenation to glyceraldehyde, and further decarbonylation; and other through dehydration of terminal hydroxyl group of glycerol, and subsequent hydrogenation to 1,2-propylene glycol. CO is further converted to methane by WGS and hydrogenation.

5. Nickel aluminate spinel precursor reduced at 600 ºC or above, shows remarkable catalytic performance in the glycerol APR. Although the most active assay is that reduced at 850 ºC (93% glycerol conversion at 250 ºC/45 bar), it shows the highest deactivation rate. The maximum specific hydrogen production rate is achieved upon reduction at 600 ºC, due to adequate Ni^0 clusters size, accessible metallic nickel surface and acidic/basic properties. Nonetheless, high selectivity to liquids of dehydration-hydrogenation is evidenced for this sample. The catalyst reduced at 700 ºC presents the best balance between conversion, selectivity to hydrogen, and stability. This catalyst shows 87% glycerol conversion, 46% conversion to gas, and 53% selectivity to gas (at 250 ºC/45 bar). Long-term catalytic runs reveal the good durability of catalysts derived from nickel aluminate spinel, deactivation occurs mainly though nickel oxidation and sinterization.

6. While nickel strongly anchors to the $NiAl_2O_4$ spinel structure, the addition of Mg and Ce further limited the coalescence of metallic Ni particles upon reduction, and increased the overall basicity. Both modifiers slightly increased the catalyst selectivity to hydrogen. The glycerol conversion notably increases after Ce addition whereas it slightly decreases after Mg addition, the latter being influenced by the strong Ni-Mg interaction. Both Mg and Ce promote the WGS activity, achieving gas streams with less CO, and concomitantly more CO_2. Characterization of the used catalysts indicates that both promoters improve the stability of the textural properties under APR conditions.

7. The physicochemical characteristics and the APR performance of the nickel aluminate spinels synthesised by nanocasting, are highly influenced by the SBA-15 removal approach. The nanocasted catalyst synthesized by NaOH etching (NiAl-NCN), for template removal, leads to a solid with improved textural characteristics, and smaller metallic nickel particles, significantly increasing Ni^0 dispersion. The ordering accomplished by the used synthesis method provides a wormhole-like rod structure that could facilitate reagent diffusion throughout the catalyst pores. This catalyst improves the performance in the glycerol APR with respect to NiAl, presenting 20% higher hydrogen production rate. Nevertheless, this catalyst yields more methane, and has lower selectivity to hydrogen. NiAl-NCN shows promising stability, as it efficiently stabilizes the active phase preventing from sintering. Both NiAl/SBA-15 and NiAl-NCF catalyst show very deficient performances in glycerol APR.

8.3 FUTURE WORKS

In this work, the feasibility of using stoichiometric nickel aluminate spinel precursor to produce catalysts with good performance in the glycerol APR has been demonstrated. In addition, it has been seen how the addition of modifiers such as Ce or Mg, or the nanocasting synthesis method, can alter the catalyst performance and stability. The results of the present work indicate that there is a wide scope for further research work as outlined below.

- The studies carried out in this doctoral thesis have made possible to propose a reaction route for the glycerol APR. However, a mechanistic investigation on the catalytic APR can help to get information for the design of new catalyst

formulations. Techniques such as Attenuated total reflection infrared spectroscopy (ATR-IR) can be used for this purpose.

- The biggest unsolved issue is instability due to nickel oxidation, which can prevent long-term use. Therefore, the NiAl catalytic formulations have to be improved to inhibit said oxidation. For example, the strategy of alloying nickel to a second metal, thus affecting activity/selectivity as little as possible, can be explored.
- Since nickel is intrinsically active in methanation reaction, new catalyst formulations to hinder the CO/CO_2 methanation and thus, improve the hydrogen selectivity, can be explored. Promotion with Sn and Cu could help to deal with this issue.
- Since NiAl catalyst is highly efficient for the synthetic glycerol APR, its application on the industrial effluents can be explored (crude glycerol feedstreams).
- The variety of bio-based substrates that can be used is very wide. Therefore, the evaluation of the NiAl catalysts performance in the APR of other biomass-derived substrates, such as sorbitol or xylitol, or even aqueous wastes such as from that obtained in Fischer-Tropsch process, can be evaluated.
- Since NiAl catalysts are active for hydrogen production, the way of consuming it in-situ, in the deoxygenation of glycerol, can be explored. This will give rise to a variety of high value-added liquid compounds. This new research topic fully connects with the concept of biorefinery. For this purpose, the original catalysts need to be more acid, which can be achieved by doping with oxophilic metals.

Chapter 9

Nomenclature

9. NOMENCLATURE

Abbreviations and acronyms

1,2-PG: 1,2-propylene glycol

^{27}Al MAS NMR: Magic Angle Spinning Nuclear Magnetic Resonance

AB_2O_4: Spinel general formula

AEL: Alkaline Electrolyser

AES: Atomic Emission Spectroscopy

APR: Aqueous-Phase Reforming

ATR: Autothermal Reforming

BET: Brunauer-Emmett-Teller

BJH: Barrett-Joyner-Halenda

CCS: CO_2 Capture and Storage

CD: Colloidal Dispersion

COP: Conference of parties

CP: Co-precipitation

DF: Dark field

DG: Decomposition of Glycerol

DOE: Design of Experiments

DP: Deposition-Precipitation

EG: Ethylene Glycol

EtOH: Ethanol

FAMES: Fatty Methyl Esters

FID: Flame Ionization Detector

FC: Fuel Cell

fcc: Face-centred cubic

FFA: Free Fatty Acids

FT: Fisher-Tropsch

FTIR: Fourier Transform Infra-Red Spectroscopy

GC: Gas Chromatography

GHG: Greenhouse gases

GR: Glycerol Reforming

HA: Hydroxyacetone

HAADF: High-Angle Annular Dark Field

HC: Hydrocarbons

HPLC: High-performance liquid chromatography

IC: Inorganic carbon

ICP: Inductively Coupled Plasma

IE: Ion Exchange

IEA: International Energy Agency

IRENA: International Renewable Energy Agency

IPCC: Intergovernmental Panel on Climate Change

IR-Pyr: Infrared spectroscopy of pyridine adsorption

IUPAC: International Union of Pure and Applied Chemistry

IWI: Incipient Wetness Impregnation

LCA: Life Cycle Assessment

MCFC: Molten Carbonate Fuel Cell

MeOH: Methanol

MeCOH: Acetaldehyde

NDIR: Non-dispersive infrared cell

MR: Mears criterion

MS: Mass Spectrometry

MSR: Methane Steam Reforming

n: Product compound

n/a: Not Applicable

n.d.: No Data

n.f.: Not Found

NDCs: National Determined Contributions

NZE: Net Zero Emissions

Oh: Octahedrally coordinated

PAFC: Phosphoric Acid Fuel Cell

PEMEL: Proton Exchange Membrane Electrolyser

PID: Proportional integral derivative controller

PLC: Programmable logic controller

POX: Partial Oxidation

PSA: Pressure Swing Adsorption

RD: Reflux Deposition

Re: Reynolds number

RI: Refractive Index

RF: Radio-Frequency

SDG: Sustainable Development Goals

SC: Super Critical

Sc: Schmidt number

SGIker: Analysis Service of the Advanced Research Facilities from the UPV/EHU

Sh: Sherwood number

SOEL: Solid Oxide Electrolyser

SOFC: Solid Oxide Fuel Cell

SR: Steam Reforming

STEM: Scanning Transmission Electron Microscopy

TC: Total Carbon

Td: Tetrahedrally coordinated

TEM: Transmission Electron Microscopy

TCD: Thermal Conductivity Detector

TG: Thermal Gravimetry

TOC: Total Organic Carbon

TOS: Time On Stream

T/P: Couple Temperature and Pressure operation conditions

TPD: Temperature-Programmed Desorption

TPH: Temperature-Programmed Hydrogenation

TPO: Temperature-Programmed Oxidation

TPR: Temperature-Programed Reduction

TQSA: Chemical Technologies for the Environmental Sustainability Group

TUM: Technical University of Munich

UNFCCC: United Nations Framework Convention on Climate Change

UPV/EHU: University of the Basque Country

VLE: Vapour-liquid equilibrium

WGS: Water-Gas Shift

WI: Wet Impregnation

XRD: X-ray Diffraction

Variables and physical constants

a: Lattice parameter

a_0: Distance between the centres of adjacent pores

A_0: Peak area of the non-chemisorbed peak.

$A_{at\text{-}Ni}$: atomic area of metallic nickel

A_i: Peak area of each pulse

$A_{S\text{-}Ni^o}$: Metallic nickel surface area

BAS: Concentration of Brønsted acid sites

B_0: Applied magnetic field

B_1: Radio-Frequency field

C: Constant factor of energy of monolayer adsorption

$C_{at,n}$: Number of carbons in the *n* compound.

C_{Gly} : Glycerol concentration

C_{Gly}^0: Fed glycerol concentration

$C_{Gly,S}$: Glycerol concentration at the catalyst surface

C_{Ni^o}: metallic Ni content

Curvatr.: Curvature check

d: Average crystallite size

d_{at} atomic diameter of metallic nickel

df: Degrees of freedom

d_{hkl}: lattice spacing

d_p: Catalyst particle diameter

$D_{Gly\text{-}W,\ eff}$: Effective diffusion coefficient of glycerol in water

d_{Ni^0}: mean diameter of the nickel particle

D_{Ni^0}: mean Ni^0 dispersion

Dp: Pore diameter

E_{app}: Apparent activation energy

F: F-statistic

$F_{C\text{-}Liq}$: Total carbon flow of liquid products

F_{CO}^0: Fed CO molar flow

F_{CO}: Outlet CO molar flow

F_{CO2}: Outlet CO_2 molar flow

F_{feed}: Feed liquid flow

$F_{Gas\text{-}n}$: *n* compound molar flow

F_{Gly}^0: Fed glycerol molar flow

F_{Gly}: Outlet glycerol molar flow

F_{H_2}: Molar flow of H_2 produced

f_{red}: Fraction of metals being reduced

FWHM: Full width at half maximum

ΔG: Standard Gibbs free energy

$H_2\text{-}TPR_{950}$: H_2 uptake in the full reduction experiments for calcined samples

$H_2\text{-}TPR_{Tred}$: H_2 uptake in the reduction at T_{red}

$H_2\text{-}TPR_{Tred\text{-}950}$: H_2 uptake for the partially reduced samples

I_{220} / I_{440}: Ratio of peaks corresponding to (2 2 0) and (4 4 0) reticular planes

IA: Integrated absorbance

i_s: Spinel inversion parameter

k: Factor in DOE

k*: Normalized factor

K: Shape factor

k_{app}: Apparent reactions rate constant

k_c: Mass transfer coefficient

$k_{central}$: Factor's value in the central point

K_{sp}: Product solubility constant

LAS: Concetration of Lewis (LAS) acid sites

$Meth_{H2}$: H_2 uptake for CH_4 formation

M_{cat}^0: Metal loading in the fresh catalyst

Md: Added metal

M_{liq}: Concentration of the metal in the liquid effluent

MS: Mean square

MW_{Ni}: Molecular weight of Ni

N: Avogadro´s number

n_c: Replicates at the centre point

n_p: Number of pulses

P/P_0: Relative pressure

R: Ideal gas constant

R_∞ : Diffuse reflectance of a layer of infinite thickness

R^2: Coefficient of multiple determination

$-r_{Gly}$: Rate of glycerol reforming reaction

r: Radius of the wafer

r_{obs}: Reaction rate

r_d: Catalyst particle radius

r_P: Pore radius

p: p-value, probability distribution

P: Pressure

P*: Normalized pressure

S_{Alkane}: Selectivity of alkanes products

S_{BET}: Specific surface area

SCH_4: Selectivity to CH_4

S_{CO2}: Selectivity to CO_2

S_{Gas}: Selectivity to gas

SH_2: Selectivity to hydrogen

$S_{H2\text{-}gas}$: Selectivity to hydrogen in the gas phase

SS: Sum of squares

Std. Error: Standard error

t: Time

t_l: Thickness of the adsorbed layer

T: Temperature

T*: Normalized temperature

T_{red}: Used temperature of reduction previous to the reaction

$TPR_{used\text{-}NiO}$: H_2 uptake of nickel species oxidized

UV-vis-NIR DRS: Diffuse Reflectance of Ultraviolet–Visible-Near Infra-Red

V_a: Volume of adsorptive

V_{Gly}: Glycerol molar volume at boiling point

V_l: Liquid molar volume

V_m: Specific monolayer capacity

V_{mol}: Molar volume

V_{NH3}: Volume of NH_3 chemisorbed

$V_{NH3,pulse}$: NH_3 volume in a pulse

Vp: Pore volume

W: Weight of mass used in the experiment

W/F_0: Space time

W/F_0*: Normalized space time

WHSV: Weight hour space velocity

W_t: Pore wall thickness

X_{CO} : CO conversion

X_{Gas}: Conversion to gas

X_{Gly}: Glycerol conversion

X'_{Gly}: Relative conversion of glycerol respect to the initial conversion

YH_2: Hydrogen yield

$Y_{Liq\text{-}n}$: Yield of the liquid compound

Greek letters

β: Peak broadening from F*W*HM

β_d: Deactivation rate constant

ε_e: External porosity

λ: Wavelength of the X-ray radiation

θ: Diffraction angle

σ: Surface tension of liquid

σ_m: Molecular cross-sectional area

μ_n: Magnetic momentum of a nucleus

μ_w: Water viscosity

ν_S: Liquid velocity

ξ: Porosity

ρ: Density

ρ_{cat}: Catalyst density

ρ_{bed}: Packed bed density

υ: Contact angle between the condensed phase and the adsorbent surface

Φ_{WP}: Weisz-Prater criterion

χ: Tortuosity

Chapter 10

References

10. REFERENCES

[1] N. Bauer, K. Calvin, J. Emmerling, O. Fricko, S. Fujimori, J. Hilaire, J. Eom, V. Krey, E. Kriegler, I. Mouratiadou, H. Sytze de Boer, M. van den Berg, S. Carrara, V. Daioglou, L. Drouet, J.E. Edmonds, D. Gernaat, P. Havlik, N. Johnson, D. Klein, P. Kyle, G. Marangoni, T. Masui, R.C. Pietzcker, M. Strubegger, M. Wise, K. Riahi, D.P. van Vuuren, Shared Socio-Economic Pathways of the Energy Sector – Quantifying the Narratives. Global Environ. Change 42 (2017) 316-330, doi: https://doi.org/10.1016/j.gloenvcha.2016.07.006.

[2] W.J. Ripple, C. Wolf, T.M. Newsome, P. Barnard, W.R. Moomaw, World Scientists' Warning of a Climate Emergency. Bioscience 70 (2020) 8-12, doi: https://doi.org/10.1093/biosci/biz088.

[3] R.D. Manzanedo, P. Manning, COVID-19: Lessons for the climate change emergency. Sci. Total Environ. 742 (2020) 140563, doi: https://doi.org/10.1016/j.scitotenv.2020.140563.

[4] D. Chen, M. Rojas, B.H. Samset, K. Cobb, A. Diongue Niang, P. Edwards, S. Emori, S.H. Faria, E. Hawkins, P. Hope, P. Huybrechts, M. Meinshausen, S.K. Mustafa, G.-K. Plattner, A.-M. Tréguier, Framing, Context, and Methods. In: Climate Change 2021: The Physical Science Basis. Contribution of Working Group I to the Sixth Assessment Report of the Intergovernmental Panel on Climate Change, 2021.

[5] D. Touma, S. Stevenson, F. Lehner, S. Coats, Human-driven greenhouse gas and aerosol emissions cause distinct regional impacts on extreme fire weather. Nat. Commun. 12 (2021) 212, doi: https://doi.org/10.1038/s41467-020-20570-w.

[6] R.K. Pachauri, M.R. Allen, V.R. Barros, J. Broome, W. Cramer, R. Christ, J.A. Church, L. Clarke, Q. Dahe, P. Dasgupta, N.K. Dubash, O. Edenhofer, I. Elgizouli, C.B. Field, P. Forster, P. Friedlingstein, J. Fuglestvedt, L. Gomez-Echeverri, S. Hallegatte, G. Hegerl, M. Howden, K. Jiang, B. Jimenez Cisneroz, V. Kattsov, H. Lee, K.J. Mach, J. Marotzke, M.D. Mastrandrea, L. Meyer, J. Minx, Y. Mulugetta, K. O'Brien, M. Oppenheimer, J.J. Pereira, R. Pichs-Madruga, G.-K. Plattner, H. Pörtner, S.B. Power, B. Preston, N.H. Ravindranath, A. Reisinger, K. Riahi, M. Rusticucci, R. Scholes, K. Seyboth, Y. Sokona, R. Stavins, T.F. Stocker, P. Tschakert, D. van Vuuren, J.-P. van Ypserle, Climate Change 2014: Synthesis Report. Contribution of Working Groups I, II and III to the Fifth Assessment Report of the Intergovernmental Panel on Climate Change, IPCC, 2014.

[7] World Resources Institute, Climate Watch Historical GHG Emissions (2021). In: https://www.climatewatchdata.org/ghg-emissions. Accessed: Jun 2021.

[8] Net-zero carbon pledges must be meaningful to avert climate disaster. Nature 592 (2021) 8, doi: https://doi.org/10.1038/d41586-021-00864-9.

[9] UN General Assembly, Transforming our world: the 2030 Agenda for Sustainable Development, A/RES/70/1 (2015). In: https://www.refworld.org/docid/57b6e3e44.html. Accessed: Jun 2021

[10] M. Luomi, The Global Governance of Sustainable Energy: Access and Sustainable Transitions (2020). In: https://www.iisd.org/articles/global-governance-sustainable-energy. Accessed: Jun 2021.

[11] P.M. Falcone, M. Hiete, A. Sapio, Hydrogen economy and sustainable development goals: Review and policy insights. Curr. Opin. Green Sustain. Chem. 31 (2021) 100506, doi: https://doi.org/10.1016/j.cogsc.2021.100506.

[12] IEA, Net Zero by 2050 (2021). In: https://www.iea.org/reports/net-zero-by-2050. Accessed: Jun 2021.

[13] IEA, The Future of Hydrogen (2019). In: https://www.iea.org/reports/the-future-of-hydrogen. Accessed: Sep 2020.

[14] IRENA, Hydrogen from renewable power: Technology outlook for the energy transition (2018). In: https://www.irena.org/publications/2018/Sep/Hydrogen-from-renewable-power#:~:text=Hydrogen%20from%20renewable%20power%3A%20Technology%20outlook%20for%20the%20energy%20transition,September%202018&text=Hydrogen%20provides%20high%2Dgrade%20heat,of%20the%20global%20energy%20system. Accessed: Sep 2021.

[15] L.P. Bloomberg finance, Hydrogen Economy Outlook. (2020). In: https://data.bloomberglp.com/professional/sites/24/BNEF-Hydrogen-Economy-Outlook-Key-Messages-30-Mar-2020.pdf.

[16] The Oxford Institute for Energy Studies, The Heralds of Hydrogen. Energy Insight 82 (2021). In: https://a9w7k6q9.stackpathcdn.com/wpcms/wp-content/uploads/2021/01/Insight-82-The-Heralds-of-Hydrogen.pdf. Accessed: Jun 21

[17] F. Epron, D. Duprez, Chapter 3. Hydrogen production by catalytic processes, in: Current Trends and Future Developments on (Bio-) Membranes. Basile, A. and Napporn, T.W. (Eds.), Elsevier (2020), pp. 57-89, doi: https://doi.org/10.1016/B978-0-12-817110-3.00003-5.

[18] M. Yue, H. Lambert, E. Pahon, R. Roche, S. Jemei, D. Hissel, Hydrogen energy systems: A critical review of technologies, applications, trends and challenges. Renew. Sust. Energy Rev. 146 (2021) 111180, doi: https://doi.org/10.1016/j.rser.2021.111180.

[19] S.E. Hosseini, B. Butler, An overview of development and challenges in hydrogen powered vehicles. Int. J. Green Energy 17 (2020) 13-37, doi: https://doi.org/10.1080/15435075.2019.1685999.

[20] S. Mekhilef, R. Saidur, A. Safari, Comparative study of different fuel cell technologies. Renew. Sustain. Energy Rev. 16 (2012) 981-989, doi: https://doi.org/10.1016/j.rser.2011.09.020.

[21] P. Nikolaidis, A. Poullikkas, A comparative overview of hydrogen production processes. Renew. Sustain. Energy Rev. 67 (2017) 597-611, doi: https://doi.org/10.1016/j.rser.2016.09.044.

[22] A. Mehmeti, A. Angelis-Dimakis, G. Arampatzis, S.J. McPhail, S. Ulgiati, Life cycle assessment and water footprint of hydrogen production methods: From conventional to emerging technologies. Environments 5(2) (2018) 1-19, doi: https://doi.org/10.3390/environments5020024.

[23] IEA, Hydrogen (2020). In: https://www.iea.org/reports/hydrogen. Accessed: Jun 2021.

[24] S.-. Kim, G. Kumar, W.-H. Chen, S.K. Khanal, Renewable hydrogen production from biomass and wastes (ReBioH_2-2020). Bioresour. Technol. 331 (2021) 125024, doi: https://doi.org/10.1016/j.biortech.2021.125024.

[25] E. Markočič, B. Kramberger, J.G. Van Bennekom, H. Jan Heeres, J. Vos, Ž Knez, Glycerol reforming in supercritical water; A short review. Renew. Sustain. Energy Rev. 23 (2013) 40-48, doi: https://doi.org/10.1016/j.rser.2013.02.046.

[26] N.D. Subramanian, J. Callison, C.R.A. Catlow, P.P. Wells, N. Dimitratos, Optimised hydrogen production by aqueous phase reforming of glycerol on Pt/Al_2O_3. Int. J. Hydrogen Energy 41 (2016) 18441-18450, doi: https://doi.org/10.1016/j.ijhydene.2016.08.081.

[27] J.N. Chheda, G.W. Huber, J.A. Dumesic, Liquid-phase catalytic processing of biomass-derived oxygenated hydrocarbons to fuels and chemicals. Angew. Chem. Int. Ed. 46 (2007) 7164-7183, doi: https://doi.org/10.1002/anie.200604274.

[28] M. El Doukkali, A. Iriondo, I. Gandarias, Enhanced catalytic upgrading of glycerol into high value-added H_2 and propanediols: Recent developments and future perspectives. Mol. Cat. 490 (2020) 110928, doi: https://doi.org/10.1016/j.mcat.2020.110928.

[29] R.D. Cortright, R.R. Davda, J.A. Dumesic, Hydrogen from catalytic reforming of biomass-derived hydrocarbons in liquid water. Nature 418 (2002) 964-967, doi: https://doi.org/10.1038/nature01009.

[30] R.R. Davda, J.A. Dumesic, Renewable hydrogen by aqueous-phase reforming of glucose. Chem. Commun. 4 (2004) 36-37, doi: https://doi.org/10.1039/b310152e.

[31] M. Alvear, A. Aho, I.L. Simakova, H. Grénman, T. Salmi, D.Y. Murzin, Aqueous phase reforming of alcohols over a bimetallic Pt-Pd catalyst in the presence of formic acid. Chem. Eng. J. 398 (2020) 125541, doi: https://doi.org/10.1016/j.cej.2020.125541.

[32] I. Coronado, M. Stekrova, L. García Moreno, M. Reinikainen, P. Simell, R. Karinen, J. Lehtonen, Aqueous-phase reforming of methanol over nickel-based catalysts for hydrogen

production. Biomass Bioenergy 106 (2017) 29-37, doi: https://doi.org/10.1016/j.biombioe.2017.08.018.

[33] J. Tao, L. Hou, B. Yan, G. Chen, W. Li, H. Chen, Z. Cheng, F. Lin, Hydrogen Production via Aqueous-Phase Reforming of Ethylene Glycol over a Nickel-Iron Alloy Catalyst: Effect of Cobalt Addition. Energy Fuels 34 (2020) 1153-1161, doi: https://doi.org/10.1021/acs.energyfuels.9b02149.

[34] A. Iriondo, V.L. Barrio, J.F. Cambra, P.L. Arias, M.B. Güemez, R.M. Navarro, M.C. Sánchez-Sánchez, J.L.G. Fierro, Hydrogen production from glycerol over nickel catalysts supported on Al_2O_3 modified by Mg, Zr, Ce or La. Top. Catal. 49 (2008) 46-58, doi: https://doi.org/10.1007/s11244-008-9060-9.

[35] N. Luo, X. Fu, F. Cao, T. Xiao, P.P. Edwards, Glycerol aqueous phase reforming for hydrogen generation over Pt catalyst - Effect of catalyst composition and reaction conditions. Fuel 87 (2008) 3483-3489, doi: https://doi.org/10.1016/j.fuel.2008.06.021.

[36] T. Xie, C.J. Bodenschatz, R.B. Getman, Insights into the roles of water on the aqueous phase reforming of glycerol. React. Chem. Eng. 4 (2019) 383-392, doi: https://doi.org/10.1039/c8re00267c.

[37] A.V. Kirilin, B. Hasse, A.V. Tokarev, L.M. Kustov, G.N. Baeva, G.O. Bragina, A.Y. Stakheev, A.R. Rautio, T. Salmi, B.J.M. Etzold, J.P. Mikkola, D.Y. Murzin, Aqueous-phase reforming of xylitol over Pt/C and Pt/TiC-CDC catalysts: Catalyst characterization and catalytic performance. Catal. Sci. Technol. 4 (2014) 387-401, doi: https://doi.org/10.1039/c3cy00636k.

[38] A. Kirilin, J. Wärnå, A. Tokarev, D.Y. Murzin, Kinetic modeling of sorbitol aqueous-phase reforming over Pt/Al_2O_3. Ind. Eng. Chem. Res. 53 (2014) 4580-4588, doi: https://doi.org/10.1021/ie403813y.

[39] I. Coronado, (2021). Catalytic Aqueous-Phase Reforming of Biorefinery Water Fractions. 9789-526402307(ELECTRONIC). Doctoral Thesis. Aalto University. Aaltodoc publication archive.

[40] B. Liu, F. Gao, Navigating glycerol conversion roadmap and heterogeneous catalyst selection aided by density functional theory: A review. Catalysts 8 (2018) 44, doi: https://doi.org/10.3390/catal8020044.

[41] Q.S. He, J. McNutt, J. Yang, Utilization of the residual glycerol from biodiesel production for renewable energy generation. Renew. Sustain. Energy Rev. 71 (2017) 63-76, doi: https://doi.org/10.1016/j.rser.2016.12.110.

[42] J.J. Bozell, G.R. Petersen, Technology development for the production of biobased products from biorefinery carbohydrates—the US Department of Energy's "top 10" revisited. Green Chem. 12 (2010) 539-55, doi: https://doi.org/10.1039/b922014c.

[43] A. Rodrigues, J.C. Bordado, R.G. Dos Santos, Upgrading the glycerol from biodiesel production as a source of energy carriers and chemicals - A technological review for three chemical pathways. Energies 10 (2017) 1817, doi: https://doi.org/10.3390/en10111817.

[44] B.V. Ayodele, T.A.R.B.T. Abdullah, M.A. Alsaffar, S.I. Mustapa, S.F. Salleh, Recent advances in renewable hydrogen production by thermo-catalytic conversion of biomass-derived glycerol: Overview of prospects and challenges. Int. J. Hydrogen Energy 45 (2020) 18160-18185, doi: https://doi.org/10.1016/j.ijhydene.2019.08.002.

[45] A. Seretis, P. Tsiakaras, Crude bio-glycerol aqueous phase reforming and hydrogenolysis over commercial SiO_2–Al_2O_3 nickel catalyst. Renew. Energy 97 (2016) 373-379, doi: https://doi.org/10.1016/j.renene.2016.05.085.

[46] M. Checa, S. Nogales-Delgado, V. Montes, J.M. Encinar, Recent advances in glycerol catalytic valorization: A review. Catalysts 10 (2020) 1-41, doi: https://doi.org/10.3390/catal10111279.

[47] S. Soam, K. Hillman, Factors influencing the environmental sustainability and growth of hydrotreated vegetable oil (HVO) in Sweden. Bioresour. Technol. Rep. 7 (2019) 100244, doi: https://doi.org/10.1016/j.biteb.2019.100244.

[48] IEA, Renewable Energy Market Update 2021 (2021). In: https://www.iea.org/reports/renewable-energy-market-update-2021. Accessed: Jul 2021.

[49] R.R. Davda, J.W. Shabaker, G.W. Huber, R.D. Cortright, J.A. Dumesic, A review of catalytic issues and process conditions for renewable hydrogen and alkanes by aqueous-phase reforming of oxygenated hydrocarbons over supported metal catalysts. Appl. Catal. B Environ. 56 (2005) 171-186, doi: https://doi.org/10.1016/j.apcatb.2004.04.027.

[50] A. Seretis, P. Tsiakaras, Aqueous phase reforming (APR) of glycerol over platinum supported on Al_2O_3 catalyst. Renew. Energy 85 (2016) 1116-1126, doi: https://doi.org/10.1016/j.renene.2015.07.068.

[51] R.M. Ripken, J. Meuldijk, J.G.E. Gardeniers, S. Le Gac, Influence of the Water Phase State on the Thermodynamics of Aqueous-Phase Reforming for Hydrogen Production. ChemSusChem 10 (2017) 4909-4913, doi: https://doi.org/10.1002/cssc.201700189.

[52] A. Seretis, P. Tsiakaras, A thermodynamic analysis of hydrogen production via aqueous phase reforming of glycerol. Fuel Process. Technol. 134 (2015) 107-115, doi: https://doi.org/10.1016/j.fuproc.2015.01.021.

[53] G.W. Huber, R.D. Cortright, J.A. Dumesic, Renewable alkanes by aqueous-phase reforming of biomass-derived oxygenates. Angew. Chem. Int. Ed. 43 (2004) 1549-1551, doi: https://doi.org/10.1002/anie.200353050.

[54] J.W. Shabaker, R.R. Davda, G.W. Huber, R.D. Cortright, J.A. Dumesic, Aqueous-phase reforming of methanol and ethylene glycol over alumina-supported platinum catalysts. J. Catal. 215 (2003) 344-352, doi: https://doi.org/10.1016/S0021-9517(03)00032-0.

[55] K. Lehnert, P. Claus, Influence of Pt particle size and support type on the aqueous-phase reforming of glycerol. Catal. Commun. 9 (2008) 2543-2546, doi: https://doi.org/10.1016/j.catcom.2008.07.002.

[56] G.W. Huber, J.W. Shabaker, S.T. Evans, J.A. Dumesic, Aqueous-phase reforming of ethylene glycol over supported Pt and Pd bimetallic catalysts. Appl. Catal. B Environ. 62 (2006) 226-235, doi: https://doi.org/10.1016/j.apcatb.2005.07.010.

[57] J. Liu, B. Sun, J. Hu, Y. Pei, H. Li, M. Qiao, Aqueous-phase reforming of ethylene glycol to hydrogen on Pd/Fe_3O_4 catalyst prepared by co-precipitation: Metal-support interaction and excellent intrinsic activity. J. Catal. 274 (2010) 287-295, doi: https://doi.org/10.1016/j.jcat.2010.07.014.

[58] Y. Guo, M.U. Azmat, X. Liu, Y. Wang, G. Lu, Effect of support's basic properties on hydrogen production in aqueous-phase reforming of glycerol and correlation between WGS and APR. Appl. Energy 92 (2012) 218-223, doi: https://doi.org/10.1016/j.apenergy.2011.10.020.

[59] Z. Tang, J. Monroe, J. Dong, T. Nenoff, D. Weinkauf, Platinum-loaded NaY zeolite for aqueous-phase reforming of methanol and ethanol to hydrogen. Ind. Eng. Chem. Res. 48 (2009) 2728-2733, doi: https://doi.org/10.1021/ie801222f.

[60] L. Han, F. Cao, Int. Conf. Mater. Renew. Energy Environ. 1 (2011) 255-258, doi: https://doi.org/10.1109/ICMREE.2011.5930808.

[61] T. Van Haasterecht, C.C.I. Ludding, K.P. De Jong, J.H. Bitter, Stability and activity of carbon nanofiber-supported catalysts in the aqueous phase reforming of ethylene glycol. J. Energy Chem. 22 (2013) 257-269, doi: https://doi.org/10.1016/S2095-4956(13)60032-7.

[62] G. Wen, Y. Xu, H. Ma, Z. Xu, Z. Tian, Production of hydrogen by aqueous-phase reforming of glycerol. Int. J. Hydrogen Energy 33 (2008) 6657-6666, doi: https://doi.org/10.1016/j.ijhydene.2008.07.072.

[63] M.M. Rahman, T.L. Church, M.F. Variava, A.T. Harris, A.I. Minett, Bimetallic Pt-Ni composites on ceria-doped alumina supports as catalysts in the aqueous-phase reforming of glycerol. RSC Adv. 4 (2014) 18951-18960, doi: https://doi.org/10.1039/c4ra00355a.

[64] H.J. Lee, G.S. Shin, Y.C. Kim, Characterization of supported Ni catalysts for aqueous-phase reforming of glycerol. Korean J. Chem. Eng. 32 (2015) 1267-1272, doi: https://doi.org/10.1007/s11814-014-0325-7.

[65] G.W. Huber, J.W. Shabaker, J.A. Dumesic, Raney Ni-Sn catalyst for H_2 production from biomass-derived hydrocarbons. Science 300 (2003) 2075-2077, doi: https://doi.org/10.1126/science.1085597.

[66] N. Luo, K. Ouyang, F. Cao, T. Xiao, Hydrogen generation from liquid reforming of glycerin over Ni-Co bimetallic catalyst. Biomass Bioenergy 34 (2010) 489-495, doi: https://doi.org/10.1016/j.biombioe.2009.12.013.

[67] R.L. Manfro, Pires, T.P.M.D., N.F.P. Ribeiro, Souza, M.M.V.M., Aqueous-phase reforming of glycerol using Ni-Cu catalysts prepared from hydrotalcite-like precursors. Catal. Sci. Technol. 3 (2013) 1278-1287, doi: https://doi.org/10.1039/c3cy20770f.

[68] J.H. Sinfelt, D.J.C. Yates, Catalytic hydrogenolysis of ethane over the noble metals of Group VIII. J. Catal. 8 (1967) 82-90, doi: https://doi.org/10.1016/0021-9517(67)90284-9.

[69] D.A. Boga, R. Oord, A.M. Beale, Y.-M. Chung, P.C.A. Bruijnincx, B.M. Weckhuysen, Highly Selective Bimetallic Pt-Cu/Mg(Al)O Catalysts for the Aqueous-Phase Reforming of Glycerol. ChemCatChem 5 (2013) 529-537, doi: https://doi.org/10.1002/cctc.201200112.

[70] T. Xie, S. Sarupria, R.B. Getman, A DFT and MD study of aqueous-phase dehydrogenation of glycerol on Pt(1 1 1): comparing chemical accuracy versus computational expense in different methods for calculating aqueous-phase system energies. Mol. Simul. 43 (2017) 370-378, doi: https://doi.org/10.1080/08927022.2017.1285403.

[71] N.H. Tran, G.S.K. Kannangara, Conversion of glycerol to hydrogen rich gas. Chem. Soc. Rev. 42 (2013) 9454-9479, doi: https://doi.org/10.1039/c3cs60227c.

[72] J.W. Shabaker, G.W. Huber, J.A. Dumesic, Aqueous-phase reforming of oxygenated hydrocarbons over Sn-modified Ni catalysts. J. Catal. 222 (2004) 180-191, doi: https://doi.org/10.1016/j.jcat.2003.10.022.

[73] M. El Doukkali, A. Iriondo, J.F. Cambra, L. Jalowiecki-Duhamel, A.S. Mamede, F. Dumeignil, P.L. Arias, Pt monometallic and bimetallic catalysts prepared by acid sol–gel method for liquid phase reforming of bioglycerol. J. Mol. Catal. A Chem. 368-369 (2013) 125-136, doi: https://doi.org/10.1016/j.molcata.2012.12.006.

[74] Argus media, Metals plataform (2021). In: https://www.argusmedia.com/metals-platform/metal/base-metals-nickel. Accessed: Jun 2021.

[75] J. Remón, J.R. Giménez, A. Valiente, L. García, J. Arauzo, Production of gaseous and liquid chemicals by aqueous phase reforming of crude glycerol: Influence of operating conditions on the process. Energy Convers. Manag. 110 (2016) 90-112, doi: https://doi.org/10.1016/j.enconman.2015.11.070.

[76] A.J. Reynoso, J.L. Ayastuy, U. Iriarte-Velasco, M.A. Gutiérrez-Ortiz, Cobalt aluminate spinel-derived catalysts for glycerol aqueous phase reforming. Appl. Catal. B Environ. 239 (2018) 86-101, doi: https://doi.org/10.1016/j.apcatb.2018.08.001.

[77] R.M. Ravenelle, J.R. Copeland, W.-G. Kim, J.C. Crittenden, C. Sievers, Structural Changes of γ-Al_2O_3-Supported Catalysts in Hot Liquid Water. ACS Catal. 1 (2011) 552-561, doi: https://doi.org/10.1021/cs1001515.

[78] G. Li, L. Hu, J.M. Hill, Comparison of reducibility and stability of alumina-supported Ni catalysts prepared by impregnation and co-precipitation. Appl. Catal. A Gen. 301 (2006) 16-24, doi: https://doi.org/10.1016/j.apcata.2005.11.013.

[79] H.S.C. O'Neill, W.A. Dollase, C.R. Ross II, Temperature dependence of the cation distribution in nickel aluminate ($NiAl_2O_4$) spinel: a powder XRD study. Phys. Chem. Minerals 18 (1991) 302-319, doi: https://doi.org/10.1007/BF00200188.

[80] J.D.S. Walker, J.R. Hayes, A.P. Grosvenor, Examination of the site preference of metals in $NiAl_{2-x}Ga_xO_4$ spinel-type oxides by X-ray absorption near-edge spectroscopy. J. Electron Spectrosc. Relat. Phenom. 195 (2014) 139-144, doi: https://doi.org/10.1016/j.elspec.2014.06.013.

[81] C. Biagioni, M. Pasero, The systematics of the spinel-type minerals: An overview. Am. Mineral. 99 (2014) 1254-1264, doi: https://doi.org/10.2138/am.2014.4816.

[82] A. Khan, P.G. Smirniotis, Relationship between temperature-programmed reduction profile and activity of modified ferrite-based catalysts for WGS reaction. J. Mol. Catal. A Chem. 280 (2008) 43-51, doi: https://doi.org/10.1016/j.molcata.2007.10.022.

[83] N.F.P. Ribeiro, R.C.R. Neto, S.F. Moya, Souza, Mariana M. V. M., M. Schmal, Synthesis of $NiAl_2O_4$ with high surface area as precursor of Ni nanoparticles for hydrogen production. Int. J. Hydrogen Energy 35 (2010) 11725-11732, doi: https://doi.org/10.1016/j.ijhydene.2010.08.024.

[84] M.E. Rivas, J.L.G. Fierro, R. Guil-López, M.A. Peña, V. La Parola, M.R. Goldwasser, Preparation and characterization of nickel-based mixed-oxides and their performance for catalytic methane decomposition. Catal. Today 133-135 (2008) 367-373, doi: https://doi.org/10.1016/j.cattod.2007.12.045.

[85] L. Zhou, L. Li, N. Wei, J. Li, J.-M. Basset, Effect of $NiAl_2O_4$ Formation on Ni/Al_2O_3 Stability during Dry Reforming of Methane. ChemCatChem 7 (2015) 2508-2516, doi: https://doi.org/10.1002/cctc.201500379.

[86] D.F.P. Suffredini, V.V. Thyssen, P.M.M. de Almeida, R.S. Gomes, M.C. Borges, A.M. Duarte de Farias, E.M. Assaf, M.A. Fraga, S.T. Brandão, Renewable hydrogen from glycerol reforming over nickel aluminate-based catalysts. Catal. Today 289 (2017) 96-104, doi: https://doi.org/10.1016/j.cattod.2016.07.027.

[87] I.A.P.S. Murthy, C.S. Swamy, Catalytic behaviour of $NiAl_2O_4$ spinel upon hydrogen treatment. J. Mater. Sci. 28 (1993) 1194-1198, doi: https://doi.org/10.1007/BF01191952.

[88] C. Jiménez-González, Z. Boukha, B. de Rivas, J.J. Delgado, M.Á Cauqui, J.R. González-Velasco, J.I. Gutiérrez-Ortiz, R. López-Fonseca, Structural characterisation of Ni/alumina reforming catalysts activated at high temperatures. Appl. Catal. A Gen. 466 (2013) 9-20, doi: https://doi.org/10.1016/j.apcata.2013.06.017.

[89] C. Jiménez-González, Z. Boukha, B. De Rivas, J.R. González-Velasco, J.I. Gutiérrez-Ortiz, R. López-Fonseca, Behavior of coprecipitated $NiAl_2O_4/Al_2O_3$ catalysts for low-temperature methane steam reforming. Energy Fuels 28 (2014) 7109-7121, doi: https://doi.org/10.1021/ef501612y.

[90] C. Jiménez-González, Z. Boukha, B. de Rivas, J.R. González-Velasco, J.I. Gutiérrez-Ortiz, R. López-Fonseca, Behaviour of nickel–alumina spinel ($NiAl_2O_4$) catalysts for isooctane steam reforming. Int. J. Hydrogen Energy 40 (2015) 5281-5288, doi: https://doi.org/10.1016/j.ijhydene.2015.01.064.

[91] A. Al-Ubaid, E.E. Wolf, Steam reforming of methane on reduced non-stoichiometric nickel aluminate catalysts. Appl. Catal. 40 (1988) 73-85, doi: https://doi.org/10.1016/S0166-9834(00)80427-3.

[92] M. Behrens, Coprecipitation: An excellent tool for the synthesis of supported metal catalysts - From the understanding of the well known recipes to new materials. Catal. Today 246 (2015) 46-54, doi: https://doi.org/10.1016/j.cattod.2014.07.050.

[93] L. Gama, M.A. Ribeiro, B.S. Barros, R.H.A. Kiminami, I.T. Weber, A.C.F.M. Costa, Synthesis and characterization of the $NiAl_2O_4$, $CoAl_2O_4$ and $ZnAl_2O_4$ spinels by the polymeric precursors method. J. Alloys Compd. 483 (2009) 453-455, doi: https://doi.org/10.1016/j.jallcom.2008.08.111.

[94] J.J. Kingsley, N. Manickam, K.C. Patil, Combustion synthesis and properties of fine particle fluorescent aluminous oxides. Bull. Mater. Sci. 13 (1990) 179-189, doi: https://doi.org/10.1007/BF02744944.

[95] J. Zhu, Q. Gao, Mesoporous MCo_2O_4 (M = Cu, Mn and Ni) spinels: Structural replication, characterization and catalytic application in CO oxidation. Micropor. Mesopor. Mater. 124 (2009) 144-152, doi: https://doi.org/10.1016/j.micromeso.2009.05.003.

[96] F.F. de Sousa, H.S.A. de Sousa, A.C. Oliveira, M.C.C. Junior, A.P. Ayala, E.B. Barros, B.C. Viana, J.M. Filho, A.C. Oliveira, Nanostructured Ni-containing spinel oxides for the dry reforming of methane: Effect of the presence of cobalt and nickel on the deactivation behaviour of catalysts. Int. J. Hydrogen Energy 37 (2012) 3201-3212, doi: https://doi.org/10.1016/j.ijhydene.2011.11.072.

[97] J. Zhang, H. Xu, X. Jin, Q. Ge, W. Li, Characterizations and activities of the nano-sized Ni/Al_2O_3 and $Ni/La\text{-}Al_2O_3$ catalysts for NH_3 decomposition. Appl. Catal. A Gen. 290 (2005) 87-96, doi: https://doi.org/10.1016/j.apcata.2005.05.020.

[98] N. Linares, A.M. Silvestre-Albero, E. Serrano, J. Silvestre-Albero, J. García-Martínez, Mesoporous materials for clean energy technologies. Chem. Soc. Rev. 43 (2014) 7681-7717, doi: https://doi.org/10.1039/c3cs60435g.

[99] B. Tian, X. Liu, H. Yang, S. Xie, C. Yu, B. Tu, D. Zhao, General Synthesis of Ordered Crystallized Metal Oxide Nanoarrays Replicated by Microwave-Digested Mesoporous Silica. Adv. Mater. 15 (2003) 1370-1374, doi: https://doi.org/10.1002/adma.200305211.

[100] D. Li, X. Li, J. Gong, Catalytic Reforming of Oxygenates: State of the Art and Future Prospects. Chem. Rev. 116 (2016) 11529-11653, doi: https://doi.org/10.1021/acs.chemrev.6b00099.

[101] P.V. Tuza, R.L. Manfro, N.F.P. Ribeiro, M.M.V.M. Souza, Production of renewable hydrogen by aqueous-phase reforming of glycerol over Ni–Cu catalysts derived from hydrotalcite precursors. Renew. Energy 50 (2013) 408-414, doi: https://doi.org/10.1016/j.renene.2012.07.006.

[102] J.W. Shabaker, D.A. Simonetti, R.D. Cortright, J.A. Dumesic, Sn-modified Ni catalysts for aqueous-phase reforming: Characterization and deactivation studies. J. Catal. 231 (2005) 67-76, doi: https://doi.org/10.1016/j.jcat.2005.01.019.

[103] J. Zheng, S. Jixin, M.O. Jones, S. Huahong, X. Tiancun, P.P. Edwards, Catalytic partial oxidation of methane over Ni-based catalysts derived from Ni-Mg/Al ternary hydrotalcites. Energy Fuels 23 (2009) 1634-1639, doi: https://doi.org/10.1021/ef800933j.

[104] J.I. Di Cosimo, V.K. Díez, M. Xu, E. Iglesia, C.R. Apesteguía, Structure and surface and catalytic properties of Mg-Al basic oxides. J. Catal. 178 (1998) 499-510, doi: https://doi.org/10.1006/jcat.1998.2161.

[105] J.L. Todolí, J.M. Mermet, Sample introduction systems for the analysis of liquid microsamples by ICP-AES and ICP-MS. Spectrochim Acta Part B At Spectrosc. 61 (2006) 239-283, doi: https://doi.org/10.1016/j.sab.2005.12.010.

[106] M. Faraldos, Técnicas de Análisis y Caracterización de Materiales, 2a. ed., Editorial CSIC, Consejo Superior de Investigaciones Científicas, Madrid, 2011.

[107] M. Thommes, K. Kaneko, A.V. Neimark, J.P. Olivier, F. Rodriguez-Reinoso, J. Rouquerol, K.S.W. Sing, Physisorption of gases, with special reference to the evaluation of surface area and pore size distribution (IUPAC Technical Report). Pure Appl. Chem. 87 (2015) 1051-1069, doi: https://doi.org/10.1515/pac-2014-1117.

[108] E.P. Barrett, L.G. Joyner, P.P. Halenda, The Determination of Pore Volume and Area Distributions in Porous Substances. I. Computations from Nitrogen Isotherms. J. Am. Chem. Soc. 73 (1951) 373-380, doi: https://doi.org/10.1021/ja01145a126.

[109] Geochemical Instrumentation and Analysis, Montana State University, X-ray Powder Diffraction (XRD). In: https://serc.carleton.edu/research_education/geochemsheets/techniques/XRD.html Accessed: May 2021.

[110] F. Krumeich, E. Müller, R.A. Wepf, R. Nesper, Characterization of catalysts in an aberration-corrected scanning transmission electron microscope. J. Phys. Chem. C 115 (2011) 1080-1083, doi: https://doi.org/10.1021/jp105997h.

[111] ETH Zürich, Electron Microscopy (2021). In: https://www.microscopy.ethz.ch/BFDF-STEM.htm Accessed: May 2021.

[112] A. Borodziński, M. Bonarowska, Relation between crystallite size and dispersion on supported metal catalysts. Langmuir 13 (1997) 5613-5620, doi: https://doi.org/10.1021/la962103u.

[113] E. Marceau, C. Perier, T. Burt, Measurement of diffuse reflection from catalyst powders using the Praying Mantis accessory and Agilent Cary 5000 UV-Vis-NIR spectrophotometer (2012). In: https://www.agilent.com/cs/library/applications/5990-9787EN_AppNote_Cary5000_Powders.pdf. Accessed: March 2021.

[114] M. Fadoni, L. Lucarelli, Temperature programmed desorption, reduction, oxidation and flow chemisorption for the characterisation of heterogeneous catalysts. Theoretical aspects, instrumentation and applications. Stud. Surf. Sci. Catal. 120 (1999) 177-225, doi: https://doi.org/10.1016/S0167-2991(99)80553-9.

[115] S. Bhatia, J. Beltramini, D.D. Do, Temperature programmed analysis and its applications in catalytic systems. Catal. Today 7 (1990) 309-438, doi: https://doi.org/10.1016/0920-5861(90)87001-J.

[116] M.I. Zaki, M.A. Hasan, F.A. Al-Sagheer, L. Pasupulety, In situ FTIR spectra of pyridine adsorbed on SiO_2-Al_2O_3, TiO_2, ZrO_2 and CeO_2: General considerations for the identification of acid sites on surfaces of finely divided metal oxides. Colloids Surf. A Physicochem. Eng. Asp. 190 (2001) 261-274, doi: https://doi.org/10.1016/S0927-7757(01)00690-2.

[117] C.A. Emeis, Determination of integrated molar extinction coefficients for infrared absorption bands of pyridine adsorbed on solid acid catalysts. J. Catal. 141 (1993) 347-354, doi: https://doi.org/10.1006/jcat.1993.1145.

[118] M.C.J. Bradford, M.A. Vannice, Catalytic reforming of methane with carbon dioxide over nickel catalysts II. Reaction kinetics. Appl. Catal. A Gen. 142 (1996) 97-122, doi: https://doi.org/10.1016/0926-860X(96)00066-X.

[119] J.S. Smith, P.A. Thrower, M.A. Vannice, Characterization of $NiTiO_2$ catalysts by TEM, X-ray diffraction, and chemisorption techniques. J. Catal. 68 (1981) 270-285, doi: https://doi.org/10.1016/0021-9517(81)90097-X.

[120] Waters, Beginners Guide to Liquid Chromatography (2021). In: https://www.waters.com/waters/en_US/How-Doe-High-Performance-Liquid-Chromatography-Work%3F/nav.htm?cid=10049055&locale=en_US. Accessed: May 2021.

[121] L.I. Godina, A.V. Kirilin, A.V. Tokarev, I.L. Simakova, D.Y. Murzin, Sibunit-Supported Mono- and Bimetallic Catalysts Used in Aqueous-Phase Reforming of Xylitol. Ind. Eng. Chem. Res. 57 (2018) 2050-2067, doi: https://doi.org/10.1021/acs.iecr.7b04937.

[122] K. Miyabe, M. Ando, N. Ando, G. Guiochon, External mass transfer in high performance liquid chromatography systems. J. Chromatogr. A 1210 (2008) 60-67, doi: https://doi.org/10.1016/j.chroma.2008.09.035.

[123] A. Carrero, J.A. Calles, L. García-Moreno, A.J. Vizcaíno, Production of renewable hydrogen from glycerol steam reforming over bimetallic Ni-(Cu,Co,Cr) catalysts supported on SBA-15 silica. Catalysts 7 (2017), doi: https://doi.org/10.3390/catal7020055.

[124] J. Lee, D.H.K. Jackson, T. Li, R.E. Winans, J.A. Dumesic, T.F. Kuech, G.W. Huber, Enhanced stability of cobalt catalysts by atomic layer deposition for aqueous-phase reactions. Energy Environ. Sci. 7 (2014) 1657-1660, doi: https://doi.org/10.1039/c4ee00379a.

[125] K.-M. Nam, H.-J. Kim, D.-H. Kang, Y.-S. Kim, S.-W. Song, Ammonia-free coprecipitation synthesis of a Ni-Co-Mn hydroxide precursor for high-performance battery cathode materials. Green Chem. 17 (2015) 1127-1135, doi: https://doi.org/10.1039/c4gc01898b.

[126] A. Quindimil, U. De-La-Torre, B. Pereda-Ayo, J.A. González-Marcos, J.R. González-Velasco, Ni catalysts with La as promoter supported over Y- and BETA- zeolites for CO_2 methanation. Appl. Catal. B Environ. 238 (2018) 393-403, doi: https://doi.org/10.1016/j.apcatb.2018.07.034.

[127] Z. Boukha, C. Jiménez-González, B. de Rivas, J.R. González-Velasco, J.I. Gutiérrez-Ortiz, R. López-Fonseca, Synthesis, characterisation and performance evaluation of spinel-derived Ni/Al_2O_3 catalysts for various methane reforming reactions. Appl. Catal. B Environ. 158-159 (2014) 190-201, doi: https://doi.org/10.1016/j.apcatb.2014.04.014.

[128] A. Choya, B. de Rivas, J.R. González-Velasco, J.I. Gutiérrez-Ortiz, R. López-Fonseca, Optimisation of bimetallic Co-Ni supported catalysts for oxidation of methane in natural gas vehicles. Appl. Catal. B Environ. 284 (2021) 119712, doi: https://doi.org/10.1016/j.apcatb.2020.119712.

[129] H. Özdemir, M.A. Faruk Öksüzömer, Synthesis of Al_2O_3, MgO and $MgAl_2O_4$ by solution combustion method and investigation of performances in partial oxidation of methane. Powder Technol. 359 (2020) 107-117, doi: https://doi.org/10.1016/j.powtec.2019.10.001.

[130] R.D.D. Putra, H.L. Trajano, S. Liu, H. Lee, K. Smith, C.S. Kim, In-situ glycerol aqueous phase reforming and phenol hydrogenation over Raney Ni®. Chem. Eng. J. 350 (2018) 181-191, doi: https://doi.org/10.1016/j.cej.2018.05.146.

[131] E.V. Golubina, E.S. Lokteva, N.E. Kavalerskaya, K.I. Maslakov, Effect of Calcination Temperature on the Efficiency of Ni/Al_2O_3 in the Hydrodechlorination Reaction. Kinet. Catal. 61 (2020) 444-459, doi: https://doi.org/10.1134/S002315842003012X.

[132] L. García, A. Valiente, M. Oliva, J. Ruiz, J. Arauzo, Influence of operating variables on the aqueous-phase reforming of glycerol over a Ni/Al coprecipitated catalyst. Int. J. Hydrogen Energy 43 (2018) 20392-20407, doi: https://doi.org/10.1016/j.ijhydene.2018.09.119.

[133] D.C. Montgomery, Design and Analysis of Experiments, Ninth edition, John Wiley & Sons, 2017.

[134] J.L. Rogers, M.C. Mangarella, A.D. D'Amico, J.R. Gallagher, M.R. Dutzer, E. Stavitski, J.T. Miller, C. Sievers, Differences in the Nature of Active Sites for Methane Dry Reforming and Methane Steam Reforming over Nickel Aluminate Catalysts. ACS Catal. 6 (2016) 5873-5886, doi: https://doi.org/10.1021/acscatal.6b01133.

[135] A. Tirsoaga, D. Visinescu, B. Jurca, A. Ianculescu, O. Carp, Eco-friendly combustion-based synthesis of metal aluminates MAl_2O_4 (M = Ni, Co). J. Nanopart. Res. 13 (2011) 6397-6408, doi: https://doi.org/10.1007/s11051-011-0392-1.

[136] Z. Skoufa, G. Xantri, E. Heracleous, A.A. Lemonidou, A study of Ni-Al-O mixed oxides as catalysts for the oxidative conversion of ethane to ethylene. Appl. Catal. A Gen 471 (2014) 107-117, doi: https://doi.org/10.1016/j.apcata.2013.11.042.

[137] N. Braidy, S. Bastien, J. Blanchard, C. Fauteux-Lefebvre, I.E. Achouri, N. Abatzoglou, Activation mechanism and microstructural evolution of a YSZ/Ni-alumina catalyst for dry reforming of methane. Catal. Today 291 (2017) 99-105, doi: https://doi.org/10.1016/j.cattod.2017.03.006.

[138] L. Karam, J. Reboul, N. El Hassan, J. Nelayah, P. Massiani, Nanostructured nickel aluminate as a key intermediate for the production of highly dispersed and stable nickel nanoparticles supported within mesoporous alumina for dry reforming of methane. Molecules 24 (2019) 4107, doi: https://doi.org/10.3390/molecules24224107.

[139] C.H. Bartholomew, Mechanisms of catalyst deactivation. Appl. Catal. A Gen. 212 (2001) 17-60, doi: https://doi.org/10.1016/S0926-860X(00)00843-7.

[140] I. Halevy, D. Dragoi, E. Üstündag, A.F. Yue, E.H. Arredondo, J. Hu, M.S. Somayazulu, The effect of pressure on the structure of $NiAl_2O_4$. J. Phys. Condens. Matter. 14 (2002) 10511-10516, doi: https://doi.org/10.1088/0953-8984/14/44/324.

[141] Y.S. Han, J.B. Li, X.S. Ning, B. Chi, Effect of preparation temperature on the lattice parameter of nickel aluminate spinel. J. Am. Ceram. Soc. 87 (2004) 1347-1349, doi: https://doi.org/10.1111/j.1151-2916.2004.tb07733.x.

[142] J. Gangwar, B.K. Gupta, S.K. Tripathi, A.K. Srivastava, Phase dependent thermal and spectroscopic responses of Al_2O_3 nanostructures with different morphogenesis. Nanoscale 7 (2015) 13313-13344, doi: https://doi.org/10.1039/c5nr02369f.

[143] Y. Absalan, I.G. Bratchikova, N.N. Lobanov, O.V. Kovalchukova, Correction to: Novel synthesis method for photo-catalytic system based on some 3d-metal titanates. J. Mater. Sci. Mater. Electron 28 (2017) 18220, doi: https://doi.org/10.1007/s10854-017-7879-1.

[144] N. Bayal, P. Jeevanandam, Synthesis of metal aluminate nanoparticles by sol-gel method and studies on their reactivity. J. Alloys Compd. 516 (2012) 27-32, doi: https://doi.org/10.1016/j.jallcom.2011.11.080.

[145] E. Leal, A.C.F. De Melo Costa, N.L. De Freita, H. De Lucena Lira, R.H.G.A. Kiminami, L. Gama, $NiAl_2O_4$ catalysts prepared by combustion reaction using glycine as fuel. Mater. Res. Bull. 46 (2011) 1409-1413, doi: https://doi.org/10.1016/j.materresbull.2011.05.011.

[146] E. Heracleous, A.F. Lee, K. Wilson, A.A. Lemonidou, Investigation of Ni-based alumina-supported catalysts for the oxidative dehydrogenation of ethane to ethylene: Structural characterization and reactivity studies. J. Catal. 231 (2005) 159-171, doi: https://doi.org/10.1016/j.jcat.2005.01.015.

[147] J. Wang, L. Dong, Y. Hu, G. Zheng, Z. Hu, Y. Chen, Dispersion of NiO supported on γ-Al_2O_3 and TiO_2/ γ-Al_2O_3 supports. J. Solid State Chem. 157 (2001) 274-282, doi: https://doi.org/10.1006/jssc.2000.9050.

[148] J.L.C. Huaman, N. Hironaka, S. Tanaka, K. Shinoda, H. Miyamura, B. Jeyadevan, Size-controlled monodispersed nickel nanocrystals using 2-octanol as reducing agent. Crystengcomm 15 (2013) 729-737, doi: https://doi.org/10.1039/c2ce26433a.

[149] A. Tribalis, G. Panagiotou, K. Bourikas, L. Sygellou, S. Kennou, S. Ladas, A. Lycourghiotis, C. Kordulis, Ni Catalysts Supported on Modified Alumina for Diesel Steam Reforming. Catalysts 6 (2016) 11, doi: https://doi.org/10.3390/catal6010011.

[150] H. Deng, Y. Yu, H. He, The role of Ag-O-Al entities in adsorption of –NCO species and reduction of NOx. Catal. Today 258 (2015) 35-40, doi: https://doi.org/10.1016/j.cattod.2015.03.023.

[151] R. Estevez, S. Lopez-Pedrajas, F. Blanco-Bonilla, D. Luna, F.M. Bautista, Production of acrolein from glycerol in liquid phase on heterogeneous catalysts. Chem. Eng. J. 282 (2015) 179-186, doi: https://doi.org/10.1016/j.cej.2015.03.018.

[152] L. Smoláková, M. Kout, E. Koudelková, L. Čapek, Effect of Calcination Temperature on the Structure and Catalytic Performance of the Ni/Al_2O_3 and Ni-Ce/Al_2O_3 Catalysts in Oxidative Dehydrogenation of Ethane. Ind. Eng. Chem. Res 54 (2015) 12730-12740, doi: https://doi.org/10.1021/acs.iecr.5b03425.

[153] M. León, E. Díaz, S. Bennici, A. Vega, S. Ordóñez, A. Auroux, Adsorption of CO_2 on hydrotalcite-derived mixed oxides: Sorption mechanisms and consequences for adsorption irreversibility. Ind. Eng. Chem. Res. 49 (2010) 3663-3671, doi: https://doi.org/10.1021/ie902072a.

[154] R. Dębek, M. Radlik, M. Motak, M.E. Galvez, W. Turek, P. Da Costa, T. Grzybek, Catal. Ni-containing Ce-promoted hydrotalcite derived materials as catalysts for methane reforming with carbon dioxide at low temperature – On the effect of basicity. Catal. Today 257 (2015) 59-65, doi: https://doi.org/10.1016/j.cattod.2015.03.017.

[155] J.R. Rostrup-Nielsen, Catalytic Steam Reforming, in: Catalysis. Anderson, J.R. and Boudart, M. (Eds.), Springer, Berlin (1984).

[156] D.C. Grenoble, M.M. Estadt, D.F. Ollis, The chemistry and catalysis of the water gas shift reaction: 1. The kinetics over supported metal catalysts. J. Catal. 67 (1981) 90-102, doi: https://doi.org/10.1016/0021-9517(81)90263-3.

[157] P.J. Dietrich, R.J. Lobo-Lapidus, T. Wu, A. Sumer, M.C. Akatay, B.R. Fingland, N. Guo, J.A. Dumesic, C.L. Marshall, E. Stach, J. Jellinek, W.N. Delgass, F.H. Ribeiro, J.T. Miller, Aqueous phase glycerol reforming by PtMo bimetallic nano-particle catalyst: Product selectivity and structural characterization. Top. Catal. 55 (2012) 53-69, doi: https://doi.org/10.1007/s11244-012-9775-5.

[158] A. Iriondo, J.F. Cambra, M.B. Güemez, V.L. Barrio, J. Requies, M.C. Sánchez-Sánchez, R.M. Navarro, Effect of ZrO_2 addition on Ni/Al_2O_3 catalyst to produce H_2 from glycerol. Int. J. Hydrogen Energy 37 (2012) 7084-7093, doi: https://doi.org/10.1016/j.ijhydene.2011.11.075.

[159] J. Ashok, M.H. Wai, S. Kawi, Nickel-based Catalysts for High-temperature Water Gas Shift Reaction-Methane Suppression. ChemCatChem 10 (2018) 3927-3942, doi: https://doi.org/10.1002/cctc.201800031.

[160] C. Italiano, J. Llorca, L. Pino, M. Ferraro, V. Antonucci, A. Vita, CO and CO_2 methanation over Ni catalysts supported on CeO_2, Al_2O_3 and Y_2O_3 oxides. Appl. Catal. B Environ. 264 (2020), doi: https://doi.org/10.1016/j.apcatb.2019.118494.

[161] F. Bastan, M. Kazemeini, A. Larimi, H. Maleki, Production of renewable hydrogen through aqueous-phase reforming of glycerol over Ni/Al_2O_3–MgO nano-catalyst. Int. J. Hydrogen Energy 43 (2018) 614-621, doi: https://doi.org/10.1016/j.ijhydene.2017.11.122.

[162] M. El Doukkali, A. Iriondo, P.L. Arias, J. Requies, I. Gandarías, L. Jalowiecki-Duhamel, F. Dumeignil, A comparison of sol-gel and impregnated Pt or/and Ni based γ-alumina catalysts for bioglycerol aqueous phase reforming. Appl. Catal. B Environ. 125 (2012) 516-529, doi: https://doi.org/10.1016/j.apcatb.2012.06.024.

[163] Y.H. Park, J.Y. Kim, D.J. Moon, N.C. Park, Y.C. Kim, Effect of $LaAlO_3$-supported modified Ni-based catalysts on aqueous phase reforming of glycerol. Res. Chem. Intermed. 41 (2015) 9603-9614, doi: https://doi.org/10.1007/s11164-015-2020-7.

[164] M.M. Rahman, Aqueous-Phase Reforming of Glycerol over Carbon-Nanotube-Supported Catalysts. Catal. Lett. 150 (2020) 2674-2687, doi: https://doi.org/10.1007/s10562-020-03167-2.

[165] F. Bastan, M. Kazemeini, A.S. Larimi, Aqueous-phase reforming of glycerol for production of alkanes over $Ni/Ce_xZr_{1-x}O_2$ nano-catalyst: Effects of the support's composition. Renew. Energy 108 (2017) 417-424, doi: https://doi.org/10.1016/j.renene.2017.02.076.

[166] J. Callison, N.D. Subramanian, S.M. Rogers, A. Chutia, D. Gianolio, C.R.A. Catlow, P.P. Wells, N. Dimitratos, Directed aqueous-phase reforming of glycerol through tailored platinum nanoparticles. Appl. Catal. B Environ. 238 (2018) 618-628, doi: https://doi.org/10.1016/j.apcatb.2018.07.008.

[167] Y. Guo, X. Liu, Y. Wang, Catalytic and DRIFTS Studies of Pt-Based Bimetallic Alloy Catalysts in Aqueous-Phase Reforming of Glycerol. Ind. Eng. Chem. Res. 58 (2019) 2749-2758, doi: https://doi.org/10.1021/acs.iecr.8b05774.

[168] D.L. King, L. Zhang, G. Xia, A.M. Karim, D.J. Heldebrant, X. Wang, T. Peterson, Y. Wang, Aqueous phase reforming of glycerol for hydrogen production over Pt-Re supported on carbon. Appl. Catal. B Environ. 99 (2010) 206-213, doi: https://doi.org/10.1016/j.apcatb.2010.06.021.

[169] C. Pendem, B. Sarkar, N. Siddiqui, L.N.S. Konathala, C. Baskar, R. Bal, K-Promoted Pt-Hydrotalcite Catalyst for Production of H_2 by Aqueous Phase Reforming of Glycerol. ACS Sustain. Chem. Eng. 6 (2018) 2122-2131, doi: https://doi.org/10.1021/acssuschemeng.7b03512.

[170] I. Gandarias, P.L. Arias, J. Requies, M.B. Güemez, J.L.G. Fierro, Hydrogenolysis of glycerol to propanediols over a Pt/ASA catalyst: The role of acid and metal sites on product selectivity and the reaction mechanism. Appl. Catal. B Environ. 97 (2010) 248-256, doi: https://doi.org/10.1016/j.apcatb.2010.04.008.

[171] A. Talebian-Kiakalaieh, N.A.S. Amin, H. Hezaveh, Glycerol for renewable acrolein production by catalytic dehydration. Renew. Sustain. Energy Rev. 40 (2014) 28-59, doi: https://doi.org/10.1016/j.rser.2014.07.168.

[172] A. Ciftci, D.A.J.M. Ligthart, A.O. Sen, A.J.F. Van Hoof, H. Friedrich, E.J.M. Hensen, Pt-Re synergy in aqueous-phase reforming of glycerol and the water-gas shift reaction. J. Catal. 311 (2014) 88-101, doi: https://doi.org/10.1016/j.jcat.2013.11.011.

[173] L.I. Godina, A.V. Tokarev, I.L. Simakova, P. Mäki-Arvela, E. Kortesmäki, J. Gläsel, L. Kronberg, B. Etzold, D.Y. Murzin, Aqueous-phase reforming of alcohols with three carbon atoms on carbon-supported Pt. Catal. Today 301 (2018) 78-89, doi: https://doi.org/10.1016/j.cattod.2017.03.042.

[174] Y.S. Yun, D.S. Park, J. Yi, Effect of nickel on catalytic behaviour of bimetallic Cu-Ni catalyst supported on mesoporous alumina for the hydrogenolysis of glycerol to 1,2-propanediol. Catal. Sci. Technolog. 4 (2014) 3191-3202, doi: https://doi.org/10.1039/c4cy00320a.

[175] I. Gandarias, P.L. Arias, J. Requies, M. El Doukkali, M.B. Güemez, Liquid-phase glycerol hydrogenolysis to 1,2-propanediol under nitrogen pressure using 2-propanol as hydrogen source. J. Catal. 282 (2011) 237-247, doi: https://doi.org/10.1016/j.jcat.2011.06.020.

[176] A.K. Agarwal, M.S. Wainwright, D.L. Trimm, N.W. Cant, Acetaldehyde hydrogenation over a Cu/SiO_2 catalyst. J. Mol. Catal. 45 (1988) 247-254, doi: https://doi.org/10.1016/0304-5102(88)80014-2.

[177] I. Gandarias, J. Requies, P.L. Arias, U. Armbruster, A. Martin, Liquid-phase glycerol hydrogenolysis by formic acid over $Ni–Cu/Al_2O_3$ catalysts. J. Catal. 290 (2012) 79-89, doi: https://doi.org/10.1016/j.jcat.2012.03.004.

[178] E.B. Pereira, N. Homs, S. Martí, J.L.G. Fierro, P. Ramírez de la Piscina, Oxidative steam-reforming of ethanol over Co/SiO_2, $Co–Rh/SiO_2$ and $Co–Ru/SiO_2$ catalysts: Catalytic behavior and deactivation/regeneration processes. J. Catal. 257 (2008) 206-214, doi: https://doi.org/10.1016/j.jcat.2008.05.001.

[179] A.V. Kirilin, A.V. Tokarev, E.V. Murzina, L.M. Kustov, J.-P. Mikkola, D.Y. Murzin, Reaction products and transformations of intermediates in the aqueous-phase reforming of sorbitol. ChemSusChem 3 (2010) 708-718, doi: https://doi.org/10.1002/cssc.200900254.

[180] M.A. Dasari, P.-P. Kiatsimkul, W.R. Sutterlin, G.J. Suppes, Low-pressure hydrogenolysis of glycerol to propylene glycol. Appl. Catal. A Gen. 281 (2005) 225-231, doi: https://doi.org/10.1016/j.apcata.2004.11.033.

[181] F. Aiouache, L. McAleer, Q. Gan, A.H. Al-Muhtaseb, M.N. Ahmad, Path lumping kinetic model for aqueous phase reforming of sorbitol. Appl. Catal. A Gen. 466 (2013) 240-255, doi: https://doi-org.ehu.idm.oclc.org/10.1016/j.apcata.2013.06.039.

[182] A. Kirilin, J. Wärnå, A. Tokarev, D.Y. Murzin, Kinetic modeling of sorbitol aqueous-phase reforming over Pt/Al_2O_3. Ind. Eng. Chem. Res. 53 (2014) 4580-4588, doi: https://doi.org/10.1021/ie403813y.

[183] I. Coronado, A. Arandia, M. Reinikainen, R. Karinen, R.L. Puurunen, J. Lehtonen, Kinetic modelling of the aqueous-phase reforming of fischer-tropsch water over ceria-zirconia supported nickel-copper catalyst. Catalysts 9 (2019) 936, doi: https://doi.org/10.3390/catal9110936.

[184] A.D. Anderson, M.P. Lanci, J.S. Buchanan, J.A. Dumesic, G.W. Huber, The Hydrodeoxygenation of Glycerol over $NiMoS_x$: Catalyst Stability and Activity at Hydropyrolysis Conditions. ChemCatChem 13 (2021) 425-437, doi: https://doi.org/10.1002/cctc.202001289.

[185] V. Shadravan, E. Kennedy, M. Stockenhuber, An experimental investigation on the effects of adding a transition metal to Ni/Al_2O_3 for catalytic hydrogenation of CO and CO_2 in presence of light alkanes and alkenes. Catal. Today 307 (2018) 277-285, doi: https://doi.org/10.1016/j.cattod.2017.05.036.

[186] D.J.M. de Vlieger, B.L. Mojet, L. Lefferts, K. Seshan, Aqueous Phase Reforming of ethylene glycol – Role of intermediates in catalyst performance. J. Catal. 292 (2012) 239-245, doi: https://doi.org/10.1016/j.jcat.2012.05.019.

[187] M. Besson, P. Gallezot, Deactivation of metal catalysts in liquid phase organic reactions. Catal. Today 81 (2003) 547-559, doi: https://doi.org/10.1016/S0920-5861(03)00153-6.

[188] F. Héroguel, B. Rozmysłowicz, J.S. Luterbacher, Improving heterogeneous catalyst stability for liquid-phase biomass conversion and reforming. Chimia 69 (2015) 582-591, doi: https://doi.org/10.2533/chimia.2015.582.

[189] Y.-P. Du, F. Héroguel, J.S. Luterbacher, Slowing the Kinetics of Alumina Sol–Gel Chemistry for Controlled Catalyst Overcoating and Improved Catalyst Stability and Selectivity. Small 14 (2018) 1801733, doi: https://doi.org/10.1002/smll.201801733.

[190] T.W. Walker, A.H. Motagamwala, J.A. Dumesic, G.W. Huber, Fundamental catalytic challenges to design improved biomass conversion technologies. J. Catal. 369 (2019) 518-525, doi: https://doi.org/10.1016/j.jcat.2018.11.028.

[191] M. El Doukkali, A. Iriondo, J.F. Cambra, I. Gandarias, L. Jalowiecki-Duhamel, F. Dumeignil, P.L. Arias, Deactivation study of the Pt and/or Ni-based γ-Al_2O_3 catalysts used in the aqueous phase reforming of glycerol for H_2 production. Appl. Catal. A Gen. 472 (2014) 80-91, doi: https://doi.org/10.1016/j.apcata.2013.12.015.

[192] T. Van Haasterecht, M. Swart, K.P. De Jong, J.H. Bitter, Effect of initial nickel particle size on stability of nickel catalysts for aqueous phase reforming. J. Energy Chem. 25 (2016) 289-296, doi: https://doi.org/10.1016/j.jechem.2016.01.006.

[193] G. Li, Y. Liu, D. Liu, L. Liu, C. Liu, Synthesis of flower-like Boehmite (AlOOH) via a simple solvothermal process without surfactant. Mater. Res. Bull. 45 (2010) 1487-1491, doi: https://doi.org/10.1016/j.materresbull.2010.06.013.

[194] F. Aupretre, C. Descorme, D. Duprez, D. Casanave, D. Uzio, Ethanol steam reforming over $Mg_xNi_{1-x}Al_2O_3$ spinel oxide-supported Rh catalysts. J. Catal. 233 (2005) 464-477, doi: https://doi.org/10.1016/j.jcat.2005.05.007.

[195] A. Iriondo, J.F. Cambra, V.L. Barrio, M.B. Guemez, P.L. Arias, M.C. Sanchez-Sanchez, R.M. Navarro, J.L.G. Fierro, Glycerol liquid phase conversion over monometallic and bimetallic catalysts: Effect of metal, support type and reaction temperatures. Appl. Catal. B Environ. 106 (2011) 83-93, doi: https://doi.org/10.1016/j.apcatb.2011.05.009.

[196] P.D. Vaidya, J.A. Lopez-Sanchez, Review of Hydrogen Production by Catalytic Aqueous-Phase Reforming. ChemistrySelect 2 (2017) 6563-6576, doi: https://doi.org/10.1002/slct.201700905.

[197] A. Arandia, I. Coronado, A. Remiro, A.G. Gayubo, M. Reinikainen, Aqueous-phase reforming of bio-oil aqueous fraction over nickel-based catalysts. Int. J. Hydrogen Energy 44 (2019) 13157-13168, doi: https://doi.org/10.1016/j.ijhydene.2019.04.007.

[198] N.D. Charisiou, K.N. Papageridis, L. Tzounis, V. Sebastian, S.J. Hinder, M.A. Baker, M. AlKetbi, K. Polychronopoulou, M.A. Goula, Ni supported on CaO-MgO-Al_2O_3 as a highly selective and stable catalyst for H_2 production via the glycerol steam reforming reaction. Int. J. Hydrogen Energy 44 (2019) 256-273, doi: https://doi.org/10.1016/j.ijhydene.2018.02.165.

[199] M.B. Bahari, N.H.H. Phuc, B. Abdullah, F. Alenazey, D.N. Vo, Ethanol dry reforming for syngas production over Ce-promoted Ni/Al_2O_3 catalyst. J. Environ. Chem. Eng. 4 (2016) 4830-4838, doi: https://doi.org/10.1016/j.jece.2016.01.038.

[200] D. Jiang, B. Zhao, Y. Xie, G. Pan, G. Ran, E. Min, Structure and basicity of γ-Al_2O_3-supported MgO and its application to mercaptan oxidation. Appl. Catal. A: Gen. 219 (2001) 69-78, doi: https://doi.org/10.1016/S0926-860X(01)00660-3.

[201] Z. Boukha, C. Jiménez-González, M. Gil-Calvo, B. de Rivas, J.R. González-Velasco, J.I. Gutiérrez-Ortiz, R. López-Fonseca, MgO/$NiAl_2O_4$ as a new formulation of reforming catalysts: Tuning the surface properties for the enhanced partial oxidation of methane. Appl. Catal. B Environ. 199 (2016) 372-383, doi: https://doi.org/10.1016/j.apcatb.2016.06.045.

[202] W. Gac, Acid-base properties of Ni-MgO-Al_2O_3 materials. Appl. Surf. Sci. 257 (2011) 2875-2880, doi: https://doi.org/10.1016/j.apsusc.2010.10.084.

[203] Y. Zhan, J. Han, Z. Bao, B. Cao, Y. Li, J. Street, F. Yu, Biogas reforming of carbon dioxide to syngas production over Ni-Mg-Al catalysts. Mol. Cat. 436 (2017) 248-258, doi: https://doi.org/10.1016/j.mcat.2017.04.032.

[204] Z. He, X. Wang, R. Liu, S. Gao, T. Xiao, Perfomances of different additives on NiO/ γ-Al_2O_3 catalyst in CO methanation. Appl. Petrochem. Res. 6 (2016) 235-241, doi: http://dx.doi.org.ehu.idm.oclc.org/10.1007/s13203-016-0160-3.

[205] A. Parmaliana, F. Arena, F. Frusteri, N. Giordano, Temperature-programmed reduction study of NiO-MgO interaction in magnesia-supported Ni catalysts and NiO-MgO physical mixture. J. Chem. Soc. Faraday Trans. 86 (1990) 2663-2669, doi: https://doi.org/10.1039/FT9908602663.

[206] S. Damyanova, C.A. Perez, M. Schmal, J.M.C. Bueno, Characterization of ceria-coated alumina carrier. Appl. Catal. A Gen. 234 (2002) 271-282, doi: https://doi.org/10.1016/S0926-860X(02)00233-8.

[207] J. Han, Y. Zhan, J. Street, F. To, F. Yu, Natural gas reforming of carbon dioxide for syngas over Ni–Ce–Al catalysts. Int. J. Hydrogen Energy 42 (2017) 18364-18374, doi: https://doi.org/10.1016/j.ijhydene.2017.04.131.

[208] A. Iriondo, V.L. Barrio, J.F. Cambra, P.L. Arias, M.B. Guemez, M.C. Sanchez-Sanchez, R.M. Navarro, J.L.G. Fierro, Glycerol steam reforming over Ni catalysts supported on ceria and ceria-promoted alumina. Int. J. Hydrogen Energy 35 (2010) 11622-11633, doi: https://doi.org/10.1016/j.ijhydene.2010.05.105.

[209] S. Moussa, M.A. Arribas, P. Concepción, A. Martínez, Heterogeneous oligomerization of ethylene to liquids on bifunctional Ni-based catalysts: The influence of support properties on nickel speciation and catalytic performance. Catal. Today 277 (2016) 78-88, doi: https://doi.org/10.1016/j.cattod.2015.11.032.

[210] N.D. Charisiou, G.I. Siakavelas, B. Dou, V. Sebastian, S.J. Hinder, M.A. Baker, K. Polychronopoulou, M.A. Goula, Nickel supported on $AlCeO_3$ as a highly selective and stable catalyst for hydrogen production via the glycerol steam reforming reaction. Catalysts 9 (2019) 411, doi: https://doi.org/10.3390/catal9050411.

[211] J. A. Rached, M.R. Cesario, J. Estephane, H.L. Tidahy, C. Gennequin, S. Aouad, A. Aboukaïs, E. Abi-Aad, Effects of cerium and lanthanum on Ni-based catalysts for CO_2 reforming of toluene. J. Environ. Chem. Eng. 6 (2018) 4743-4754, doi: https://doi.org/10.1016/j.jece.2018.06.054.

[212] C. Sievers, S.L. Scott, Y. Noda, L. Qi, E.M. Albuquerque, R.M. Rioux, Phenomena affecting catalytic reactions at solid−Liquid interfaces. ACS Catal. 6 (2016) 8286-8307, doi: https://doi.org/10.1021/acscatal.6b02532.

[213] Y.Y. Gorbanev, S. Kegnæs, A. Riisager, Selective aerobic oxidation of 5-hydroxymethylfurfural in water over solid ruthenium hydroxide catalysts with magnesium-based supports. Catal. Lett. 141 (2011) 1752-1760, doi: https://doi.org/10.1007/s10562-011-0707-y.

[214] I.C. Freitas, R.L. Manfro, M.M.V.M. Souza, Hydrogenolysis of glycerol to propylene glycol in continuous system without hydrogen addition over Cu-Ni catalysts. Appl. Catal. B Environ. 220 (2018) 31-41, doi: https://doi.org/10.1016/j.apcatb.2017.08.030.

[215] Y. He, X. Liang, B. Chen, Globin-like mesoporous CeO_2: A CO-assisted synthesis based on carbonate hydroxide precursors and its applications in low temperature CO oxidation. Nano. Res. 8 (2015) 1269-1278, doi: https://doi.org/10.1007/s12274-014-0614-9.

[216] M. Stekrova, A. Rinta-Paavola, R. Karinen, Hydrogen production via aqueous-phase reforming of methanol over nickel modified Ce, Zr and La oxide supports. Catal. Today 304 (2018) 143-152, doi: https://doi.org/10.1016/j.cattod.2017.08.030.

[217] J.P.D.S.Q. Menezes, A.P.D.S. Dias, M.A.P. da Silva, M.M.V.M. Souza, Effect of alkaline earth oxides on nickel catalysts supported over γ-alumina for butanol steam reforming: Coke formation and deactivation process. Int. J. Hydrogen Energy 45 (2020) 22906-22920, doi: https://doi.org/10.1016/j.ijhydene.2020.06.187.

[218] A. Morales-Marín, J.L. Ayastuy, U. Iriarte-Velasco, M.A. Gutiérrez-Ortiz, Biohydrogen production by glycerol Aqueous-Phase Reforming: Effect of promoters (Ce or Mg) in the $NiAl_2O_4$ spinel-derived catalysts. J. Environ. Chem. Eng. 9 (2021) 106433, doi: https://doi.org/10.1016/j.jece.2021.106433.

[219] S.D. Senanayake, J. Evans, S. Agnoli, L. Barrio, T.-L. Chen, J. Hrbek, J.A. Rodriguez, Water-gas shift and CO methanation reactions over Ni-CeO_2(111) catalysts. Top. Catal. 54 (2011) 34-41, doi: https://doi.org/10.1007/s11244-011-9645-6.

[220] J. Gao, C. Jia, M. Zhang, F. Gu, G. Xu, F. Su, Effect of nickel nanoparticle size in Ni/α-Al_2O_3 on CO methanation reaction for the production of synthetic natural gas. Catal. Sci. Technol. 3 (2013) 2009-2015, doi: https://doi.org/10.1039/c3cy00139c.

[221] B. Roy, U. Martinez, K. Loganathan, A.K. Datye, C.A. Leclerc, Effect of preparation methods on the performance of Ni/Al_2O_3 catalysts for aqueous-phase reforming of ethanol: Part I-catalytic activity. Int. J. Hydrogen Energy 37 (2012) 8143-8153, doi: https://doi.org/10.1016/j.ijhydene.2012.02.056.

[222] D.K. Singh, K.S. Krishna, S. Harish, S. Sampath, M. Eswaramoorthy, No More HF: Teflon-assisted ultrafast removal of silica to generate high-surface-area mesostructured carbon for enhanced CO_2 capture and supercapacitor performance. Angew. Chem. Int. Ed. 55 (2016) 2032-2036, doi: https://doi.org/10.1002/anie.201509054.

[223] H. Kim, T. Kim, H.J. Park, K. Jeong, H. Chae, S. Jeong, C. Lee, C. Kim, Hydrogen production via the aqueous phase reforming of ethylene glycol over platinum-supported ordered mesoporous carbon catalysts: Effect of structure and framework-configuration. Int. J. Hydrogen Energy 37 (2012) 12187-12197, doi: https://doi.org/10.1016/j.ijhydene.2012.05.126.

[224] A. Gouveia Gil, Z. Wu, D. Chadwick, K. Li, Ni/SBA-15 Catalysts for combined steam methane reforming and water gas shift—Prepared for use in catalytic membrane reactors. Appl. Catal. A Gen. 506 (2015) 188-196, doi: https://doi.org/10.1016/j.apcata.2015.09.009.

[225] D. Zhao, J. Feng, Q. Huo, N. Melosh, G.H. Fredrickson, B.F. Chmelka, G.D. Stucky, Triblock copolymer syntheses of mesoporous silica with periodic 50 to 300 angstrom pores. Science 279 (1998) 548-552, doi: https://doi.org/10.1126/science.279.5350.548.

[226] X. Deng, K. Chen, H. Tüysüz, Protocol for the Nanocasting Method: Preparation of Ordered Mesoporous Metal Oxides. Chem. Mater. 29 (2017) 40-52, doi: https://doi.org/10.1021/acs.chemmater.6b02645.

[227] J.P. Thielemann, F. Girgsdies, R. Schlögl, C. Hess, Pore structure and surface area of silica SBA-15: Influence of washing and scale-up. Beilstein J. Nanotechnol. 2 (2011) 110-118, doi: https://doi.org/10.3762/bjnano.2.13.

[228] M. Sakeye, S. Ziller, H. Amenitsch, M. Lindén, J.-H. Smatt, Detailed study of the nanocasting process by in situ X-ray scattering and diffraction. J. Phys. Chem. C 120 (2016) 1854-1862, doi: https://doi.org/10.1021/acs.jpcc.5b07993.

[229] A. Vinu, D.P. Sawant, K. Ariga, K.Z. Hossain, S.B. Halligudi, M. Hartmann, M. Nomura, Direct synthesis of well-ordered and unusually reactive FeSBA-15 mesoporous molecular sieves. Chem. Mater. 17 (2005) 5339-5345, doi: https://doi.org/10.1021/cm050883z.

[230] J. Wang, H. Ge, W. Bao, Synthesis and characteristics of SBA-15 with thick pore wall and high hydrothermal stability. Mater. Lett. 145 (2015) 312-315, doi: https://doi.org/10.1016/j.matlet.2015.01.113.

[231] A.H.M. Batista, F.S.O. Ramos, T.P. Braga, C.L. Lima, F.F. de Sousa, E.B.D. Barros, J.M. Filho, A.S. de Oliveira, J.R. de Sousa, A. Valentini, A.C. Oliveira, Mesoporous MAl_2O_4 (M = Cu, Ni, Fe or Mg) spinels: Characterisation and application in the catalytic dehydrogenation of ethlylbenzene in the presence of CO_2. Appl. Catal. A Gen. 382 (2010) 148-157, doi: https://doi.org/10.1016/j.apcata.2010.04.027.

[232] L.B. Råberg, M.B. Jensen, U. Olsbye, C. Daniel, S. Haag, C. Mirodatos, A.O. Sjåstad, Propane dry reforming to synthesis gas over Ni-based catalysts: Influence of support and operating parameters on catalyst activity and stability. J. Catalysis 249 (2007) 250-260, doi: https://doi.org/10.1016/j.jcat.2007.04.004.

[233] Y. Cai, X. Xu, H. Wang, L. Wang, L. Chen, R. Li, J. Ding, H. Wan, G. Guan, Bifunctional Co/Al-SBA-15 Catalyst with Tunable Acidity for Selective Production of Aviation Fuel. Ind. Eng. Chem. Res. 57 (2018) 3844-3854, doi: https://doi.org/10.1021/acs.iecr.7b04470.

[234] V. Nichele, M. Signoretto, F. Menegazzo, A. Gallo, V. Dal Santo, G. Cruciani, G. Cerrato, Glycerol steam reforming for hydrogen production: Design of Ni supported catalysts. Appl. Catal. B Environ. 111-112 (2012) 225-232, doi: https://doi.org/10.1016/j.apcatb.2011.10.003.

[235] J.C. Park, H.J. Lee, J.U. Bang, K.H. Park, H. Song, Chemical transformation and morphology change of nickel-silica hybrid nanostructures via nickel phyllosilicates. Chem. Commun. (2009) 7345-7347, doi: https://doi.org/10.1039/b916837k.

[236] T. van Haasterecht, C.C.I. Ludding, K.P. de Jong, J.H. Bitter, Toward stable nickel catalysts for aqueous phase reforming of biomass-derived feedstock under reducing and alkaline conditions. J. Catal. 319 (2014) 27-35, doi: https://doi.org/10.1016/j.jcat.2014.07.014.

[237] S.A.L. Bastos, P.A.L. Lopes, F.N. Santos, L.A. Silva, Experimental design as a tool to study the reaction parameters in hydrogen production from photoinduced reforming of glycerol over CdS photocatalyst. Int. J. Hydrogen Energy 39 (2014) 14588-14595, doi: https://doi.org/10.1016/j.ijhydene.2014.07.073.

Appendices

APPENDICES

A. COMPLETE 2^k FACTORIAL DESIGN: 2^k+2, k= 3 (T, P, W/F_0)

The complete factorial design is used for multivariable optimization, being the number of experiments required 2^k, where k is the number of factors, i.e., system variables. The 2^k factorial design allows the study of the joint effect of the factors on a response. The multivariable procedure reduces the number of experiments since just two levels of each factor are studied without losing information [237].

The factor effect (or main effect) is the change in the process due to a variation in the factor's level. A two level DOE evaluates the low (-1) and the high values (1) of the factors. Repetitions at the central point of both levels (c), commonly called 0 level, can be added when the available resources only allow a single replicate of the design [133].

The influence of the factors temperature (T), pressure (P) and space time (W/F_0), over the catalytic performance of the glycerol APR is evaluated. The DOE also determines how the effect of each factor varies with the change in the level of other factors. Therefore, interaction effects of the above factors have also been attained. The response variables are glycerol conversion (X_{Gly}), conversion to gas (X_{Gas}), hydrogen yield (YH_2), and selectivity to hydrogen (SH_2). The glycerol APR process focused on hydrogen production aimed at maximizing those response variables.

The number of experiments and the evaluated levels are summarized in Table A.1. The level in which the operative variables (T, P and W/F_0) were performed in each of the experiments is shown, being the levels of these variables low (-1), central (0) and high (1). Each observation in the proposed experiment is called a run. Reproducibility runs were 9C and 10C, which correspond to the central point. The response variable column refers to the numerical value of this variable.

As shown in Figure A.1. the combinations in the factorial design, denoted by lowercase letters a, b, and c, are represented on a three-coordinate axis forming a rectangular prism; (1) refers to the combination of the factors, each at the low level. This experimental design system presents seven degrees of freedom among the eight possible combinations of variables. Three degrees are associated with the effects

produced by each variable separately, while the remaining four are associated with the interactions between factors [133], corresponding to the combination T-P, T-W/F_0, P-W/F_0 and T-P-W/F_0.

Table A.1. Planning of the factorial design 2^3+2.

Run	Response variable	Temperature level	Pressure level	Space time level
8	abc	1	1	1
1	(1)	-1	-1	-1
4	bc	-1	1	1
6	ac	1	-1	1
9C	centre	0	0	0
2	c	-1	-1	1
3	b	-1	1	-1
10C	centre	0	0	0
5	a	1	-1	-1
7	ab	1	1	-1

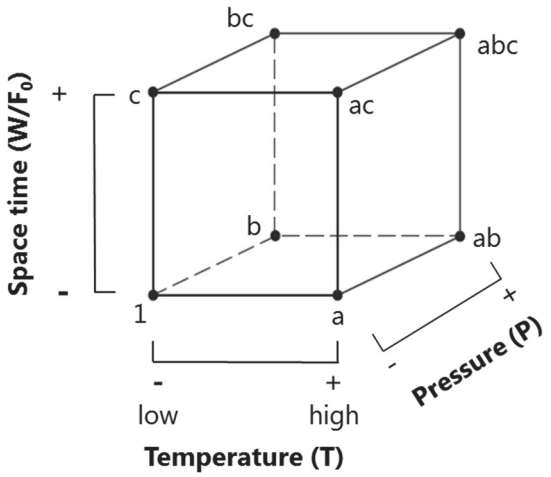

Figure A.1. Geometric representation of the 2^3+2 factorial design.

To estimate the main effects of variable T, four considerations are taken into account. First, effect *[a-(1)]/n* of T, when P and W/F_0 are at the low level. Second, effect *[ab-b]/n* when P is at the high level and W/F_0 at the low level. Third, effect *[ac-c]/n* when

W/F_0 is the high level and P at the low level. And last, effect *[abc-bc]/n* when P and W/F_0 are both at the high level. Hence, the effect of the variable T on the design is estimated as the average of the four effects of the factor:

$$T_{effect} = \frac{\left[a+ab+ac+abc-(1)-b-c-bc\right]}{4n} \quad (A.1)$$

being a, b, c, and their combinations the numerical values of the response variable. Similarly, the average effects of other factors are estimated as shown in equations A.2 and A.3:

$$P_{effect} = \frac{\left[b+ab+bc+abc-(1)-a-c-ac\right]}{4n} \quad (A.2)$$

$$W/F_{0effect} = \frac{\left[c+ac+bc+abc-(1)-a-b-ab\right]}{4n} \quad (A.3)$$

The interaction between T and P (T-P) is used as an example to estimate the effect of the two-factors interaction, by the difference between the average effect of T in the high and low levels of P (Table A.2.). The interaction between two factors is considered to be one-half of this difference [133].

Table A.2. Two-factors interaction effect of T at the two P levels.

Factor P	T average effect
High level	$\frac{\left[abc-bc\right]+\left[ab-b\right]}{2n}$
Low level	$\frac{\left[ac-c\right]+\left[a-(1)\right]}{2n}$
Difference	$\frac{\left[abc+ab+c+(1)-bc-b-ac-a\right]}{2n}$

Then, the effect of the interaction between T-P is half the difference:

$$T\text{-}P_{effect} = \frac{\left[abc+ab+c+(1)-bc-b-ac-a\right]}{4n} \quad (A.4)$$

In the same way, the main effect of the other interactions between two factors are estimated as follows:

$$T\text{-}W/F_{0\ effect} = \frac{\left[(1)+b+ac+abc-a-ab-c-bc\right]}{4n} \quad (A.5)$$

$$P\text{-}W/F_{0\ effect} = \frac{\left[(1)+a+bc+abc-b-ab-c-ac\right]}{4n} \quad (A.6)$$

Finally, the effect of the three-factors interaction, defined as the average of the difference between T-P interaction, at the two levels of W/F_0, is calculated:

$$T\text{-}P\text{-}W/F_{0\ effect} = \frac{\left[abc+a+b+c-(1)-ab-ac-bc\right]}{4n} \quad (A.7)$$

The terms in square brackets in the equations are contrasts of the combinations. From those contrasts, the factor or combination of factors effects in the experiments are identified, as presented in Table A.3, by summarizing the level of each possible combination in every experiment.

Table A.3. Effects in the 2^3 design calculated by algebraic signs.

Operative variables combinations	**Factorial effect**						
	T	P	T-P	W/F_0	$T\text{-}W/F_0$	$P\text{-}W/F_0$	$T\text{-}P\text{-}W/F_0$
(1)	-	-	+	-	+	+	-
a	+	-	-	-	-	+	+
b	-	+	-	-	+	-	+
ab	+	+	+	-	-	-	-
c	-	-	+	+	-	-	+
ac	+	-	-	+	+	-	-
bc	-	+	-	+	-	+	-
abc	+	+	+	+	+	+	+

The high and low levels are associated with + and – signs, respectively. First, the main effects T_{effect}, P_{effect} and $W/F_{0\ effect}$ are assigned with the correspondent sign, then the interaction sign is designated as the product of the signs of the factors involved (same row), and yield to a new column in the table, and so on [133].

A.1. ANALYSIS OF VARIANCE AND PROBABILITY TEST

The differences in the observed runs, for a certain response variable, can be due to fluctuation (or noise), which is a statistical error. The presence of error implies that the response variable is a random variable with a set of possible values, which is usually described graphically (probability structure). The probability distribution of a response variable assists in the statistical analysis for the estimation of the sample mean, variance, expected values and hypothesis testing.

The variability or dispersion of the probability distribution is measured by the variance, which is expressed as the sum of squares [133]. In the 2^3 design where n replicates the sum of squares for any effect (SS_f), is normally calculated by equation A.8, where f is the factor effect (T_{effect}, P_{effect} or $W/F_{0\ effect}$), the two-factor and three-factor interactions effect. As each effect has a single-degree-of-freedom contrast, which makes SS_f calculations easier [133],

$$SS_f = \frac{(Contrast)_f^2}{8n} \tag{A.8}$$

Equation A.9 shows the usual way to calculate the total sum of squares:

$$SS_T = \sum_{i=1}^{a}\sum_{j=1}^{b}\sum_{k=1}^{c}\sum_{l=1}^{n} y_{ijkl}^2 - \frac{y^2}{abcn} \tag{A.9}$$

where y is related to the sum of all the response variables observed; y_i corresponds to the total observations under the ith level of T (i= 1, 2, …, a); y_j the total observations under the jth level of P (j= 1, 2, …, b); and y_k the total observations under the kth level of W/F_0 factor (k= 1, 2, …, c). Similarly y_{ij}, y_{ik} and y_{jk} refer to the observation of the corresponding two-factors interaction.

To determine which variables are likely to be important, the factor effect on a response variable is accepted when the factor mean square is higher than the error mean square, which indicates the unlikeliness of obtaining equal values of the response variables, in experiments with different values of the factor tested.

Analysis of variance (ANOVA) is used to confirm these determinations. The F distribution is employed for the probability testing. One way to report the results of a hypothesis test is to state that the null hypothesis H_0 in equation A.10, was or was not rejected at a specified level of significance α_s. By rejecting H_0, confirms that the effect of the factor (or factors interaction) over the response variable is significant.

$$H_0: \mu_{(1)} = \mu_{(-1)} \tag{A.10}$$

being $\mu_{(1)}$ and $\mu_{(-1)}$ the mean of a factor in the levels (1) and (-1) respectively.

The F distribution is used to calculate the confidence interval or p-value (p) from the respective statistic tables. Nonetheless, in this work, ANOVA estimations are carried out by the *Statistica 10* software. The p-value is the probability that the test statistic will take on a value that is at least as extreme as the observed value of the statistic when the null hypothesis H_0 is true [133]. The p-value gives information about the weight of evidence against H_0, thus conclusions can be taken at any specified level of significance, in this case, α_s=0.05. In this line, p is the smallest level at which the effect is significant, with a 95% confidence level ($p < \alpha_s$). Recall that α_s is the value of the probability of type I error, which is when the null hypothesis is rejected when it is true.

A.2. SINGLE REPLICATE 2^k FACTORIAL DESIGN AND CENTRE POINT REPLICATES

The factorial experiments in the proposed design are 8 (l= 8) since the design of experiments completed herein is a single replicate (n= 1) of 2^3 factorial design. The proposed design includes n_c= 2 replicates at the centre point of T, P and W/F_0 at their 0 levels (rows 9C and 10C in Table A.1.). An independent estimation of the mean square for pure error ($MS_{Pure\ Error}$) is obtained from the replicates at the centre point as shown in the following equation:

$$MS_{PureError} = \frac{SS_E}{n_c - 1} = \frac{\sum_{CenterPoints} \left(y_i - \bar{y}_c\right)^2}{n_c - 1} \quad (A.11)$$

being y_i the observed values at the centre points and $\bar{y}_c$ the average of the observations of the centre points.

A.3. MODELLING FITTING AND RESPONSE SURFACE METHODOLOGY

The experimental results given as an empirical model facilitate understanding and predictions. The relationship between T, P and W/F_0 is defined by a regression model, which is fitted by the sample data in the design. The following empirical models f_1, f_2, f_3 and f_4 are aimed to be defined,

$$X_{Gly} = f_1(T, P, W/F_0)$$
$$X_{Gas} = f_2(T, P, W/F_0)$$
$$YH_2 = f_3(T, P, W/F_0)$$
$$SH_2 = f_4(T, P, W/F_0)$$

The 2^k design considers a linear relationship between the effects of the different factors. The response hyperplane is defined by fitting to a standard multiple linear regression model, as follows:

$$y = \beta_o + \beta_i T_i + \beta_j P_j + \beta_k W/F_{0\,k} + \beta_{ij}(T\text{-}P)_{ij} + \beta_{ik}(T - W/F_0)_{ik} + \beta_{jk}(P - W/F_0)_{jk} + \varepsilon \quad (A.12)$$

where y refers to the response (X_{Gly}, X_{Gas}, YH_2 and SH_2); β are the regression coefficients, which quantify the expected change in y due to a unit change in the value of a respective variable (i, j or k), when all other independent variables remain constant; T_i, P_j and $W/F_{0\,k}$ are the independent variables (or regressor variables) related to the value of T, P and W/F_0, respectively; and ε is a random error term.

Any regression model that is linear in the parameters (β), is a linear regression model, regardless of the shape of the response surface that it generates [133]. Nonetheless, with the addition of two-factor interactions $(T\text{-}P)_{ij}$, $(T - W/F_0)_{ik}$ and (P-

$W/F_0)_{jk}$ certain curvature is added (equation A.12). Worthy of mentioning is that the fitting model used is considered a first-order response surface, which in a certain situation, the curvature acquired by the response variable could be underestimated. However, replicating centre points in the 2^k design protects from second-order curvature effects in the modelling. Accordingly, the pure quadratic curvature sum of squares is calculated as presented in equation A.13, indicating if there is or not evidence of second-order curvature in the response over the region of experimentation [133].

$$SS_{Curvatr.} = \frac{n_f n_c (\overline{y}_f - \overline{y}_c)^2}{n_f + n_c} \tag{A.13}$$

being $\overline{y}_f$ the average of the observations in the design and n_f the number of factorial design points.

That is by calculating the p-value statistic by using the $SS_{Curvatr.}$ in equation A.13, which determines if there is evidence of second-order curvature in the response over the region of exploration. To be more specific, when centre points are added to the 2^k design, the curvature test responds to the hypothesis in equations A.14 [133], indicating that there is no second-order curvature by accepting H_0, which means that the value of the quadratic regression coefficients in the model is 0.

$$H_0 : \sum_{i=1}^{I} \beta_{ii} = 0 \tag{A.14}$$

In this line, the effect of the factors and interactions between factors over the quantitative model is tested by the probability statistic. The ANOVA for a model contains different parameters than those for the sample experiments. Depicted there, are the regression coefficients, as well as the R^2, which measure the proportion of total variability as explained by the model. The test of significance of any effect is conducted by comparing the effect estimates to its standard error, this is a t statistic with (N_r-p_m= total number of runs – number of model parameters) [133]. The 100(1-α_s) percentage confidence intervals are also calculated, indicating the important factors when the intervals do not include zero, with approximately 95% confidence.

B. MASS TRANSFER LIMITATION

The criteria for mass transfer limitations are estimated through the Weisz-Prater criterion Φ_{WP} and the Mears criterion *MR* as explained in Chapter 2.

The Table B.1 depicts the parameters involved for estimations relative to the supported and bulk Ni-based catalysts evaluated during the screening in Chapter 3. All the evaluated catalysts meet Φ_{WP} and *MR* criteria, confirming the absence of internal and external mass diffusion effects, which can affect the activity results.

Table B.1. Parameters of mass transfer limitation for the supported and bulk catalysts studied in Chapter 3.

Parameters	Ni/Al	Ni/Y	MgNiAl	CoNiAl	NiAl
r_{obs} ($mol_{Gly}·s^{-1}·kg_{cat}^{-1}$)	$9.74x10^{-4}$	$5.60\ x10^{-5}$	$1.57x10^{-3}$	$5.02\ x10^{-3}$	$4.44x10^{-3}$
ρ_{cat} ($kg·m^{-3}$)	2283	2358	6331	2793	3473
$C_{Gly,S}$ ($mol_{Gly}·m^{-3}$)	1136	1013	1050	1177	1038
Φ_{WP}< 0.6	0.01	$6.99x10^{-4}$	0.05	0.06	0.08
ρ_{bed} ($kg·m^{-3}$)	1212	788	1212	1212	1212
Re	0.19	0.19	0.19	0.19	0.2
Sc	11.61	11.61	11.61	11.61	11.61
Sh	4.36	2.20	4.36	4.36	4.4
K_c ($m·s^{-1}$)	$3.26x10^{-4}$	$1.65x10^{-4}$	$3.26x10^{-4}$	$3.26x10^{-4}$	$3.26x10^{-4}$
***MR*< 0.15**	$2.56x10^{-4}$	$2.12x10^{-5}$	$4.45x10^{-4}$	$1.27\ x10^{-3}$	$1.24x10^{-3}$

The Weisz–Prater parameter (Φ_{WP}) and Mears's criterion (*MR*) evaluated for NiAl-T solids, which were addressed in Chapter 5 are depicted in Table B.2. Values of Φ_{WP} were lower than 0.6 indicating that there are no internal diffusion limitations [121]. In addition, external mass transfer effects are neglected since values of the MS were lower than 0.15.

Table B.2. Parameters of mass transfer limitations for NiAl-T catalysts tested at 250 ºC and 45 bar.

Parameter	NiAl-300	NiAl-450	NiAl-600	NiAl-700	NiAl-850
r_{obs} ($mol_{Gly}·s^{-1}·kg_{cat}^{-1}$)	$1.37x10^{-5}$	$2.79x10^{-4}$	$5.23x10^{-3}$	$6.02x10^{-3}$	$7.85x10^{-3}$
ρ_{cat} ($kg·m^{-3}$)	3473	3473	3473	3473	3473
$C_{Gly,S}$ ($mol_{Gly}·m^{-3}$)	1175	1148	1183	1038	1270
Φ_{WP}< 0.6	$2.1x10^{-4}$	$4.4x10^{-3}$	$7.9x10^{-2}$	$1.0x10^{-1}$	$1.1x10^{-1}$
ρ_{bed} ($kg·m^{-3}$)	1212	1212	1212	1212	1212
Re	0.19	0.19	0.19	0.19	0.19
Sc	11.13	11.13	11.13	11.13	11.13
Sh	4.31	4.31	4.31	4.31	4.31
K_c ($m·s^{-1}$)	$3.33x10^{-4}$	$3.33x10^{-4}$	$3.33x10^{-4}$	$3.33x10^{-4}$	$3.33x10^{-4}$
***MR*< 0.15**	$3.4x10^{-6}$	$7.1x10^{-5}$	$1.3x10^{-3}$	$1.7x10^{-3}$	$1.8x10^{-3}$

Besides, limitations of diffusional control were evaluated for the reactions performed in the frame of the coupled T/P variable conditions in the APR over NiAl-T catalysts in Chapter 5, results are shown in Table B.3. The values of Φ_{WP} were between $2.2x10^{-5}$ to $1.1x10^{-1}$ depending on the operating conditions. Therefore, internal diffusion limitation can be neglected. In the same line, the absence of external mass transfer limitation is confirmed according with *MS* values between $3.6x10^{-7}$ to $1.1x10^{-3}$ subjected to the operating conditions.

Table B.3. Parameters of mass transfer limitations for the study of the effect of temperature in the APR with NiAl-T catalysts.

Conditions T/P	Parameter	NiAl-300	NiAl-450	NiAl-600	NiAl-700	NiAl-850
235 ºC/ 35 bar	Φ_{WP}<0.6	$2.2x10^{-5}$	$6.2x10^{-3}$	$7.0x10^{-2}$	$8.7x10^{-2}$	$9.7x10^{-2}$
	MR<0.15	$3.6x10^{-7}$	$9.8x10^{-5}$	$1.1x10^{-3}$	$1.4x10^{-3}$	$1.5x10^{-3}$
250 ºC/ 60 bar	Φ_{WP}<0.6	$3.4x10^{-4}$	$6.3x10^{-3}$	$8.4x10^{-2}$	$1.1x10^{-1}$	$1.1x10^{-1}$
	MR<0.15	$5.7x10^{-6}$	$1.0x10^{-4}$	$1.4x10^{-3}$	$1.7x10^{-3}$	$1.9x10^{-3}$

Diffusion limitations have also been discarded for the Mg- and Ce-modified catalysts as shown in Table B.4.

Table B.4. Parameters of mass transfer limitations for XMg/NiAl and XCe/NiAl catalysts.

Parameter	3Mg/NiAl	5Mg/NiAl	10Mg/NiAl	3Ce/NiAl	5Ce/NiAl	10Ce/NiAl
r_{obs} ($mol_{Gly} \cdot s^{-1} \cdot kg_{cat}^{-1}$)	4.10×10^{-3}	$\times 10^{-3}$	2.93×10^{-3}	5.07×10^{-3}	5.21×10^{-3}	5.93×10^{-3}
ρ_{cat} ($kg \cdot m^{-3}$)	3049	2874	2645	3049	3145	2959
$C_{Gly,S}$ ($mol_{Gly} \cdot m^{-3}$)	1038	1046	1046	1046	1062	1046
Φ_{WP}<0.6	6.5×10^{-2}	6.2×10^{-2}	4.0×10^{-2}	7.9×10^{-2}	8.3×10^{-2}	9.0×10^{-2}
ρ_{bed} ($kg \cdot m^{-3}$)	1212	1212	1212	1212	1211	1212
Re	0.19	0.19	0.19	0.19	0.19	0.19
Sc	11.13	11.13	11.13	11.13	11.13	11.13
Sh	4.31	4.31	4.31	4.31	4.31	4.31
K_c ($m \cdot s^{-1}$)	3.26×10^{-4}	3.26×10^{-4}	3.26×10^{-4}	3.26×10^{-4}	3.26×10^{-4}	3.26×10^{-4}
***MR*<0.15**	1.2×10^{-3}	1.2×10^{-3}	8.3×10^{-4}	1.4×10^{-3}	1.5×10^{-3}	1.7×10^{-3}

The same diffusion limitation calculations were performed for the catalytic test of nanocasting catalysts in Chapter 7. Obtained values of Φ_{WP} and MR properly accomplish the criteria as shown in Table B.5, which indicates the absence of diffusion limitations [121].

Tabla B.5. Parameters of mass transfer limitations for supported (NiAl/SBA-15) and nanocasted catalysts.

Parameter	NiAl/SBA-15	NiAl-NCF	NiAl-NCN
r_{obs} ($mol_{Gly} \cdot s^{-1} \cdot kg_{cat}^{-1}$)	4.06×10^{-4}	1.38×10^{-3}	5.73×10^{-3}
ρ_{cat} ($kg \cdot m^{-3}$)	6490	2797	6490
$C_{Gly,S}$ ($mol_{Gly} \cdot m^{-3}$)	1016	1033	1046
Φ_{WP}<0.6	1.4×10^{-2}	2.0×10^{-2}	1.9×10^{-1}
ρ_{bed} ($kg \cdot m^{-3}$)	788	788	788
Re	0.19	0.19	0.19
Sc	11.13	11.13	11.13
Sh	2.20	4.37	2.20
K_c ($m \cdot s^{-1}$)	1.64×10^{-4}	3.26×10^{-4}	1.64×10^{-4}
MR<0.15	1.5×10^{-4}	2.6×10^{-4}	2.0×10^{-3}

C. DERIVED CONTRIBUTIONS

C1. Scientific publications

Authors: A. Morales-Marín, J.L. Ayastuy, U. Iriarte-Velasco, M.A. Gutiérrez-Ortiz

Title: Biohydrogen production by glycerol Aqueous-Phase Reforming: Effect of promoters (Ce or Mg) in the $NiAl_2O_4$ spinel-derived catalysts

Source: J. Environ. Chem. Eng. 9 (2021) 106433.

Impact factor (2020): 5.88.

Authors: A. Morales-Marín, J.L. Ayastuy, U. Iriarte-Velasco, M.A. Gutiérrez-Ortiz.

Title: Nickel aluminate spinel-derived catalysts for the aqueous pase reforming of glycerol: Effect of reduction temperature.

Source: Appl. Catal. B Environ. 244 (2019) 931-945.

Impact factor (2019): 16.79.

C2. Congress contributions

IV Encuentro de Jóvenes Investigadores de la Sociedad Española de Catálisis (JJII 2020), Bilbao (Spain), 21-23 September 2020.

Contribution type: Poster.

Title: APR de glicerol sobre catalizadores de niquel optimizados: efecto del tiempo de contacto.

Authors: A. Morales-Marín, J.L. Ayastuy, U. Iriarte-Velasco, M.A. Gutiérrez-Ortiz.

14th European Congress on Catalysis (EUROPACAT 2019), Aachen (Germany), 18-23 August 2019.

Contribution type: Poster.

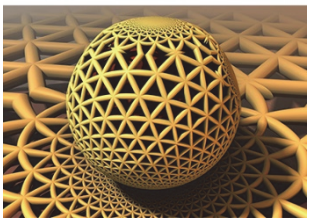

Title: Effect of a promoter (Ce or Mg) on the catalytic performance of nickel aluminate catalysts in the Aqueous Phase Reforming (APR) of glycerol.

Authors: A. Morales-Marin, A.J. Reynoso, U. Iriarte, M.A. Gutierrez-Ortiz, J.L. Ayastuy.

XXVI Congresso Ibero-Americano de Catálise (CICAT 2018), Coimbra (Portugal), 9-14 September 2018.

Contribution type: Poster.

Title: Efecto de la adición de Ce sobre el rendimiento en el reformado acuoso de glicerol de catalizadores de Ni y Co obtenidos a partir de sus aluminatos.

Authors: A. Morales-Marin, A.J. Reynoso, J.L. Ayastuy, U. Iriarte, M.A. Gutierrez-Ortiz, A. Molinuevo.

III Encuentro de Jóvenes Investigadores de la Sociedad Española de Catálisis (JJII 2018), Valencia (Spain), 25-27 June 2018.

Contribution type: Oral.

Title: Ce como promotor de catalizadores de níquel derivados de $NiAl_2O_4$ para obtención de H_2 por reformado acuoso de glicerol.

Authors: A. Morales-Marín, J.L. Ayastuy, A.J. Reynoso, U. Iriarte-Velasco, M.A. Gutiérrez-Ortiz.

HYdrogen POwer THeoretical & Engineering Solutions International Symposium (HYPOTHESIS XII), Siracusa (Italy), June 2017.

Contribution type: Poster.

Title: Glycerol aqueous phase reforming on spinel-derived Ni-alumina catalysts: effect of the process variables.

Authors: A. Morales-Marín, A.J. Reynoso, J.L. Ayastuy, M.A. Gutiérrez-Ortiz.

Reunión Bienal de la Sociedad Española de Catálisis (SECAT'17), Oviedo (Spain), 26-28 June 2017.

Contribution type: Oral.

Title: Hydrogen production by glycerol aqueous phase reforming on spinel-derived Ni/Al_2O_3 catalysts: Study of the nickel speciation.

Authors: A. Morales-Marín, A.J. Reynoso, J.L. Ayastuy, U. Iriarte-Velasco, M.A. Gutiérrez-Ortiz.

II Encuentro de Jóvenes Investigadores de la Sociedad Española de Catálisis (JJII 2016), Ciudad Real (Spain), 27-29 June 2016.

Contribution type: Poster.

Title: Preparación y caracterización de catalizadores de espinela de níquel para reformado en fase acuosa de glicerol.

Authors: A. Morales-Marín, A.J. Reynoso, M.A. Gutiérrez-Ortiz, J.L. Ayastuy.

V Jornadas de Investigación de la Facultad de Ciencia y Tecnología de la UPV/EHU, Leioa (Spain), 6-7 April 2016.

Contribution type: Oral.

Title: Obtención de hidrógeno por reformado catalítico en fase acuosa de compuestos oxigenados derivados de la biomasa (glicerol).

Authors: A. Morales-Marín, A.J. Reynoso, J.L. Ayastuy, M.A. Gutiérrez-Ortiz.

I Jornadas Doctorales de la UPV/EHU, Leioa (Spain), 11-12 July 2016.

Contribution type: Poster.

Title: Caracterización de precursores catalíticos tipo espinela de níquel para reformado en fase acuosa de glicerol.

Authors: A. Morales-Marín, A.J. Reynoso, M.A. Gutiérrez-Ortiz, J.L. Ayastuy.

Reunión Bienal de la Sociedad Española de Catálisis (SECAT'15), Barcelona (Spain), 13-15 July 2015.

Contribution type: Poster.

Title: Efecto de la temperatura de reducción del precursor catalítico espinela $NiAl_2O_4$ en el reformado en fase acuosa (APR) de glicerol.

Authors: A. Morales-Marín, M. Gil-Calvo, R. López-Fonseca, B. de Rivas, J.I. Gutiérrez-Ortiz, J.L. Ayastuy*, M.A. Gutiérrez-Ortiz

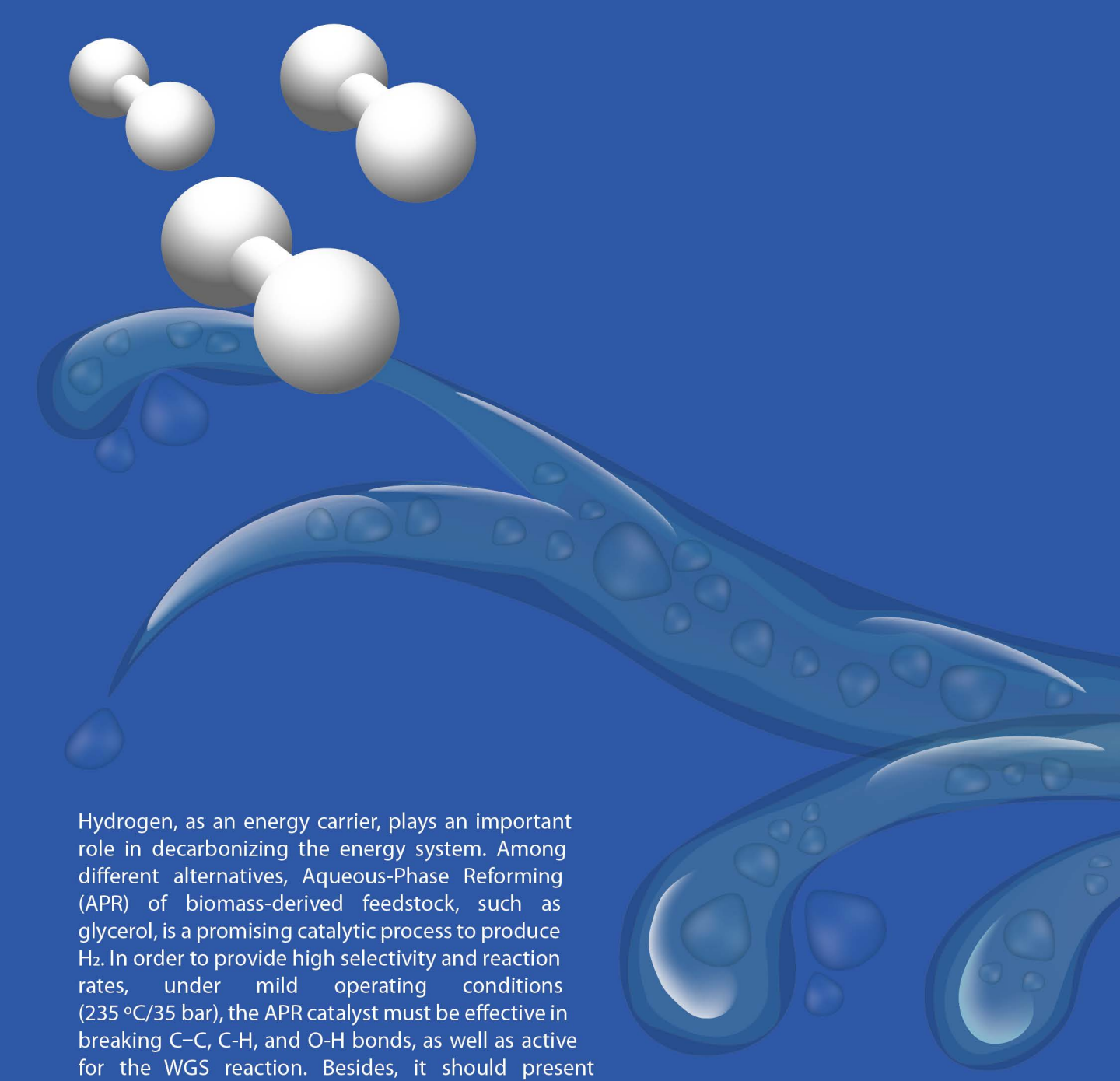

Hydrogen, as an energy carrier, plays an important role in decarbonizing the energy system. Among different alternatives, Aqueous-Phase Reforming (APR) of biomass-derived feedstock, such as glycerol, is a promising catalytic process to produce H_2. In order to provide high selectivity and reaction rates, under mild operating conditions (235 °C/35 bar), the APR catalyst must be effective in breaking C−C, C-H, and O-H bonds, as well as active for the WGS reaction. Besides, it should present resistance to deactivation under the harsh hydrothermal conditions of the APR.

In this thesis, the potential of nickel aluminate spinel ($NiAl_2O_4$) as a catalytic precursor is determined. The effect of the reduction temperature on the catalytic precursor is studied establishing correlations between the physicochemical properties and the catalytic performance. Complementarily, two strategies for the $NiAl_2O_4$ optimization are examined. First, the addition of Mg and Ce surface promoters, and then, the alternative synthesis by the novel nanocasting method. Upon reduction, the spinel precursor allows the formation of small (< 14 nm) and stable metallic Ni particles. Besides, its adequate stability leads to stable H_2 yield during long term runs (50 h TOS) and shows potential to be used in the APR of glycerol.